Comparison of Turbulence Model Predictions in Rod Bundles with Supercritical Up-Flow

by

Cale M. Bergmann

A Thesis submitted to the Faculty of Graduate Studies of
The University of Manitoba
in partial fulfillment of the requirements of the degree of

MASTER OF SCIENCE

Department of Mechanical Engineering
University of Manitoba
Winnipeg

ABSTRACT

Vertical up-flow of supercritical fluid in the subchannel of a heated rod bundle was numerically simulated using the Computational Fluid Dynamics (CFD) codes ANSYS CFX and ANSYS FLUENT. A total of seven cases from three different sets of experiments were simulated. Three-dimensional steady-state predictions of fluid velocity, pressure, and temperature were made using five versions of two-equation RANS turbulence models with accompanying wall treatments. In addition, the temperature distribution in a solid region comprising a heater and sheathing was also computed in some cases.

The k-epsilon turbulence model, implemented using CFX and scalable wall functions, provided the numerical results that have the smallest overall deviation from experimental results for three of the seven cases, and predicts the experimental data of the remaining four cases reasonably well, unlike other turbulence models that severely over-predict the experimental data for wall surface temperature.

ACKNOWLEDGEMENTS

I would like to thank my advisors, Dr. S.J. Ormiston and Dr. V. Chatoorgoon for giving me the opportunity to work on this project and for their valuable support. The financial support of the NSERC/NRCan/AECL Gen IV Energy Technologies Program, the University of Manitoba, the University of Manitoba Faculty of Graduate Studies (FGS), the University of Manitoba Graduate Students' Association (UMGSA), the University of Manitoba Faculty of Engineering, and the University of Manitoba Department of Mechanical Engineering is gratefully acknowledged.

TABLE OF CONTENTS

LIST OF TABLES

LIST OF FIGURES

NOMENCLATURE

A	Area, m^2
a	Matrix containing the coefficients of the coupled system of linear equations
a_p	Representative coefficient of the control volume calculated by CFX
B	Constant appearing in log law of the wall
$\mathcal{B}$	Advection scheme variable
b	Matrix on the right hand side of the coupled system of linear equations
b_{ij}	Normalized Reynolds stress anisotropy
c_p	Specific heat capacity at constant pressure, J/kgK
D_h	Hydraulic diameter, m
D_i, D_o	Inside and outside diameter of hollow heater rod, m
E	Total energy, J/kg
F_k	Turbulence kinetic energy flux, kg/s^3

F_U	Momentum flux, kg/ms
f_μ	Damping function for low Reynolds k-ε turbulence models
$f_{\mu,LB}$	Damping function of the Lam-Bremhorst low Reynolds k-ε turbulence model
$f_{\mu,YS}$	Damping function of the Yang-Shih low Reynolds k-ε turbulence model
G	Mass flux, kg/m^{2}s
g_i	Acceleration of gravity in i-direction, where i is *x*, *y*, or *z*, m/s^2
$\vec{g}$	Acceleration of gravity in vector form, m/s^2
h	Specific enthalpy, J/kg
h_b	Bulk specific enthalpy, J/kg
I	Turbulence intensity, %
k	Turbulence kinetic energy, m^2/s^2
k_{inlet}	Turbulence kinetic energy at inlet, m^2/s^2
N	Total number of sample locations along a reference line or in a reference plane

$\mathcal{N}$	Shape function
$N_{boundaries}$	The total number of boundaries in each domain
$\mathbb{N}_{faces}$	Total number of faces of a control volume
$\mathbb{N}_{ip}$	Total number of integration points on a control volume
$\mathbb{N}_{node}$	Total number of nodes of a mesh element
P	Static pressure, Pa
P'	Modified pressure, Pa
P_{abs}	Absolute pressure, Pa
P_f	Pressure at cell faces, Pa
P_k	Turbulence production due to viscous forces, kg/ms^3
P_{kb}	Turbulence production due to buoyancy, kg/ms^3
$P_{\varepsilon b}$	Turbulence dissipation due to buoyancy, used in k-ε turbulence models, kg/ms^3
$P_{\omega b}$	Turbulence dissipation due to buoyancy, used in the SST turbulence model, kg/ms^3

$\mathrm{Pr_t}$	Turbulent Prandtl number
q	Heat rate, W
$\dot{q}$	Volumetric heat rate, W/m^3
q_w"	Heat flux at the wall, W/m^2
R	Radial position in a cylindrical coordinate system, m
R_y	Turbulence Reynolds number
Re	Reynolds number
$\vec{r}$	Position vector, m
$\vec{r}_{ref}$	Buoyancy reference location, specified at the centroid of the outlet, m
r_ψ	Raw residual calculated by CFX
$\tilde{r}_\psi$	Normalizes residual calculated by CFX
S	Magnitude of strain rate tensor, 1/s
S_E	Thermal energy source term, W/m^3
S_{ij}	Strain rate tensor, 1/s

$S_{M,buoy}$	Momentum source term due to buoyancy, kg/m^2s^2
S_{U_i}	Momentum source term, kg/m^2s^2
S_ε	Low Reynolds k-ε turbulence model source term, kg/ms^4
S_φ	Scalar source term
T	Temperature, K
T^+	Non-dimensional temperature
T_{in}	Fluid inlet temperature, K
T_{ref}	Reference temperature, K
$T_{s,o}$, $T_{s,i}$	Outer and internal surface temperature of hollow heater rods, K
T_w	Fluid temperature at the wall, K
t	Time, s
t	Turbulent fluctuating temperature, K
U	Mean flow velocity, m/s

U_i, U_j, U_k	Mean flow velocities relative to i, j, and k in a three dimensional Cartesian coordinate system, m/s
u^*	Modified friction velocity, m/s
u_i, u_j	Turbulent fluctuating velocities, m/s
u_τ	Friction velocity, m/s
$u_{\tau,CFX}$	Friction velocity, specific to automatic wall treatment of CFX, m/s
u_τ^{log}	Component of friction velocity from log layer of the near wall region, m/s
u_τ^{vis}	Component of friction velocity from viscous sublayer of the near wall region, m/s
$Vel_{par,g}$	Component of the velocity parallel to the gravitational vector, m/s
$Vel_{perp,g}$	Component of the velocity perpendicular to the gravitational vector, m/s
$\forall$	Volume, m^3
w	Velocity in *z*-direction, m/s

x, y, z	Position in a Cartesian coordinate system, m
x', y', z'	Local coordinate system to describe nodal positions in a mesh element, m
x_i, x_j, x_k	Position relative to i, j, and k in a three dimensional Cartesian coordinate system, m
y^+	Non-dimensional wall-normal distance
y^*_{Auto}	Non-dimensional wall-normal distance used by CFX for the automatic near wall treatment
y^*_{Scale}	Non-dimensional wall-normal distance used by CFX for the scalable wall function near wall treatment
y^*_{FLUENT}	Non-dimensional wall-normal distance used by FLUENT for the scalable wall function near wall treatment

Greek Letters

β^*	Variable appearing in the near wall treatment of the thermal energy equation
Γ, Γ_t	Dummy variable for scalar molecular diffusion and turbulent diffusion terms

Γ_{CFX}	Variable appearing in the automatic near wall treatment of the thermal energy equation of CFX
Γ_{CFX}	Variable appearing in the enhanced wall treatment of CFX
Δ	Difference between two quantities
Δn	Wall-normal distance between the first and second mesh points away the wall, m
$\Delta \mathbb{m}$	Discrete outward surface vector, m
∇	Vector differential operator
δ_{ij}	Kronecker delta function
ε	Turbulence dissipation rate, m^2/s^3
ε_{inlet}	Turbulence dissipation rate at inlet, m^2/s^3
θ	Angular position in a cylindrical coordinate system, rad
κ	von Kármán constant
λ	Thermal conductivity, W/mK
λ_t	Turbulent thermal conductivity, W/mK
μ	Dynamic viscosity, Pa s

μ_t	Eddy viscosity, Pa s
ν	Kinematic viscosity, m^2/s
ν_t	Eddy viscosity divided by density, m^2/s
ρ	Density, kg/m^3
ρ_{ref}	Reference density, kg/m^3
$\rho\overline{u_i u_j}$	Reynolds stress, N/m^2
τ	Magnitude of shear stress, N/m^2
τ_t	Turbulent time scale, s
τ_w	Shear stress at the wall, N/m^2
τ_{ij}	Shear stress, N/m^2
$(\tau_{ij})_{eff}$	Deviatoric stress tensor, N/m^2
Φ	Dummy variable for thermophysical property values
Φ_{CFX}, Φ_{NIST}	Dummy variable for thermophysical properties obtained through CFX FORTRAN and NIST REFPROP, respectively
φ	Dummy variable for representing scalar

ψ	Dummy variable representing solution variable
ψ_f	Dummy variable representing the face value of a solution variable
ψ_{range}	Representative value of the overall range in the solution variable calculated by CFX
ψ_{up}	Dummy variable representing the upwind cell centre value of a solution variable
ω	Specific turbulence dissipation, 1/s
$\omega_{l,CFX}$, $\omega_{l,FLUENT}$	Specific turbulence dissipation in the log layer for CFX and FLUENT, 1/s
ω_{inlet}	Specific turbulence dissipation at inlet, 1/s
ω_s	Specific turbulence dissipation in the viscous sublayer, 1/s
ω_ω	Specific turbulence dissipation throughout entire near wall region, 1/s

Subscripts

f	Face value
ip	Integration point

up	Upwind node of current integration point under consideration

Turbulence Equation Terms

$\arg_1$, $\arg_2$	Arguments of SST turbulence model blending functions
a_1, β'	SST turbulence model coefficients
α, β, σ_k, σ_ω	SST turbulence model coefficients, general form
α_i, β_i, σ_{ki}, $\sigma_{\omega i}$	SST turbulence model coefficients where i = 1, 2, or 3. If i = 1 then coefficients are specific to near wall region, if i = 2 then coefficient values are specific to the freestream region, and if i = 3 then coefficient values are a blend of the near wall and freestream coefficient values.
α_{RNG}	Generic terms used as placeholder in equation for two variables of the RNG k-ε turbulence model
$C_{\varepsilon 1,RNG}$, $C_{\varepsilon 2,RNG}$, $C_{\mu,RNG}$, $\alpha_{k,RNG}$, $\alpha_{\varepsilon,RNG}$, η	RNG k-ε turbulence model coefficients
$CD_{k\omega}$	Term in $\arg_1$, kg/m^{3}s^2
C_3, $C_{3\varepsilon}$, σ_ρ	Turbulence model coefficients related to buoyancy

C_μ, $C_{\varepsilon 1}$, $C_{\varepsilon 2}$, C_μ, σ_ε, $\sigma_{k\varepsilon}$	k-ε turbulence model coefficients
F_1, F_2	SST turbulence model blending functions
ϕ_1, ϕ_2, ϕ_3	Generic terms used as placeholders in SST turbulence model blending function

Abbreviations

BSL	Menter Baseline turbulence model
DNS	Direct numerical simulation
EARSM	Explicit Algebraic Reynolds Stress Model
EWT	Enhanced wall treatment, used in FLUENT
GIF	Generation IV International Forum
HTD	Heat transfer deterioration
JAEA	Japan Atomic Energy Agency
Low-Re k-ε	Low Reynolds k-ε turbulence model
RANS	Reynolds-averaged Navier–Stokes
RSM	Reynolds Stress turbulence model

ω-RSM	omega-Reynolds Stress turbulence model
$RMS_{RN,T}$	Range-normalized root mean square of temperature differences, %
SCWR	Supercritical water-cooled reactor
SSG	Speziale-Sarkar-Gatski two-equation or Reynolds Stress turbulence model
SST	Shear Stress Transport turbulence model
SST-SAS	Shear Stress Transport based Scale-Adaptive Simulation turbulence model
UDS	Upwind Difference Scheme
VBA	Visual Basic for Applications

CHAPTER 1: INTRODUCTION

1.1. Supercritical Water Cooled Reactors

A Supercritical Water Cooled Reactor (SCWR) is a nuclear reactor design that uses supercritical water as the working fluid. Water at a pressure and temperature beyond the thermodynamic critical point, 22.06 [MPa] and 647.096 [K] (373.946 [ºC]), is considered supercritical. A SCWR is one of the six proposed nuclear reactor designs that is currently being researched by the Generation IV International Forum (GIF) for development in commercial applications as a Generation IV reactor. The five other proposed nuclear reactor designs are the Sodium-Cooled Fast Reactor (SFR), the Gas-Cooled Fast Reactor (GFR), the Lead-Cooled Fast Reactor (LFR), the Very-High-Temperature Reactor (VHTR), and the Molten Salt Reactor (MSR). The first meeting of the GIF took place in January 2000, when the U.S. Department of Energy's Office of Nuclear Energy, Science and Technology convened a meeting involving government representatives from various countries to begin discussions on international collaboration in the development of Generation IV nuclear energy systems. There are currently 13 member countries of the GIF: Argentina (non-active member), Brazil (non-active member), Canada, China, the European Atomic Energy Community (Euratom), France, Japan, South Korea, Russia, South Africa, Switzerland, United Kingdom (non-active member), and the United States.

There are currently two main design concepts for SCWRs: a pressure vessel concept proposed by Japan and Euratom, and a pressure tube concept proposed by Canada. The major difference between the two concepts are with the core design, otherwise they are very similar in terms of operating pressures, operating temperatures, materials, etc. The reason for the GIF pursuing the

commercialization of SCWRs is the improved economics that results from higher thermodynamic efficiency and simplified plant design. The thermal efficiency of SCWRs is expected to be 44 % or more compared to 34-36 % for current reactors [1].

Heat transfer and critical flow data are needed to validate thermal-hydraulic codes that are, or will be used to design SCWRs. Data from conventional water reactors cannot necessarily be used, since these reactors do not use supercritical water. The thermal-hydraulic behaviour, along with the large changes in thermophysical properties of the fluid near the critical point necessitates the gathering of supercritical and pseudocritical specific data. The Thermal-hydraulics and Safety Project Management Board is one of the four Project Management Boards in the SCWR system, and exists for the purpose of gathering these needed data. The work performed in the present study adds to this heat transfer and critical flow database for the design of SCWRs. The construction and operation of a prototype or demonstration SCWR system is expected to begin around 2025 and last approximately 10 years according to the GIF 2014 Technology Roadmap [1]. After this time the commercial implementation of SCWRs is expected to begin.

In the currently proposed SCWR design, water will be supplied directly to the reactor core in a once-through cycle, similar to current Boiling Water Reactors. A schematic of this SCWR design is given by Figure 1.

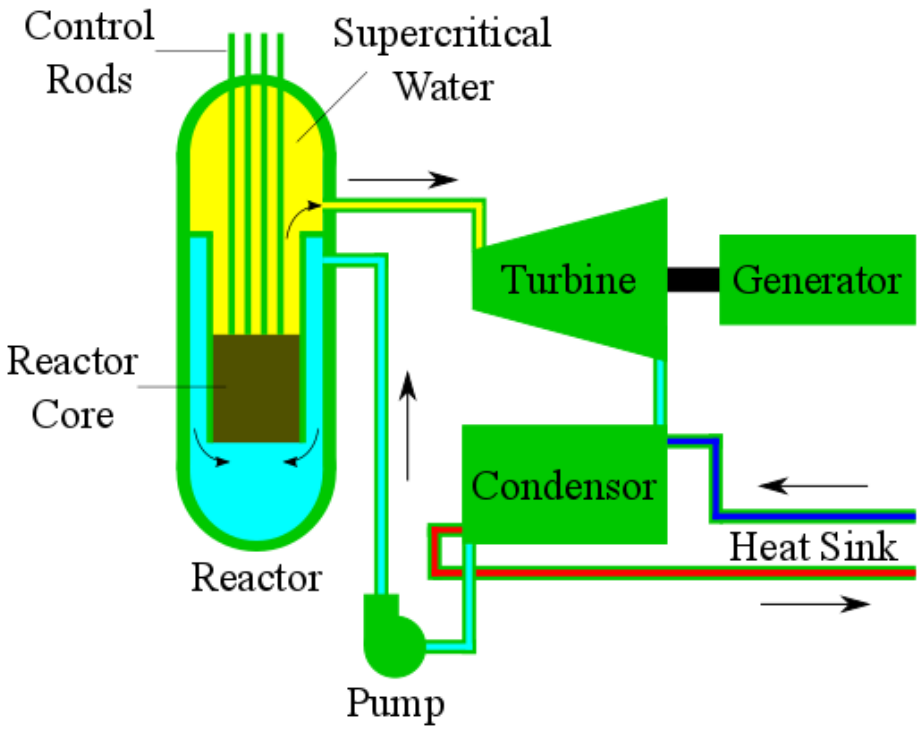

Figure 1: Schematic of the currently proposed SCWR.

The water becomes supercritical as it is heated in the reactor core. Because supercritical water has a much lower density than sub-supercritical water, its velocity must increase in order to maintain the same mass flow rate, thus satisfying the fundamental requirement of conservation of mass. This supercritical water is then supplied directly to a high pressure turbine which drives a generator, thereby producing electrical power. The water from the turbine will then cool as it passes through a condenser, and will no longer be at a supercritical state. This water is then supplied to the reactor core to complete the cycle.

1.2. Properties of Supercritical Fluids

The critical point is defined as the pressure and temperature, beyond which a liquid and its vapor can no longer coexist and phase boundaries disappear. A substance at a greater pressure and

temperature than that of the critical point exists as a single phase, and is referred to as a supercritical fluid. The pressure and temperature of the critical point of water is 22.06 [MPa] and 647.096 [K] (373.946 [ºC]), respectively. The pressure and temperature of the critical point of the refrigerant R12 (dichlorodifluoromethane) is 4.136 [MPa] and 385.12 [K] (111.97 [ºC]), respectively. The pseudocritical point is defined for a given pressure as the temperature at which the specific heat capacity at constant pressure, c_p, reaches a maximum value, so long as the pressure and temperature have both exceeded that of the critical point.

A phase diagram for water is given by Figure 2, and shows the critical point of water, a pseudocritical line that connects all pseudocritical points, and the various phases of water.

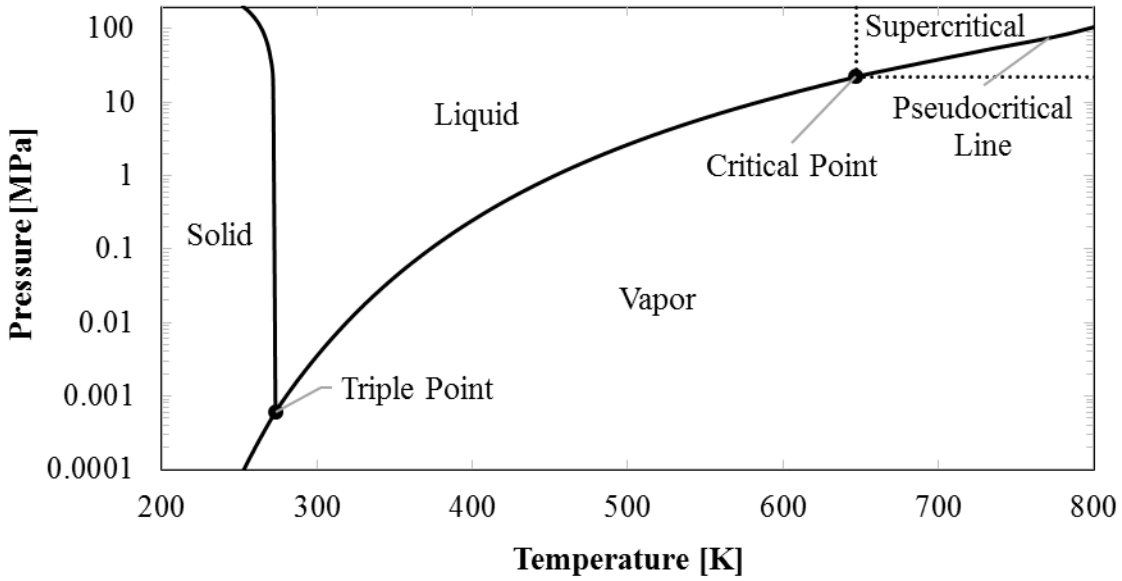

Figure 2: Phase diagram for water. Thermophysical property data obtained from NIST REFPROP v9.0 [2] and NIST WebBook [3].

The supercritical phase encompasses everything above and to the right of the critical point, and is enclosed by the dashed lines seen in Figure 2. The pseudocritical point is useful in describing certain heat transfer processes, such as the heating of fluids in rod bundles, the main topic of the

present study. For example, a fluid enters a rod bundle at a pressure exceeding that of the critical point but at a temperature lower than that of the critical point. This fluid is in the liquid phase, seen in Figure 2. The liquid is then heated as it flows along the heated rods, and eventually the temperature of the fluid exceeds that of the pseudocritical point as it enters the supercritical phase.

A hallmark of the critical and pseudocritical point is the simultaneous sudden spike in specific heat capacity, and sudden drop in density, thermal conductivity, and viscosity. The specific heat capacity at constant pressure and density of water near the pseudocritical temperature of 658.045 [K] are plotted in Figure 3, and the dynamic viscosity and thermal conductivity are plotted in Figure 4. The pressure of the water for these plots is 25 [MPa], the operating pressure of the experiments in the present study that use water. The same trends found in the following plots of the thermophysical properties of water can be seen at other pseudocritical points, as well as the critical point. These same trends can also be seen in other fluids, namely R12, which is the other fluid used in the experiments of the present study.

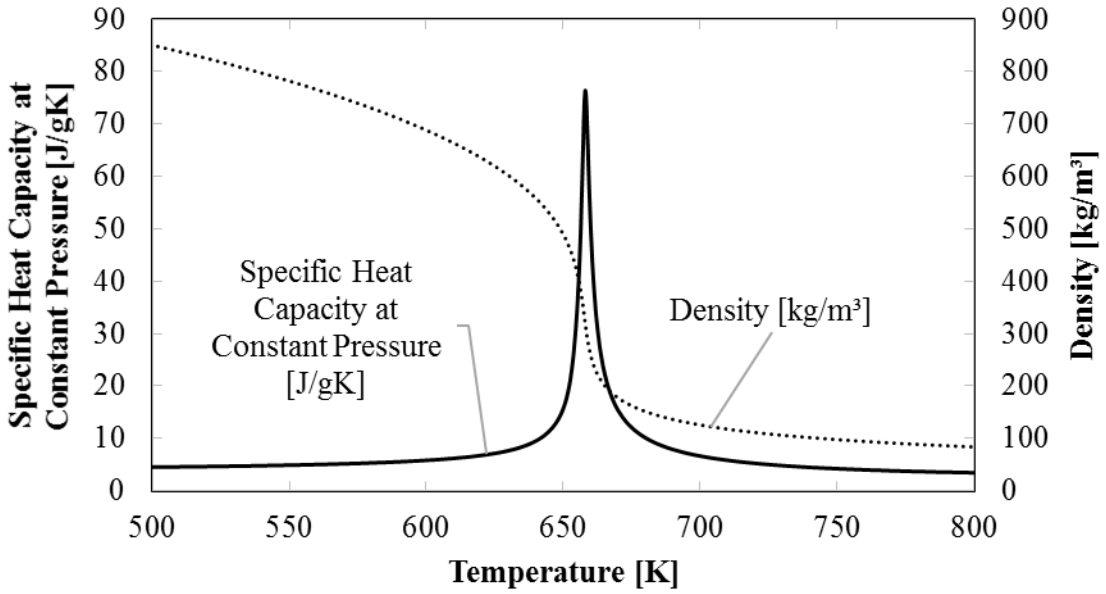

Figure 3: Specific heat capacity at constant pressure and density of water near the pseudocritical pressure and temperature of 25 [MPa] and 658.045 [K], respectively. Thermophysical property data obtained from NIST WebBook [3].

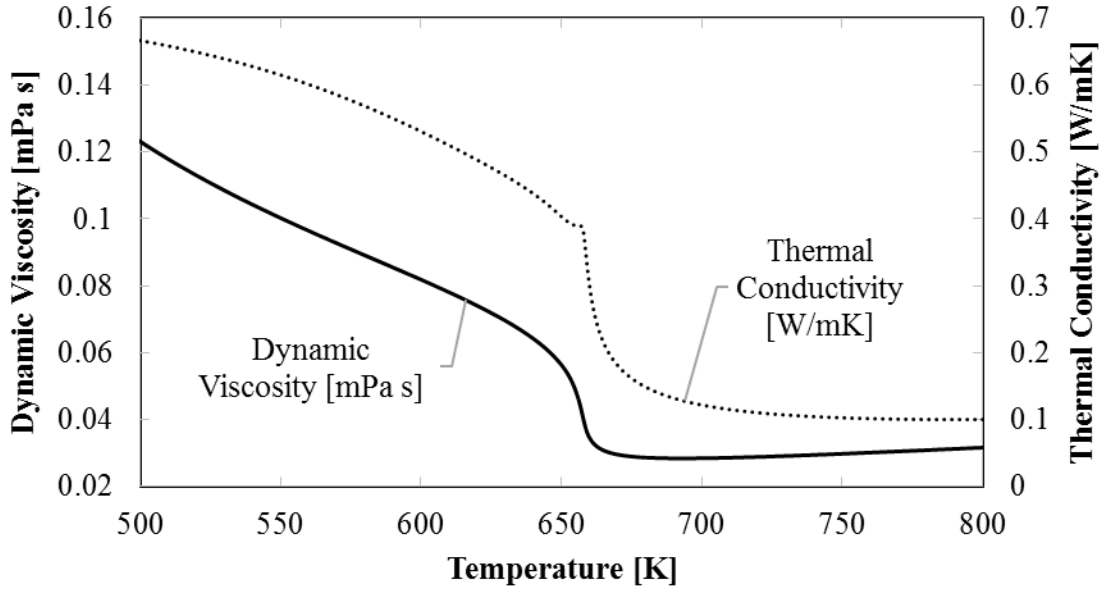

Figure 4: Dynamic viscosity and thermal conductivity of water near the pseudocritical pressure and temperature of 25 [MPa] and 658.045 [K], respectively. Thermophysical property data obtained from NIST WebBook [3].

As a fluid approaches the pseudocritical (or critical) point, the specific heat capacity rises sharply, while at the same time the density, thermal conductivity, and dynamic viscosity drop sharply. The specific heat capacity reaches a maximum when the fluid reaches the pseudocritical (or critical) point, then falls sharply to values similar to what they were before the pseudocritical (or critical) point. The density, thermal conductivity, and dynamic viscosity level off at values much lower than they were before the pseudocritical (or critical) point.

These sudden changes in the thermophysical properties of fluids contributes to the heat transfer phenomena known as heat transfer deterioration (HTD). HTD is a phenomena that causes sudden spikes in wall surface temperature, and has been observed in many heated tube, annuli, and rod bundle experiments. HTD is difficult to predict, and a large body of research has been and continues to be devoted to the topic of HTD in supercritical fluids.

1.3. SCWR Bundle Modelling

In order to use certain numerical methods in the design of SCWRs, they must first be validated with experiments that simulate real world conditions. Many experiments that have been performed were focused on studying the heat transfer behaviour of supercritical fluid in heated tubes and annuli, as is explained in better detail in Section 2.1.1. Experiments using heated rod bundles were later performed, as these better simulated the rod bundle assemblies in the reactor core of commercial nuclear reactors. Section 2.1.2 gives more details on these experiments. However, these heated rod bundle experiments are more costly and difficult to operate than heated tube and annuli experiments, and so there are far fewer experiments that use heated rod bundles than heated tube and annuli. Currently, heated rod bundle experiments are the closest representation of real SCWR conditions.

Carbon dioxide (CO_2) or other refrigerants such as R134a, R12, and R22 are sometimes used instead of water due to their lower critical point, 7.39 [MPa] and 304.25 [K] (31.10 [ºC]) for CO_2, allowing for the use of experimental equipment that does not need to be used in the more extreme pressure conditions of supercritical water. CO_2 and other refrigerants such as R134a, R12, and R22, behave similarly to water at their critical and pseudocritical points, where the specific heat capacity spikes and the density, thermal conductivity, and dynamic viscosity drop suddenly. This allows for the use of these fluids in place of water when studying the heat transfer behaviour in supercritical fluids.

Numerical methods that have a good history of accurately predicting supercritical fluid experiments will be used in the design of SCWRs. Studies have been performed that sought to validate various numerical methods using experimental data, as explained in detail in Section 2.2. Some of these numerical methods include commercial and in-house computational fluid dynamics (CFD) codes that use turbulence models and direct numerical simulation (DNS), subchannel codes, and one-dimensional analytical methods. One of the outcomes of the present study is assessing the numerical method of using CFD codes with two-equation Reynolds-averaged Navier-Stokes (RANS) turbulence models in their accuracy of predicting heated rod bundle experiments that use supercritical fluids. Chapter 2 explains the numerical methods used in the present study, including turbulence models and CFD codes.

Another outcome of the present study is to seek a better understanding of HTD in the numerical predictions of CFD codes with two-equation RANS turbulence models.

CHAPTER 2: LITERATURE REVIEW

There have been many heated tube and annulus experimental studies done with fluid at or near the pseudocritical point since the 1950's. Numerical studies have been done to try and simulate these experiments using many different codes and turbulence models with differing levels of success. However, experiments using rod bundles are better suited for the design and analysis of SCWRs than heated tubes, because of the more complex flow pattern and heat transfer phenomena that occur in the subchannels of rod bundles. Unfortunately, there are far fewer rod bundle experiments available than heated tube experiments. Numerical analysis of some of these rod bundle experimental data has been performed in an attempt to identify the turbulence model(s) that will best predict the heat transfer, and to a lesser extent the fluid flow phenomena.

This literature review summarizes all experimental studies that have been performed using heated tubes, annuli, and rod bundles with fluid at or near the pseudocritical point. A review of all numerical studies in which three or more turbulence models were used to numerically simulate heated tube and annulus experiments is then presented and discussed. Additionally, a review of all numerical studies that have simulated a rod bundle experiment is presented and discussed. The review of numerical studies that simulated heated tube and annulus experiments using three or more turbulence models and the review of numerical studies that simulated heated rod bundle experiments will be used to determine the turbulence models that will be used in the present study to simulate certain heated rod bundle experiments. The choice of turbulence models will be based on the assumption that the turbulence model plays a key role in predicting the heat transfer phenomena in heated tube, annulus, and rod bundle experiments with fluid at or near the pseudocritical point. The rod bundle experiments that will be simulated using ANSYS

CFX and ANSYS FLUENT [4] will be selected from the review of experimental studies of heated rod bundle experiments.

The rod bundle experiments that will be numerically simulated, as well as the turbulence models with corresponding wall treatments will be presented in greater detail, along with the objectives and outline of the present study.

2.1. Experimental Studies

2.1.1. Heated Tube and Annulus

The first experiments using fluids at or near the pseudocritical point were performed in the 1950's using a heated tube or annulus oriented vertically or horizontally with either water or CO_2 as the coolant. There have been numerous experiments performed since then that cover a wide range of operating conditions. For an in-depth review and summary of experiments using water consult Pioro and Duffey 2005 [5] and Groeneveld et al. 2008 [6], and for experiments using CO_2 consult Duffey and Pioro 2005 [7]. Table 1 lists additional heated tube experiments that were performed from 2000 onwards and which were not included in the reviews and summaries.

Table 1: Vertically oriented heated tube experiments, listing fluid, internal tube diameter, pressure, mass flux, inlet temperature, and wall heat flux.

Authors	Fluid	D_i [mm]	P [MPa]	G [kg/m²s]	T_{in} [°C]	q_w" [kW/m²]
Yoshida and Mori 2000 [8]	Water	10, 16	24.5	376, 1180	-	230-330
Jiang et al. 2004 [9]	CO_2	0.948	9.5	579-1641	31-51	31-108
Kirillov et al. 2005 [10]	Water	10	24-25	200-1500	300-380	<1050
He et al. 2005 [11]	CO_2	0.948	8.5, 9.5	539-1641	31-51	10-200
Pis'menny et al. 2006 [12]	Water	6.28-9.5	23.5	250-2200	100-415	<3200
Kim et al. 2007 [13]	CO_2	4.4	7.75, 8.12, 8.85	400-1200	27	<150
Cho et al. 2008 [14]	CO_2	4.4	8.12	1200	27	50-130
Song et al. 2008 [15]	CO_2	4.4, 9.0	8.12	400, 1200	5.5-32	30, 50
Bae and Kim 2009 [16]	CO_2	4.4, 9	7.75, 8.12, 8.85	400-1200	5-27	<150
Bae et al. 2010 [17]	CO_2	6.32	7.75, 8.12	285-1200	-	30-170
Kim and Kim 2011 [18]	CO_2	4.5	7.46-10.26	208-874	29-115	38-234
Withag et al. 2012 [19]	Water	10	24	6.6, 10	300	-
Zhang et al. 2012 [20]	Water	10	23, 25	596, 2021	301, 320	772, 1385
Zhang et al. 2014 [21]	R134a	7.6	4.3-4.7	600-2500	71-115	20-180

All of the experimental studies listed in Table 1 used heated tubes, with diameters that ranged from 0.948 [mm] to 16 [mm], mass fluxes that ranged 6.6 [kg/m^{2}s] to 2500 [kg/m^{2}s], pressures that ranged from 4.3 [MPa] to 25 [MPa], inlet temperatures that ranged from 5 [°C] to 380 [°C], and heat fluxes that ranged from 10 [kW/m^2] to 3 200 [kW/m^2]. The wall temperatures at various axial locations, and sometimes the overall pressure drop, was presented in these experimental studies. A common theme among these studies is the presence of HTD, as evident by the spikes in surface temperature.

A majority of these experimental studies used CO_2 instead of water, and only one experiment used R134a. CO_2 and other refrigerants such as R134a are used instead of water due to their lower critical point, allowing for the use of experimental equipment that does not need to be used in the more extreme conditions of supercritical water. These fluids behave similarly to water at their critical and pseudocritical points, where the specific heat capacity spikes and the density, thermal conductivity, and dynamic viscosity drop suddenly.

2.1.2. Heated Rod Bundles

Experiments of heated rod bundles with vertical up-flow are presented here. There are far fewer rod bundle experiments than heated tube experiments, as the experimental setup for rod bundles is more complex and costly. The rod bundle experimental results were examined to see if enough information are available to define a corresponding numerical model, including whether or not the experimental study included wall temperature data that could be compared to numerical predictions.

Table 2 lists articles in which the authors present experimental results of vertically oriented heated rod bundle experiments with various fluids, and gives the number of rods, pressure, mass flux, inlet temperature (T_{in}) or inlet bulk fluid enthalpy (h_b), and wall heat flux (q_w") or wall heat rate (q).

Table 2: Vertically oriented rod bundle experiments, listing fluid, number of rods, pressure, mass flux, inlet temperature or inlet bulk fluid enthalpy, and wall heat flux or wall heat rate.

Author(s)	Fluid	No. of Rods	P [MPa]	G [kg/m²s]	T_{in} [°C]	q_w" [kW/m²]
Dyadyakin and Popov 1977 [22]	Water	7	24.5	500-4000	90-570	<4700
Silin et al. 1993 [23]	Water	271	23.5, 29.4	350-5000	h_b: 1000-3000 [kJ/kg]	180-4500
Razumovskiy et al. 2008 [24]	Water	7	22.5, 24.5, 27.5	700-1500	125-325	<1600
Razumovskiy et al. 2009 [25]	Water	3	22.6, 24.5, 27.5	1000-2700	125-327	1250-4580
Mori et al. 2012 [26]	R22	3, 7	5.5	400-1000	h_b: 220-455 [kJ/kg]	5-90
Richards 2012 [27]	R12	7	4.61-4.67	440-1320	72.9-119.3	q: 2.05-25 [kW]
Yang et al. 2013 [28]	Water	4	25	450, 845	340, 345	550, 800
Zhao et al. 2013 [29]	Water	4	25.1	112.7	351.15	756.5
Wang et al. 2014 [30]	Water	4	23-28	350-1000	200-450	200-1000
Rohde et al. 2015 [31]	Water	7	25	1433	246	q: 34 [kW]

Dyadyakin and Popov 1977 [22] were the first to perform experiments using rod bundles. They used water as the coolant and the experimental setup consisted of a seven-rod bundle. The article was written in Russian, so the experimental conditions of the experiment were obtained from a secondary source, Pioro and Duffey 2005 [5].

Silin et al. 1993 [23] performed experiments on full scale, 271 rod bundles using water as the coolant. Their article does not contain any surface temperature plots, so it would not be possible to compare numerical predictions to their experimental results.

Razumovskiy et al.'s experiments with a seven-rod bundle [24] and a three-rod bundle [25] where published in 2008 and 2009, respectively. Numerical predictions cannot be compared with these either because, for the seven-rod bundle, the plots of wall temperature do not have enough detail regarding boundary conditions and, for the three-rod bundle, the angular location of the thermocouples on the rods is unknown. The missing information required to numerically simulate these two experiments was requested from the authors by email, but it was not provided.

Mori et al. 2012 [26] performed experiments using three- and seven-bundles using R22 as the coolant. The three-rod experimental setup and results have sufficient detail for comparison with numerical predictions, but the seven-rod experiments lack the necessary information regarding thermocouple locations to compare with numerical results. This necessary information was requested from the corresponding author by email, but no response was received.

Richards 2012 [27] presented the seven-rod bundle experimental results of Kirillov et al. 2006 [32]. R12 was used as the coolant and the heater rod surface temperature plots are presented for 20 different cases. Richards provided sufficient detail so that the bundle experiments can be numerically simulated and predictions could be compared to experimental results.

Yang et al. 2013 [28] performed experiments on a four-rod bundle using water as the coolant. Only a summary of the experimental results are available from Liu et al. 2013 [33] at the time of the present study. This summary does not provide enough information regarding the thermocouple locations to enable a proper comparison with numerical predictions.

Zhao et al. 2013 [29] performed experiments on a four-rod bundle using water as the coolant. A summary of the experimental results is available from Xiong et al. 2015 [34], but the Zhao et al. article was not available at the time of the present study. The summary from Xiong et al. provides sufficient detail so that the bundle experiments can be numerically simulated and predictions could be compared to experimental results.

Wang et al. 2014 [30] performed experiments using a four-rod bundle with water as the coolant. They presented a number of cases with different pressures, flow rates, heat rates, and inlet temperatures. The researcher's surface temperature plots only show the average heater surface temperature at a given axial location. Sufficient detail is given regarding the experimental setup so that the experimental results could be compared to numerical predictions.

Rohde et al. 2015 [31] presented seven-rod bundle results from The Japan Atomic Energy Agency (JAEA) for the benchmark exercise that was organized by the GIF Project Management board. Water was the coolant, and three cases were presented. Pseudocritical water conditions were only present in one of the three cases: case B2. Sufficient detail regarding the experimental setup and surface temperature plots is available so that numerical predictions could be compared to experimental results.

2.2. Numerical Studies

2.2.1. Heated Tube and Annulus

Numerical studies in which the author(s) used three or more turbulence models in an attempt to simulate experimental results of heated tubes and annuli are presented here. Some authors used only one or two turbulence models to simulate the experimental results; those numerical studies

are not included. This is because the goal of the following review was to summarize numerical studies in which the authors compared the results from using various turbulence models. Therefore, for each of these numerical studies the turbulence models could be ranked in terms of accuracy in predicting experimental results. If a turbulence model was found to predict experimental results closer than any other turbulence model in multiple numerical studies, then it is assumed that that turbulence model stands a better chance at predicting the experiments of the present study closer than other turbulence models. If a numerical study only used a single turbulence model, then the accuracy of that turbulence model could not have been compared to the accuracy of other turbulence models, and so no conclusions could have been made regarding its accuracy in predicting experimental results compared to the results of other turbulence models.

There exists a large number of numerical studies that compared the results of three or more turbulence models, and so out of convenience it was concluded that numerical studies that compare the results of only two turbulence models will not be included in the following review, since there exists a large number of these studies.

Table 3 lists studies in which vertically oriented heated tube and annuli experiments where simulated using either a commercial code or an in-house code using at least three turbulence models. The turbulence models and corresponding wall treatments for the respective experimental data that provided the best agreement between numerical and experimental wall temperatures are given. For some studies, the turbulence models and corresponding wall treatment are ranked in order of their accuracy in predicting the experimental data, while for other studies there were a number of turbulence models and corresponding wall treatments that

provided results that had a similar degree of accuracy; these were not ranked. The experiments that were simulated, geometry, fluid, code, and recommended turbulence models and wall treatments were given. Some turbulence models do not require additional wall treatments, such as the v^2-f and Low Reynolds k-ε turbulence models. A DNS case was chosen as one of the experiments, as these results are assumed to be as accurate as experimental data.

Table 3: Numerical studies of vertically oriented heated tube and annuli experiments that used 3 or more turbulence models, listing experiment simulated, geometry, fluid, author(s) of numerical study, code, and recommended turbulence model(s) and wall treatment(s).

Exp. Simulated	Geom. / Fluid	Author(s) of Numerical Study	Code	Recommended Turbulence Model / Wall Treatment (If applicable)
Shitsman 1963 [35]	Tube / Water	Seo et al. 2006 [36]	FLUENT	k-ε / Standard Wall Function
		Wen and Gu 2010 [37]	FLUENT	SST / Automatic and v^2-f
Swenson et al. 1965 [38]	Tube / Water	Kiss and Aszodi 2010 [39]	CFX	1. SST / Automatic, 2. k-ε / Standard Wall Function
Tanaka et al. 1967 [40]	Tube / CO_2	Dang and Hihara 2004 [41]	In-House	Jones-Launder Low-Reynolds k-ε
Watts 1970 [42][1]	Tube / Water	Zhou and Novog 2014 [43]	STAR-CCM+	Abe-Kondoh-Nagano Low-Reynolds k-ε and Lien et al. Low-Reynolds k-ε
Ornatskii et al. 1971 [44]	Tube / Water	Wen and Gu 2011 [45]	FLUENT	SST / Automatic
Yamagata et al. 1972 [46]	Tube / Water	Kim et al. 2004 [47]	FLUENT	RNG k-ε / EWT
		Seo et al. 2006 [36]	FLUENT	k-ε / Standard Wall Function
		Cheng et al. 2007 [48]	CFX	1. RSM / Standard Wall Function, 2. k-ε / Standard Wall Function, RNG k-ε / Standard Wall Function, and Launder Reynolds Stress /

				Standard Wall Function
		Yang et al. 2007 [49]	STAR-CD	1. Two-Layer / Hassid and Poreh Wall Treatment, 2. k-ε / Standard Wall Function
		Sharabi and Ambrosini 2009 [50][2]	THEMAT (In-House)	k-τ
		Gou et al. 2010 [51]	STAR-CD	Speziale Quadratic k-ε / Two-Layer Wall Treatment
		Zhang et al. 2011 [52]	FLUENT	Nothing recommended
		Li et al. 2012 [53]	CFX	Menter Baseline Explicit Algebraic Reynolds Stress Model (BSL EARSM)
		Wang et al. 2012 [54]	FLUENT	RNG k-ε / EWT
		Xu et al. 2013 [55]	In-House	SST for low heat flux case, RNG k-ε for high heat flux case
Weinberg 1972 [56]	Tube / CO_2	He et al. 2004 [57]	SWIRL (In-House)	Lam-Bremhorst Low-Reynolds k-ε and Chien Low-Reynolds k-ε
Glushchenko and Gandzyuk 1972 [58]	Annulus / Water	Liu et al. 2013 [59]	FLUENT	SST / Automatic
Dang and Hihara 2004 [41]	Tube / CO_2	Dang and Hihara 2004 [41]	In-House	Jones-Launder Low-Reynolds k-ε
Kirillov et al. 2005 [10]	Tube / Water	Mokry 2009 [60]	FLUENT	Low-Reynolds k-ε
		Farah 2012 [61]	FLUENT	SST / Automatic
	Square and Triangular Channels / CO_2	Sharabi et al. 2007 [62]	FLUENT	1. Yang-Shih Low-Reynolds k-ε, 2. Abe-Kondo-Nagano Low-Reynolds k-ε and Lam-Bremhorst Low-Reynolds k-ε
Kim et al. 2005 [63]	Tube / CO_2	Sharabi and Ambrosini 2009 [50]	THEMAT (In-House)	Chien Low-Reynolds k-ε
Bae et al. 2005 [64] (DNS)	Tube / CO_2	He et al. 2008 [65]	SWIRL (In-House)	1. v^2-f, 2. Myong-Kasagi Low-Reynolds k-ε and Chien Low-Reynolds k-ε
Pis'menny 2006 [12]	Tube / Water	Wen and Gu 2010	FLUENT	SST / Automatic and v^2-f

		[37]		
		Li et al. 2012 [53]	CFX	k-ω, BSL k-ω, SST, ω-RSM, BSL Reynolds Stress, BSL EARSM / Automatic
Zhang 2006 [66]	Tube / CO_2	Zhang et al. 2011 [52]	FLUENT	Nothing recommended
Cho et al. 2009 [14]	Tube / CO_2	Cho et al. 2009 [14]	FLUENT	RNG k-ε / EWT
	Annulus / CO_2	Cho et al. 2009 [14]	FLUENT	SST / Automatic and Abid Low-Reynolds k-ε
Song et al. 2008 [15]	Tube / CO_2	Mohseni and Bazargan 2009 [67] and 2011 [68]	In-House	Myong-Kasagi Low-Reynolds k-ε
Zhang et al. 2012 [20]	Tube / Water	Zhang et al. 2012 [20]	In-House	k_t-ε_t
Zahlan 2013 [69]	Tube / CO_2	Zhou and Novog 2014 [43]	STAR-CCM+	SST / Automatic and RSM
Wang et al. 2015 [70]	Annulus / Water	Wang et al. 2015 [70]	CFX	SST / Automatic

[1]Watts experimental data are presented in [25]. [2]Also used FLUENT, but only used the SST turbulence model for FLUENT simulations.

There are turbulence models that were recommended as they provided the best approximation of experimental results, but they cannot be implemented in either CFX or FLUENT, so they will not be considered in the following discussions. The v^2-f turbulence can be used in FLUENT, but requires the purchase of an additional license, so it was not considered. Additionally, turbulence models that use three or more equations, such as the Reynolds stress turbulence model, require far greater computing power and time than two-equation turbulence models, and they were also not be considered for the present study. Only two-equation turbulence models that can be implemented in CFX or FLUENT are discussed in the review that follows.

For the Shitsman 1963 [35] experiment, Seo et al. 2006 [36] recommended the k-ε turbulence model with wall functions, and Wen and Gu 2010 [37] recommended the SST turbulence model with automatic wall treatment. Kiss and Aszodi 2010 [39] recommended the SST turbulence model with automatic wall treatment for the Swenson et al. 1965 [38] experimental data. The k-ε with wall functions provided the second best agreement with the experimental data. Zhou and Novog 2014 [43] recommended the Abe-Kondoh-Nagano low-Reynolds k-ε turbulence model for the Watts 1970 [42] experimental data, and the SST turbulence model with automatic wall treatment for the Zahlan 2013 [69] experimental data. Wen and Gu 2011 [45] found that the SST turbulence model with automatic wall treatment best predicted the experimental data of Ornatskii et al. 1971 [44]. He et al. 2004 [57] recommended the Lam-Bremhorst low-Reynolds k-ε turbulence model for predicting the Weinberg 1972 [56] experimental data. They used an in-house code, named SWIRL. Liu et al. 2013 [59] recommended the SST turbulence model with automatic wall treatment for the Glushchenko and Gandzyuk 1972 [58] annulus experiment that used water as the coolant.

There are more numerical studies comparing turbulence models for the Yamagata et al. 1972 [46] experimental data than any other experimental data. Of these numerical studies, the k-ε turbulence model with wall functions is recommended by Seo et al. 2006 [36] and Yang et al. 2007 [49], and the RNG k-ε turbulence model is recommended with EWT by Kim et al. 2004 [47] and Wang et al. 2012 [54] and is also recommended by Xu et al. 2013 [55], but with an unknown wall treatment. Both the k-ε and RNG k-ε turbulence models with wall functions are recommended as the second best option by Cheng et al. 2007 [48]. Xu et al. 2013 [55] are the only authors that recommend the SST turbulence model for the Yamagata et al. experiment, but

do not state the wall treatment that was used. They are also the only authors that used an in-house code for predicting the Yamagata et al. experiment.

For the heated tube experiment of Kirillov et al. 2005 [10], Mokry 2009 [60] recommended the general low-Reynolds k-ε turbulence model, while Farah 2012 [61] recommended the SST turbulence model with automatic wall treatment. For the square and triangular channel experiments of Kirillov et al. 2005, Sharabi et al. 2007 [62] recommends the Yang-Shih low-Reynolds k-ε turbulence model, while the turbulence models that yield the second best results are the Abe-Kondo-Nagano low-Reynolds k-ε and Lam-Bremhorst low-Reynolds k-ε turbulence models.

Wen and Gu 2010 [37] and Li et al. 2012 [53] recommend the SST turbulence model with automatic wall treatment and an unknown wall treatment, respectively, for the Pis'menny 2006 [12] experimental data. Li et al. also recommended the k-ω and BSL k-ω with an unknown wall treatment for the Pis'menny experimental data. Cho et al. 2009 [14] recommended the RNG k-ε turbulence model with EWT for their own heated tube with CO_2 experimental data, whereas for their annulus with CO_2 experimental data they recommended the SST and Abid low-Reynolds k-ε turbulence models with automatic and no wall treatment, respectively. Wang et al. 2015 [70] recommended the SST with automatic wall treatment for predicting their own annulus experiment that used water as the coolant.

2.2.2. Heated Rod Bundles

Numerical studies in which the researchers simulated experimental results of heated rod bundles are presented here. Some researchers did not simulate an experiment, but instead simulated

conditions that might be used for heated rod bundle experiments. Those numerical studies are not included here.

Table 4 lists studies in which vertically oriented rod bundle experiments where simulated using either a commercial code or an in-house code. The experiments that were simulated, bundle setup, fluid, code, turbulence models, and wall treatments are given for all studies.

Table 4: Numerical studies of vertically oriented rod bundle experiments, listing the experiment that was simulated, bundle setup, fluid, numerical code, turbulence models used (if any), and wall treatment (if any).

Authors of Numerical Study	Exp. Simulated	Bundle Setup and Fluid	Code	Turbulence Models	Wall Treatment
Liu et al. 2013 [33]	Yang et al. 2013 [28]	4-Rod, Water	COBRA-SC (In-house)	None Used (Subchannel Code)	None Used (Subchannel Code)
Huang et al. 2014 [71]	Richards 2012 [27]	7-Rod, R12	ANSYS FLUENT v6.3.26	k-ε, SST, Reynolds Stress (RSM)	Wall Function, Enhanced Wall Treatment (EWT)
				ω-Reynolds Stress (ω-RSM)	EWT
Zhang et al. 2014 [72]	Richards 2012 [27]	7-Rod, R12	ANSYS CFX v11.0	RNG k-ε, SSG Reynolds Stress	Scalable Wall Function
				SST, ω-RSM	Automatic Wall Treatment
Xiong et al. 2015 [34]	Zhao et al. 2013 [29]	4-Rod, Water	ANSYS CFX 5.6	SSG Reynolds Stress	Scalable Wall Function
				ω-RSM, Menter Baseline (BSL) Reynolds Stress	Automatic Wall Treatment
Chang and Tavoularis 2015 [73]	Rohde et al. 2015 [31]	7-Rod, Water	Star-CCM+ 9.04	Abe-Kondoh-Nagano low Reynolds k-ε, v^2-f, k-ε-v^2/k, SST	Not stated by authors

Liu et al. 2013 [33] simulated the four-rod bundle water experiments of Yang et al. 2013 [28] using an in-house COBRA-SC code. This is a custom subchannel code that does not use turbulence models or wall treatments, and is applicable to supercritical flows.

Huang et al. 2014 [71] simulated the seven-rod R12 bundle experiments of Richards 2012 [27] using FLUENT v6.3.26. They used the k-ε, SST, and Reynolds stress turbulence model (RSM) with both wall functions and Enhanced Wall Treatment (EWT), and the ω-Reynolds stress turbulence model (ω-RSM) with EWT. The turbulent Prandtl number varied from wall to freestream for certain cases. Cases 2, 3, 6, and 9 of the Richards experiments were simulated, and HTD was captured best when EWT was enabled compared to when the standard wall function was enabled. The heater rod surface temperatures near the inlet of case 2 were predicted better using the RSM turbulence model compared to the SST turbulence model. For the remaining cases, the RSM turbulence model with EWT resulted in the best heater rod surface temperature predictions.

Zhang et al. 2014 [72] simulated cases 2, 3, and 9 of Richards experiments using CFX v11.0 and the RNG k-ε, SSG Reynolds stress, SST, and ω-RSM turbulence models. They found that the SST and ω-RSM turbulence models were able to capture HTD. The Reynolds stress turbulence models were able to predict secondary flow structures, although these were shown to have minimal influence on heat transfer behaviour. The turbulent Prandtl number was set to a constant value of 0.85 for all cases.

Xiong et al. 2015 [34] simulated the four-rod bundle water experiments of Zhao et al. 2013 [29] using CFX 5.6 and the SSG Reynolds stress, ω-RSM, and Menter Baseline (BSL) Reynolds stress turbulence models. They found that the ω-RSM and BSL Reynolds stress turbulence

models over-predict heater rod surface temperatures, while the SSG Reynolds stress turbulence model under-predicts heater rod surface temperatures.

Chang and Tavoularis 2015 [73] simulated the seven-rod bundle water experiments of Rohde et al. 2015 [31] using Star-CCM+ 9.04 and the Abe-Kondoh-Nagano low Reynolds k-ε, v^2-f, k-ε-v^2/k, and SST turbulence models. The authors did not state what wall treatment was used for any of the turbulence models. They found that the v^2-f turbulence model predicted wall surface temperatures better than the other turbulence models.

2.3. Summary of Literature

Not all of the articles on rod bundle experiments include sufficient information regarding the experimental setup and/or thermocouple locations for simulation by CFD codes. Plots of the surface temperatures are also not always included with sufficient detail so that numerical predictions can be compared to experimental results. Therefore, only a portion of the articles can be used to compare with numerical predictions. Those articles by Mori et al. (three-rod only), Richards, Zhao et al., Wang et al., and Rohde et al. have sufficient information so that a numerical model can be created, and numerical predictions can be compared to experimental results.

There does not appear to be a general consensus among researchers as to which turbulence model provides the best numerical predictions of the experimental data when it comes to vertically oriented heated tubes and annuli with fluid at or near the pseudocritical point. This is evident by the multitude of turbulence models that are recommended for the various experiments given in Table 3. Although not all authors tried every possible turbulence model and wall

treatment. There is not always a consensus among researchers for the same experiment. For example, both the k-ε and RNG k-ε turbulence models are recommended for the Yamagata et al 1972 experiment by authors that each used both the k-ε and RNG k-ε turbulence models. Another example of this is the Shitsman 1963 experiment, where the k-ε and SST turbulence models are recommended by Seo et al. 2006 and Wen and Gu 2010, respectively. An exception to this is the Pis'menny 2006 experiment where the SST turbulence model was recommended by Wen and Gu 2010 and was also recommended by Li et al. 2012. For the rod bundle experiments, only the numerical study of Zhang et al. 2014 recommended a two-equation turbulence model that can be used in CFX or FLUENT: the SST turbulence model. It was used for predicting the Richards 2012 experiments.

From the review of heated tube and annulus and heated rod bundle numerical studies, a number of turbulence models were recommended because they gave the best or relatively good predictions of the heat transfer phenomena. Of these turbulence models, the only two-equation turbulence models that can be used in CFX or FLUENT and which do not require the purchase of an additional license are the k-ε, RNG k-ε, SST, k-ω, BSL k-ω, low-Reynolds k-ε, and the low-Reynolds k-ε models of Abid, Lam-Bremhorst, Launder-Sharma, Yang-Shih, Abe-Kondoh-Nagano, and Chang-Hsieh-Chen. Not all of these turbulence models can be used due to a limited amount of time and resources. Therefore, only those turbulence models that were recommended most often will be used in the present study, they are the k-ε, RNG k-ε, SST, and the low-Reynolds k-ε models of Lam-Bremhorst and Yang-Shih. When the two low-Reynolds k-ε turbulence models were selected, the numerical studies of He et al. 2004 and Sharabi et al. 2007 where considered above all others as they both used five different low-Reynolds k-ε turbulence models before recommending either one or a number of these models. He et al. came to the

conclusion that the Lam-Bremhorst model gave the best results for the Weinberg 1972 experiment. Sharabi et al. recommended the Yang-Shih model as giving the best predictions of the Kim et al. 2005 experiment, but recommended the Lam-Bremhorst and Abe-Kondoh-Nagano models as giving the second best predictions.

As for the wall treatment, EWT was recommended when using the RNG k-ε turbulence model, and it is only available for use in FLUENT. Wall functions were recommended when using the k-ε turbulence model. For the SST turbulence model, there is no option to select a different wall treatment than the default wall treatment, which is EWT when using FLUENT and automatic wall treatment when using CFX. The low-Reynolds k-ε models of Lam-Bremhorst and Yang-Shih are only available for use in FLUENT, and there is no special wall treatment that can be used with these turbulence models.

2.4. Objectives

The objectives of this thesis are as follows:

- Numerically simulate two or three cases each of three heated rod bundle experiments with upwards flowing fluid at or near the pseudocritical point.
- Investigate HTD that occurs at or near the pseudocritical point of fluids in heated rod bundles with upwards flowing fluid.
- Compare the results of various two-equation turbulence models in predicting heat transfer and fluid flow of the various cases of the heated rod bundle experiments.
- Compare the results of two commercial CFD codes in predicting the various heated rod bundle experiments.

2.5. Scope of the Thesis

The experiments of Rohde et al., Richards, and Wang et al. where selected for the present study. Two cases will be simulated from each of Rohde et al. and Richards, and three cases will be simulated from Wang et al. An attempt was made to simulate the Mori et al. three-rod bundle using CFX, but a steady state converged solution could not be achieved using a multitude of different meshes. The Zhao et al. four-rod bundle was not selected because the above-mentioned three experiments were considered to have sufficient variety of geometry and working fluid.

ANSYS CFX and ANSYS FLUENT [4] will be used to perform numerical simulations for all cases. The turbulence models that will be used are the Shear Stress Transport model (SST), k-ε, RNG k-ε, Yang-Shih low-Reynolds k-ε, and Lam-Bremhorst low-Reynolds k-ε. FLUENT will be used to simulate the experimental rod bundle cases using the RNG k-ε turbulence model with EWT, the SST turbulence model with the default EWT, and the low-Reynolds k-ε turbulence models of Lam-Bremhorst and Yang-Shih. CFX will be used to simulate the experimental rod bundle cases using the k-ε turbulence model with scalable wall functions, as these are recommended over standard wall functions by CFX [74]. CFX will also be used to simulate the experimental rod bundle cases using the SST turbulence model with automatic wall treatment, in order to compare the results of using the same turbulence model with different codes.

2.6. Thesis Outline

Chapter 3 will explain the numerical models that are used by both CFX and FLUENT. Each experiment will be presented in a separate chapter: Chapter 4, Chapter 5, and Chapter 6 for the Rohde et al., Richards, and Wang et al. experiments respectively. Each of these chapters will

present the experimental setup, specific details about the numerical simulation, grid independence study, results, and discussion for each of the three bundle experiments. Chapter 7 will provide the overall discussion and conclusion for all cases, and will include a comparison between the various turbulence models that were used as well as a comparison between the CFX and FLUENT. Appendix A.1 through A.4 contain additional studies that were performed for the SST turbulence model and the Rohde et al. experiment, including a sensitivity study of the SST turbulence model parameters. Appendix B.1 and B.2 contains details on implementing custom material properties in CFX and FLUENT. A separate document is available that contains a step-by-step guide for creating the mesh of the Wang et al. four-rod bundle using ICEM CFD [75].

CHAPTER 3: NUMERICAL MODELS

Two commercially available computational fluid dynamics programs were used to generate numerical solutions to the experimental cases under consideration. These two programs are ANSYS CFX (v14.5, v15.0, v16.1, and v16.2) and ANSYS FLUENT (v15.0, v16.1, and v16.2) [4]. The governing equations that are solved by both of these programs are given in this chapter. ANSYS CFD-Post (v14.5, v15.0, v16.1, and v16.2) [4] was used to post process the results from both CFX and FLUENT. ANSYS ICEM CFD (v14.5, v15.0, and v16.1) [4] was used to generate meshes in the .cfx5 and .msh format for use in CFX and FLUENT respectively. Unless otherwise noted, the following equations are solved by both CFX and FLUENT.

3.1. Governing Equations

The following governing equations are given in Cartesian coordinates, using summation notation where appropriate, and were taken from ANSYS digital reference documentation [74]. The governing equations consist of continuity, momentum, thermal energy, and turbulence quantities. The turbulence quantities are the turbulence kinetic energy, k, and either the turbulence dissipation rate, ε, or the specific turbulence dissipation, ω. Steady state versions of the equations are presented.

The following assumptions are made in regards to the governing equations: incompressible flow (the Mach number is less than 0.3 for all cases), all fluids are Newtonian, no radiation heat transfer, and negligible pressure work. Additionally, the thermophysical properties that are used in the governing equations vary with pressure and temperature.

3.1.1. Continuity, Momentum, and Energy

The continuity equation is:

$$\frac{\partial(\rho U_i)}{\partial x_i} = 0 \tag{1}$$

The conservation of momentum equation is:

$$\frac{\partial(\rho U_i U_j)}{\partial x_j} = -\frac{\partial P}{\partial x_i} + \frac{\partial}{\partial x_j}\left[\mu\left(\frac{\partial U_i}{\partial x_j} + \frac{\partial U_j}{\partial x_i}\right)\right] - \frac{\partial}{\partial x_j}\left(\rho\overline{u_i u_j}\right) + S_{M,buoy} \tag{2}$$

Where $\rho\overline{u_i u_j}$ are the Reynolds stresses and $S_{M,buoy}$ is the momentum source term due to buoyancy. The eddy-viscosity assumption is used to approximate the Reynolds stresses:

$$-\rho\overline{u_i u_j} = \mu_t\left(\frac{\partial U_i}{\partial x_j} + \frac{\partial U_j}{\partial x_i}\right) - \frac{2}{3}\delta_{ij}\left(\rho k + \mu_t\frac{\partial U_k}{\partial x_k}\right) \tag{3}$$

where μ_t is the eddy viscosity, k is the turbulence kinetic energy, and δ_{ij} is the Kronecker delta function. The $\frac{\partial U_k}{\partial x_k}$ term is expected to be negligible for this application. The turbulence kinetic energy is the kinetic energy per unit mass of the turbulence fluctuations

$$k = \frac{1}{2}\overline{u_i u_i} \tag{4}$$

but because the turbulence fluctuations are not solved for in any of the turbulence models used in this study, the turbulence kinetic energy is determined from a transport equation, and not from Equation (4).

Using the previous eddy-viscosity assumption, the conservation of momentum equations for use with two equation turbulence models become:

$$\frac{\partial(\rho U_i U_j)}{\partial x_j} = -\frac{\partial P'}{\partial x_i} + \frac{\partial}{\partial x_j}\left[(\mu + \mu_t)\left(\frac{\partial U_i}{\partial x_j} + \frac{\partial U_j}{\partial x_i}\right)\right] + S_{M,buoy} \tag{5}$$

where P' is the modified pressure and $S_{M,buoy}$ is the momentum source term due to buoyancy. The eddy viscosity, μ_t, is determined from equations that require the turbulence kinetic energy, k, and the turbulence dissipation rate, ε, or specific turbulence dissipation, ω, among other variables and constants. Using the full buoyancy model in CFX, the momentum source term due to buoyancy is:

$$S_{M,buoy} = g_i(\rho - \rho_{ref}) \tag{6}$$

The momentum source term used in FLUENT is:

$$S_{M,buoy} = \rho\vec{g} \tag{7}$$

The reference density (ρ_{ref}) is defined as the average density over the entire fluid domain. For the *z* axis aligned with the upward flow direction the acceleration due to gravity (g_z) is -9.81 [m/s^2] (32.185 [ft/s^2]) and 0 in the *x* and *y* directions (g_x and g_y).

The modified pressure used in CFX is defined using the static pressure (P) and turbulence kinetic energy (k) as follows:

$$P' = P + \frac{2}{3}\rho k \tag{8}$$

The modified pressure used in FLUENT is simply the static pressure (P).

When the full buoyancy model is enabled in CFX, the absolute pressure includes the static pressure (P) and the hydrostatic pressure due to the reference density (ρ_{ref}):

$$P_{abs} = P_{ref} + P + \rho_{ref}\vec{g}\left(\vec{r} - \vec{r}_{ref}\right) \tag{9}$$

where $\vec{g}$ is the acceleration of gravity, and $\vec{r}_{ref}$ is the buoyancy reference location, specified at the centroid of a pressure defined boundary. In this case the outlet is a pressure-defined boundary. The absolute pressure and the temperature are used to define fluid properties as described in detail in Section 3.2.

CFX solves the thermal energy equation for turbulent flows, since all flows under consideration are incompressible:

$$\frac{\partial(\rho U_j h)}{\partial x_j} = \frac{\partial}{\partial x_j}\left(\lambda\frac{\partial T}{\partial x_j} + \frac{\mu_t}{\mathrm{Pr_t}}\frac{\partial h}{\partial x_j}\right) + \frac{\partial}{\partial x_j}\left[U_i\left(\tau_{ij} - \rho\overline{u_\iota u_j}\right)\right] + S_E \tag{10}$$

where $\mathrm{Pr_t}$ is the turbulent Prandtl number, S_E is the energy source term, and $\frac{\partial}{\partial x_j}\left[U_i\left(\tau_{ij} - \rho\overline{u_\iota u_j}\right)\right]$ is the viscous work term. When two equation turbulence models are used the Reynolds Stress term ($\rho\overline{u_\iota u_j}$) is approximated using the eddy viscosity hypothesis.

The turbulent Prandtl number, $\mathrm{Pr_t}$, is set at 0.9 by default in CFX. This value will be used for all CFX and FLUENT runs in this study.

FLUENT solves the following total energy equation for turbulent flows:

$$\frac{\partial}{\partial x_i}\left(U_i(\rho E + P)\right) = \frac{\partial}{\partial x_j}\left(\left(\lambda + \frac{\mu_t c_p}{\mathrm{Pr_t}}\right)\frac{\partial T}{\partial x_j} + U_i\left(\tau_{ij}\right)_{eff}\right) + S_E \tag{11}$$

where E is the total energy defined as follows:

$$E = h - \frac{P}{\rho} + \frac{U^2}{2} \tag{12}$$

and $U_i(\tau_{ij})_{eff}$ is the viscous dissipation term. The deviatoric stress tensor, $(\tau_{ij})_{eff}$, is:

$$(\tau_{ij})_{eff} = (\mu + \mu_t)\left(\frac{\partial U_i}{\partial x_j} + \frac{\partial U_j}{\partial x_i}\right) - \frac{2}{3}(\mu + \mu_t)\delta_{ij}\frac{\partial U_k}{\partial x_k} \tag{13}$$

The turbulent thermal conductivity, λ_t, is defined as follows:

$$\lambda_t = \frac{\mu_t c_p}{\mathrm{Pr_t}} \tag{14}$$

3.1.1.1. Continuity, Momentum, and Energy Boundary Conditions

All numerical cases in this study use the following boundary conditions: mass flow rate and temperature defined inlet, static pressure outlet, various symmetry planes, and various no-slip adiabatic walls. Additionally, fluid-solid and solid-solid interfaces are defined between the various fluid and solid domains.

The fluid total mass flow rate and direction is defined at the inlet. The direction is always defined normal to the inlet plane, in the positive z-direction. The temperature of the fluid over the entire inlet is also defined.

The outlets are defined using as a static pressure boundary condition. The relative static pressure is set at a certain value, which is zero for all cases of the present study, over the entire outlet.

Symmetry boundary conditions are used when all aspects of the flow are assumed to be symmetric about a symmetry plane.

All fluid-solid interfaces are “no-slip”, where the fluid directly in contact with the solid has a relative velocity of zero. When a fluid-solid interface is defined using the “conservative interface heat flux” or “coupled” options in CFX and FLUENT, respectively, heat flux is allowed to flow through the interface. When a wall is defined as “adiabatic” in CFX or when the heat flux is set to zero in FLUENT, heat flux is not allowed to flow through the interface.

3.1.2. SST Turbulence Model

The following Shear Stress Transport (SST) model is the Menter SST model [76]. The SST turbulence model effectively uses the k-ε turbulence model of Launder and Sharma [77] in the free stream and the k-ω model of Wilcox [78] in the near wall region, with a blending function to merge the two models between the free stream and the near wall region. This turbulence model determines the eddy viscosity using the turbulence kinetic energy, k, and the specific turbulence dissipation, ω.

The eddy viscosity is calculated using the following equation:

$$\mu_t = \frac{a_1 k \rho}{\mathrm{Max}(a_1 \omega, S F_2)} \tag{15}$$

where a_1 is 0.31, F_2 is a blending function, and S is the magnitude of the strain rate tensor S_{ij}:

$$S_{ij} = \frac{1}{2}\left(\frac{\partial U_i}{\partial x_j} + \frac{\partial U_j}{\partial x_i}\right) \tag{16}$$

$$S = \sqrt{2S_{ij}S_{ij}} \tag{17}$$

The blending function F_2 is:

$$F_2 = \tanh(\arg_2^2) \tag{18}$$

where $\arg_2$ is:

$$\arg_2 = \text{Max}\left(\frac{2\sqrt{k}}{\beta'\omega y}, \frac{500\nu}{y^2\omega}\right) \tag{19}$$

where β' is 0.09 and y is the distance to the closest wall.

The turbulence kinetic energy (k) and specific turbulence dissipation (ω) of the SST model result from solving the following transport equations:

$$\frac{\partial}{\partial x_j}(\rho U_j k) = \frac{\partial}{\partial x_j}\left[\left(\mu + \frac{\mu_t}{\sigma_{k3}}\right)\frac{\partial k}{\partial x_j}\right] + P_k - \beta'\rho k\omega + P_{kb} \tag{20}$$

$$\frac{\partial}{\partial x_j}(\rho U_j \omega) = \frac{\partial}{\partial x_j}\left[\left(\mu + \frac{\mu_t}{\sigma_{\omega 3}}\right)\frac{\partial \omega}{\partial x_j}\right] + (1 - F_1)\, 2\rho \frac{1}{\sigma_{\omega 2}\omega}\frac{\partial k}{\partial x_j}\frac{\partial \omega}{\partial x_j} + \alpha_3 \frac{\omega}{k} P_k - \beta_3 \rho \omega^2 + P_{\omega b} \tag{21}$$

where P_k is the production of turbulence due to viscous forces, P_{kb} is the turbulence production due to buoyancy, $P_{\omega b}$ is the turbulence dissipation due to buoyancy, and F_1 is a blending function. The turbulence production and dissipation due to buoyancy terms, P_{kb} and $P_{\omega b}$ respectively, are absent in FLUENT and cannot be enabled. σ_{k3}, $\sigma_{\omega 3}$, α_3, and β_3 are constants that result from the following blending function:

$$\phi_3 = F_1\phi_1 + (1 - F_1)\phi_2 \quad (22)$$

where ϕ is σ_k, σ_ω, α, or β. The constants used in Equation (22) are: σ_{k1}= 1.17647, σ_{k2}= 1.0, $\sigma_{\omega1}$= 2.0, $\sigma_{\omega2}$= 1.16822, α_1= 0.553167, α_2= 0.440355, β_1= 0.075, and β_2= 0.0828.

The blending function $F_1$is:

$$F_1 = \tanh(\arg_1^4) \quad (23)$$

where $\arg_1$ is:

$$\arg_1 = \text{Min}\left(\text{Max}\left(\frac{\sqrt{k}}{\beta'\omega y}, \frac{500\nu}{y^2\omega}\right), \frac{4\rho k}{CD_{k\omega}\sigma_{\omega2}y^2}\right) \quad (24)$$

$$CD_{k\omega} = \text{Max}\left(2\rho\frac{1}{\sigma_{\omega2}\omega}\frac{\partial k}{\partial x_j}\frac{\partial \omega}{\partial x_j}, 10^{-10}\right) \quad (25)$$

The turbulence production due to viscous forces is:

$$P_k = \mu_t\left(\frac{\partial U_i}{\partial x_j} + \frac{\partial U_j}{\partial x_i}\right)\frac{\partial U_i}{\partial x_j} - \frac{2}{3}\frac{\partial U_k}{\partial x_k}\left(3\mu_t\frac{\partial U_k}{\partial x_k} + \rho k\right) \quad (26)$$

The turbulence production due to buoyancy is calculated by CFX using the following equation:

$$P_{kb} = -\frac{\mu_t}{\rho\sigma_\rho}g_i\frac{\partial \rho}{\partial x_i} \quad (27)$$

where the turbulent Schmidt number, σ_ρ, is 1.0.

The turbulence dissipation due to buoyancy is determined by CFX using the following equation:

$$P_{\omega b} = \frac{\omega}{k}\left((\alpha_3 + 1)C_3 \mathrm{Max}(P_{kb}, 0) - P_{kb}\right) \tag{28}$$

where C_3 is 1.0.

3.1.2.1. Wall Treatment - CFX

To generate a solution in the near wall region when solving the SST turbulence model, CFX uses a method termed: automatic wall treatment. This method seeks to blend the readily known solutions in the viscous sub-layer with those in the log-layer of the near wall region. A value of y^+ less than one is required for this method to function as desired.

The flux for the momentum equation is:

$$F_U = -\rho u_{\tau,CFX} u^* \tag{29}$$

where the modified friction velocity, u^*, is:

$$u^* = \sqrt[4]{\left(\sqrt{\frac{\mu}{\rho}\left|\frac{\Delta U}{\Delta y}\right|}\right)^4 + (a_1 k)^4} \tag{30}$$

and the friction velocity specific to CFX automatic wall treatment, $u_{\tau,CFX}$, is computed using components from the viscous and log layers:

$$u_{\tau,CFX} = \sqrt[4]{(u_\tau^{vis})^4 + \left(u_\tau^{log}\right)^4} \tag{31}$$

where the component of the friction velocity from the viscous sublayer is:

$$u_\tau^{vis} = \sqrt{\frac{\mu}{\rho}\left|\frac{\Delta U}{\Delta y}\right|} \tag{32}$$

and the component of the friction velocity from the log layer is:

$$u_\tau^{log} = \frac{U}{\frac{1}{\kappa}\log y^+ + B} \tag{33}$$

where κ is 0.41, B is 5.2, and the universal equation for dimensionless distance from the wall, y^+ is

$$y^+ = \frac{u_\tau \Delta \mathrm{n}}{\nu} \tag{34}$$

where Δn is the wall-normal distance between the first and second mesh points away the wall and the universal equation for friction velocity is

$$u_\tau = \sqrt{\frac{\tau_w}{\rho}} \tag{35}$$

where τ_w is the near wall shear stress.

The turbulence kinetic energy flux is zero at the wall:

$$F_k = 0 \tag{36}$$

The specific turbulence dissipation flux is not specified. Instead, the specific turbulence dissipation is a blend of the analytical expressions for the viscous sublayer:

$$\omega_s = \frac{6\nu}{\beta_3(\Delta y)^2} \tag{37}$$

and the log layer:

$$\omega_{l,CFX} = \frac{u^*}{a_1 \kappa y} = \frac{(u^*)^2}{a_1 \kappa \nu y^+} \tag{38}$$

giving the following formulation:

$$\omega_\omega = \omega_s \sqrt{1 + \left(\frac{\omega_{l,CFX}}{\omega_s}\right)^2} \tag{39}$$

where Δy is the wall-normal distance between the first and second mesh points away from the wall.

The thermal boundary layer is modelled by blending the non-dimensional analytical expressions for the viscous sublayer and log layer into a single equation, given by Kader [79]. This allows for a continuous solution over the entire boundary layer, including the buffer layer. This formulation is given below, where the contribution from the viscous sublayer is the first part of the right hand side, and the contribution from the log layer is the second part of the right hand side:

$$T^+ = \mathrm{Pr}\, y^*_{Auto} e^{-\Gamma_{CFX}} + (2.12 \ln y^*_{Auto} + \beta^*) e^{-\frac{1}{\Gamma_{CFX}}} \tag{40}$$

where y^*_{Auto} is defined for this automatic wall treatment as:

$$y^*_{Auto} = \frac{u^* \Delta n}{\nu} \tag{41}$$

where Δn is wall-normal distance between the first and second mesh points away from the wall. The values of β^* and Γ_{CFX} are determined for Equation (40) using the following equations:

$$\beta^* = \left(3.85\mathrm{Pr}^{\frac{1}{3}} - 1.3\right)^2 + 2.12 \ln \mathrm{Pr} \tag{42}$$

$$\Gamma_{CFX} = \frac{0.01(\mathrm{Pr}\, y^*_{Auto})^4}{1 + 5\ \mathrm{Pr}^3 y^*_{Auto}} \tag{43}$$

where the Prandtl number is defined as:

$$\mathrm{Pr} = \frac{\mu c_p}{\lambda} \tag{44}$$

The temperature can then be determined from the non-dimensional temperature using the following equation:

$$T = T_w - \frac{T^+ q_w{}''}{\rho c_p u^*} \tag{45}$$

where T_w is the temperature at the wall and $q_w{}''$ is the heat flux at the wall

3.1.2.2. Wall Treatment - FLUENT

To generate a solution in the near wall region when solving the SST turbulence model, FLUENT uses a method termed: enhanced wall treatment (EWT). This method seeks to blend the readily known solutions in the viscous sub-layer with those in the log-layer of the near wall region. A value of y^+ less than one is required for this method to function as desired.

The non-dimensional velocity in the boundary layer is obtained by combining the analytical expressions for the viscous sublayer and log layer into a single equation, given by Kader [79]. This allows for a continuous solution over the entire boundary layer, including the buffer layer. This equation is given as

$$u^+ = u^+_{lam} e^{\Gamma_{FLUENT}} + u^+_{turb} e^{\frac{1}{\Gamma_{FLUENT}}} \tag{46}$$

where u^+_{lam} and u^+_{turb} are the analytical expressions for the non-dimensional velocity in the viscous (laminar) sublayer and the log (turbulent) layer respectively, and Γ_{FLUENT} is

$$\Gamma_{FLUENT} = -\frac{0.01(y^+)^4}{1+5y^+} \tag{47}$$

and u^+_{lam} is

$$u^+_{lam} = y^+\left(1 + \frac{y^+\mu}{2\rho^2(u_\tau)^3}\frac{dP}{dz}\right). \tag{48}$$

where $\frac{dP}{dz}$ is the pressure gradient in the direction of the mean flow.

To obtain the non-dimensional velocity in the log layer, u^+_{turb}, FLUENT solves the following ordinary differential equation that is based on a combination of the approaches by White and Christoph [80] and Huang et al. [81]:

$$\frac{du^+_{turb}}{dy^+} = \frac{1}{\kappa y^+}\sqrt{S'\left(1 - \frac{u^+\mathrm{Pr_t}q''_w}{\rho c_p u_\tau T_w} - \frac{(u^+)^2\mathrm{Pr_t}(u_\tau)^2}{2c_p T_w}\right)} \tag{49}$$

where S' is

$$S' = \begin{cases} 1 + \dfrac{y^+ \mu}{\rho^2 (u_\tau)^3} \dfrac{dP}{dz}, & y^+ < 60 \\ 1 + \dfrac{60\mu}{\rho^2 (u_\tau)^3} \dfrac{dP}{dz}, & y^+ \geq 60 \end{cases} \tag{50}$$

The non-dimensional velocity can be converted to the dimensional velocity using the following universal equation:

$$U = u_\tau u^+ \tag{51}$$

which is needed in subsequent equations for T^+.

To obtain the non-dimensional temperature profile in the thermal boundary layer, FLUENT uses the function of Kader [79] to blend the analytical solutions of non-dimensional temperature in the viscous sublayer and log layer:

$$T^+ = T^+_{lam} e^{\Gamma_{FLUENT}} + T^+_{turb} e^{\frac{1}{\Gamma_{FLUENT}}} \tag{52}$$

where T^+_{lam} and T^+_{turb} are the analytical expressions for the non-dimensional temperature in the viscous (laminar) sublayer and the log (turbulent) layer respectively, and Γ_{FLUENT} is calculated using Equation (47). The values of T^+_{lam} and T^+_{turb} are determined using the following equations:

$$T^+_{lam} = \mathrm{Pr}\left(u^+_{lam} + \frac{\rho u_\tau}{2q"_w} U^2\right) \tag{53}$$

$$T^+_{turb} = \mathrm{Pr_t}\left(u^+_{turb} + P_{\mathrm{Pr}} + \frac{\rho u_\tau}{2q"_w}\left[U^2 - \left(\frac{\mathrm{Pr}}{\mathrm{Pr_t}} - 1\right)(u^+_c)^2 (u_\tau)^2\right]\right) \tag{54}$$

where u^+_c is the value of u^+ at the fictitious crossover point between the viscous sublayer and log layer (y^+ = 11.06), u^+_{lam} is determined using Equation (48), u^+_{turb} is determined by solving the

ordinary differential Equation (49), and P_{Pr} is a function of the Prandtl and turbulent Prandtl numbers:

$$P_{\mathrm{Pr}} = 9.24\left[\left(\frac{\mathrm{Pr}}{\mathrm{Pr_t}}\right)^{\frac{3}{4}} - 1\right]\left(1 + 0.28e^{-0.007\frac{\mathrm{Pr}}{\mathrm{Pr_t}}}\right) \tag{55}$$

The temperature is determined from the non-dimensional temperature using the following equation:

$$T = T_w - \frac{T^+ q_w{}''}{\rho c_p u_\tau} \tag{56}$$

Similar to the method used by CFX, FLUENT sets the turbulence kinetic energy flux at the wall, F_k, to 0. The specific turbulence dissipation in the near wall region is calculated using either the analytical expression in the viscous sublayer or the analytical expression in the log layer, depending upon the location within the boundary layer. The expression for the specific turbulence dissipation in the viscous sublayer is given by Equation (37) in Section 3.1.2.1, and the expression for the specific turbulence dissipation in the log layer is:

$$\omega_{l,FLUENT} = \frac{(u_\tau)^2}{\sqrt{\beta'}\nu}\frac{du^+_{turb}}{dy^+} \tag{57}$$

3.1.3. Standard k-ε Turbulence Model

The following turbulence model implemented in CFX is the standard k-ε turbulence model of Launder and Sharma [77]. It is based on solving the governing equations of the turbulence kinetic energy, k, and turbulence dissipation rate, ε, in order to determine the eddy viscosity.

The eddy viscosity is calculated using the following equation:

$$\mu_t = C_\mu \rho \frac{k^2}{\varepsilon} \tag{58}$$

where C_μ is 0.09.

The turbulence kinetic energy, k, and turbulence dissipation rate, ε, result from solving the following transport equations:

$$\frac{\partial}{\partial x_j}(\rho U_j k) = \frac{\partial}{\partial x_j}\left[\left(\mu + \frac{\mu_t}{\sigma_{k\varepsilon}}\right)\frac{\partial k}{\partial x_j}\right] + P_k - \rho\varepsilon + P_{kb} \tag{59}$$

$$\frac{\partial}{\partial x_j}(\rho U_j \varepsilon) = \frac{\partial}{\partial x_j}\left[\left(\mu + \frac{\mu_t}{\sigma_\varepsilon}\right)\frac{\partial \varepsilon}{\partial x_j}\right] + \frac{\varepsilon}{k}(C_{\varepsilon 1} P_k - C_{\varepsilon 2}\rho\varepsilon + C_{\varepsilon 1} P_{\varepsilon b}) \tag{60}$$

where $\sigma_{k\varepsilon}$= 1.0, σ_ε= 1.3, $C_{\varepsilon 1}$= 1.44, and $C_{\varepsilon 2}$= 1.92. The turbulence production due to viscous forces, P_k, and the turbulence production due to buoyancy, P_{kb} are calculated using Equations (26) and (27). The turbulence dissipation due to buoyancy, $P_{\varepsilon b}$, is determined using the following equation:

$$P_{\varepsilon b} = C_3 \mathrm{Max}(P_{kb}, 0) \tag{61}$$

3.1.3.1. Wall Treatment

Scalable wall functions are used in CFX for the k-ε turbulence model and are based on those of Launder and Spalding [82]. These wall functions only use equations that are specific to the log layer. The non-dimensional distance from the wall for this wall treatment is

$$y^*_{Scale} = \frac{\rho C_\mu^{1/4} k^{1/2} \frac{\Delta n}{4}}{\mu} \tag{62}$$

where Δn is the wall-normal distance between the first and second mesh points away the wall. When the value of y^*_{Scale} is less than 11.06, then the minimum value of y^*_{Scale} used in the equations for the wall treatment is 11.06. The variable $\tilde{y}^*_{Scale}$ is used in place of y^*_{Scale} in the boundary layer equations for this reason:

$$\tilde{y}^*_{Scale} = Max(y^*_{Scale}, 11.06) \tag{63}$$

This ensures the log layer equations are never used in a region for which they were not intended.

The law-of-the-wall for the non-dimensional velocity is:

$$u^+_{Scale} = \frac{1}{\kappa} \ln(\tilde{y}^*_{Scale}) + B \tag{64}$$

The velocity is calculated using the following equation

$$U = C_\mu^{1/4} k^{1/2} u^+_{Scale} \tag{65}$$

which is used by the governing equations of mass, momentum, energy, turbulence kinetic energy, and turbulence dissipation rate.

The thermal boundary layer is modelled by assuming a universal non-dimensional temperature profile in the log layer:

$$T^+ = 2.12 \ln \tilde{y}^*_{Scale} + \beta^* \tag{66}$$

where β^* is determined using Equation (42) in Section 3.1.2.1. The temperature is determined from the non-dimensional temperature using Equation (45) in Section 3.1.2.1.

3.1.4. RNG k-ε Turbulence Model

The RNG k-ε turbulence model was derived using a statistical technique called renormalization group theory by Yakhot et al. [83]. It is similar to the standard k-ε turbulence model except that it has an extra term in the turbulence dissipation rate equation to account for highly strained flows, and it uses an analytical equation for the two coefficients appearing in the turbulent diffusion terms of the turbulence kinetic energy and turbulence dissipation rate equations. Values of the constants appearing in the governing equations are also different than for the standard k-ε model.

The eddy viscosity is calculated using the following equation:

$$\mu_t = C_{\mu,RNG} \rho \frac{k^2}{\varepsilon} \tag{67}$$

where $C_{\mu,RNG}$ is 0.0845

The turbulence kinetic energy, k, and turbulence dissipation rate, ε, result from solving the following transport equations:

$$\frac{\partial}{\partial x_i}(\rho U_i k) = \frac{\partial}{\partial x_j}\left[\alpha_{k,RNG}(\mu + \mu_t)\frac{\partial k}{\partial x_j}\right] + P_k - \rho\varepsilon + P_{kb} \tag{68}$$

$$\begin{aligned}\frac{\partial}{\partial x_i}(\rho U_i \varepsilon) = \frac{\partial}{\partial x_j}\left[\alpha_{\varepsilon,RNG}(\mu + \mu_t)\frac{\partial \varepsilon}{\partial x_j}\right] + \frac{\varepsilon}{k}\left(C_{\varepsilon 1,RNG}P_k + C_{\varepsilon 1,RNG}P_{\varepsilon b}\right) \\ - \frac{\rho\varepsilon^2}{k}\left(C_{\varepsilon 2,RNG} + \frac{C_\mu \eta^3(1-\eta/4.38)}{1+0.012\eta^3}\right)\end{aligned} \tag{69}$$

where $C_{\varepsilon 1,RNG}$=1.42, $C_{\varepsilon 2,RNG}$=1.68, $\eta = Sk/\varepsilon$, $\alpha_{k,RNG}$ and $\alpha_{\varepsilon,RNG}$ are coefficients determined using Equation (73) and the turbulence production due to viscous forces, P_k, is calculated using Equation (26) in Section 3.1.2. The turbulence production due to buoyancy, P_{kb}, and the turbulence dissipation due to buoyancy, $P_{\varepsilon b}$, are determined using the following equations

$$P_{kb} = -\frac{\mu_t}{\rho \mathrm{Pr_t}} g_i \frac{\partial \rho}{\partial x_i} \tag{70}$$

$$P_{\varepsilon b} = C_{3\varepsilon} P_{kb} \tag{71}$$

where $C_{3\varepsilon}$ is a constant that depends on the orientation of the mean flow velocity relative to the gravitational vector according to the following equation

$$C_{3\varepsilon} = \tanh\left|\frac{Vel_{par,g}}{Vel_{perp,g}}\right| \tag{72}$$

where $Vel_{par,g}$ is the component of the velocity parallel to the gravitational vector and $Vel_{perp,g}$ is the component of the velocity perpendicular to the gravitational vector. For all cases in the present study, the mean flow is parallel to the gravitational vector, therefore according to the above equation the value of $C_{3\varepsilon}$ will be 1.0.

The values of the $\alpha_{k,RNG}$ and $\alpha_{\varepsilon,RNG}$ constants results from solving the following equation

$$\left|\frac{\alpha_{RNG}-1.3929}{0.3929}\right|^{0.6321}\left|\frac{\alpha_{RNG}+2.3929}{3.3929}\right|^{0.3679}=\frac{\mu}{\mu_t} \tag{73}$$

where α_{RNG} is either $\alpha_{k,RNG}$ or $\alpha_{\varepsilon,RNG}$. The value of α_{RNG} is found from Equation (73) and then assigned to both $\alpha_{k,RNG}$ and $\alpha_{\varepsilon,RNG}$.

3.1.4.1. Wall Treatment

Enhanced wall treatment is used to model the boundary layer in FLUENT when the RNG k-ε model is enabled. This is the same method that is used for the SST turbulence model in FLUENT, and is explained in Section 3.1.2.2.

3.1.5. Low Reynolds k-ε Turbulence Model

The Yang-Shih low Reynolds k-ε (Yang-Shih Low-Re k-ε) [84] and Lam-Bremhorst low Reynolds k-ε (Lam-Bremhorst Low-Re k-ε) [85] turbulence models are presented in this section. They are based on the standard k-ε turbulence model, but include damping functions that are sensitive to near wall conditions. The effects of these damping functions are diminished as the flow approaches the free stream, just as the effects of the wall diminishes as the flow approaches the free stream. Additionally, the damping functions approach zero as the distance to the wall approaches zero, thereby causing the eddy viscosity to approach zero in the viscous sublayer, a physically realistic trend. Where the standard k-ε turbulence model requires wall functions to solve solution variables in the near wall region, Low-Re k-ε turbulence models can solve

solution variables all the way through the viscous sublayer. A value of y^+ less than one is required for these turbulence models to function as desired.

The eddy viscosity for the Yang-Shih Low-Re k-ε and Lam-Bremhorst Low-Re k-ε turbulence models are calculated using Equations (74) and (75), respectively.

$$\mu_t = C_\mu f_{\mu,YS} \tau_t \rho k \tag{74}$$

$$\mu_t = C_\mu f_{\mu,LB} \rho \frac{k^2}{\varepsilon} \tag{75}$$

where $f_{\mu,YS}$ and $f_{\mu,LB}$ are the damping functions of the Yang-Shih and Lam-Bremhorst Low-Re k-ε turbulence models given by Equations (77) and (76), respectively.

$$f_{\mu,YS} = \left[1 - \exp\left(-1.5 \cdot 10^{-4} R_y - 5 \cdot 10^{-7} R_y^3 - 10^{-10} R_y^5\right)\right]^{1/2} \tag{76}$$

$$f_{\mu,LB} = \left(1 - \exp\left(-0.0165 R_y\right)\right)^2 \left(1 + \frac{20.5\mu\varepsilon}{\rho k^2}\right) \tag{77}$$

The turbulent time scale, τ_t, is determined from the following equation

$$\tau_t = \frac{k}{\varepsilon} + \sqrt{\frac{\mu}{\rho\varepsilon}} \tag{78}$$

and the turbulence Reynolds number, R_y, is given as

$$R_y = \frac{\sqrt{k}\rho y}{\mu} \tag{79}$$

where y is the distance from the wall. The turbulence kinetic energy, k, and the turbulence dissipation rate, ε, result from solving the following transport equations:

$$\frac{\partial}{\partial x_i}(\rho U_i k) = \frac{\partial}{\partial x_j}\left[\left(\mu + \frac{\mu_t}{\sigma_{k,LowRe}}\right)\frac{\partial k}{\partial x_j}\right] + P_k - \rho\varepsilon + P_{kb} \tag{80}$$

$$\begin{aligned}\frac{\partial}{\partial x_i}(\rho U_i \varepsilon) = &\frac{\partial}{\partial x_j}\left[\left(\mu + \frac{\mu_t}{\sigma_{\varepsilon,LowRe}}\right)\frac{\partial \varepsilon}{\partial x_j}\right] \\ &+ \frac{1}{\tau_t}\left(C_{\varepsilon 1,LowRe}P_k f_1 - C_{\varepsilon 2,LowRe}f_2\rho\varepsilon + C_{\varepsilon 1,LowRe}P_{\varepsilon b}\right) + \rho S_\varepsilon\end{aligned} \tag{81}$$

where the corresponding values or equations used to determine the values of $\sigma_{k,LowRe}$, $\sigma_{\varepsilon,LowRe}$, $C_{\varepsilon 1,LowRe}$, $C_{\varepsilon 2,LowRe}$, f_1, and f_2 are given in Table 5, and the source term, S_ε, is given in Table 6. The turbulence production due to viscous forces, P_k, the turbulence production due to buoyancy, P_{kb}, and the turbulence dissipation due to buoyancy, $P_{\varepsilon b}$, are determined using Equations (26), (70), and (71), respectively.

Table 5: Values and equations for variables of the Lam-Bremhorst and Yang-Shih Low-Re k-ε turbulence models in FLUENT

	Lam-Bremhorst	Yang-Shih
$\sigma_{k,LowRe}$	1	1
$\sigma_{\varepsilon,LowRe}$	1.3	1.3
$C_{\varepsilon 1,LowRe}$	1.44	1.44
$C_{\varepsilon 2,LowRe}$	1.92	1.92
f_1	$1 + \left(\frac{0.05}{f_{\mu,LB}}\right)^3$	1
f_2	$1 - \exp\left(-\left(\frac{\rho k^2}{\mu\varepsilon}\right)^2\right)$	$1 - 0.22\exp-\left(\frac{\rho k\tau_t}{6\mu}\right)^2$

Table 6: Value and equation for source term of the Lam-Bremhorst and Yang-Shih Low-Re k-ε turbulence models in FLUENT

	Lam-Bremhorst	Yang-Shih
S_ε	0	$\frac{\mu\mu_t}{\rho^2}\left(\frac{\partial^2 U_i}{\partial x_j \partial x_k}\right)^2$

3.1.5.1 Wall Treatment

FLUENT does not offer enhanced wall treatment for Low-Re k-ε turbulence models. Therefore, there is no special treatment for the near wall region, other than specifying the boundary conditions of the turbulence kinetic energy and turbulence dissipation rate.

The turbulent kinetic energy is zero at the wall, because the viscous sublayer in the immediate vicinity of the wall is laminar leading to zero turbulence fluctuations, according to the definition of the turbulence kinetic energy, given by Equation (4) in Section 3.1.1.

$$k_{wall} = 0 \tag{82}$$

The boundary condition for the near wall turbulence dissipation rate is

$$\varepsilon_{wall} = \frac{2\mu}{\rho}\left(\frac{\partial\sqrt{k}}{\partial x_j}\right)^2 \tag{83}$$

3.1.6. Turbulence Model Inlet Boundary Conditions

Boundary conditions of the turbulence models for both CFX and FLUENT are defined at the inlet by specifying a turbulence intensity, I, and an eddy viscosity ratio, μ_t/μ. The dynamic

viscosity, μ, is already known, since it is determined from the temperature and pressure of the fluid at the inlet. The turbulence kinetic energy, turbulence dissipation rate, and specific turbulence dissipation rate are defined at the inlet using Equations (84), (85), and (86) respectively.

The turbulence kinetic energy at the inlet is:

$$k_{inlet} = \frac{3}{2} I^2 U^2 \tag{84}$$

Where I is the turbulence intensity and U is the magnitude of the mean flow velocity.

The turbulence dissipation rate at the inlet is:

$$\varepsilon_{inlet} = \frac{k_{inlet}^{3/2}}{0.3 D_h} \tag{85}$$

where D_h is the hydraulic diameter.

The turbulence dissipation rate can be converted to a specific turbulence dissipation using the following equation:

$$\omega_{inlet} = \frac{\varepsilon_{inlet}}{\beta' k} \tag{86}$$

3.2. Supercritical Fluid Properties

3.2.1. Water - CFX

In CFX, properties of water are calculated based on the temperature and pressure of water and steam using the IAPWS-IF97 database, formulated as in [86]. This database provides an accurate equation of state for water and steam properties. The range of validity of this property package as implemented in CFX is as follows:

$0\ [°C] < T \leq 800\ [°C]$ for $10\ [MPa] \leq P \leq 100\ [MPa]$

$800\ [°C] < T < 2000\ [°C]$ for $P < 10\ [MPa]$

The minimum and maximum temperature and pressure must be given in CFX, as well as the maximum number of integration points. A maximum of 1000 points is used for all cases in this study. This allows CFX to calculate a lookup table of all the necessary physical properties of the fluid for the entire range of temperatures and pressures that will be encountered in each run.

3.2.2. Water - FLUENT

In FLUENT, the National Institute of Standards and Technology (NIST) real gas model is used to calculate the physical properties of water whenever needed by the solver. This model uses the NIST Thermodynamic and Transport Properties of Refrigerants and Refrigerant Mixtures Database Version 9.0 (REFPROP v9.0) which itself uses the equations of state from the IAPWS-IF97 database [87]. Specific details on implementing this model are given in Appendix B.2.

3.2.3. R12 - CFX

The thermophysical properties of R12 where obtained from the NIST Chemistry WebBook [3] at various temperatures and absolute pressures. Lookup tables that use both the temperature and absolute pressure were then generated for the density, specific heat capacity at constant pressure, thermal conductivity, and dynamic viscosity. A custom macro, written in the Visual Basic for Applications (VBA) programming language, within Microsoft Excel was then used to generate lookup tables that were implemented in CFX as FORTRAN subroutines.

The thermophysical properties were obtained from the NIST Chemistry WebBook at temperature intervals of either 0.5 [K] or 0.1 [K] at pressures of 2,000 [Pa] and 4,000 [Pa] below the operating pressure for the cases 2 and 3, respectively, and at pressures of 18,000 [Pa] and 36,000 [Pa] above the operating pressure for case 2 and 3, respectively. In this work, the properties of R12 were produced for a range of pressures: between 4.626 [MPa] and 4.646 [MPa] for case 2, and between 4.641 [MPa] and 4.681 [MPa] for case 3. In creating the tables, the 0.5 [K] temperature intervals were used when the gradients in thermophysical properties were small, and the 0.1 [K] temperature intervals were used when the gradients in thermophysical properties were large. For a given pressure, there are 512 data points. The thermophysical properties where copied into Microsoft Excel, and a custom macro, written in VBA, generated a lookup table for the density, specific heat capacity at constant pressure, thermal conductivity, and dynamic viscosity in a FORTRAN compatible format. A complete description on how to create and implement these lookup tables in CFX is given in Appendix B.1. In order for CFX to obtain a thermophysical property at a certain location, the temperature and absolute pressure at that location is passed to the FORTRAN subroutine for the desired thermophysical property, and the

property value is passed back to CFX. The lookup tables use linear interpolation between two temperatures and absolute pressures to estimate the thermophysical property at a given temperature and absolute pressure.

To ensure these lookup tables provided accurate thermophysical property data, a test case was run on CFX and the resulting thermophysical properties were compared to those obtained from NIST Thermodynamic and Transport Properties of Refrigerants and Refrigerant Mixtures Database Version 9.0 (REFPROP v9.0). This test case consisted of a 1 [m^3] grid with nodes in the x, y, and z direction of 4, 4, and 20,001, respectively. The domain was stationary R12 under constant pressure. The temperature at the x-y plane boundaries was fixed at just above the minimum and just below the maximum temperatures of the lookup tables, 350.5 [K] and 520 [K], respectively. The boundary condition on the remaining four planes was symmetry. A solution was then obtained using CFX. The thermophysical properties where sampled at every nodal location along a line that ran through the centre of the domain, parallel to the z-axis. These properties were then compared to those obtained from REFPROP for the same temperature and absolute pressure. A summary of the resulting comparison is given in Table 7, where the dummy variable, Φ_{CFX} represents a thermophysical property value obtained through FORTRAN subroutines when using CFX, and Φ_{NIST} represents a thermophysical property value obtained through NIST REFPROP. In Table 7 the subscript i is added to the Φ_{CFX} and Φ_{NIST} variables to represent the nodal location with respect to the z-axis, where i varies from 1 to the maximum number of nodes in the z-axis, 20,001. The three rows of comparisons of Table 7 are the maximum range in property values, range-normalized maximum difference between values obtained through FORTRAN subroutines and NIST REFPROP, and range-normalized root mean

square of the difference between values obtained through FORTRAN subroutines and NIST REFPROP. The maximum range in temperature is 700 [K].

Table 7: Comparison between thermophysical property values determined through FORTRAN subroutine when using CFX and values determined using NIST REFPROP.

	Φ			
	ρ [kg/m^3]	c_p [J/kgK]	λ [W/mK]	μ [Pa s]
$\mathrm{Max}(\Phi_{CFX}) - \mathrm{Min}(\Phi_{CFX})$	949.5	68363	0.5993	0.0008224
$\frac{\mathrm{Max}\lvert\Phi_{i,CFX} - \Phi_{i,NIST}\rvert}{\mathrm{Max}(\Phi_{CFX}) - \mathrm{Min}(\Phi_{CFX})} \cdot 100$ [%]	0.2802	8.545	1.345	0.1940
$\sqrt{\frac{1}{\mathrm{N}}\sum_{\mathrm{i}=1}^{\mathrm{N}}\left(\frac{\mathrm{Max}\lvert\Phi_{i,CFX} - \Phi_{i,NIST}\rvert}{\mathrm{Max}(\Phi_{CFX}) - \mathrm{Min}(\Phi_{CFX})} \cdot 100\right)^2}$ [%]	0.01402	0.3596	0.05830	0.03387

From Table 7 it can be seen that the maximum root mean square of the difference in thermophysical properties is 0.3596 % for the specific heat capacity at constant pressure. The root mean square of the difference in thermophysical properties is an order of magnitude less for the remaining properties. These values are very low, therefore the conclusion can be made that the thermophysical properties implemented using FORTRAN subroutines in CFX are reasonably accurate when compared to those properties obtained through NIST REFPROP. From this conclusion, FORTRAN subroutines were implemented in CFX to obtain thermophysical properties of R12.

3.2.4. R12 - FLUENT

In FLUENT, the NIST real gas model is used to calculate the physical properties of R12 whenever needed by the solver. This model uses the NIST Thermodynamic and Transport Properties of Refrigerants and Refrigerant Mixtures Database Version 9.0 (REFPROP v9.0). Specific details on implementing this model are given in Appendix B.2. To enable this model, the same process described in Section 3.2.2 is used, except that “R12.fld" is entered, instead of “water.fld”.

3.3. Solid Properties

Thermophysical properties of the various solid materials used in the experiments that were numerically modelled in this study were obtained from various sources, and implemented in CFX and FLUENT by various methods. One of the following approaches was used to define the thermophysical properties of all solid materials:

1. A constant value was defined
2. A temperature dependant polynomial was given
3. A temperature dependent lookup table using a FORTRAN subroutine was given
4. A temperature dependent piecewise linear profile was given

3.3.1. Rohde et al. Seven-Rod Bundle Solid Properties

Inconel 600 density, specific heat capacity, and thermal conductivity property data were supplied by Rohde et al. [31] for a temperature range of 300 [K] to 900 [K]. Microsoft Excel was used to curve fit first order polynomials to the density and thermal conductivity data, and a third order

polynomial was curve fit to the specific heat capacity data. These polynomials where used in both CFX and FLUENT to model the thermophysical properties of Inconel 600, with one exception: FLUENT only allows a constant density be defined for a solid material.

Nichrome and boron nitride density, specific heat capacity, and thermal conductivity property data were obtained from Touloukian [88]. Microsoft Excel was used to curve fit a first order polynomial to the nichrome thermal conductivity data, and a second order polynomial was curve fit to the boron nitride thermal conductivity data. These polynomials, and constant values of density and specific heat capacity where used in both CFX and FLUENT to model the thermophysical properties of nichrome and boron nitride.

The polynomial functions used for these properties are given later along with the detailed description of the problem.

3.3.2. Richards Seven-Rod Bundle Solid Properties

Thermophysical property data of stainless steel 304L were obtained from Graves et al. [89]. The density was constant and the specific heat capacity was modelled as a second order polynomial with temperature. To model the thermal conductivity in CFX, a lookup table was implemented using a FORTRAN subroutine that used 13 data points between 333.7 [K] and 975.3 [K], and are given in Appendix C.1. This lookup table used temperature to assign the thermal conductivity, and was implemented in a similar way to that of the R12 thermophysical properties.

To model the thermal conductivity in FLUENT, a lookup table was implemented using a built-in feature, and used the same 13 data points as the lookup table used in CFX. This lookup table also used temperature to assign the thermal conductivity.

3.3.3. Wang et al. Four-Rod Bundle Solid Properties

Thermophysical properties of stainless steel 304L for the Wang et al. cases were modelled in the same way as for the Richards seven-rod bundle cases. Section 3.3.2 describes the method by which the thermophysical properties were modelled in CFX and FLUENT for stainless steel 304L.

3.4. Grid Generation

Meshes consisting of many hexahedral elements were created that represented the geometries of the various rod bundle cases. CFX and FLUENT create control volumes using these meshes and the discretized linearized system of equations is solved for each control volume. ANSYS ICEM CFD v14.5, v15.0, and v16.1 were used to generate meshes in the .cfx5 and .msh format for use in CFX and FLUENT, respectively.

To reduce the total number of nodes of the Rohde et al. and Richards meshes, the spacers were not modelled. These spacers would have required the number of nodes to be substantially increased in the vicinity of the spacers, and would have increased the complexity of the x-y cross section of the mesh in order for the mesh to only contain hexahedral elements. The spacers were shown to only locally affect the cladding surface temperature and increase the overall pressure drop of the Rohde et al. B2 case [90]. This conclusion is assumed to be applicable to the Richards cases as well.

To further reduce the total number of nodes of the meshes, only a portion of the entire bundle domain is modelled and a symmetry boundary condition is imposed on the necessary faces. Only $1/12^{th}$ of the entire x-y cross section of the seven-rod bundles of Rohde et al. and Richards was

modelled, and 1/8th of the entire x-y cross section of the Wang et al. four-rod bundle was modelled. The planes of symmetry of the Rohde et al., Richards, and Wang et al. bundles can be seen in Figure 8 in Section 4.1, Figure 40 in Section 5.1, and Figure 80 in Section 6.1 respectively.

Meshes were generated for all three geometries, and a grid independence study was performed for case B2 of Rohde et al., case 2 of Richards, and case T65000 of Wang et al. The SST turbulence model with automatic wall treatment was used in CFX to perform the grid independence study. The grid spacing of the nodes directly in contact with the solid walls was reduced to certain values so that the non-dimensional wall distance, y^+_{Auto}, was one, or less, for all meshes. After the final mesh was chosen for each geometry, runs were performed for other cases and different turbulence models were used for all cases. The non-dimensional wall distance was checked with each of these runs to ensure the value was one or less when automatic wall treatment was used in CFX, or when enhanced wall treatment or a Low-Re k-ε model was used in FLUENT. The scalable wall treatment of FLUENT does not require the non-dimensional near wall distance, y^*_{Scale}, to be less than one, because the minimum value of y^*_{Scale} is restricted to 11.06, according to Equation (63) in Section 3.1.3.1.

To generate the meshes in ICEM CFD, the following steps were followed:

- Points were created using x, y, and z coordinates. The dimensions of all meshes were entered in millimeters (i.e. 1.83 [m] would be entered as 1830 in ICEM CFD), convenience when modelling the geometry. (The mesh was scaled in the final steps to give the mesh the correct units of measurement.)
- Lines were created that connected all points.

- Surfaces were created using lines, and were given names that corresponded to the boundary condition that was be imposed at that surface.
- An initial block was created that enclosed all the points, lines, and surfaces.
- The block was split at certain locations and/or vertices.
- Vertices, edges, and faces of the blocks were associated to the appropriate points, lines, and surfaces, respectively, and in that order.
- For meshes with multiple domains which have more than just a fluid domain, each domain was saved as a separate part with an appropriate name that reflected the material of the domain.
- The number of and distribution of the nodes were defined using edge parameters, and were copied to parallel edges.
- A pre-mesh was generated, which was then converted to an unstructured mesh.
- The unstructured mesh was then converted to either an ANSYS CFX (.cfx5) or ANSYS FLUENT (.msh) mesh file, and 0.001 was used as the x, y, and z scaling factors to allow for the proper units of measurement in the final mesh.

The resulting .cfx5 and .msh mesh files were then imported into CFX-Pre and FLUENT, respectively, to be used for runs. A separate document is available that gives a step-by-step guide on how to create a mesh of the Wang et al. four-rod bundle [75].

3.5. Numerical Solution Method

The governing equations of mass, momentum, energy, and turbulence are replaced by algebraic approximations, and solved numerically by the CFX and FLUENT solvers to obtain solution

fields for all desired variables. CFX and FLUENT use an element-based finite volume method, whereby the spatial domain is discretized into a mesh of finite volumes, and relevant quantities (mass, momentum, etc.) are conserved on a control-volume basis.

3.5.1. CFX

CFX uses a co-located grid layout, where the solution field values are stored at control volume centres, which are defined as mesh nodes in CFX. This allows for the use of a single mesh to solve all the governing equations. Normally this co-located grid would lead to a de-coupled pressure field, but due to the work of Rhie and Chow [91], which involves an alternative discretization of the mass flows, the pressure field is instead coupled with the velocity field.

Solution variables and domain properties are stored at mesh nodes. Control volumes are generated around each mesh node using the median dual as the control volume boundary. Median duals are created using planes that join the centres of each control volume. Figure 5 shows a typical control volume in CFX, simplified for 2D.

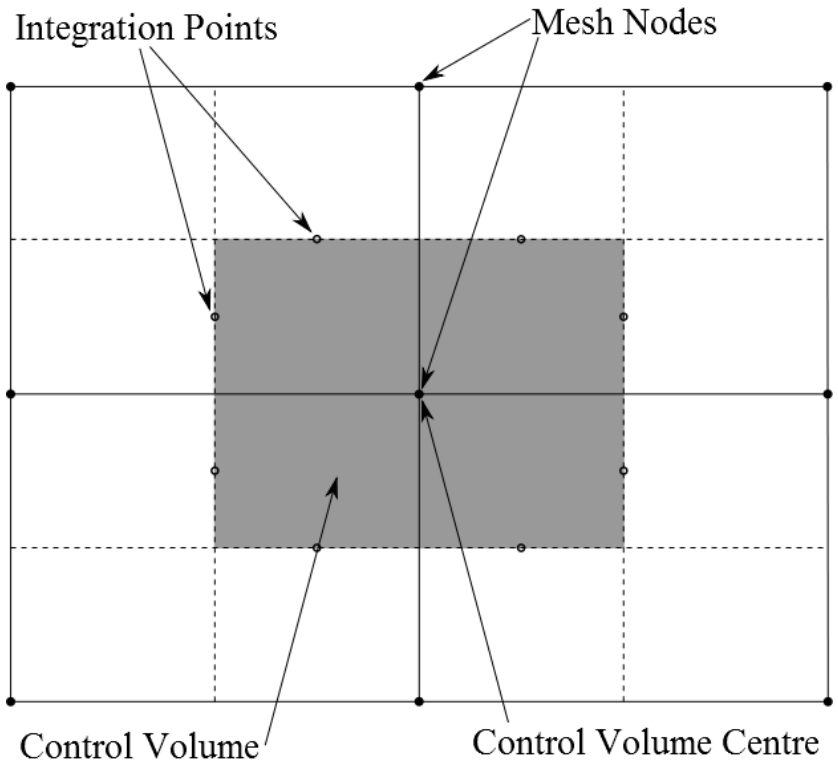

Figure 5: 2D simplification of a typical control volume (shaded region) surrounding a mesh node in CFX. Mesh nodes are solid circles and integration points are hollow circles.

The governing equations of mass, momentum, energy, and turbulence are integrated over each control volume and Gauss' Divergence Theorem is used to convert volume integrals of divergence and gradient operators to surface integrals.

Volume integrals are discretized within each sector of each element, and accumulated to the node of the control volume which the element sector belongs to. Surface integrals are evaluated at integration points, located at the centre of the surfaces that separate element sectors. The resulting algebraic equations for mass, momentum, and scalars are as follows:

$$\sum_{ip=1}^{\mathbb{N}_{ip}} \left(\rho U_j \Delta \mathbb{m}_j\right)_{ip} = 0 \tag{87}$$

$$\sum_{ip=1}^{\mathbb{N}_{ip}} \left(\rho U_j \Delta \mathbb{m}_j\right)_{ip} (U_i)_{ip} = \sum_{ip=1}^{\mathbb{N}_{ip}} (P \Delta \mathbb{m}_i)_{ip} + \sum_{ip=1}^{\mathbb{N}_{ip}} \left((\mu + \mu_t) \left(\frac{\partial U_i}{\partial x_j} + \frac{\partial U_j}{\partial x_i} \right) \Delta \mathbb{m}_j \right)_{ip} + \overline{S_{U_i}} \forall \quad (88)$$

$$\sum_{ip=1}^{\mathbb{N}_{ip}} \left(\rho U_j \Delta \mathbb{m}_j\right)_{ip} (\varphi)_{ip} = \sum_{ip=1}^{\mathbb{N}_{ip}} \left((\Gamma + \Gamma_t) \frac{\partial \varphi}{\partial x_j} \Delta \mathbb{m}_j \right)_{ip} + \overline{S_\varphi} \forall \quad (89)$$

where the subscript ip represents the current integration point, $\mathbb{N}_{ip}$ is the total number of integration points, $\Delta \mathbb{m}$ is the discrete outward surface vector, $\overline{S_{U_i}}$ is the average momentum source term over the control volume, $\forall$ is the volume of the control volume, φ represents a scalar variable (T, k, ε, or ω), Γ is the molecular diffusion coefficient of the scalar variable (in the case of temperature being the scalar, this would be thermal conductivity, λ), Γ_t is the turbulent diffusion coefficient of the scalar variable (in the case of temperature being the scalar, this would be the turbulent thermal conductivity, λ_t), and $\overline{S_\varphi}$ is the average scalar source term over the control volume.

To evaluate solution variables and gradients at integration points, CFX uses shape functions to approximate values from nodal values. The following summation shows how the solution variable at a particular location within an element, $\psi(x', y', z')$, is approximated from nodal values of the solution variable, ψ_i, and shape functions, $\mathcal{N}_i(x', y', z')$:

$$\psi(x', y', z') = \sum_{i=1}^{\mathbb{N}_{node}} \mathcal{N}_i(x', y', z')\, \psi_i \quad (90)$$

where $\mathcal{N}_i(x', y', z')$ is the shape function for node i, the location of node i is given by x', y', z', the value of the solution variable at node i is ψ_i, and $\mathbb{N}_{node}$ is the total number of nodes of the

element under consideration. Because all meshes in this study use hexahedral elements, the value of $\mathbb{N}_{node}$ is eight. Figure 6 shows a typical hexahedral element in a local x', y', z' coordinate system, with nodes labeled 1 to 8. Shape functions that are used for this hexahedral element are given by Equations (91) to (98).

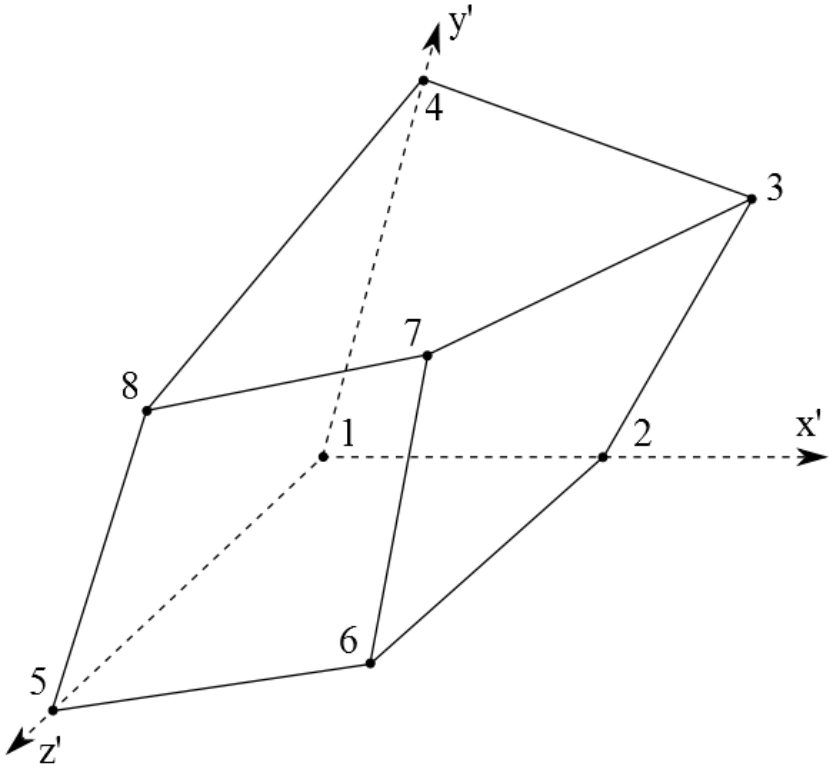

Figure 6: Hexahedral element with nodes labeled from 1 to 8. Local x', y', z' coordinate system is used.

$$\mathcal{N}_1(x', y', z') = (1 - x')(1 - y')(1 - z') \tag{91}$$

$$\mathcal{N}_2(x', y', z') = x'(1 - y')(1 - z') \tag{92}$$

$$\mathcal{N}_3(x', y', z') = x'\, y'\, (1 - z') \tag{93}$$

$$\mathcal{N}_4(x', y', z') = (1 - x')\, y'\, (1 - z') \tag{94}$$

$$\mathcal{N}_5(x', y', z') = (1 - x')(1 - y')z' \tag{95}$$

$$\mathcal{N}_6(x', y', z') = x'(1 - y')z' \tag{96}$$

$$\mathcal{N}_7(x', y', z') = x'y'z' \tag{97}$$

$$\mathcal{N}_8(x', y', z') = (1 - x')\, y'\, z' \tag{98}$$

The gradient of the solution variable at a particular location within an element, $\nabla\psi$, is approximated from nodal values using a form of Gauss' divergence theorem:

$$\nabla\psi = \frac{1}{\forall} \sum_{ip=1}^{\mathbb{N}_{ip}} (\psi\, \Delta\vec{\mathbb{m}})_{ip} \tag{99}$$

where $\Delta\vec{\mathbb{m}}$ is the outward surface vector at ip, and ψ is the value of the solution variable at ip, determined using Equation (90).

To calculate the values of the solution variables at integration points, two different advection schemes are used. The first order Upwind Difference Scheme (UDS) is used for the turbulence variables and the High Resolution Scheme is used for all other variables. The general form for both these advection schemes is:

$$\psi_{ip} = \psi_{up} + \mathcal{B}\, \nabla\psi \cdot \Delta\vec{r} \tag{100}$$

where $\psi_{up}$is the value of the solution variable at the upwind node, $\vec{r}$ is the vector from the upwind node to the current integration point, and the values of $\mathcal{B}$ and $\nabla\psi$ are chosen based on the particular advection scheme being used.

The first order Upwind Difference Scheme sets $\mathcal{B}$ to zero, yielding a very robust scheme, which is ideal for turbulence quantities, however diffusive discretization errors that smear large gradients can appear in the solution.

The High Resolution Scheme sets the value of the advection flux term using the values of $\mathcal{B}$ and $\nabla\psi$ from the upwind node. The value of $\mathcal{B}$ is determined using the non-linear method of Barth and Jesperson [92] as follows. The minimum and maximum values of the solution variables are first calculated at each node, using the values of neighbouring nodes and the value of the node itself. The values of $\mathcal{B}$ for each integration point are then determined so that the solution variables at each integration point do not exceed or fall below the maximum and minimum values at the node to which the integration points belong to. The value of $\mathcal{B}$ at each node is then selected as the minimum value of $\mathcal{B}$ of all integration points surrounding each node, with the additional constraint that $\mathcal{B}$ cannot exceed 1.

Spatial derivatives are calculated using shape functions as follows:

$$\left.\frac{\partial\psi}{\partial x_i}\right|_{ip} = \sum_{n=1}^{\mathbb{N}_{node}} \left.\frac{\partial\mathcal{N}_n}{\partial x_i}\right|_{ip} \psi_n \tag{101}$$

where the value of the solution variable at each of the eight nodes and the value of all eight of the spatial derivatives of the shape functions at the integration point must be known. The spatial derivatives of each shape function are determined using the Jacobian transformation matrix:

$$\begin{bmatrix} \frac{\partial N}{\partial x} \\ \frac{\partial N}{\partial y} \\ \frac{\partial N}{\partial z} \end{bmatrix} = \begin{bmatrix} \frac{\partial x}{\partial x'} & \frac{\partial y}{\partial x'} & \frac{\partial z}{\partial x'} \\ \frac{\partial x}{\partial y'} & \frac{\partial y}{\partial y'} & \frac{\partial z}{\partial y'} \\ \frac{\partial x}{\partial z'} & \frac{\partial y}{\partial z'} & \frac{\partial z}{\partial z'} \end{bmatrix}^{-1} \begin{bmatrix} \frac{\partial N}{\partial x'} \\ \frac{\partial N}{\partial y'} \\ \frac{\partial N}{\partial z'} \end{bmatrix} \tag{102}$$

The pressure term at each integration point, P_{ip}, is calculated using shape functions as follows:

$$P_{ip} = \sum_{n=1}^{\mathbb{N}_{node}} \mathcal{N}_n\left(x'_{ip}, y'_{ip}, z'_{ip}\right) P_n \tag{103}$$

where the pressure at each of the eight nodes, P_n, and the value of all eight of the shape functions at the integration point must be known.

The general form of the coupled system of linear equations that result from applying the finite volume method to all control volumes is:

$$\sum_{nb_i}^{\mathbb{N}_{cv}} a_i^{nb} \psi_i^{nb} = b_i \tag{104}$$

where a is the matrix that contains the coefficients of the solution variable matrix ψ, and b is the matrix on the right hand side. The subscript i identifies the specific control volume under consideration and the superscript nb signifies the neighbouring nodes, including the control volume under consideration. The complete set of these equations for every control volume is the

whole linearized equation system, and is solved by CFX using a coupled solver. This coupled solver solves the hydrodynamic equations (velocities and pressure) as a single system. This solution approach uses a fully implicit discretization of the equations. For steady-state problems, the time step is used as a relaxation parameter that guides the approximate solutions to a steady-state solution. The coefficients of the linearized equations are updated after a solution and the non-linear set is iterated until steady-state convergence is obtained. A Multigrid accelerated Incomplete Lower Upper factorization technique is used by CFX for solving the system of equations.

The normalized residual, $\tilde{r}_{\psi}$, is computed for every control volume at each iteration. Residuals are the imbalance of the linear discretized system of equations. These normalized residuals are one of the factors that are used to judge convergence. CFX calculates these normalized residuals using the raw residual, r_{ψ}, which is the imbalance in the linearized system of discrete equations, a representative coefficient of the control volume, a_p, and a representative value of the overall range in the solution variable, ψ_{range}:

$$\tilde{r}_{\psi,i} = \frac{r_{\psi,i}}{a_p \psi_{range}} \tag{105}$$

The subscript i identifies the current control volume for which the residual is being computed. The method used to calculate a_p and ψ_{range} is 'not simple', and is not available in CFX Reference documents.

Domain imbalances are calculated by CFX at each iteration by summing the solution variables at the boundary of every domain, then normalizing the resulting sum using the largest contributor

of that solution variable to give an imbalance percentage. This imbalance percentage is calculated for each domain as follows:

$$Imbalance = \frac{100}{Max\left(\left|\sum_{i=1}^{N} \psi_{i,j}\right|\right)} \cdot \sum_{j=1}^{N_{boundaries}} \sum_{i=1}^{N} \psi_{i,j} \tag{106}$$

where ψ is the solution variable, N is the total number of sampled locations on a boundary, and $N_{boundaries}$ is the total number of boundaries in each domain. The above equation yields the domain imbalance as a percentage.

To ensure proper convergence of the solution, CFX recommends the maximum normalized residual for all equations be at most $1x10^{-4}$ [74]. This criterion is usually sufficient for most engineering applications, but to achieve tight convergence the maximum normalized residual should be at most $1x10^{-5}$. Additionally, the domain imbalances should be less than 1 %, as recommended by the CFX Solver Modelling Guide [74]. For CFX runs for the present study, unless stated otherwise, the maximum value of the continuity, momentum, and energy equation residuals were less than $1x10^{-5}$, the maximum value of the turbulence equation residuals were less than $1x10^{-4}$, and the maximum value of the domain imbalances for the continuity, momentum, energy, and turbulence equations were less than 0.1 %.

Various solution variable monitor points are defined for the CFX runs, to provide an additional means to check convergence of the runs. The solution variable at the monitor points are reported at each iteration, and provide further assurance that a solution is converged when a minimal change in these variables over a given number of iterations is achieved. The monitor points consist of the surface temperature of the cladding or heater rod, depending on the experimental

setup, at various locations and the pressure near the centroid of both the inlet and outlet. Monitor points may also include the velocity w at various locations, pressure at locations other than the inlet or outlet, and internal solid domain temperatures.

3.5.2. FLUENT

A pressure-based coupled algorithm is used in FLUENT to solve the momentum and pressure based continuity system of equations. FLUENT uses a co-located grid layout, similar to CFX, where the solution field values are stored at control volume centres. The difference between CFX and FLUENT is that control volume centres are defined as mesh nodes in CFX and defined as the centres of mesh elements in FLUENT. The method of Rhie and Chow [91] is used to discretize the governing equations so that the pressure field is coupled with the velocity field. Integration points are located at the centroid of control volume faces.

Solution variables must be calculated at control volume faces for various convection terms. Figure 7 shows a typical control volume, simplified to 2D.

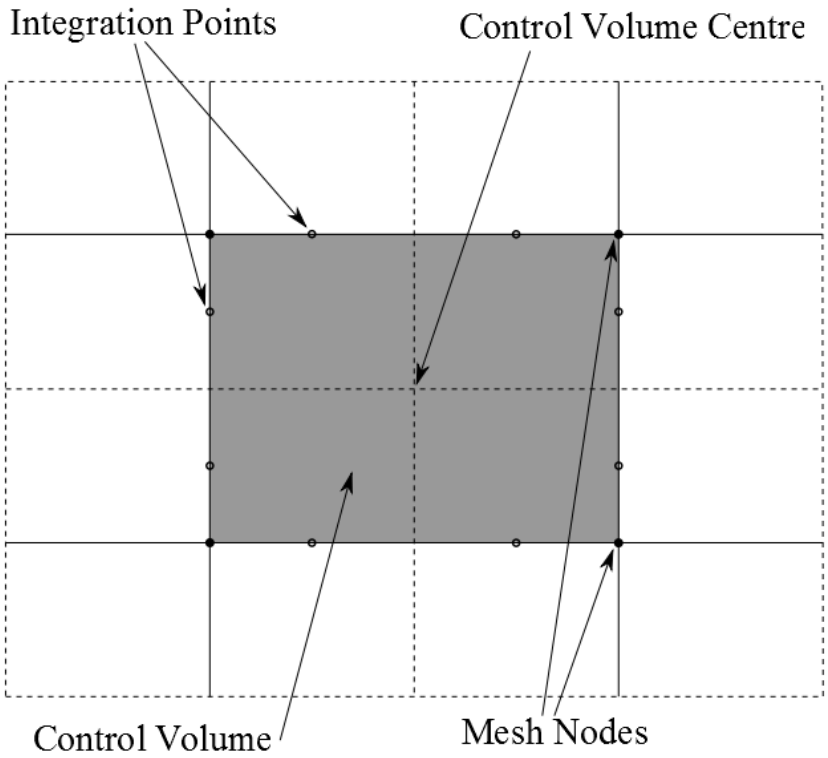

Figure 7: 2D simplification of a typical control volume (shaded region) surrounding a cell centre in FLUENT. Mesh nodes are solid circles and integration points at the centroids of control volume faces are hollow circles.

The governing equations of mass, momentum, energy, and turbulence are integrated over each control volume. These integrated equations are discretized for each control volume for mass, momentum, and a scalar variable as shown by Equations (107), (108), and (109), respectively.

$$\sum_{f=1}^{\mathbb{N}_{faces}} \left(\rho \vec{U} \cdot \vec{A}\right)_f = 0 \tag{107}$$

$$\sum_{f=1}^{\mathbb{N}_{faces}} \left(\rho \vec{U}\vec{U} \cdot \vec{A}\right)_f = \sum_{f=1}^{\mathbb{N}_{faces}} \left(P\vec{A}\right)_f + \sum_{f=1}^{\mathbb{N}_{faces}} \left((\mu + \mu_t)\nabla \vec{U} \cdot \vec{A}\right)_f + \overline{S_{U_i}}\,\forall \tag{108}$$

$$\sum_{f=1}^{\mathbb{N}_{faces}} \left(\rho\vec{U}\varphi \cdot \vec{A}\right)_f = \sum_{f=1}^{\mathbb{N}_{faces}} \left((\Gamma + \Gamma_t)\nabla\varphi \cdot \vec{A}\right)_f + \overline{S_\varphi}\,\forall \tag{109}$$

where the subscript f represents the current face, $\mathbb{N}_{faces}$ is the total number of faces of the control volume, $\vec{A}$ is the area of the current face, $\overline{S_{U_i}}$ is the average momentum source term over the control volume, $\forall$ is the volume of the control volume, φ represents a scalar variable at the current face (temperature, turbulence kinetic energy, etc.), Γ is the molecular diffusion coefficient of the scalar variable (in the case of temperature being the scalar, this would be thermal conductivity, λ), Γ_t is the turbulent diffusion coefficient of the scalar variable (in the case of temperature being the scalar, this would be the turbulent thermal conductivity, λ_t), $\nabla\varphi$ is the gradient of the scalar variable at the current face, and $\overline{S_\varphi}$ is the average scalar source term over the control volume.

Turbulence quantities are calculated at faces using the First-Order Upwind Scheme, and for the remaining solution variables a Second-Order Upwind Scheme is used. The First-Order Upwind Scheme sets the face values of solution variables to the upwind cell centre values. The Second-Order Upwind Scheme uses the multidimensional linear reconstruction method of Barth and Jesperson [92] to compute cell face values. The following equation is used to compute the face values of a solution variable, ψ_f, from the upwind cell centre values of the solution variable, ψ_{up}, and its gradient, $\nabla\psi_{up}$:

$$\psi_f = \psi_{up} + \nabla\psi_{up} \cdot \vec{r} \tag{110}$$

where $\vec{r}$ is the vector from the upwind cell centroid to the current face centroid. The gradient used in this equation is limited so as not to give new maximum or minimum values.

The Least Squares Cell-Based Gradient Evaluation method is used to calculate solution variable gradients at cell centres. This method assumes the solution varies linearly between cell centres, and is given below:

$$\nabla\psi \cdot \Delta r_i = (\psi_i - \psi) \tag{111}$$

where $\nabla\psi$ is the solution variable gradient at the cell centre under consideration, Δr_i is the distance from the cell centre under consideration to the cell centre at the i^{th} cell, ψ is the solution variable at the cell centre under consideration, and ψ_i is the solution variable at the i^{th} cell centre. Equation (111) is written for each cell surrounding the cell under consideration, and the resulting system of linear equations is solved to obtain the solution variable gradient at a cell centre.

The pressures at cell faces, P_f, are computed using a central differencing scheme, and is known as the Second Order scheme:

$$P_f = \frac{1}{2}(P_i + P_0) + \frac{1}{2}(\nabla P_i \cdot \vec{r}_i + \nabla P_0 \cdot \vec{r}_0) \tag{112}$$

where P_i and P_0 are the pressures at the cell centres adjacent to the face under consideration, ∇P_i and ∇P_0 are the pressure gradients at the cell centres adjacent to the face under consideration, and $\vec{r}_i$ and $\vec{r}_0$ are the vectors from the face under consideration to the adjacent cell centres.

The general form of the coupled system of linear equations that result from applying the finite volume method to all control volumes is given by Equation (104) in Section 3.5.1. The complete set of these equations for every control volume is the whole linearized equation system, and is solved by FLUENT using a coupled solver. This coupled solver solves the hydrodynamic equations (velocities and pressure) as a single system. This solution approach uses a fully implicit discretization of the equations. For steady-state problems, under-relaxation of the solution is controlled through a pseudo transient under-relaxation method, where the pseudo time step value is defined so as to accelerate the solution towards convergence. The coefficients of the linearized equations are updated after a solution and the non-linear set is iterated until steady-state convergence is obtained. An Algebraic Multigrid accelerated Incomplete Lower Upper factorization technique is used by FLUENT for solving the system of equations.

FLUENT calculates the globally scaled residuals at each iteration by first taking the absolute value of the residuals of the linear discretized system of equations for every control volume and summing them over all control volumes. This 'unscaled' residual is then divided by the $\sum_{nb_i}^{\mathbb{N}_{cv}} a_i^{nb}\psi_i^{nb}$ term that appears in the linear discretized system of equations, given by Equation (104) in Section 3.5.1 to give the globally scaled residual.

Domain imbalances in FLUENT can be calculated by summing the solution variables at the boundary of every domain, then normalizing the resulting sum using the largest contributor of that solution variable to give an imbalance percentage. This imbalance percentage is calculated for each domain using Equation (106) in Section 3.5.1. This imbalance is only calculated for the continuity and energy solution variables, where the largest contributor to those solution variables are the mass flow rate at the inlet and the total heat rate at the heated wall, respectively.

To ensure the solution is converged FLUENT recommends the globally scaled residual for all equations be at most $1x10^{-3}$, except for the energy equation which should be at most $1x10^{-5}$ [74]. For FLUENT runs for the present study, unless stated otherwise, the maximum value of the continuity equation residuals were less than $1x10^{-3}$, the maximum value of the momentum and energy equation residuals were less than $1x10^{-5}$, the maximum value of the turbulence equation residuals were less than $1x10^{-4}$, and the maximum value of the domain imbalances for the continuity, momentum, energy, and turbulence equations were less than 0.1 %.

Various solution variable monitor points are defined for the FLUENT runs, similar to the CFX runs, and again provide an additional means to check convergence of the runs. The monitor points consist of the surface temperature of the cladding or heater rod, depending on the experimental setup, at various locations, and the area averaged pressure at the inlet and outlet. In addition to surface temperatures, monitor points may also be placed in the solid domains to measure internal temperatures.

CHAPTER 4: ROHDE ET AL. 2015 SEVEN-ROD BUNDLE WITH WATER

4.1. Experimental Setup

The experimental data of Rohde et al. were obtained from the JAEA for use in the GIF SCWR 2013-2014 seven-rod subchannel benchmark exercise, organised by the GIF Project Management board. The experimental setup consists of seven heater rods, orientated in a hexagonal arrangement, enclosed in a shroud to create subchannels with water flowing vertically upwards. Six spacers that are 25 [mm] (0.984252 [in]) in length position the rods inside the shroud, and position the rods relative to one another. The heater rods consist of a C-shaped cross-section (possibly helical) Nichrome element with a diameter of 4.2 [mm] (0.165354 [in]), encased in a boron nitride insulator with a diameter of 6 [mm] (0.236220 [in]), all of which is encased in a protective Inconel 600 cladding with a diameter of 8 [mm] (0.314961 [in]).

Figure 8 shows an x-y cross section of the Rohde et al. experimental setup, showing the heater rods, insulator, cladding, water channel, spacer, shroud, and external housing. The symmetry planes that will be used to simplify the modelling of this rod bundle are also shown.

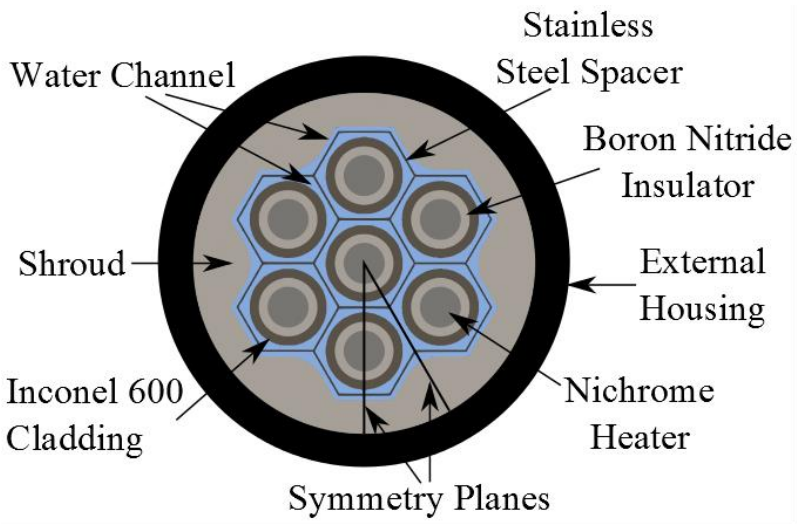

Figure 8: Cross section of Rohde et al. 2015 seven-rod bundle, showing composition of heater rods, spacers, shroud, external housing, and planes of symmetry.

Pressure taps are placed at 144 [mm] (5.66929 [in]) and 1340 [mm] (52.7559 [in]) from the start of the heated section. A total of 42 thermocouples are embedded into the external surface of the cladding at various locations along the heater rods, to measure the cladding surface temperature. Figure 9 shows a y-z cross section of the Rohde et al. experimental setup, showing the unheated inlet and outlet sections, heated section, location of all six spacers relative to the inlet, and the location of the pressure taps.

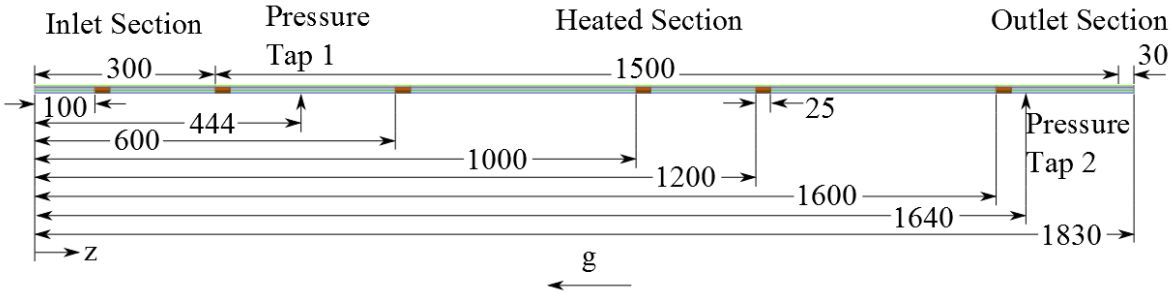

Figure 9: Schematic y-z cross section of the Rohde et al. 2015 domain, showing inlet, heated section, outlet, location of all six spacers relative to the inlet, and location of the pressure taps. All spacers are of the same length. Dimensions are in [mm].

There are three cases for this experiment, case A1, B1, and B2. Case A1 is an isothermal case with temperatures well below the pseudocritical point of water. Results for Case A1 are given in Appendix A.4, but only consist of the overall pressure drop. Case B1 is a heated case in which the fluid is below the pseudocritical point. The inlet temperature of case B2, which is also heated, is close to the pseudocritical point of water. The conditions of all three cases of the Rohde et al. experiments are given in Table 8.

Table 8: Experimental conditions of Rohde et al. 2015 experiments.

Case	Inlet Temperature [K]	Inlet Pressure [MPa]	Flow Rate [kg/min]	Mass Flux [kg/m²s]	Heater A [kW]	Heater B, D, F [kW]	Heater C, E, G [kW]
A1	297.35	25.00	26.33	2283.44	0	0	0
B1	353.58	24.98	16.69	1447.56	19.67	22.51	22.52
B2	519.58	25.03	16.52	1432.97	34.14	34.08	34.13

The pseudocritical temperature of water using the inlet pressures of cases B1 and B2 are given in Table 9, where the pseudocritical temperature is defined as the temperature at which the specific heat capacity at constant pressure reaches a maximum value.

Table 9: Pseudocritical temperatures of water at inlet pressures of Rohde et al. cases

Case	Inlet Pressure [MPa]	Pseudocritical Temperature [K]
B1	24.98	657.972
B2	25.03	658.153

4.2. Numerical Domain Definition, Boundary Condition, and Mesh

A 1/12th section of the Rohde et al. seven-rod bundle was modelled, and symmetry was assumed on both section planes. The Nichrome elements with their C-shaped cross sections were

modelled as solid rods of the same outside diameter as the C-shape. The hydraulic diameter of the subchannel is 2.84038 [mm] (0.111826 [in]). An x-y cross section of the bundle showing the section that has been modelled is given in Figure 8 in Section 4.1.

The total length of the domain is 1.83 [m] (6.00394 [ft]) in the z-direction, which includes a 0.3 [m] (0.984252 [ft]) inlet section, 1.5 [m] (4.92126 [ft]) heated section, and a 0.03 [m] (0.0984252 [ft]) outlet section. The six spacers are 0.025 [m] (0.082021 [ft]) long, and are located at various positions throughout the domain. A y-z cross section, showing the locations of these spacers, as well as the inlet, outlet, heated section, and location of the pressure taps is given in Figure 9. These spacers were not modelled in order to substantially reduce the total number of nodes.

The thermocouples are attached to the heater rods at various angles and axial locations. When the entire domain is simplified to the $1/12^{th}$ section, the total number of locations of thermocouples on the x-y plane is reduced to five because of symmetry. These locations correspond to lines a, b, c, d, and e as shown in Figure 10, which gives more details about the geometry of the computational domain.

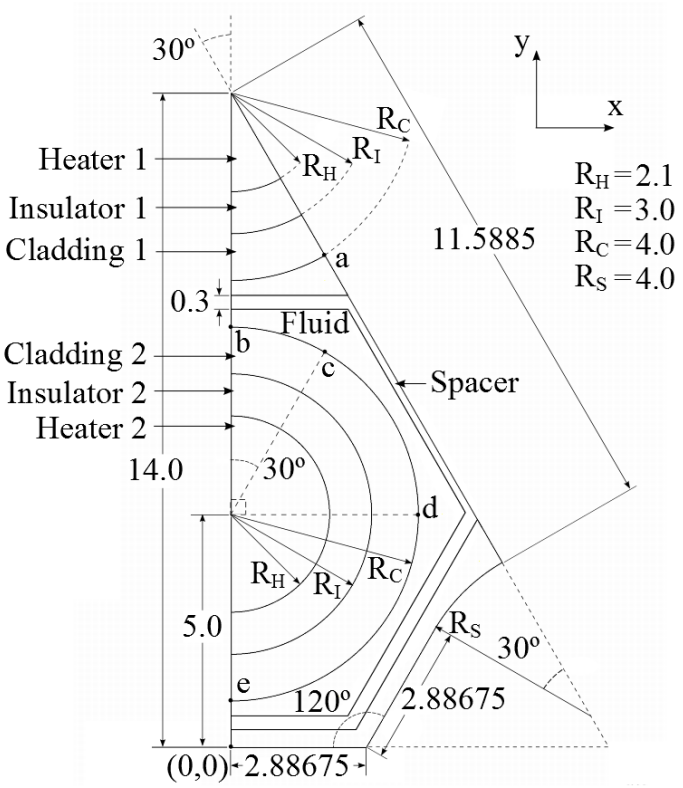

Figure 10: Typical x-y cross section of Rohde et al. 2015 domain showing fluid and solid domains and locations of thermocouples: lines a, b, c, d, and e. All dimensions in [mm].

The thermocouples are located at certain axial locations along lines a, b, c, d, and e. Tables 10 to 13 provide domain definitions and boundary conditions for each of the domains shown in Figure 10.

Table 10: Domain definition and boundary conditions of Rohde et al. 2015 fluid domain.

Fluid	
Domain Properties	Material: Water Turbulence Model: SST, k-ε, RNG k-ε, Lam-Bremhorst Low-Re k-ε, Yang-Shih Low-Re k-ε Turbulent Prandtl Number (Pr_t): 0.9 Reference Pressure: 24.98 [MPa] (Case B1), 25.0110 [MPa] (Case B2)
Material Properties	IAPWS-IF97 Database (CFX), NIST REFPROP v9.0 Database (FLUENT)
Inlet	Mass Flow Rate: 0.0231806 [kg/s] (Case B1), 0.0229444 [kg/s] (Case B2) Temperature: 353.58 [K] (Case B1), 519.58 [K] (Case B2) Turbulence: Low Intensity (I = 1 %), Low Eddy Viscosity Ratio (μ_t / μ = 1.0)[1] w = 1.44172 [m/s] (Case B1), 1.73644 [m/s] (Case B2) Re = 11188.8 (Case B1), 35957.3 (Case B2)
Fluid Properties at Inlet, Case B1	ρ = 982.336 [kg/m^3] μ = 3.59528x10^{-4} [Pa s] c_p =4144.9 [J/kgK] λ = 0.68284 [W/mK]
Fluid Properties at Inlet, Case B2	ρ = 825.735 [kg/m^3] μ = 1.13316x10^{-4} [Pa s] c_p = 4611.90 [J/kgK] λ = 0.649645 [W/mK]
Outlet	Reference Static Pressure: 0 [Pa]
Wall	Adiabatic no-slip at Shroud, coupled (FLUENT) or conservative interface heat flux (CFX) to Cladding 1 and 2 domains (R_C)

[1]The turbulence intensity at the inlet doesn't significantly affect surface temperatures: maximum values of $RMS_{RN,T}$ from using medium and high inlet turbulence intensity was 0.01 % and 0.02 %, respectively using low inlet turbulence intensity result as reference, for case B2 using the SST turbulence model and CFX. Therefore, low inlet turbulence intensity was used for all cases, since it provided more stable convergence than medium or high intensity inlet turbulence.

Table 11: Domain definition and boundary conditions of Rohde et al. 2015 cladding 1 and 2 domains.

Cladding 1 and 2	
Domain Properties	Material: Inconel 600
Material Properties	ρ = - 0.3922057147 [kg/m^{3}K] T + 8528.0312491363 [kg/m^3] c_p = 7.524x10^{-7} [J/kgK^4] T^3 - 0.0012939439 [J/kgK^3] T^2 + 0.9069264845 [J/kgK^2] T + 262.8297423839 [J/kg^{1}K^1] λ = 0.0160336023 [W/mK^2] T + 9.6331381197 [W/mK]
Wall	Adiabatic wall across *x-y* plane at *z* = 0.0 [m] and *z* = 1.83 [m], coupled (FLUENT) or conservative interface heat flux (CFX) across x-y plane at z = 0.3 [m] and z = 1.8 [m], coupled (FLUENT) or conservative interface heat flux (CFX) to Fluid (R_C) and Insulator 1 and 2 domains (R_I)

Table 12: Domain definition and boundary conditions of Rohde et al. 2015 insulator 1 and 2 domains.

Insulator 1 and 2	
Domain Properties	Material: Boron Nitride
Material Properties	ρ = 2130 [kg/m^3] c_p = 1265.3 [J/kgK] λ = 1.792707x10^{-4} [W/mK^3] T^2 - 0.3714505815 [W/mK^2] T + 298.4687499009 [W/mK]
Wall	Adiabatic wall across *x-y* plane at *z* = 0.0 [m] and *z* = 1.83 [m], coupled (FLUENT) or conservative interface heat flux (CFX) across x-y plane at z = 0.3 [m] and z = 1.8 [m], coupled (FLUENT) or conservative interface heat flux (CFX) to Cladding 1 and 2 (R_I), and Heater 1 and 2 domains (R_H)

Table 13: Domain definition and boundary conditions of Rohde et al. 2015 heater 1 and 2 domains.

Heater 1 and 2	
Domain Properties	Material: Nichrome
Material Properties	ρ = 8410 [kg/m^3] c_p = 420 [J/kgK] λ = 0.0179188239 [W/mK^2] T + 4.5115124321 [W/mK]
Wall	Adiabatic wall across *x*-*y* plane at *z* = 0.0 [m] and *z* = 1.83 [m], coupled (FLUENT) or conservative interface heat flux (CFX) across x-y plane at z = 0.3 [m] and z = 1.8 [m], coupled (FLUENT) or conservative interface heat flux (CFX) to Insulator 1 and 2 domains (R_H)
Heated Section Energy Source	Heater 1 Volumetric Heat Rate (from heat rates of Heater A): 9.46509x10^8 [W/m^3] (Case B1), 1.64280x10^9 [W/m^3] (Case B2) Heater 2 Volumetric Heat Rate (from average heat rate of Heaters B, C, D, E, F, and G): 1.08341x10^9 [W/m^3] (Case B1), 1.64111x10^9 [W/m^3] (Case B2)

Various solution variable monitor points are defined for CFX and FLUENT runs, to provide an additional means to check convergence of the runs. Solution variables at the monitor points are reported at each iteration, and provide further assurance that a solution is converged when a minimal change in these variables over a given number of iterations is achieved. For FLUENT runs, two of these monitor points were placed on line b and line c, and one was placed in the Cladding 2 domain, in order to measure temperature. The area averaged pressure at the inlet and outlet was also monitored. For CFX runs, two of these monitor points were placed on line b and line c, two were placed in the Heater 1 domain, and another two were placed in the Heater 2 domain, in order to measure temperature. Additionally for CFX runs, the pressure and velocity *w* were monitored at points that were scattered throughout the domain at many different locations, including the centroids near the inlet and outlet.

4.3. Grid Independence Study

A mesh of the 1/12th section of the seven-rod bundle was generated using ANSYS ICEM CFD, and the spacers were not modelled in order to substantially reduce the total number of nodes. Figure 8 in Section 4.1 shows this 1/12th section defined by the symmetry planes in relation to the entire x-y cross section. CFX was used to numerically solve case B2 using the SST turbulence model with automatic wall treatment. The SST turbulence model was chosen because, out of those turbulence models that were selected to provide final results, it was the only turbulence model that can be used in CFX that required a y^+ of less than one. The maximum residuals and domain imbalances were monitored during the runs, and a solution was considered to be converged when these variables reached values given in Section 3.5.1.

A number of initial meshes were first generated for which solutions were obtained for case B2 using CFX. Case B2 was chosen because the fluid temperature at the inlet was closer to the pseudocritical point than the other two cases, which would most likely cause the greatest variation in the heat transfer phenomena near the wall. A very fine mesh with a large number of nodes was eventually created and a solution was obtained. This mesh is referred to here as the BNSP-1 mesh and it had 18,035,143 nodes. Eight meshes were then generated and solutions were obtained, where the x-y and/or z cross-sections grid spacing were increased incrementally for each mesh, so that the total number of nodes was reduced for each newly created mesh. The coarsest mesh had 480,438 nodes.

The percent difference in overall pressure drop and difference in cladding surface temperature along each of the lines a, b, c, d, and e between each mesh and the mesh with the greatest number

of nodes were compared. The differences in temperature were quantified using a range-normalized root mean square parameter, $\mathrm{RMS}_{\mathrm{RN,T}}$, defined below:

$$\mathrm{RMS}_{\mathrm{RN,T}} = 100 \cdot \sqrt{\frac{1}{N}\sum_{i=1}^{N}\left(\frac{T_{ref,i} - T_i}{\mathrm{Max}(T_{ref}) - \mathrm{Min}(T_{ref})}\right)^2} \quad [\%] \tag{113}$$

where N is the total number of samples taken along each of the sampled lines, $T_{ref,i}$ is the surface temperature at sample location i of the reference mesh, T_i is the surface temperature at sample location i of the mesh currently being compared, $\mathrm{Max}(T_{ref})$ is the maximum surface temperature of the reference mesh, and $\mathrm{Min}(T_{ref})$ is the minimum surface temperature of the reference mesh. The sampled lines for this experiment are lines a, b, c, d, and e, the reference mesh refers to the mesh with the greatest number of nodes, and the surface temperature refers to the cladding surface temperature.

Table 14 lists the meshes that were generated, the total number of nodes, the difference in nodes compared to the previous mesh, and notes on which mesh was modified to generate the mesh. These meshes are listed in descending order of total number of nodes.

Table 14: Overall mesh properties for Rohde et al. grid independence study, listed in descending order of total nodes.

Mesh ID	Notes	Total Nodes	Difference in Nodes Relative to Previous Mesh	Percentage Decrease in Nodes Relative to Previous Mesh
BNSP-1	Finest Mesh	18,035,143	-	-
BNSP-4	BNSP-3 w/increased z nodes	4,495,768	13,539,375	75.07
BNSP-2	BNSP-1 w/reduced x,y,z nodes	4,389,824	105,944	2.36
BNSP-3	BNSP-2 w/reduced x,y nodes	3,753,688	636,136	14.49
BNSP-5	BNSP-3 w/reduced x,y,z nodes	2,362,572	1,391,116	37.06
BNSP-6	BNSP-5 w/reduced z nodes	2,077,434	285,138	12.07
BNSP-7	BNSP-6 w/reduced x,y nodes	1,510,110	567,324	27.31
BNSP-8	BNSP-7 w/reduced x,y nodes	1,016,226	493,884	32.71
BNSP-9	BNSP-8 w/reduced z nodes	480,438	535,788	52.72

The changes made to each mesh can be described using a cylindrical r-θ coordinate system. Figure 11 shows the equivalent r-θ coordinate system superimposed on a typical x-y cross section of the BNSP-6 mesh. The z-axis cross section has constant nodal spacing.

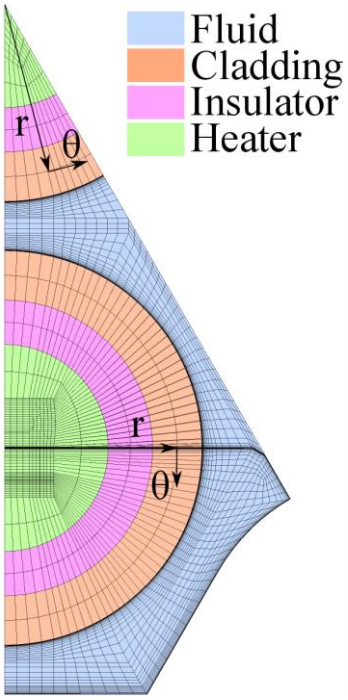

Figure 11: Equivalent r-θ coordinate system for describing mesh modification procedure shown on typical x-y cross section of Rohde et al. BNSP-6 mesh.

Table 15 lists the geometric parameters of each mesh. The meshes were created by taking the previously created mesh and reducing the number of nodes in the z, r, and/or θ direction, i.e. the BNSP-1 mesh was created first, and then the BNSP-2 mesh was created from the BNSP-1 mesh, and so on. The exception to this is the BNSP-4 mesh: the number of nodes in the z-direction was increased from the previously created mesh. The near wall grid spacing was only modified to maintain y^+ at approximately one.

Table 15: Geometric parameters of individual Rohde et al. meshes.

Mesh ID	Max z-Spacing [mm]	Max θ-Spacing [mm]	Max r-Spacing, Fluid [mm]	Near Wall Grid Spacing [mm] / Expansion Ratio Next to Cladding	Near Wall Grid Spacing [mm] / Expansion Ratio Next to Shroud	Solid Domain Nodes in r-Direction: Heater/Insulator/ Cladding
BNSP-1	2.340	0.105	0.074	0.0006/1.3	0.0006/1.3	4/4/7
BNSP-2	3.125	0.210	0.134	0.0006/1.3	0.0006/1.48	4/4/4
BNSP-3	3.125	0.270	0.134	0.0006/1.3	0.0006/1.48	3/3/3
BNSP-4	2.529	0.270	0.134	0.0006/1.3	0.0006/1.48	3/3/3
BNSP-5	3.571	0.270	0.222	0.00055/1.4	0.0007/1.65	3/3/3
BNSP-6	4.167	0.270	0.222	0.00055/1.4	0.0007/1.65	3/3/3
BNSP-7	4.167	0.333	0.206	0.00055/1.6	0.0007/2.0	3/3/3
BNSP-8	4.167	0.472	0.250	0.00055/2.0	0.0007/2.0	3/3/3
BNSP-9	8.774	0.472	0.250	0.00055/2.0	0.0007/2.0	3/3/3

The maximum and minimum y^+ values of the nodes closest to the cladding and shroud domains of each mesh is given in Table 16. As can be seen in the table, the maximum y^+ value was maintained at approximately one for all meshes.

Table 16: Maximum and minimum y^+ values of nodes closest to cladding and shroud domains.

Mesh ID	y^+ Max	y^+ Min
BNSP-1	1.03690	0.13440
BNSP-4	1.03553	0.13461
BNSP-2	1.03597	0.13459
BNSP-3	1.03559	0.13461
BNSP-5	0.95114	0.12385
BNSP-6	0.95107	0.12385
BNSP-7	0.95411	0.12197
BNSP-8	0.96233	0.12411
BNSP-9	0.96629	0.12412

The minimum angle, maximum expansion factor, and maximum aspect ratio between individual elements in the fluid domain are given in Table 17. The minimum angle never changed

significantly for each mesh, and the maximum expansion factor stayed between 6 and 17. The maximum aspect ratio had a large range, where values ranged between 11,476 and 46,866.

Table 17: Mesh quality parameters in the fluid domain of each mesh.

Mesh ID	Min Angle [degree]	Max Expansion Factor	Max Aspect Ratio
BNSP-1	19.9	6	11,476
BNSP-4	21.7	7	14,616
BNSP-2	21.5	6	15,221
BNSP-3	21.7	6	15,225
BNSP-5	21.9	9	18,982
BNSP-6	21.9	10	22,140
BNSP-7	20.0	10	22,990
BNSP-8	22.6	8	22,047
BNSP-9	22.5	17	46,866

Figure 12 shows the percent difference in total pressure drop between each mesh and the BNSP-1 mesh.

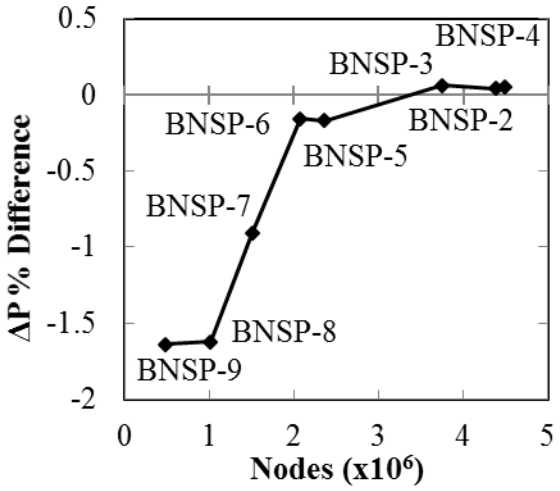

Figure 12: Total pressure drop percentage difference between each mesh and the BNSP-1 mesh vs total nodes.

The total pressure drop for all meshes greater than 2,000,000 nodes is effectively the same. Selecting any of the meshes with greater than 2,000,000 nodes will yield a result with a pressure drop that is accurate to within ±1 % of the BNSP-1 mesh.

A plot of the cladding surface temperature $RMS_{RN,T}$ along lines a, b, c, d, and e for each mesh is given in Figure 13.

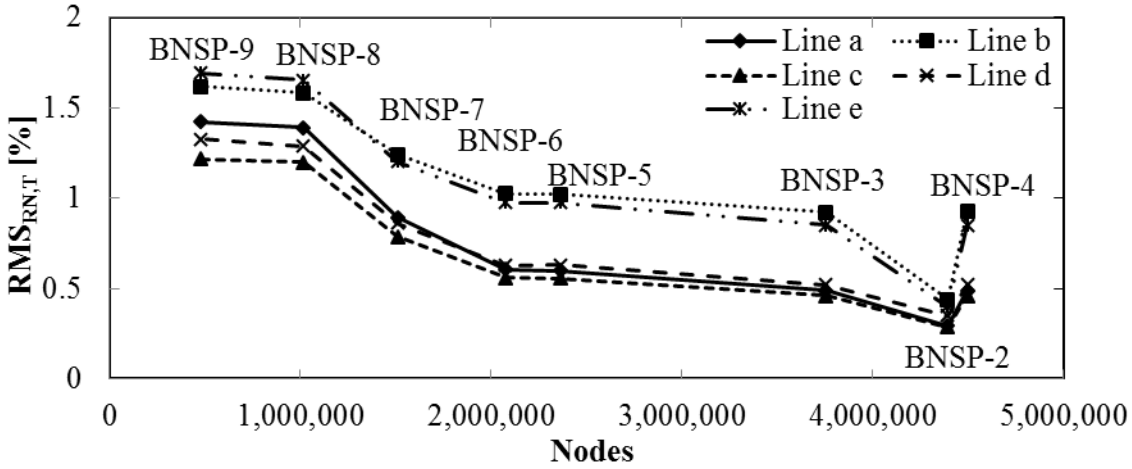

Figure 13: Cladding surface temperature $RMS_{RN,T}$ vs. total nodes.

From Figure 13, it can be seen that as the number of nodes increases, the cladding surface temperature $RMS_{RN,T}$ along each line decreases with the exception of the mesh with 4,389,824 nodes, BNSP-2. The $RMS_{RN,T}$ values are a minimum for this mesh, and then increase for the next largest mesh, BNSP-4. The BNSP-4 mesh has x-y grid spacings that are identical to the BNSP-3 mesh, but has more nodes in the z-direction. The BNSP-2 mesh has a finer x-y grid than the BNSP-3 (and BNSP-4) mesh, but has fewer nodes in the z-direction than the BNSP-4 mesh. This leads to the BNSP-2 mesh having fewer nodes than the BNSP-4 mesh, yet the finer x-y grid leads to results with a lower cladding surface temperature $RMS_{RN,T}$. Thus, the grid spacing in the

z-direction does not significantly affect cladding surface temperature results, but the x-y grid spacing does significantly affect cladding surface temperature results.

Mesh BNSP-6 was selected as the final mesh because it provided a reasonably low pressure drop percent difference and cladding surface temperature $RMS_{RN,T}$ while having the least possible number of nodes. The maximum and minimum y^+ values for this mesh are 0.951072 and 0.123853 respectively. The BNSP-6 mesh gives an overall pressure drop percent difference of -0.15 % and a cladding surface temperature $RMS_{RN,T}$ of 1 % or less. An x-y cross section of the mesh can be seen in Figure 11.

4.4. Results and Discussion

The numerical results of case B1 and B2 of the Rohde et al. tests are presented here. Case B1 and B2 were selected because they were the only cases involving heating of the fluid. Case B2 showed local spikes in cladding surface temperature close to the outlet, indicating HTD was present. The temperatures of case B1 where not close enough to the pseudocritical temperature for HTD to occur.

Multiple authors (including the present author), performed numerical simulations on the Rohde et al. experimental data in the context of the GIF SCWR 2013-2014 seven-rod subchannel benchmark exercise. The organizations of the contributing authors to this benchmark exercise are as follows: Delft University of Technology (TUD); University of Pisa (UPisa); Budapest University of Technology (BME NTI); Canadian Nuclear Laboratories (CNL); Czech Research Center Rez Ltd (CVREZ); Karlsruhe Institute of Technology (KIT-IKET); University of Manitoba (UMan); Royal Institute of Technology, Stockholm, Sweden (KTH); University of

Ottawa (UOttawa); and McMaster University (McMU). The CFD code used, turbulence model used, mesh size, and domain are given for each of the organizations that contributed to the benchmark exercise are given in Table 18.

Table 18: CFD code used, turbulence model used, mesh size, and domain for each of the organizations that contributed to the benchmark exercise.

Organization	CFD Code	Turbulence Model	Mesh Size	Domain Modelled
TUD	In-house 1D analytical solver	-	-	Entire, no spacers
UPisa	STAR-CCM+ v7.06	Abe-Kondoh-Nagano (AKN) Low-Re k-ε, SST	24M	1/12, incl. spacers
BME NTI	CFX v14.5	SST-based Scale-Adaptive Simulation (SAS-SST)	14M	1/3, incl. spacers
CNL[1]	ASSERT-PV Subchannel Code	-	-	1/6, incl. spacers
CVREZ	FLUENT v12	SST	5.6M	1/12, incl. spacers
KIT-IKET[2]	ANSYS CFX and ANSYS-Structure	k-ε w/Fluid-Structure Interaction, SST	0.5M (k-ε), 3.2M (SST)	1/6, no spacers
UMan	CFX v14.5	SST	63M	1/12, incl. spacers
KTH	CFX v15	SST	28M	Entire, incl. spacers
UOttawa	FLUENT v15	SST-SAS (B2), SST (B1)	62M	1/6, incl. spacers
McMU	STAR-CCM+ v9.02	SST	37M (B2), 54M (B1)	1/3, incl. spacers

[1]CNL only provided cladding surface temperatures for lines a, c, and d. [2]KIT-IKET only provided results for case B2.

Only the initial conditions and experimental setup were given to the authors, in order for a blind numerical study to be performed. The cladding surface temperatures of case B1 and B2 and the pressure drop of case A1 of the experiment where provided to the authors after they submitted their numerical predictions. This was done in order to compare how well their numerical

methods simulated the experiment. Each group of authors modelled either a 1/12 section, a 1/6 section, a 1/3 section, or the entire domain, and either included or did not include spacers in the domain. Numerical results of cladding surface temperatures are presented and discussed later in Sections 4.4.1 and 4.4.2 for cases B1 and B2, respectively.

After the experimental data were released, Chang and Tavoularis [73] of the University of Ottawa performed additional numerical simulations of case A1 and B2 using the Abe-Kondoh-Nagano (AKN) Low-Re k-ε, v^2-f, k-ε-v^2/k, and SST turbulence models using STAR-CCM+. The authors used a turbulent Prandtl number of 0.9 for all cases, and also performed two additional runs using the v^2-f turbulence model in which the turbulent Prandtl number was set to 0.85 and 0.8. They modelled a 1/3rd section of the domain and included the spacers. Their mesh had a 0.2 [m] unheated unlet and a 1.5 [m] heated section, and consisted of 57M elements. The authors did not perform a grid independence study for their mesh. The maximum y^+ values were less than one, except near the spacers where they were approximately 10. The authors only provided cladding surface temperatures for lines b and c.

The present author also performed additional simulations after the benchmark experimental data was released [90]. Case B2 was numerically simulated using the SST turbulence model, and implemented using CFX. A sensitivity study was performed for the coefficients of the SST turbulence model in order to provide predictions of the cladding surface temperature that were closer to experimental data. The mesh used in that study is that same mesh that is used in the present study.

For the present study, the maximum residuals and domain imbalances were monitored during the following runs, and a solution was considered to be converged when these variables reached

values given in Section 3.5.1 and Section 3.5.2 for CFX and FLUENT, respectively. An exception to this was case B1 using the Yang-Shih Low-Re k-ε turbulence model: the continuity residual was $3x10^{-3}$. The FLUENT Solver Modelling Guide recommends the residuals be less than $1x10^{-3}$ except for the energy residual which should be less than $1x10^{-5}$. The one case with the higher than desired continuity residual was still considered converged because the solution variables at the monitor points did not change significantly over a large number of iterations. The solution variables at the monitor points were not changing significantly over a large number of iterations, where the maximum change in temperature or pressure at a monitor location was less than 0.1 % over at least approximately 400 iterations, and the vast majority of monitor locations had much less than a 0.1 % change in temperature or pressure over the same number of iterations. Typically, the maximum change in temperature or pressure at a monitor location was less than 0.1 % over at least approximately 400 iterations, and the vast majority of monitor locations had much less than a 0.1 % change in temperature or pressure over the same number of iterations. It was also not possible to reduce the residual by changing under-relaxation factors or the pseudo time step, which are the only methods that can be used to affect convergence during FLUENT runs. The mesh could have been altered to possibly reduce the residuals, but a grid independence study would need to be performed on that mesh and all other cases would have to be performed again with the new mesh. For these reasons, the slightly larger continuity residual for the one case was considered acceptable.

All CFX and FLUENT runs were performed using either local servers at the University of Manitoba, or using the advanced research computing facilities of WestGrid (a partner of Compute Canada), both of which use the Linux operating system. The total wall clock time for case B1 CFX simulations was between 51 and 134 hours using between 4 and 10 cores in

parallel computing. For case B1 FLUENT simulations, the total wall clock time was between 154 and 303 hours using between 4 and 10 cores in parallel. The total wall clock time for case B2 CFX simulations was between 34 and 54 hours using between 4 and 10 cores in parallel computing. For case B2 FLUENT simulations, the total wall clock time was between 143 and 245 hours using between 4 and 10 cores in parallel.

Rohde et al. provided the thermocouple temperatures at various locations on the cladding surfaces. These locations correspond to lines a, b, c, d, and e, seen in Figure 10 in Section 4.2, when the domain is modelled as a $1/12^{th}$ section through the use of symmetry planes. There was only three points of temperature data along line a, two points of temperature data along line d, and one temperature data point along line e, so the temperatures along these lines was not included in the plots in the following sections. The experimental temperatures of the thermocouples corresponding to lines b and c are denoted as “Line b Experiment” and “Line c Experiment”, in the following plots.

4.4.1. Case B1

The numerical results of case B1 of the Rohde et al. experiments will be presented here, followed by a comparison with the other numerical results from the GIF SCWR benchmark exercise.

Figure 14 gives the cladding surface temperatures of case B1 using the SST turbulence model with both CFX and FLUENT.

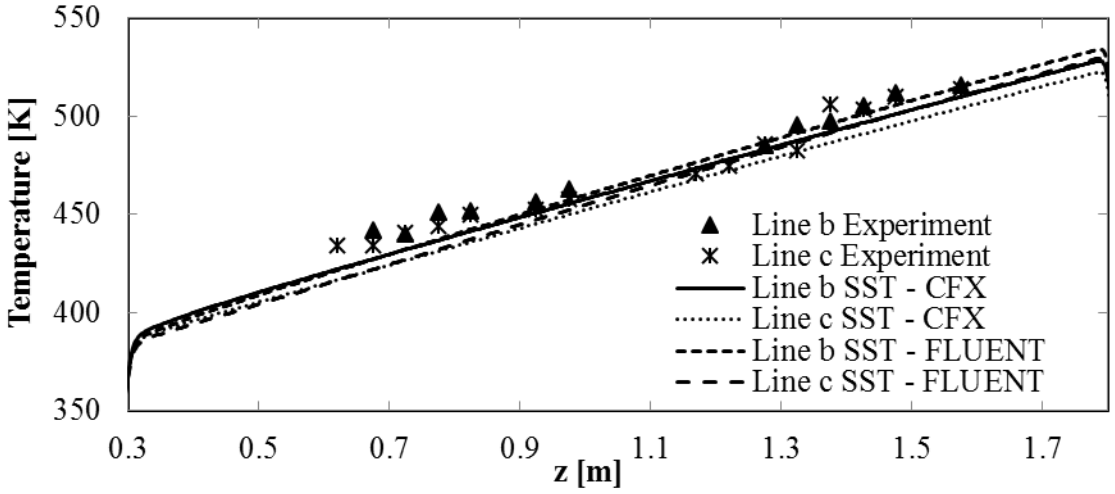

Figure 14: Cladding surface temperatures for case B1 using SST turbulence model with CFX and FLUENT. The pseudocritical temperature is 657.972 [K].

The cladding surface temperatures predicted by CFX and FLUENT using the same turbulence model are very similar. Both cases show temperatures along line c as being lower overall than line b temperatures.

Figure 15 gives the cladding surface temperatures of case B1 using the k-ε turbulence model, implemented using CFX, and the RNG k-ε turbulence model, implemented using FLUENT.

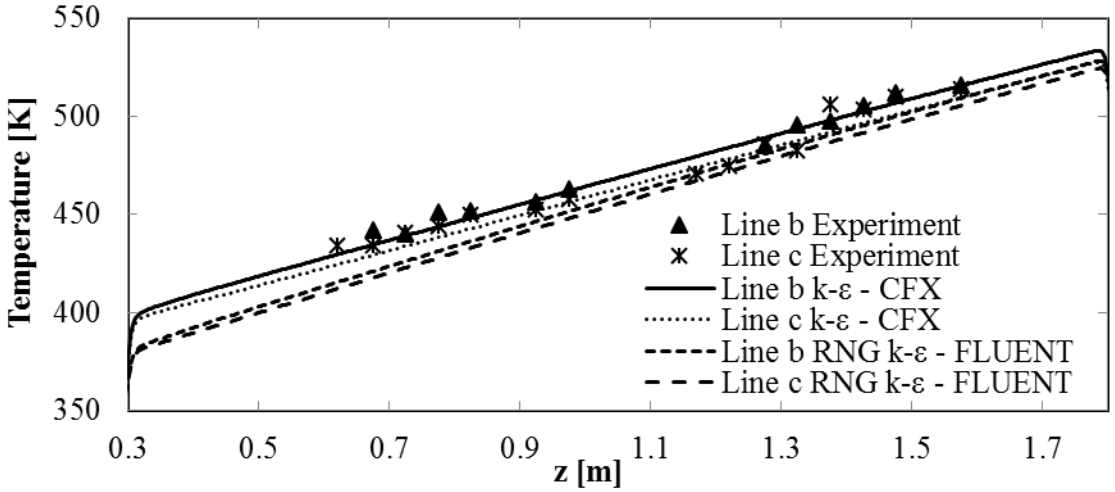

Figure 15: Cladding surface temperatures for case B1 using CFX with the k-ε turbulence model and FLUENT with the RNG k-ε turbulence model. The pseudocritical temperature is 657.972 [K].

The cladding surface temperatures predicted by the k-ε turbulence model are greater overall than those predicted by the RNG k-ε turbulence model. The RNG k-ε turbulence model under-predicts the experimental temperatures along both lines b and c.

Figure 16 gives the cladding surface temperatures of case B1 using the Low-Re k-ε turbulence models of Yang-Shih and Lam-Bremhorst, implemented using FLUENT.

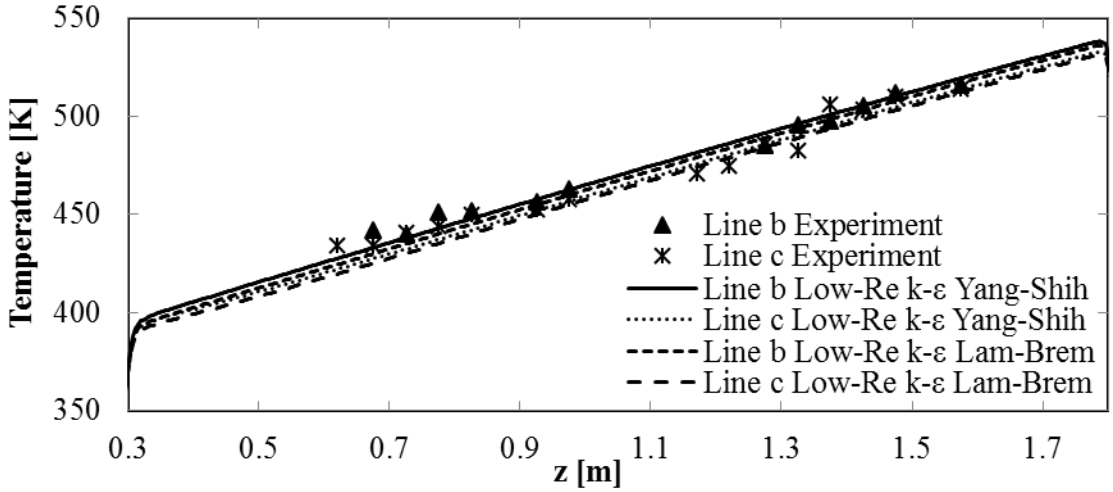

Figure 16: Cladding surface temperatures for case B1 using FLUENT and the Low-Re k-ε turbulence models of Yang-Shih and Lam-Bremhorst. The pseudocritical temperature is 657.972 [K].

Both Low-Re k-ε turbulence models predict similar cladding surface temperatures, and are relatively accurate in predicting these temperatures.

To quantify the differences between the numerical predictions and experimental results of cladding surface temperatures for case B1, the $RMS_{RN,T}$ is calculated and presented in Table 19. Equation (113) in Section 4.3 is used to calculate the $RMS_{RN,T}$, where the reference temperatures come from the experimental data. When calculating the $RMS_{RN,T}$, the experimental data from all thermocouples were used, not just the data corresponding to lines b and c.

Table 19: $RMS_{RN,T}$ between numerical results and experimental results for case B1.

Case	$RMS_{RN,T}$ [%]
B1 SST CFX	6.88
B1 k-ε CFX	4.20
B1 SST FLUENT	5.78
B1 RNG k-ε FLUENT	8.30
B1 Low-Re k-ε Lam-Bremhorst FLUENT	5.10
B1 Low-Re k-ε Yang-Shih FLUENT	4.52

The k-ε turbulence model, implemented using CFX, had the smallest overall deviation from the experimental cladding surface temperatures. The Yang-Shih Low-Re k-ε and Lam-Bremhorst Low-Re k-ε turbulence models, implemented using FLUENT, are the second and third closest at predicting the experimental temperatures. RNG k-ε had the greatest deviation in terms of predicting the experimental cladding surface temperatures. This inaccuracy can be attributed to the under-prediction of cladding surface temperatures near the inlet, as seen in Figure 15. All turbulence models predicted the experimental results fairly well: the $RMS_{RN,T}$ for all turbulence models was between 4.2 % and 8.3 %.

Various plots from case B1 using FLUENT and the Yang-Shih Low-Re k-ε turbulence model are given to illustrate trends in the flow when there is no HTD in either the experiment or numerical predictions. A y^+ value of zero corresponds to the location of line b in the following plots. Additionally, the y^+ value corresponding to the midpoint of the flow channel is different at each z location, and so it may appear as though the profiles end prematurely for certain z location profiles.

Figure 17 shows the near wall fluid temperature profiles at various z locations of case B1 using FLUENT and the Yang-Shih Low-Re k-ε turbulence model.

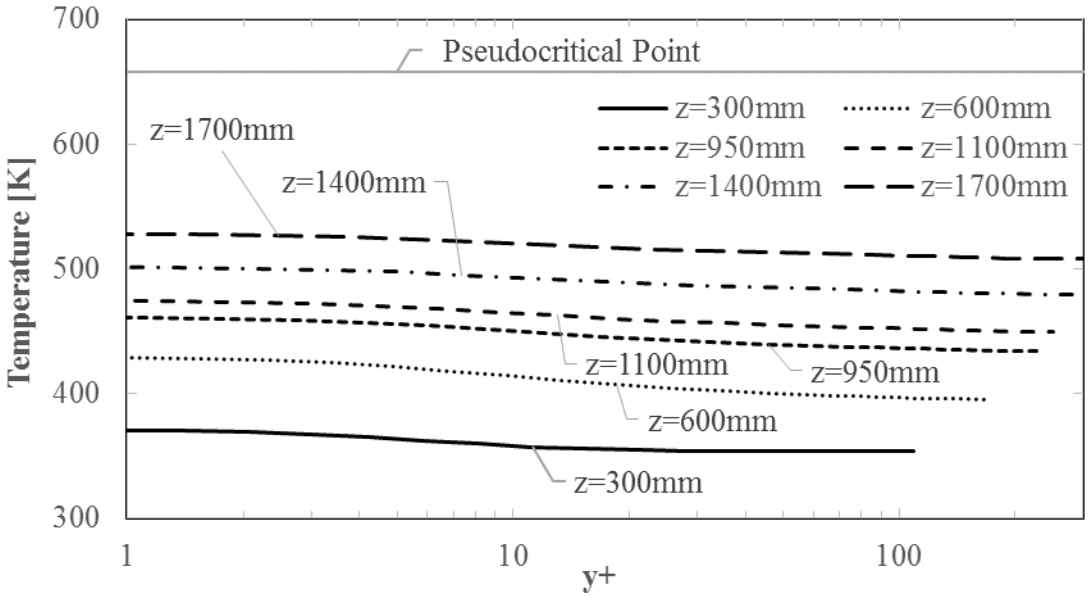

Figure 17: Fluid temperature vs. y+ at various z locations of case B1 using FLUENT and Yang-Shih Low-Re k-ε turbulence model. A y+ value of zero corresponds to the location of line b.

The fluid closest to the cladding surface gradually increase in temperature as the fluid progresses along z, but the temperature never reaches the pseudocritical temperature. The thermophysical properties of the fluid therefore do not change significantly at any location.

Figure 18 shows the near wall fluid density profiles at various z locations of case B1 using FLUENT and the Yang-Shih Low-Re k-ε turbulence model.

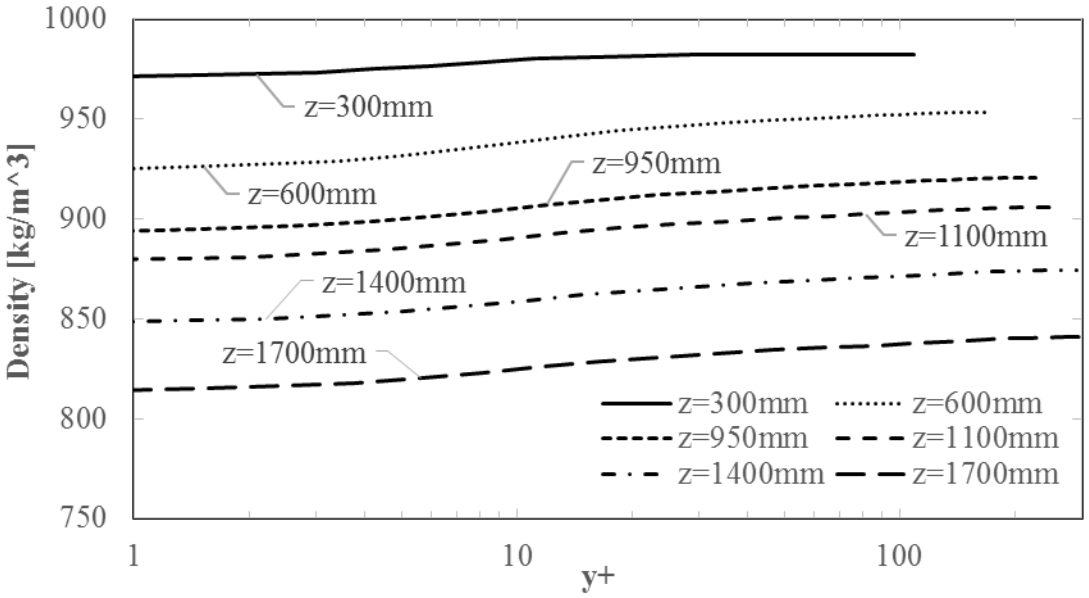

Figure 18: Density vs. y+ at various z locations of case B1 using FLUENT and Yang-Shih Low-Re k-ε turbulence model. A y+ value of zero corresponds to the location of line b.

The density of the fluid decreases as it is heated along z, but the gradients normal to the cladding surface are not large.

Figure 19 shows the near wall velocity *w* profiles at various z locations of case B1 using FLUENT and the Yang-Shih Low-Re k-ε turbulence model.

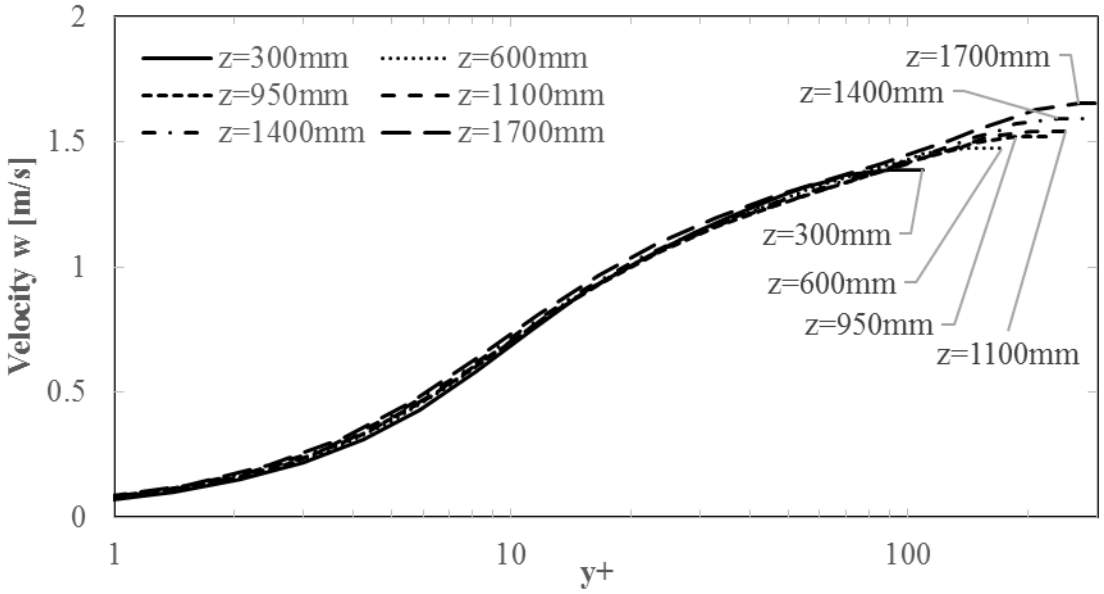

Figure 19: Velocity w vs. y+ at various z locations of case B1 using FLUENT and Yang-Shih Low-Re k-ε turbulence model. A y+ value of zero corresponds to the location of line b.

The velocity *w* profiles at all z locations follow similar trends, and there are no major differences between the velocity at the beginning of the heated section, z = 300 [mm], and near the end of the heated section, z = 1700 [mm].

Figure 20 shows the μ_t/μ ratio profiles at various z locations of case B1 using FLUENT and the Yang-Shih Low-Re k-ε turbulence model.

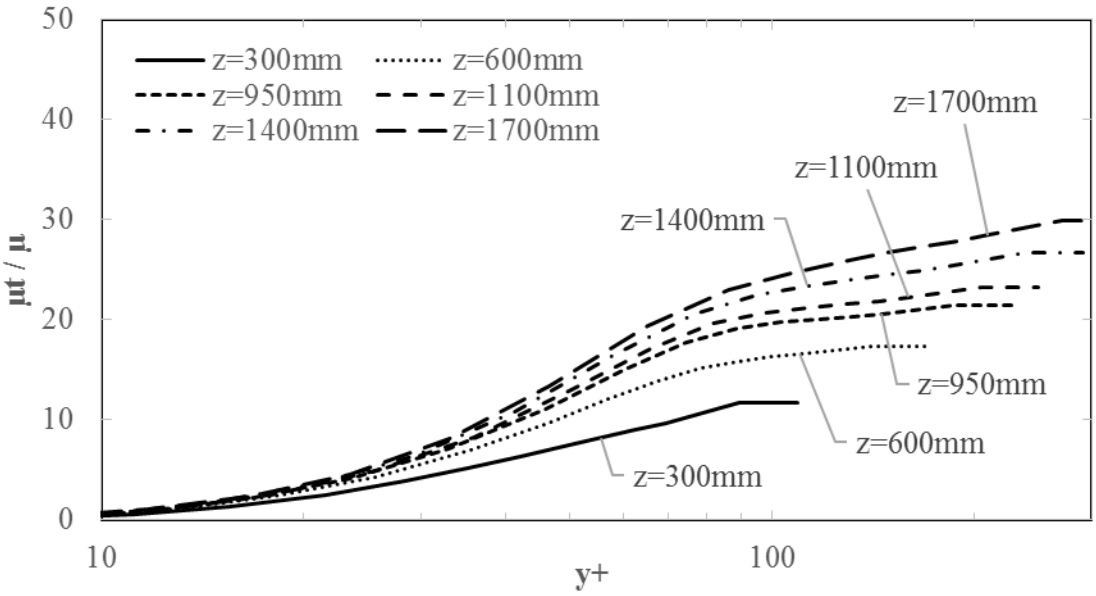

Figure 20: Ratio between eddy viscosity and dynamic viscosity vs. y+ at various z locations of case B1 using FLUENT and Yang-Shih Low-Re k-ε turbulence model. A y+ value of zero corresponds to the location of line b.

The μ_t/μ ratio is lowest at the beginning of the heated section, then gradually increases in value over all y^+ values as the fluid progresses along z. The profiles of μ_t/μ have very similar shape for all z locations, and only the values after y^+ = 10 increase as the fluid progresses along z.

The μ_t/μ profiles for y^+ less than 10 are similar in shape for all z locations, and the value of μ_t/μ in this region is always less than one. This is to be expected because this region is the viscous sublayer and, according to the log law of the wall, and the flow is effectively laminar. Therefore, the eddy viscosity will be very low in value. This is evident for the y^+ less than 10 region, where the value of μ_t/μ is never larger than one, and so the eddy viscosity is never larger than the dynamic viscosity.

Figure 21 shows the λ_t/λ ratio profiles at various z locations of case B1 using FLUENT and the Yang-Shih Low-Re k-ε turbulence model.

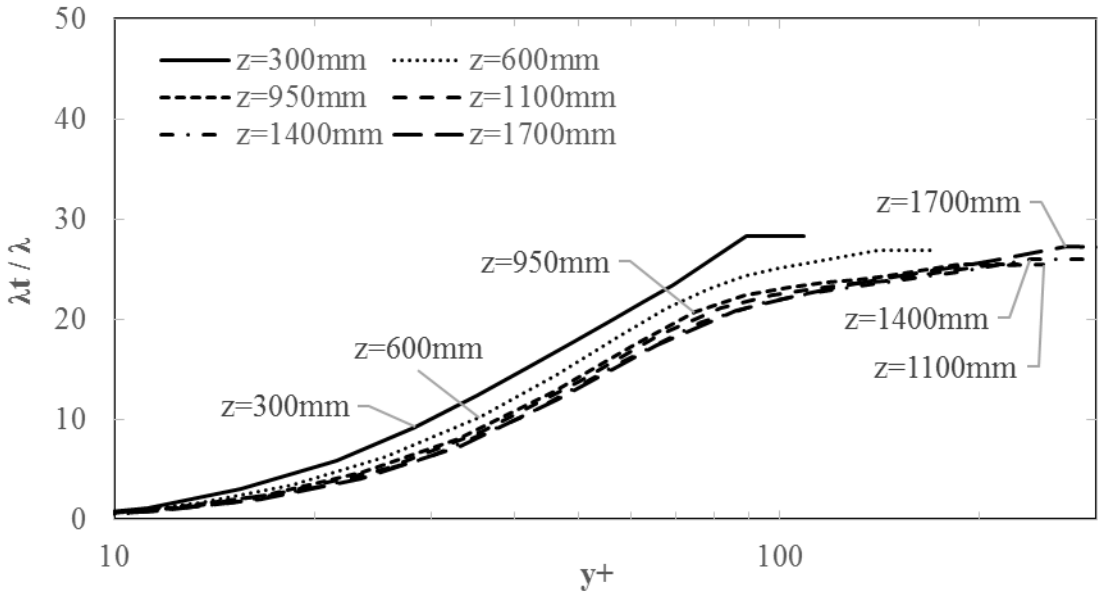

Figure 21: Ratio between turbulent thermal conductivity and thermal conductivity vs. y+ at various z locations of case B1 using FLUENT and Yang-Shih Low-Re k-ε turbulence model. A y+ value of zero corresponds to the location of line b.

The λ_t/λ profiles at all z locations follow a similar trend, and are low in value over all y^+ values. The λ_t/λ values are largest at the beginning of the heated section, z = 300 [mm], but do not decrease significantly as the fluid progresses along z. The Reynolds number at the inlet of this case is 11,189. The relatively low value of the Reynolds number is an indicator of low values of turbulence quantities; hence, the small values of turbulent thermal conductivity, and therefore the λ_t/λ values.

Table 20 summarizes the $RMS_{RN,T}$ for the case B1 numerical results of all authors and/or their respective organization. Whether or not the numerical results were created for the benchmark (experimental results unknown to authors), or after the benchmark (experimental results known to authors) is identified by the column on the left.

Table 20: $RMS_{RN,T}$ for case B1 numerical results of all authors and/or their respective organization.

	Authors / Organization	CFD Code	Turbulence Model	$RMS_{RN,T}$ [%]
Benchmark Exercise	TUD[1]	In-house 1D analytical solver	-	6.28
	UPisa	STAR-CCM+ v7.06	AKN Low-Re k-ε	5.76
			SST	6.45
	BME NTI	CFX v14.5	SAS-SST	6.31
	CNL[2]	ASSERT-PV subchannel code	-	4.82
	CVREZ	FLUENT v12	SST	6.85
	UMan	CFX v14.5	SST	6.80
	KTH	CFX v15	SST	8.50
	UOttawa	FLUENT v15	SST	8.32
	McMU	STAR-CCM+ v9.02	SST	5.49
Post Benchmark	Present Study (UMan)	CFX v14.5	SST	6.88
			k-ε	4.20
		FLUENT v14.5	SST	5.78
			RNG k-ε	8.30
			Yang-Shih Low-Re k-ε	4.52
			Lam-Bremhorst Low-Re k-ε	5.10

[1]Only numerical results from using the Mokry correlation are given in this table, because the other correlations were not as close to the experimental results. The correlations that were used but not presented here are the Dittus-Boelter, Dyadyakin, and Jackson correlations. [2]CNL only provided cladding surface temperatures for lines a, c, and d.

The present author included the spacers for the benchmark exercise, but not for the present study. The numerical results from using the same turbulence model and code, SST and CFX, are closer to the experimental results when the spacers are included than if they are not included. This can be seen in the $RMS_{RN,T}$ where the case from the benchmark exercise (spacers were included) has an $RMS_{RN,T}$ of 6.8 %, while the $RMS_{RN,T}$ from the present study (spacers were not included) with the same turbulence model and code has an $RMS_{RN,T}$ of 6.9 %. Although, the mesh that included spacers had significantly more nodes than the mesh used in the present study:

49,053,090 compared to 2,077,434, and so the mesh was finer in various location. The reason the mesh that included spacers predicted the experimental data closer than the mesh that did not include spacers may be that that the mesh was finer overall, and not necessarily that the spacers were modelled.

The present study provided numerical results that had the smallest overall deviation from experimental results of case B1 using the k-ε turbulence model, implemented using CFX. For results from the benchmark exercise, the closest predictions were provided by CNL using a subchannel code, ASSERT-PV. Although they were not able to provide a full set of data to compare with the experimental data, and so their $RMS_{RN,T}$ may not reflect the true accuracy of their numerical results. The results of CNL and those of the present study using the Yang-Shih Low-Re k-ε turbulence model are plotted in Figure 22.

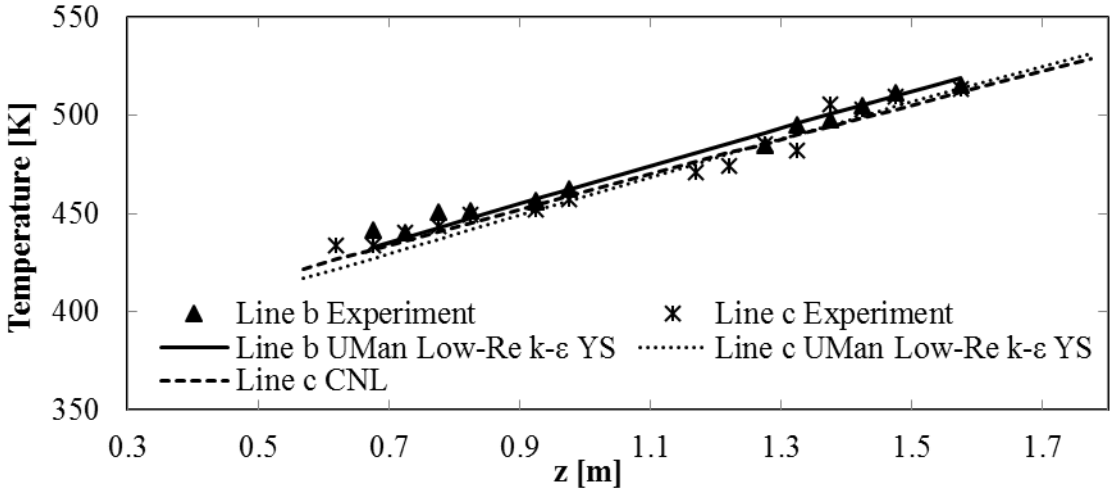

Figure 22: Cladding surface temperatures of CNL using ASSERT-PV and the present study using the Yang-Shih Low-Re k-ε turbulence model.

Both CNL with the ASSERT-PV subchannel code and the present study using the Yang-Shih Low-Re k-ε turbulence model generally under-predict the experimental cladding surface

temperatures. Although, there is not a large difference in temperatures between either of these results and the experimental result.

For results from the benchmark exercise, McMU and UPisa, using the SST and AKN Low-Re k-ε turbulence models respectively, provided numerical results that were in second and third best agreement with the experiment. All numerical results provided a relatively similar degree of accuracy, since the values of $RMS_{RN,T}$ of all the cases presented in Table 20 fell between 4.2 % and 8.5 %. The $RMS_{RN,T}$ of all the SST results fell between 5.5 % and 8.5 %, while the $RMS_{RN,T}$ of the Low-Re k-ε results fell between 4.5 % and 5.8 %. Therefore, all RANS turbulence models predicted the case B1 experimental results fairly well.

4.4.2. Case B2

The numerical results of case B2 of the Rohde et al. experiments will be presented here, followed by a comparison with the other numerical results from the GIF SCWR benchmark exercise.

Figure 23 gives the cladding surface temperatures of case B2 using the SST turbulence model with both CFX and FLUENT.

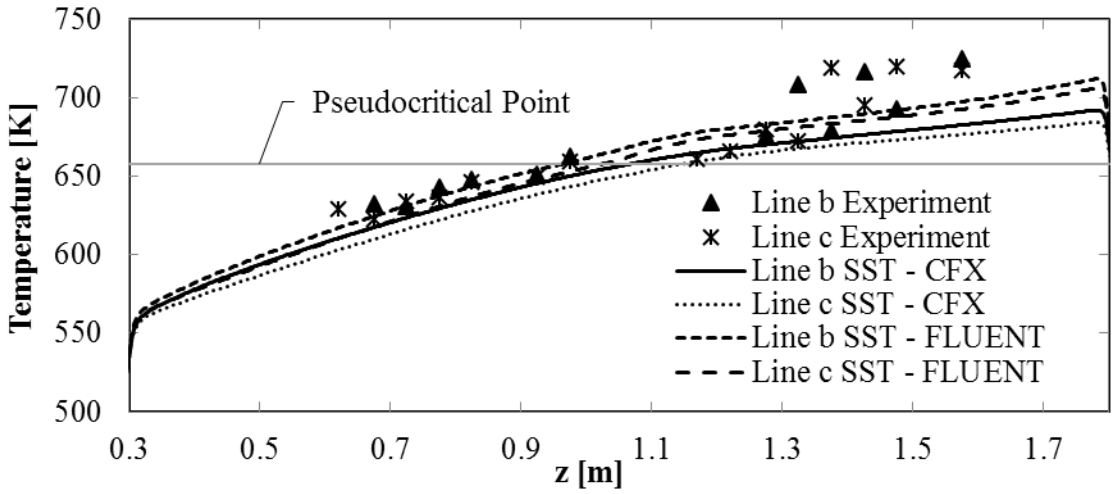

Figure 23: Cladding surface temperatures for case B2 using SST turbulence model with CFX and FLUENT.

FLUENT predicts greater temperatures overall along both lines b and c compared to CFX, even though the SST turbulence model is used for both of these cases. The main difference between these two cases is the wall treatment; automatic wall treatment is used in CFX, and EWT is used in FLUENT. These wall treatments are different in some ways, but use similar governing equations, as seen in Section 3.1.2.1 for automatic wall treatment and Section 3.1.2.2 for EWT. This could be the reason for the discrepancies between the two cases. Neither code model predicts the rise in cladding surface temperatures after the cladding reaches the pseudocritical temperature, and instead actually predict a slight dip in temperatures. Both cases show temperatures along line c as being lower overall than line b temperatures. At line b, the heated surfaces, Cladding 1 and Cladding 2, are relatively closer together than they are at line c. Therefore, the volume of fluid that is heated by these heated surfaces is less in the vicinity of line b than in the vicinity of line c, leading to more concentrated heating at line b which results in greater temperatures at line b than line c.

Figure 24 gives the cladding surface temperatures of case B2 using the k-ε turbulence model, implemented using CFX, and the RNG k-ε turbulence model, implemented using FLUENT.

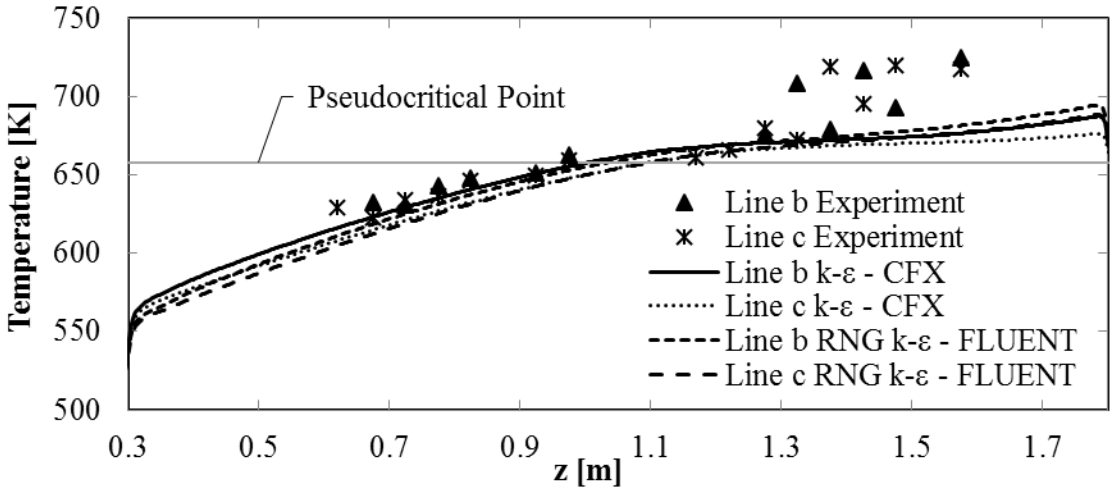

Figure 24: Cladding surface temperatures for case B2 using CFX with the k-ε turbulence model and FLUENT with the RNG k-ε turbulence model.

The results from the k-ε and RNG k-ε turbulence models are similar, and resemble those from the SST turbulence model, presented in Figure 23. Neither code model predicts the rise in cladding surface temperatures after the cladding reaches the pseudocritical temperature, and instead predict a slight dip in temperatures. Both cases show temperatures along line c as being slightly lower overall than line b temperatures of the same case.

Figure 25 gives the cladding surface temperatures of case B2 using the Low-Re k-ε turbulence models of Yang-Shih and Lam-Bremhorst, implemented using FLUENT.

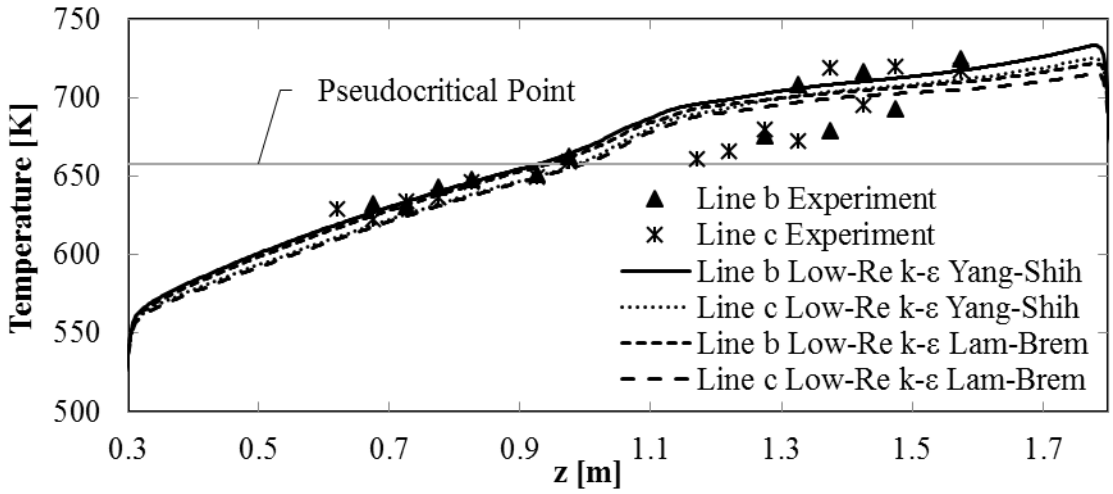

Figure 25: Cladding surface temperatures for case B2 using FLUENT and the Low-Re k-ε turbulence models of Yang-Shih and Lam-Bremhorst.

Both Low-Re k-ε turbulence models predict a rise in cladding surface temperatures after the pseudocritical temperature is reached. This more closely resembles the trend seen in the experimental data, except the experimental temperatures increase later along z than predicted by the Low-Re k-ε turbulence models. The Yang-Shih Low-Re k-ε turbulence model generally predicts greater cladding surface temperatures than the Lam-Bremhorst Low-Re k-ε turbulence model. Overall, the Low-Re k-ε turbulence models predict the HTD that appears in the experimental data. Although this HTD is not overly severe compared to other experiments studies in this thesis.

To quantify the differences between the numerical predictions and experimental results of cladding surface temperatures for case B2, the $RMS_{RN,T}$ is calculated and presented in Table 21. Equation (113) in Section 4.3 is used to calculate the $RMS_{RN,T}$, where the reference temperatures come from the experimental data. When calculating the $RMS_{RN,T}$, the experimental data from all thermocouples were used, not just the data corresponding to lines b and c.

Table 21: $RMS_{RN,T}$ between numerical results and experimental results for case B2.

Case	$RMS_{RN,T}$ [%]
B2 SST CFX	11.13
B2 k-ε CFX	11.28
B2 SST FLUENT	7.45
B2 RNG k-ε FLUENT	11.13
B2 Low-Re k-ε Lam-Bremhorst FLUENT	6.86
B2 Low-Re k-ε Yang-Shih FLUENT	7.08

The Lam-Bremhorst Low-Re k-ε turbulence model has the least deviation from the experimental cladding surface temperatures of case B2. The Yang-Shih Low-Re k-ε and SST turbulence models, implemented using FLUENT, have the second and third closest predictions of the cladding surface temperatures. The results of the SST turbulence model using FLUENT have similar accuracy to the Low-Re k-ε results, approximately 7 %, even though the results show a dip in cladding surface temperatures when the Low-Re k-ε turbulence models predict a rise in temperatures. This could be due to the Low-Re k-ε turbulence models predicting the rise in cladding surface temperatures immediately after the pseudocritical temperature is reached, whereas the experimental temperatures show a rise in cladding surface temperatures further along z. The remaining three cases are all relatively similar in their accuracy in predicting the experimental results, since the $RMS_{RN,T}$ of these cases are approximately 11 %.

Case B2 using FLUENT and the Yang-Shih Low-Re k-ε turbulence model will be used to explain what causes the HTD seen in Figure 25. Various solution variables and derived quantities are plotted with respect to y^+ in the following figures at different z locations. The y^+ values for the plots were calculated using Equation (34) in Section 3.1.2.1, where Δn is replaced with the wall distance. A y^+ value of zero corresponds to the location of line b, shown in Figure

10 in Section 4.2, and y^+ increases in value in the positive y direction, normal to the Cladding 2 surface. Figure 26 shows the heater rod surface temperatures along lines a, b, c, d and e for case B2, plotted against z. The location of these lines on the x-y plane can be seen in Figure 10 in Section 4.2.

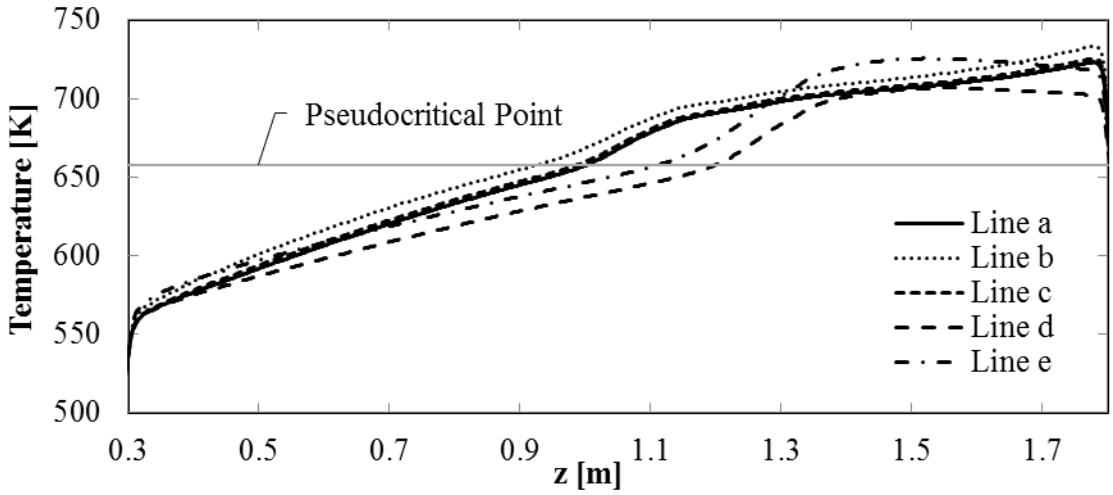

Figure 26: Cladding surface temperatures along lines a, b, c, d, and e for case B2 using FLUENT and the Yang-Shih Low-Re k-ε turbulence model.

The cladding surface temperature along lines a, b, and c follow the same trend, and reach the pseudocritical temperature of the fluid earlier than lines d and e, around z = 950 [mm], after which the temperatures increase at a greater rate. Lines d and e follow their own trend, and also experience a greater increase in cladding surface temperatures than lines a, b, and c. The cladding surface temperatures of lines d and e increase at a greater rate after z = 1100 [mm]. Lines a, b, and c are in close proximity to one another, between Heater 1 and Heater 2, and so it follows that that they should experience similar trends in temperature. The cladding surface temperature trends for lines d and e are different because they are located further away from lines a, b, and c.

For the following plots of solution variables and derived quantities, the y^+ value corresponding to the midpoint of the flow channel is different at each z location, and so it may appear as though the profiles end prematurely for certain z location profiles. In the following plots unless otherwise stated, a y^+ value of zero corresponds to the location of line b.

Figure 27 shows the near wall fluid temperature profiles at various z locations of case B2 using FLUENT and the Yang-Shih Low-Re k-ε turbulence model.

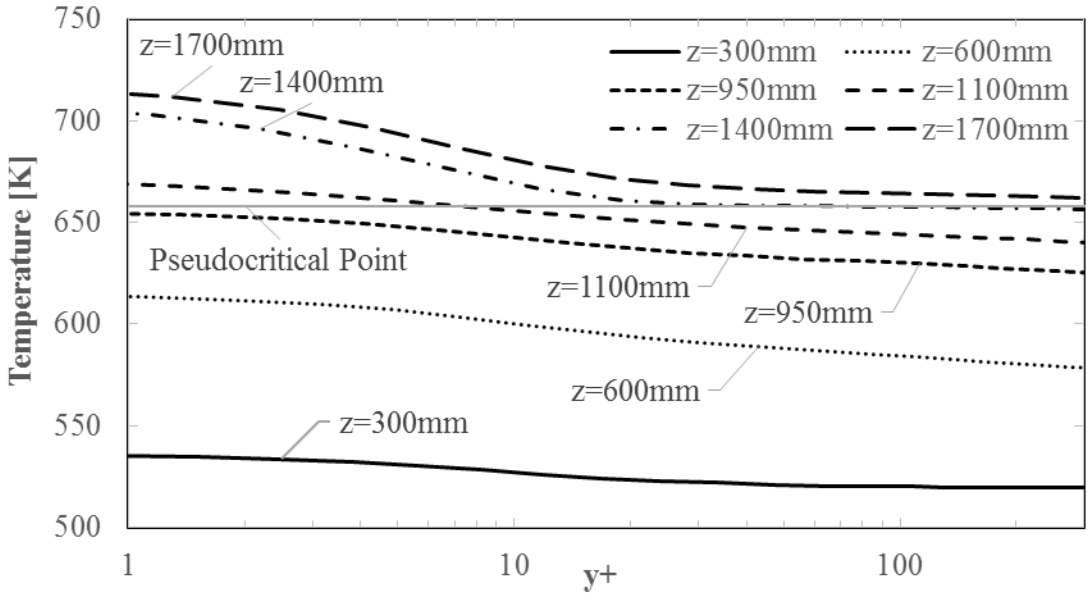

Figure 27: Fluid temperature vs. y+ at various z locations of case B2 using FLUENT and the Yang-Shih Low-Re k-ε turbulence model. A y+ value of zero corresponds to the location of line b.

The fluid reaches the start of the heated section at z = 300 [mm] and the fluid closest to the cladding surface is slightly greater in temperature than at the freestream. This is a result of axial heat conduction into the unheated portions of the heater rods, causing the ends of the unheated sections that are in contact with the heated sections of the heater rods to increase in temperature.

This causes the fluid closest to the wall to increase in temperature before the start of the heated section.

The fluid closest to the cladding surface does not reach the pseudocritical point until just after z = 950 [mm], but by z = 1700 [mm] the temperature along the entire profile has exceeded the pseudocritical temperature.

Figure 28 shows the near wall fluid density profiles at various z locations of case B2 using FLUENT and the Yang-Shih Low-Re k-ε turbulence model.

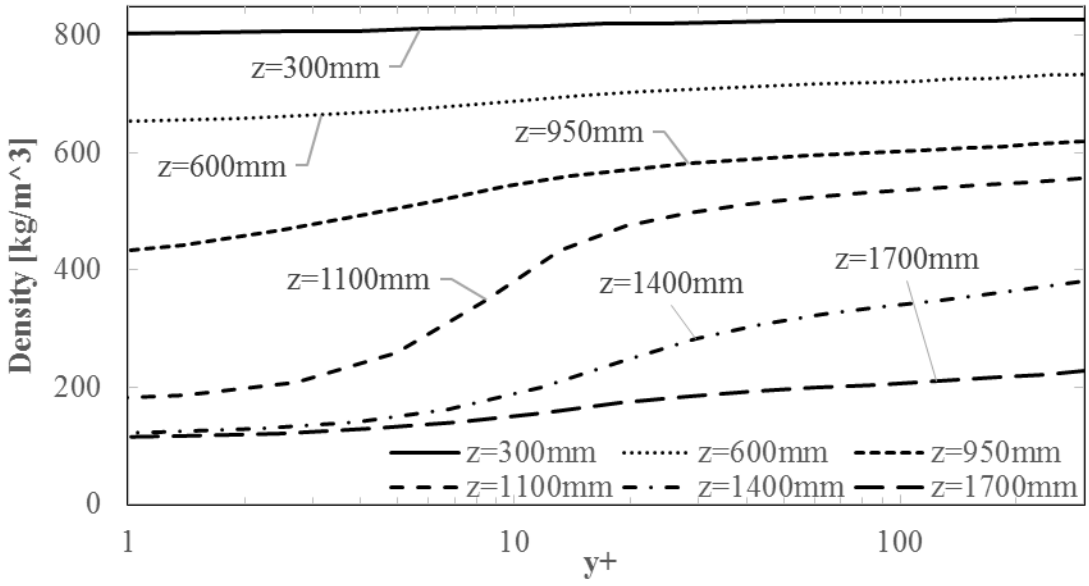

Figure 28: Density vs. y+ at various z locations of case B2 using FLUENT and the Yang-Shih Low-Re k-ε turbulence model. A y+ value of zero corresponds to the location of line b.

Looking at the density profile at z = 1100 [mm], the density of the fluid closest to the cladding surface is significantly less relative to the freestream, because the temperature of the fluid exceeds the pseudocritical temperature in the region closest to the cladding surface at this z location. This large density gradient gradually diminishes in size as the fluid in the freestream

region increases in temperature. The relatively flat density profile shape at z = 1700 [mm] (100 [mm] from the end of the heated section) is very similar to the profile shape at z = 600 [mm].

Figure 29 shows the near wall velocity w profiles at various z locations of case B2 using FLUENT and the Yang-Shih Low-Re k-ε turbulence model.

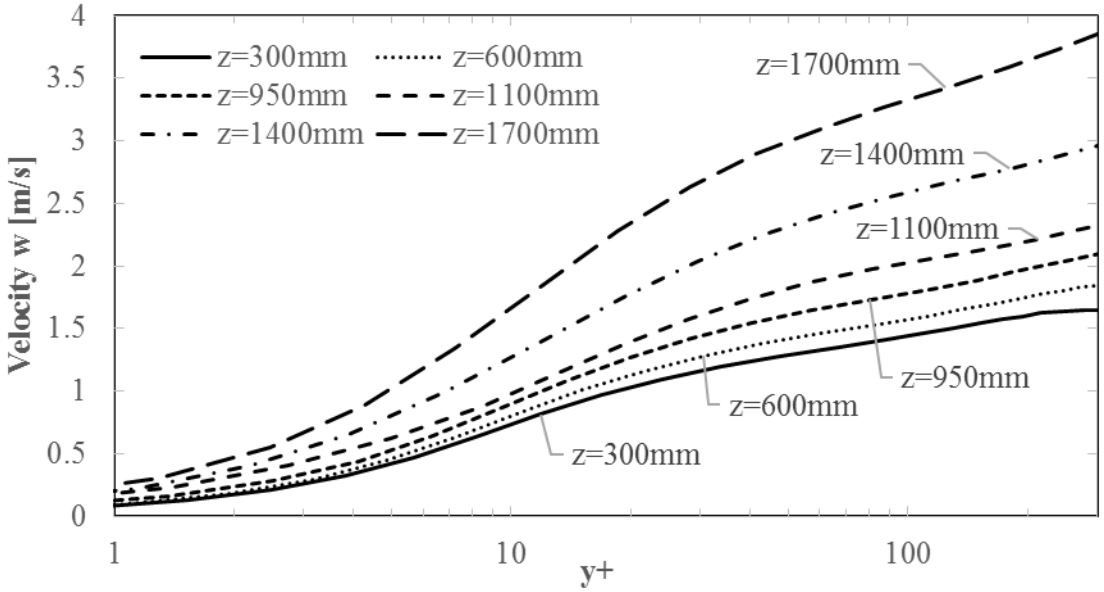

Figure 29: Velocity w vs. y+ at various z locations of case B2 using FLUENT and the Yang-Shih Low-Re k-ε turbulence model. A y+ value of zero corresponds to the location of line b.

The velocity profiles at all z locations appear to follow the same trend, and follow the log law of the wall, where there is a viscous sublayer adjacent to the wall, and a log law region away from the wall that is separated from the viscous sublayer by a buffer layer. The only difference being that the velocities gradually increase in magnitude along the entire y^+ profile. This can be attributed to the gradual decrease in density as the fluid progresses along z, as seen in Figure 28, which is caused by the gradual heating of the fluid.

Similar trends in the velocity *w* profiles can be found at other locations in the fluid domain. The velocity *w* profiles at z = 1100 [mm] for locations a, b, c, d, and e are plotted with respect to y^+ in Figure 30. The location of a, b, c, d, and e on the x-y plane can be seen in Figure 10 in Section 4.2.

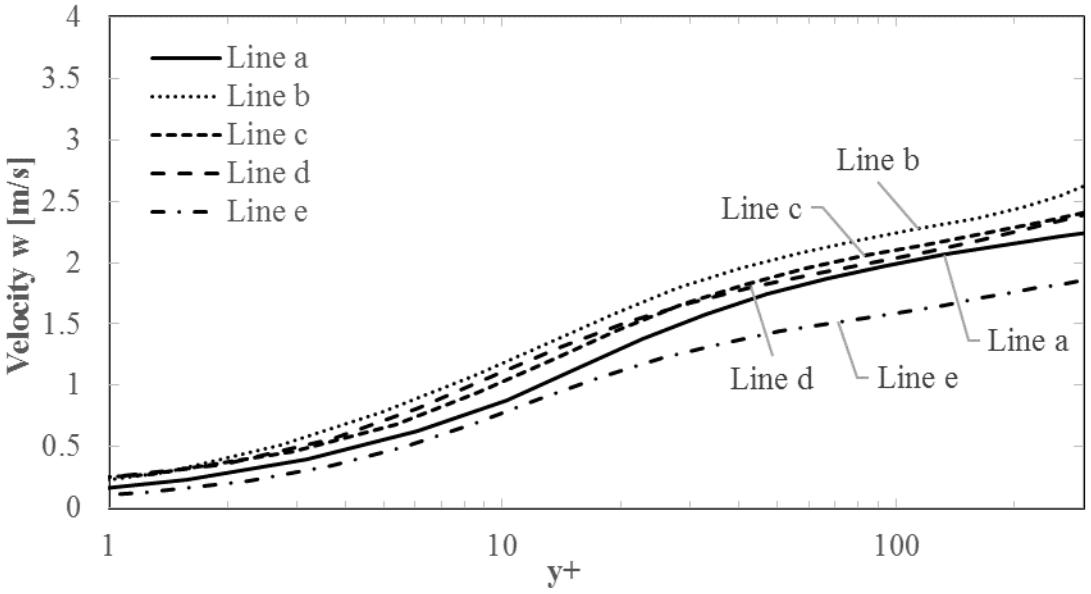

Figure 30: Velocity w profiles at z = 1100 [mm] for case B2 using FLUENT and the Yang-Shih Low-Re k-ε turbulence model at locations a, b, c, d, and e.

Similar trends in the velocity profile can be seen between each location, with line b having the largest magnitude in velocity, away from the wall. The smallest velocity occurs for location e. The differences in velocities at each of the locations a, b, c, d, and e are not nearly as large as between different z locations for location b, shown in Figure 29. The small differences in velocity in Figure 30 are likely due to the differences in density which are caused by the differences in temperature, since the fluid is either close to or beyond the pseudocritical point depending on the location on the cladding surface.

The velocity *w* profiles at z = 1100 [mm] for all case B2 results are given in Figure 31.

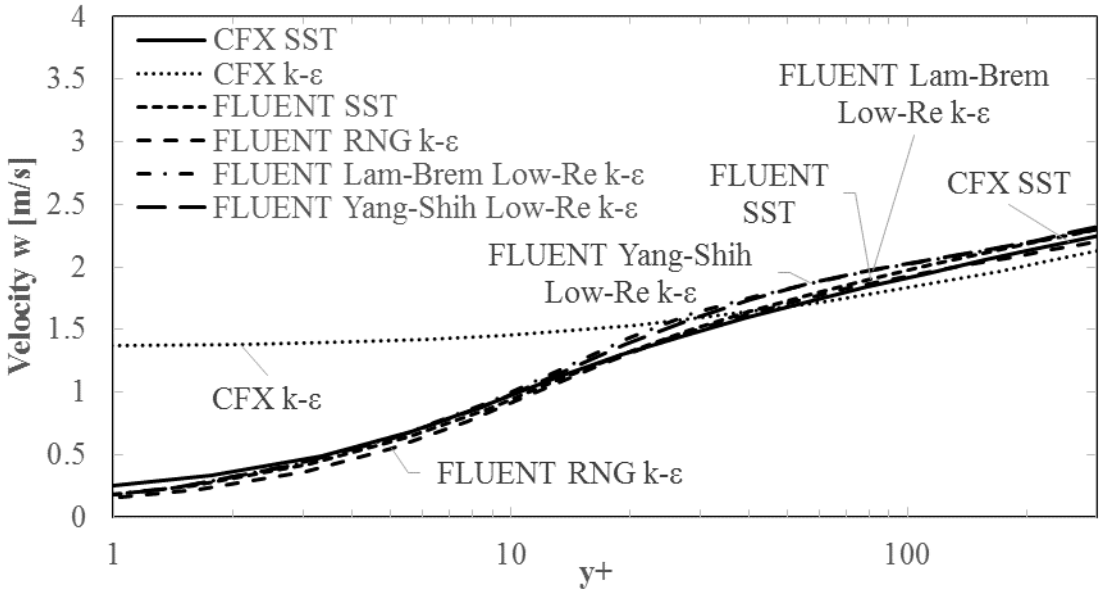

Figure 31: Velocity w vs. y+ at z = 1100 [mm] for all case B2 results. A y+ value of zero corresponds to the location of line b.

The Yang-Shih Low-Re k-ε and Lam-Bremhorst Low-Re k-ε cases show the same trend in velocity profile, where a slightly greater velocity exists between y^+ = 15 and y^+ = 100. This rise in velocity in this y^+ region leads to a slightly larger velocity gradient in around y^+ = 20, and a slightly flatter velocity profile after y^+ = 50, when compared with the cases that use other turbulence models. The z location of this rise in velocity, increased velocity gradient, and flattened velocity profile corresponds to the same location, z = 1100 [mm], where a rise in cladding surface temperature exists, seen in Figure 25. It is absent in cases that do not have a rise in cladding surface temperature: k-ε, RNG k-ε, and both SST results.

The velocity w of the k-ε case does not decrease in value close to the wall, such as for the other cases. The reason for this is that the k-ε turbulence model, when implemented with CFX, relies on scalable wall functions to determine the velocity in this near wall region. The turbulence model uses Equation (66) in Section 3.1.3.1 to determine the non-dimensional velocity in the

near wall region as a function of the non-dimensional wall distance, y^*_{Scale}. However the value of the non-dimensional wall distance can never be less than 11.06 according to Equation (63) in Section 3.1.3.1. This means the velocity can never be less than the value of the velocity at y^*_{Scale} = 11.06. This non-dimensional wall distance, y^*_{Scale}, is closely related to non-dimensional wall distance used in the plots, y^+, since they are both functions of wall distance and fluid properties.

Similarly, the non-dimensional temperature in the near wall region is a function of the non-dimensional wall distance, as seen in Equation (66) in Section 3.1.3.1, and so the fluid temperature can never be less than the temperature at y^*_{Scale} = 11.06. The greatest fluid temperature gradients occur close to the wall, as can be seen in the plot of fluid temperature at various z locations using the Yang-Shih Low-Re k-ε turbulence model, Figure 27. Because scalable wall functions, used by the k-ε turbulence model, do not allow the fluid temperature to vary in this region close to the wall, the wall temperature cannot experience sudden increases in temperature that would be evident by large temperature gradients in the fluid in the region close to the wall.

He et al. [65] performed an in-depth numerical analysis on vertically oriented heated tubes with supercritical CO_2, and found that HTD, or spikes in surface temperature, were caused by flow laminarization. He et al. performed numerical simulations using RANS turbulence models and compared their results with the DNS data of Bae et al. [64].

Buoyancy had the strong effect of producing high velocity gradients very close to the wall, and causing the velocity profile to flatten further away from the wall. The high velocity gradients where caused by a region of low density fluid very close to the wall accelerating upwards faster than the higher density fluid in the region further away from the wall. The flattened velocity

profile in the region away from the wall leads to a reduction in shear stress. Shear stress plays a dominant role in the Reynolds stresses, $\rho\overline{u_i u_j}$, and turbulence production, P_k, as can be seen in the equation for Reynolds stresses, Equation (3) in Section 3.1.1, and turbulence production due to viscous forces, Equation (26) in Section 3.1.2. Therefore a reduction in shear stress leads to a reduction in turbulence. He et al. refers to this reduction in turbulence as flow laminarization.

Velocity w profiles in the near wall region of the case B2 results do not show large gradients very close to the wall in general, nor do they show a significant flattening in the region away from the wall. However, the Low-Re k-ε cases do show slightly larger velocity gradients in the near wall region, and a slight flattening of the velocity profile in the region away from the wall, when compared with the cases that use the k-ε, RNG k-ε, and SST turbulence models, as seen in Figure 31. This could be the reason why the HTD seen in the Low-Re k-ε results are not overly severe.

According to He et al., the slight flattening of the velocity profile should lead to a reduction in the shear stress, resulting in a reduction in turbulence. This reduction in turbulence can be seen by observing the eddy viscosity in the near wall region, since eddy viscosity is a variable that is directly related to the strength of the turbulence.

Profiles for the ratio between eddy viscosity and dynamic viscosity, μ_t/μ, at various z locations of case B2 using FLUENT and the Yang-Shih Low-Re k-ε turbulence model are shown in Figure 32.

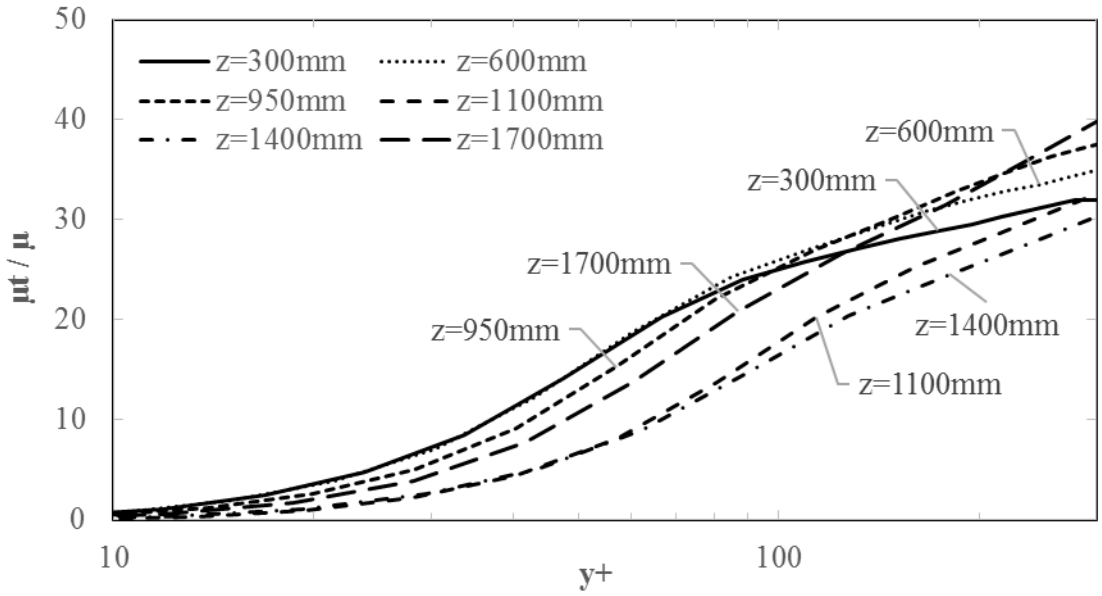

Figure 32: Eddy viscosity to dynamic viscosity ratio vs. y+ at various z locations of case B2 using FLUENT and the Yang-Shih Low-Re k-ε turbulence model. A y+ value of zero corresponds to the location of line b.

This ratio can be used to determine the strength of turbulence at any location. For a laminar flow, μ_t/μ should be less than one, and for flows with strong turbulence, μ_t/μ should be much greater than one. When the flow reaches the start of the heated section, at z = 300 [mm], the value of μ_t/μ is approximately one at y^+ = 12. The values of μ_t/μ increase away from the wall towards the freestream. One way to look at this is that the flow is close to laminar at y^+ = 12, and becomes more turbulent towards the freestream. The values of μ_t/μ increase slightly near the freestream at z = 600 [mm], then again at z = 950 [mm]. However the values of μ_t/μ in the region close to the wall at z = 950 [mm] are less than for the previous z locations. By z = 1100 [mm] the values of μ_t/μ are at their lowest in the region close to the wall. At z = 1100 [mm], the value of μ_t/μ is approximately one at y^+ = 19, which is not a large change from z = 300 [mm]. The low μ_t/μ values that exist slightly further away from the wall at this location is evidence that the turbulence is lower here than at z = 300 [mm] and is the reason why HTD exists at this

location, although only to a small degree. The μ_t/μ values increase over all y^+ values by z = 1700 [mm].

The μ_t/μ profiles for y^+ less than 10 are similar in shape for all z locations, and the value of μ_t/μ in this region is always less than one. This is to be expected because this region is the viscous sublayer and, according to the log law of the wall, and the flow is effectively laminar. Therefore, the eddy viscosity will be very low in value. This is evident for the y^+ less than 10 region, where the value of μ_t/μ is never larger than one, and so the eddy viscosity is never larger than the dynamic viscosity.

Figure 33 shows profiles of the turbulent thermal conductivity to thermal conductivity ratio, λ_t/λ, at various z locations of case B2 using FLUENT and the Yang-Shih Low-Re k-ε turbulence model.

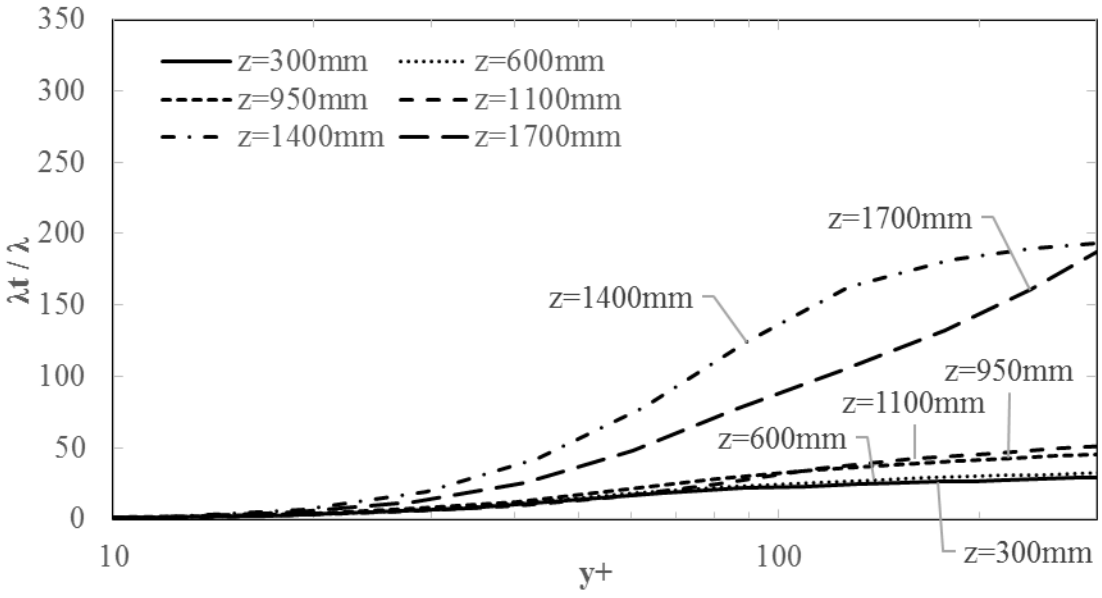

Figure 33: Turbulent thermal conductivity to thermal conductivity ratio vs. y+ at various z locations of case B2 using FLUENT and the Yang-Shih Low-Re k-ε turbulence model. A y+ value of zero corresponds to the location of line b.

The turbulent thermal conductivity, λ_t, is defined by Equation (14) in Section 3.1.1, and can be used as an indicator of the contribution to heat transfer by turbulence effects. For a laminar flow, λ_t/λ should be less than approximately one, and for flows with strong turbulence, λ_t/λ should be much greater than one. Looking at the governing equations for energy used by CFX and FLUENT, Equation (10) and (11) in Section 3.1.1, respectively, it can be seen that a fluid should conduct heat much better when the λ_t/λ ratio is much greater than one. This is because the turbulent thermal conductivity acts in the same way as the thermal conductivity in conducting heat. When the λ_t/λ ratio is less than approximately one, the flow is close to laminar and heat conduction through the fluid should be less than if the λ_t/λ ratio was greater.

The λ_t/λ profiles at the various z locations, as shown in Figure 33, do not necessarily follow the same trend as the μ_t/μ profiles at the same z locations, as shown in Figure 32. The λ_t/λ values at z = 300 [mm] are relatively low, compared to other z locations, and remain low at z = 600 [mm]. There is a slight increase in λ_t/λ values close to the freestream at z = 950 [mm], and again at z = 1100 [mm]. The biggest change in λ_t/λ can be seen at z = 1400 [mm], where the values increase over the entire near wall region. The λ_t/λ values then decrease again at z = 1700 [mm]. The increase in λ_t/λ values at z = 1400 [mm] leads to an increase in the ability of the fluid to allow heat to flow through the fluid, leading to a decrease of the axial temperature gradient at the cladding surface when compared to the axial temperature gradient at z = 1100 [mm], as seen in Figure 25.

The λ_t/λ profiles at z = 1100 [mm] at locations a, b, c, d, and e are plotted with respect to y^+ in Figure 34.

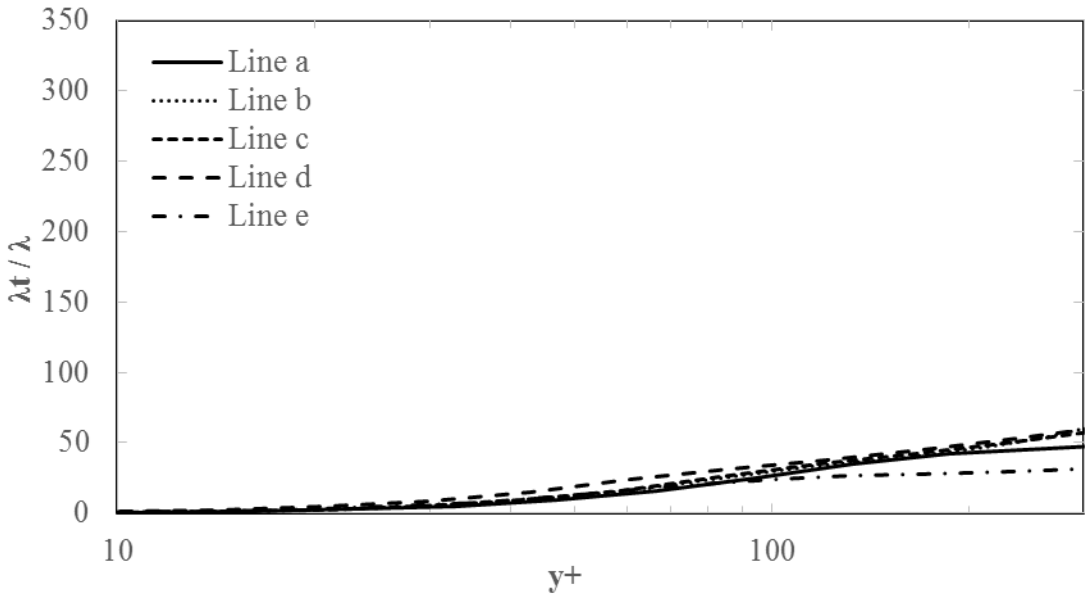

Figure 34: Turbulent thermal conductivity to thermal conductivity ratio profiles at z = 1100 [mm] for case B2 using FLUENT and the Yang-Shih Low-Re k-ε turbulence model at locations a, b, c, d, and e.

As can be seen in the figure, the λ_t/λ values are small and relatively similar for all locations a, b, c, d, and e in the near wall region at z = 1100 [mm]. This suggests that nothing significant, in terms of turbulent heat transfer, is occurring at a certain location at z = 1100 [mm], and instead there is a trend at all locations a, b, c, d, and e. This trend is that the turbulent heat transfer is inhibited, a result of the low turbulence caused by a reduced shear stress that results from a slight flattening of the velocity *w* profile.

The λ_t/λ profiles at various z locations of case B2 using FLUENT and the Lam-Bremhorst Low-Re k-ε turbulence model are given by Figure 35. This is the only other turbulence model that predicted HTD for the B2 case.

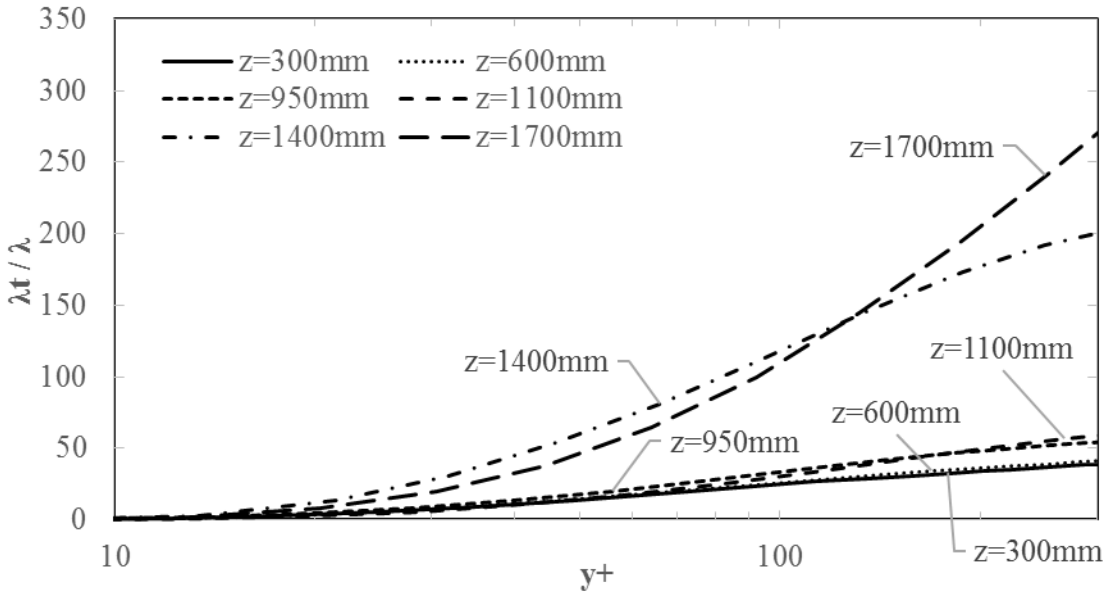

Figure 35: Turbulent thermal conductivity to thermal conductivity ratio vs. y+ at various z locations of case B2 using FLUENT and the Lam-Bremhorst Low-Re k-ε turbulence model. A y+ value of zero corresponds to the location of line b.

The λ_t/λ profiles of the Lam-Bremhorst Low-Re k-ε case are nearly identical to those of the Yang-Shih Low-Re k-ε case. Because of this, there is also a nearly identical trend in the cladding surface temperature, where the temperature rises at the same z location, as seen in Figure 25.

The k-ε, RNG k-ε, and both SST results do not show HTD for case B2, as can be seen in Figure 23 and Figure 24. The profiles of the λ_t/λ ratio at various z locations for the SST result using FLUENT and the k-ε result using CFX are shown by Figure 36 and Figure 37, respectively. The trends in λ_t/λ found in the SST results using FLUENT are similar to those found in the SST results using CFX and the RNG k-ε result using FLUENT.

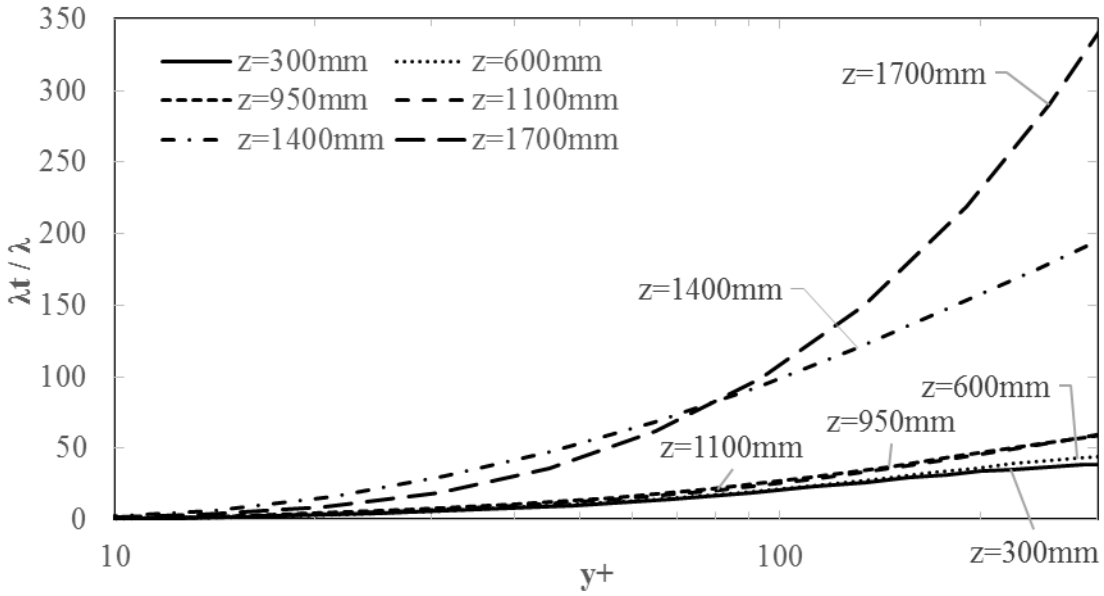

Figure 36: Turbulent thermal conductivity to thermal conductivity ratio vs. y+ at various z locations of case B2 using FLUENT and the SST turbulence model. A y+ value of zero corresponds to the location of line b.

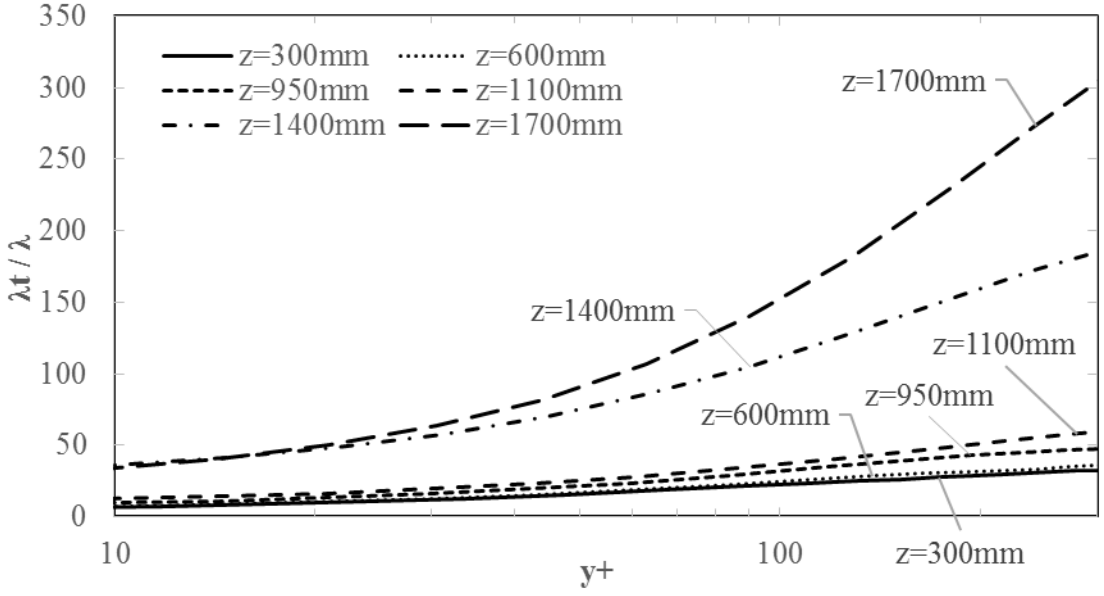

Figure 37: Turbulent thermal conductivity to thermal conductivity ratio vs. y+ at various z locations of case B2 using CFX and the k-ε turbulence model. A y+ value of zero corresponds to the location of line b.

For the SST result using FLUENT, the λ_t/λ profiles are very similar to both of the Low-Re k-ε cases, and by extension are similar to the SST result using CFX and the RNG k-ε case. The profiles of the λ_t/λ ratio for the k-ε case are also similar to the Low-Re k-ε cases, although the values of λ_t/λ never drop below four. There is no HTD in the SST, RNG k-ε, or k-ε cases. This makes it difficult to draw the conclusion that HTD is directly related to the λ_t/λ ratio at certain z locations, as was stated previously, and instead HTD could be caused by other factors. The λ_t/λ ratio may still have a large role in HTD, but perhaps this ratio is not the ideal variable with which to understand HTD for this case. The HTD for the Low-Re k-ε cases is not overly severe compared to other cases, such as case 2 of the Richards experiments, seen in Figure 58, and so the factors that contribute to the HTD may not be readily visible in the numerical data.

Table 22 summarizes the $RMS_{RN,T}$ for the case B2 numerical results of all authors and/or their respective organization. Whether or not the numerical results were created for the benchmark (experimental results unknown to authors), or after the benchmark (experimental results known to authors) is identified by the column on the left.

Table 22: $RMS_{RN,T}$ for case B2 numerical results of all authors and/or their respective organization.

	Authors / Organization	CFD Code	Turbulence Model	$RMS_{RN,T}$ [%]
Benchmark Exercise	TUD[1]	In-house 1D analytical solver	-	12.70
	UPisa	STAR-CCM+ v7.06	AKN Low-Re k-ε	8.21
			SST	10.50
	BME NTI	CFX v14.5	SAS-SST	12.89
	CNL[2]	ASSERT-PV subchannel code	-	9.96
	CVREZ	FLUENT v12	SST	63.88
	KIT-IKET	ANSYS CFX and ANSYS-Structure	k-ε w/Fluid-Structure Interaction	18.40
			SST	11.24
	UMan	CFX v14.5	SST	10.82
	KTH	CFX v15	SST	16.08
	UOttawa	FLUENT v15	SST-SAS	12.07
	McMU	STAR-CCM+ v9.02	SST	8.84
Post Benchmark	Chang and Tavoularis[3] [69] (UOttawa)	STAR-CCM+	SST	7.61
			AKN Low-Re k-ε	7.49
			k-ε-v^2/k	7.91
			v^2-f, Pr_t = 0.9	6.73
			v^2-f, Pr_t = 0.85	5.77
			v^2-f, Pr_t = 0.8	5.81
	Bergmann et al. [90] (UMan)	CFX v14.5	SST w/Modified Coefficients	6.21
	Present Study (UMan)	CFX v14.5	SST	11.13
			k-ε	11.28
		FLUENT v14.5	SST	7.45
			RNG k-ε	11.13
			Yang-Shih Low-Re k-ε	7.08
			Lam-Bremhorst Low-Re k-ε	6.86

[1]Only numerical results from using the Mokry correlation are given in this table, because the other correlations were not as close to the experimental results. The correlations that were used but not presented here are the Dittus-Boelter, Dyadyakin, and Jackson correlations. [2]CNL only provided cladding surface temperatures for lines a, c, and d. [3]Only temperature data along lines b and c provided by authors.

The present author included the spacers for the benchmark exercise, but not for the present study.

The numerical results from using the same turbulence model and code, SST and CFX, are closer

to the experimental results when the spacers are included than if they are not included. This can be seen in the $RMS_{RN,T}$ where the case from the benchmark exercise (spacers were included) has an $RMS_{RN,T}$ of 10.8 %, while the $RMS_{RN,T}$ from the present study (spacers were not included) has an $RMS_{RN,T}$ of 11.1 %. Although, the mesh that included spacers had significantly more nodes than the mesh used in the present study: 62,740,257 compared to 2,077,434, and so the mesh was finer in various location. The reason the mesh that included spacers predicted the experimental data closer than the mesh that did not include spacers may be that that the mesh was finer overall, and not necessarily that the spacers were modelled.

Chang and Tavoularis provided numerical results that had the smallest overall deviation from experimental results of case B2, using the v^2-f turbulence model, implemented using STAR-CCM+, and setting the turbulent Prandtl number to 0.85. Using the same turbulence model and code and setting the turbulent Prandtl number to 0.8 gave numerical results that were in the second best agreement with experimental results. Although these authors did not provide a full set of data to compare with the experiment, and only gave temperature data along lines b and c. Therefore their $RMS_{RN,T}$ may not reflect the true accuracy of their numerical results. The sensitivity study performed on the SST turbulence model coefficients that was performed by the present author [90], provided numerical results that were in third best agreement with the experimental data. The results of Chang and Tavoularis using the v^2-f turbulence model with a turbulent Prandtl number of 0.85, the results of the sensitivity study performed on the SST turbulence model coefficients by the present author, and the Lam-Bremhorst Low-Re k-ε turbulence model results of the present study are plotted in Figure 38.

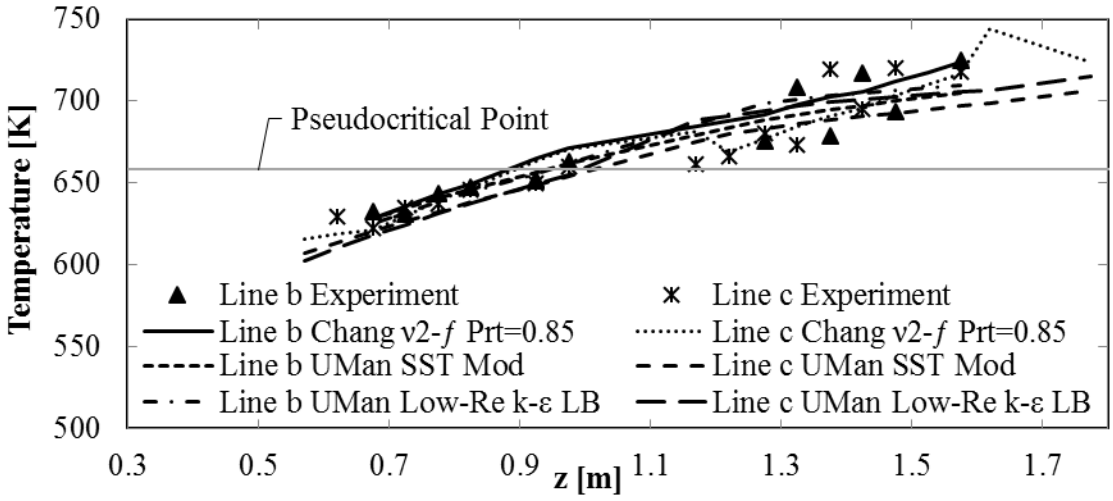

Figure 38: Cladding surface temperatures of Chang and Tavoularis using the v^2-f turbulence model with a turbulent Prandtl number of 0.85, the sensitivity study performed on the SST turbulence model coefficients, and the Lam-Bremhorst Low-Re k-ε turbulence model results.

The cladding surface temperatures predicted by Chang and Tavoularis are generally greater than those predicted by the present author's sensitivity study of the SST turbulence model and the Lam-Bremhorst Low-Re k-ε turbulence model, especially after z = 1.4 [m].

Of the numerical results from the benchmark exercise, the first and second closest predictions were provided by UPisa and McMU using the AKN Low-Re k-ε turbulence model and the SST turbulence model, respectively. STAR-CCM+ was used for both cases. The cladding surface temperatures of these two cases are plotted in Figure 39.

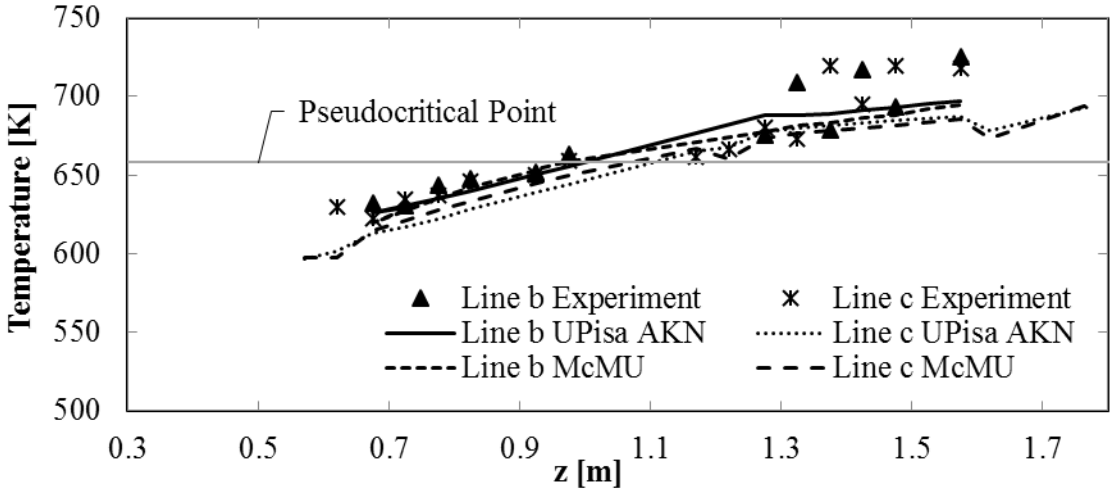

Figure 39: Cladding surface temperatures from UPisa and McMU using the AKN Low-Re k-ε turbulence model and the SST turbulence model, respectively.

UPisa, using the AKN Low-Re k-ε turbulence model generally predicts lower cladding surface temperatures before the pseudocritical point compared to McMU who use the SST turbulence model. After the pseudocritical point, UPisa predicts either slightly greater or similar cladding surface temperatures compared to McMU. Neither UPisa nor McMU predict the spike in cladding surface temperatures that appears after z = 1.3 [m].

CHAPTER 5: RICHARDS 2012 SEVEN-ROD BUNDLE WITH R12

5.1 Experimental Setup

The experimental data of Richards was obtained from the State Scientific Center of Russian Federation – Institute for Physics and Power Engineering Supercritical Test Facility in Obninsk, Russian Federation [32] [93]. For the purpose of the present study, these will be referred to as the "Richards 2012 Experiments". The experimental setup consists of seven hollow AISI 304L stainless steel heater rods orientated in a hexagonal arrangement and enclosed in an aluminum dioxide shroud to create a subchannel with R12 flowing vertically upwards. The heater rods have a diameter of 9.5 [mm] (0.374016 [in]) and a thickness of 0.6 [mm] (0.0236220 [in]). Three stainless steel spacers that are 19 [mm] (0.748031 [in]) in length position the rods inside the shroud, and position the rods relative to one another. Figure 40 shows an x-y cross section of the Richards experimental setup, showing the hollow heater rods, water channel, spacer, shroud, and external housing. The symmetry planes used to simplify the modelling of this rod bundle are also shown.

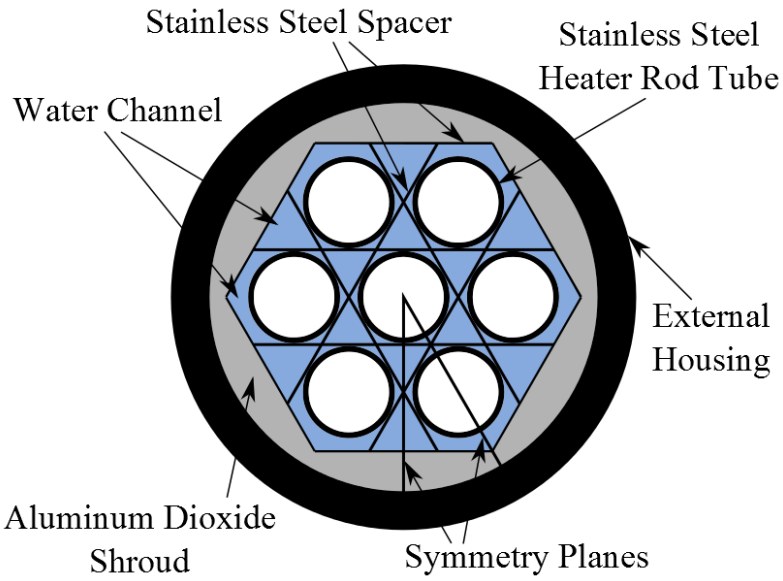

Figure 40: Cross section of Richards 2012 seven-rod bundle, showing heater rods, spacers, shroud, external housing, and planes of symmetry.

Pressure taps are located at the inlet and outlet of the bundle. Figure 41 shows a y-z cross section of the Richards experimental setup, showing the unheated inlet and outlet sections, heated section, and the location of all three spacers relative to the inlet.

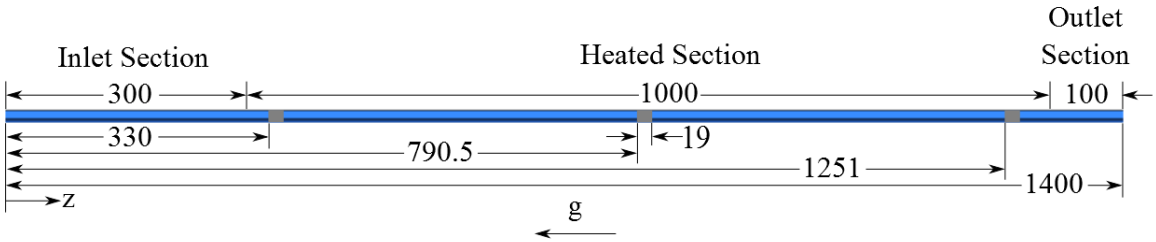

Figure 41: Schematic y-z cross section of the Richards 2012 domain, showing inlet, heated section, outlet, and location of all three spacers relative to inlet. All spacers are of the same length. Dimensions are in [mm].

To measure the bulk fluid temperature at the inlet and outlet, five thermocouples where inserted into the flow at various locations across the x-y plane. To measure the internal surface temperature of the centre heating rod, a movable probe with three thermocouples oriented 120º relative to one another, was positioned at various axial locations along the inside of the centre

heater rod. The internal surface temperature was converted to an outer surface temperature using the following equation [27]:

$$T_{s,o} = T_{s,i} - \frac{\dot{q} D_i^2}{16\lambda}\left[\left(\frac{D_o}{D_i}\right)^2 - 2\ln\left(\frac{D_o}{D_i}\right) - 1\right] \tag{114}$$

where $T_{s,o}$ is the outer surface temperature of the heater rod, $T_{s,i}$ is the internal surface temperature of the heater rod, $\dot{q}$ is the volumetric heat rate of the heater rod, λ is the thermal conductivity of the heater rod, D_o is the outside diameter of the heater rod, and D_i is the internal diameter of the heater rod.

The heat rate, mass flux, inlet and outlet pressure, and inlet temperature of all 20 cases of the Richards experiments are given in Table 23.

Table 23: Experimental conditions of Richards 2012 Experiments.

Case	Heat Rate [kW]	Mass Flux [kg/m^2s]	Inlet Pressure [MPa]	Outlet Pressure [MPa]	Inlet Temperature [^oC]
1	2.05	441.3	4.64	4.64	86.1
2	9.98	447.1	4.629	4.628	89.85
3	4.05	508.4	4.649	4.645	74.42
4	11.0	510.8	4.67	4.67	77.5
5	14.01	516.9	4.64	4.64	73.8
6	17.0	515.6	4.631	4.625	73.39
7	6.98	517.2	4.64	4.63	111.8
8	6.99	516.5	4.63	4.63	119.0
9	9.09	515.6	4.646	4.643	119.26
10	11.03	1023.6	4.64	4.63	78.6
11	16.89	1020.2	4.63	4.61	80.0
12	25.0	1019.4	4.64	4.63	80.1
13	9.7	998.2	4.63	4.62	100.2
14	20.13	1002.6	4.64	4.63	100.4
15	7.09	1220.2	4.65	4.65	72.9
16	18.02	1197.4	4.64	4.63	73.3
17	20.06	1210.0	4.64	4.64	74.1
18	10.0	1225.1	4.62	4.62	101.4
19	13.84	1219.3	4.65	4.64	99.2
20	16.2	1316.2	4.64	4.63	90.74

Note: More accurate data for the pressure and temperature of cases 2, 3, 6, and 9 were given in Huang et al. [71].

The pseudocritical temperature of R12 using the inlet pressures of cases 2 and 3 are given in Table 24, where the pseudocritical temperature is defined as the temperature at which the specific heat capacity at constant pressure reaches a maximum value.

Table 24: Pseudocritical temperatures of R12 at inlet pressures of Richards 2012 Experiments.

Case	Inlet Pressure [MPa]	Pseudocritical Temperature [K]
2	4.629	391.552
3	4.649	391.806

5.2 Numerical Domain Definition, Boundary Condition, and Mesh

A $1/12^{th}$ section of the Richards seven-rod bundle was modelled, and symmetry was assumed on both section planes. The hydraulic diameter of the subchannel is 4.69251 [mm] (0.184744 [in]). An x-y cross section of the bundle showing the section that has been modelled is given in Figure 40 in Section 5.1.

The total length of the domain is 1.4 [m] (4.59318 [ft]) in the z-direction, which includes a 0.3 [m] (0.984252 [ft]) inlet section, 1.0 [m] (3.28084 [ft]) heated section, and a 0.1 [m] (0.328084 [ft]) outlet section. The actual lengths of both the inlet and outlet sections were not given in literature, so it was assumed that these lengths are similar to those of the Rohde et al. bundle. The outlet length was partially chosen to make modelling the mesh easier. The three spacers are 0.019 [m] (0.062336 [ft]) long, and are located at various positions throughout the domain. A y-z cross section, showing the locations of these spacers, as well as the inlet, outlet, and heated section is given in Figure 41 in Section 5.1. These spacers were not modelled in order to substantially reduce the total number of nodes.

When the entire domain is simplified to the $1/12^{th}$ section, the total number of locations of thermocouples on the x-y plane is reduced to one because of symmetry. This location corresponds to line TC as shown in Figure 42, which gives more details about the geometry of the computational domain. TC, H1, H2, H3, and H4 are lines in the computational domain that run the entire z-axis length and will be used to sample wall temperatures.

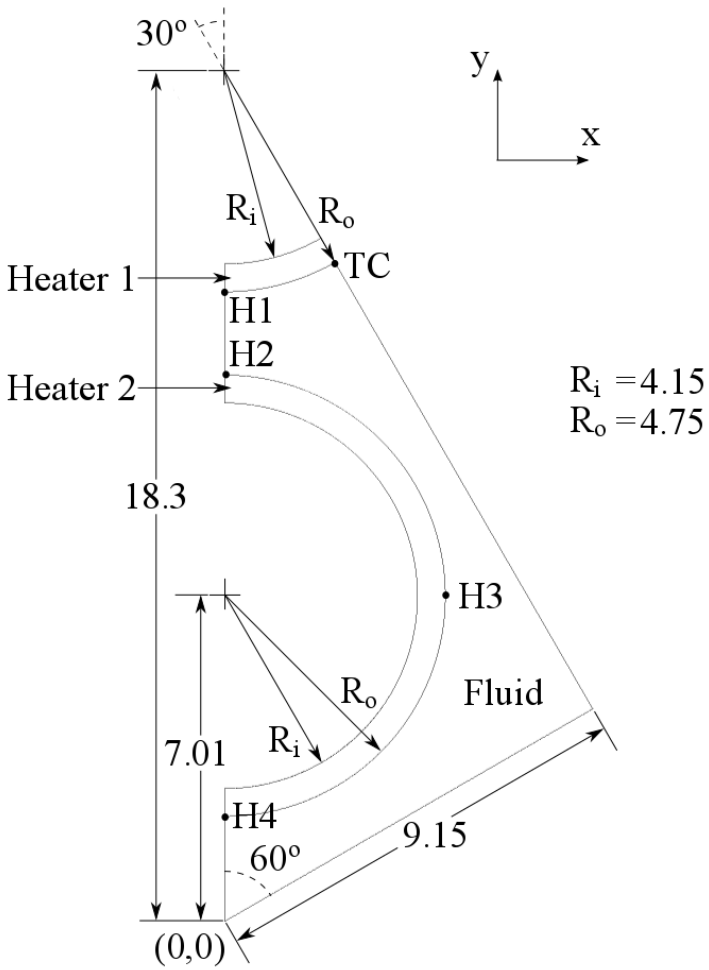

Figure 42: Typical x-y cross section of Richards 2012 domain showing fluid domain, solid domains, location of the thermocouples (TC), and the location of lines H1, H2, H, and H4. All dimensions in [mm].

The thermocouples are located at certain axial locations along line TC. Table 25 and Table 26 provide domain definitions and boundary conditions for each of the domains shown in Figure 42.

Table 25: Domain definition and boundary conditions of Richards 2012 fluid domain.

Fluid	
Domain Properties	Material: R12 Turbulence Model: SST, k-ε, RNG k-ε, Lam-Bremhorst Low-Re k-ε, Yang-Shih Low-Re k-ε Turbulent Prandtl Number (Pr_t): 0.9 Reference Pressure: 4.628 [MPa] (Case 2), 4.645 [MPa] (Case 3)
Material Properties	FORTRAN Subroutines using NIST Chemistry WebBook Data (CFX), NIST REFPROP v9.0 Database (FLUENT)
Inlet	Mass Flow Rate: 0.01393068 [kg/s] (Case 2), 0.01584066 [kg/s] (Case 3) Temperature: 363.00 [K] (Case 2), 347.57 [K] (Case 3) Turbulence: Low Intensity (I = 1 %), Low Eddy Viscosity Ratio (μ_t / μ = 1.0)[1] w = 0.419394 [m/s] (Case 2), 0.440563 [m/s] (Case 3) Re = 21120.6 (Case 2), 19579.8 (Case 3)
Fluid Properties at Inlet, Case 2	ρ = 1051.61 [kg/m^3] μ = 9.79891x10^{-5} [Pa s] c_p = 1242.06 [J/kgK] λ = 0.0481102 [W/mK]
Fluid Properties at Inlet, Case 3	ρ = 1137.83 [kg/m^3] μ = 1.20138x10^{-4} [Pa s] c_p = 1119.07 [J/kgK] λ = 0.0536086 [W/mK]
Outlet	Reference Static Pressure: 0 [Pa]
Wall	Adiabatic no-slip at Shroud, coupled (FLUENT) or conservative interface heat flux (CFX) to Heater 1 and 2 domains (R_o)

[1]Same values as those used for the Rohde et al. cases, because they were found to provide more stable convergence than medium or high intensity inlet turbulence.

Table 26: Domain definition and boundary conditions of Richards 2012 heater domains.

Heater 1 and 2	
Domain Properties	Material: AISI 304L Stainless Steel
Material Properties	ρ = 8030 [kg/m^3] c_p = 5.2 x10^{-5} [J/kgK^3] T^2 + 0.17 [J/kgK^2] T + 426.7 [J/kgK] λ: FORTRAN Subroutine (CFX), lookup table (FLUENT)
Wall	Adiabatic wall across *x*-*y* plane at *z* = 0.0 [m] and *z* = 1.4 [m], coupled (FLUENT) or conservative interface heat flux (CFX) across x-y plane at z = 0.3 [m] and z = 1.3 [m], coupled (FLUENT) or conservative interface heat flux (CFX) to Fluid domain (R_o) Adiabatic wall at R_i
Heated Section Energy Source	Heater 1 and 2 Volumetric Heat Rate (from total heat rate): 8.49848x10^7 [W/m^3] (Case 2), 3.44878x10^7 [W/m^3] (Case 3)

Various solution variable monitor points are defined for CFX and FLUENT runs, to provide an additional means to check convergence of the runs. These monitor points were placed at 11 axial locations along line TC to record temperature. Additionally, for CFX runs, pressure was monitored at points that were in close proximity to the centroid of the inlet and outlet, and for FLUENT runs, the area averaged pressure at the inlet and outlet was monitored.

5.3 Grid Independence Study

A mesh of the 1/12th section of the seven-rod bundle was generated using ICEM CFD, and the spacers were not modelled in order to substantially reduce the total number of nodes. Figure 40 in Section 5.1 shows this 1/12th section defined by the symmetry planes in relation to the entire x-y cross section. CFX was used to numerically solve case 2 using the SST turbulence model with automatic wall treatment. The SST turbulence model was chosen because, out of those turbulence models that were selected to provide final results, it was the only turbulence model that can be used in CFX that required a y^+ of less than one. The maximum residuals and domain

imbalances were monitored during the runs, and a solution was considered to be converged when these variables reached values given in Section 3.5.1.

A number of initial meshes were first generated for CFX, and solutions were obtained for case 2. Case 2 was chosen because the fluid temperature at the inlet was close to the pseudocritical point, and the experimental results showed two pronounced spikes in wall temperature, which were likely a result of large variation in the heat transfer phenomena near the wall and, therefore, a good test of the models. A mesh with a large number of nodes was eventually created and a solution was obtained. This mesh is referred to here as the R-1 mesh and it had 17,422,281 nodes. Five other meshes were created by either increasing or decreasing the uniform z cross section grid spacing of this R-1 mesh. These meshes were given names that correspond to the order in which they were created, i.e. mesh R-1 was created first, and mesh R-6 was the sixth mesh to be created. The changes made to each mesh can be described using a cylindrical r-θ coordinate system. Figure 43 shows the equivalent r-θ coordinate system superimposed on a typical x-y cross section. The mesh shown in Figure 43, R-17, will eventually be selected as the mesh to be used for the final results. The z-axis cross section has constant nodal spacing.

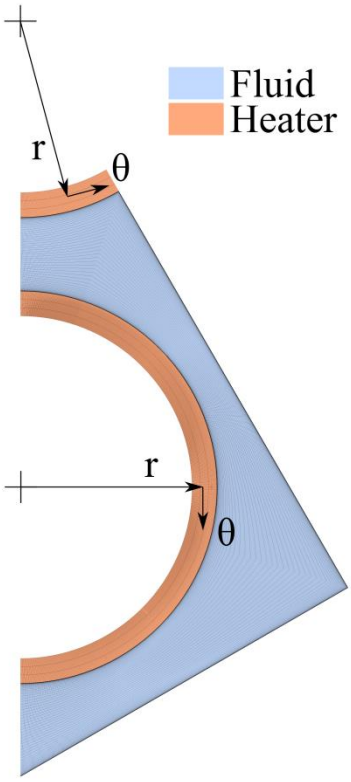

Figure 43: Equivalent r-θ coordinate system for describing mesh modification procedure shown on typical x-y cross section of Richards R-17 mesh

Tables 27 to 30 provide mesh parameters of these six meshes that have identical r-θ cross section mesh parameters, and different z cross section parameters.

Table 27: Overall properties of meshes with different z cross section nodal spacing and identical r-θ cross section nodal spacing, listed in descending order of total nodes.

Mesh ID	Total Nodes	Difference in Nodes Relative to Previous Mesh	Percentage Decrease in Nodes Relative to Previous Mesh
R-6	43,462,701	-	-
R-4	28,706,463	14,756,238	33.95
R-1	17,422,281	11,284,182	39.31
R-2	12,214,197	5,208,084	29.89
R-3	9,610,155	2,604,042	21.32
R-5	7,874,127	1,736,028	18.06

Table 28: Geometric parameters of meshes with different z cross section nodal spacing and identical r-θ cross section nodal spacing.

Mesh ID	Max z-Spacing [mm]	Max θ-Spacing [mm]	Max r-Spacing, Fluid [mm]	Near Wall Grid Spacing [mm] / Expansion Ratio Next to H1 and H2	Near Wall Grid Spacing [mm] / Expansion Ratio Next to Shroud	Solid Domain Nodes in r-Direction: H1/H2
R-6	2.00000	0.022662	0.159105	0.0008/1.3	0.0008/1.3	4/4
R-4	3.03030	0.022662	0.159105	0.0008/1.3	0.0008/1.3	4/4
R-1	5.00000	0.022662	0.159105	0.0008/1.3	0.0008/1.3	4/4
R-2	7.14286	0.022662	0.159105	0.0008/1.3	0.0008/1.3	4/4
R-3	9.09091	0.022662	0.159105	0.0008/1.3	0.0008/1.3	4/4
R-5	11.1111	0.022662	0.159105	0.0008/1.3	0.0008/1.3	4/4

Table 29: Maximum and minimum y^+ values of meshes with different z cross section nodal spacing and identical r-θ cross section nodal spacing.

Mesh ID	y^+ Max	y^+ Min
R-6	0.834854	0.0555693
R-4	0.834925	0.0556286
R-1	0.836454	0.0557133
R-2	0.835873	0.0558415
R-3	0.833851	0.0559026
R-5	0.831500	0.0559884

Table 30: Mesh quality parameters in the fluid domain of meshes with different z cross section nodal spacing and identical r-θ cross section nodal spacing.

Mesh ID	Min Angle [degree]	Max Expansion Factor	Max Aspect Ratio
R-6	42.9	2	9348
R-4	42.9	2	14163
R-1	42.9	2	23369
R-2	42.9	2	33384
R-3	42.9	2	42488
R-5	42.9	2	51930

The number of nodes in the r-direction in the solid domains was be kept at four, as shown in Table 28, for this study. This was done to reduce the number of different mesh modifications, in order to reduce the number of meshes that must be created. The number four was chosen as this is one node more than the number of nodes in the r-direction of the solid domains selected for the final Rohde et al. mesh, BNSP-6. The mesh with the greatest number of nodes and, thus, had the finest z cross section spacing, was the R-6 mesh with 43,462,701 nodes. The mesh with the least number of nodes was the R-5 mesh with 7,874,127 nodes. The $RMS_{RN,T}$ parameter, defined by Equation (113) in Section 4.3, is used to quantify the heated wall surface temperature differences between the results of each of the meshes, where the sampled lines are lines H1, H2, and TC. The $RMS_{RN,T}$ is plotted in Figure 44 for the results of these meshes using the mesh with the greatest number of nodes, mesh R-6, as the reference mesh.

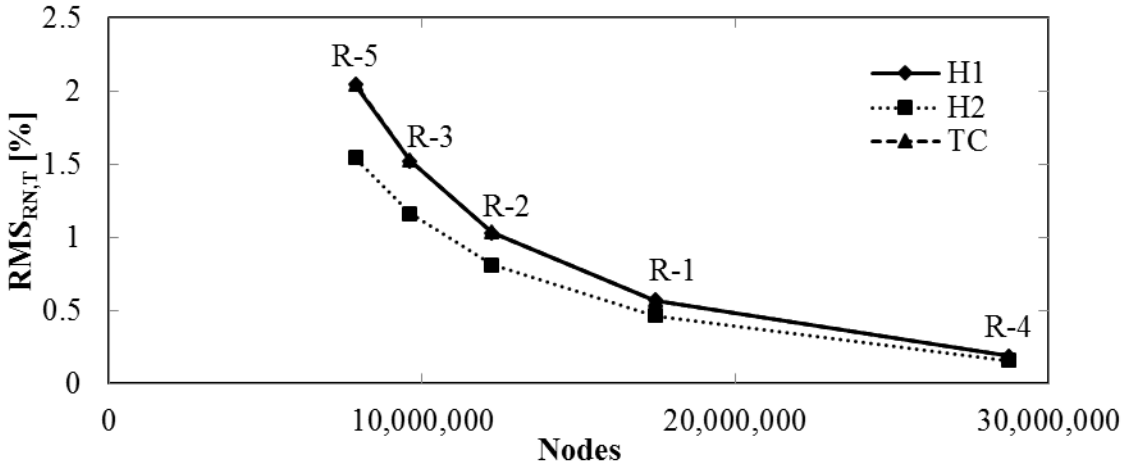

Figure 44: $RMS_{RN,T}$ vs. total nodes for meshes with different z cross section nodal spacing and identical r-θ cross section nodal spacing. Mesh R-6 is the reference mesh. Line H1 is hidden underneath line TC.

Figure 44 shows that the heated wall temperature is dependent on the number of z nodes, and as the number of nodes in the z-direction increases, the $RMS_{RN,T}$ converges towards zero.

The mesh that had a maximum $RMS_{RN,T}$ of approximately 1 %, mesh R-2, was then modified by increasing and then decreasing the number of nodes in the r-direction of the fluid domain while maintaining the same expansion ratio close to the wall, to create meshes R-7 and R-8, respectively. Tables 31 to 34 provide mesh parameters of these three meshes that have identical z and θ cross section mesh parameters, and different r cross-sectional parameters.

Table 31: Overall properties of meshes with different r cross section nodal spacing and identical z-θ cross section nodal spacing, listed in descending order of total nodes.

Mesh ID	Total Nodes	Difference in Nodes Relative to Previous Mesh	Percentage Decrease in Nodes Relative to Previous Mesh
R-7	15,593,338	-	-
R-2	12,214,197	3,379,141	21.67
R-8	11,021,559	1,192,638	9.76

Table 32: Geometric parameters of meshes with different r cross section nodal spacing and identical z-θ cross section nodal spacing.

Mesh ID	Max z-Spacing [mm]	Max θ-Spacing [mm]	Max r-Spacing, Fluid [mm]	Near Wall Grid Spacing [mm] / Expansion Ratio Next to H1 and H2	Near Wall Grid Spacing [mm] / Expansion Ratio Next to Shroud	Solid Domain Nodes in r-Direction: H1/H2
R-7	7.14286	0.022662	0.0796051	0.0008/1.3	0.0008/1.3	4/4
R-2	7.14286	0.022662	0.159105	0.0008/1.3	0.0008/1.3	4/4
R-8	7.14286	0.022662	0.329569	0.0008/1.3	0.0008/1.3	4/4

Table 33: Maximum and minimum y^+ values of meshes with different r cross section nodal spacing and identical z-θ cross section nodal spacing.

Mesh ID	y^+ Max	y^+ Min
R-7	0.835356	0.0557362
R-2	0.835873	0.0558415
R-8	0.835777	0.0558889

Table 34: Mesh quality parameters in the fluid domain of meshes with different r cross section nodal spacing and identical z-θ cross section nodal spacing.

Mesh ID	Min Angle [degree]	Max Expansion Factor	Max Aspect Ratio
R-7	42.9	2	33384
R-2	42.9	2	33384
R-8	42.9	2	33384

The mesh with the greatest number of nodes and, thus, the finest r-direction spacing, was the R-7 mesh with 15,593,338 nodes. The mesh with the least number of nodes was the R-8 mesh with 11,021,559 nodes. The $RMS_{RN,T}$ is plotted in Figure 45 for the results of these meshes using mesh R-7 as the reference mesh.

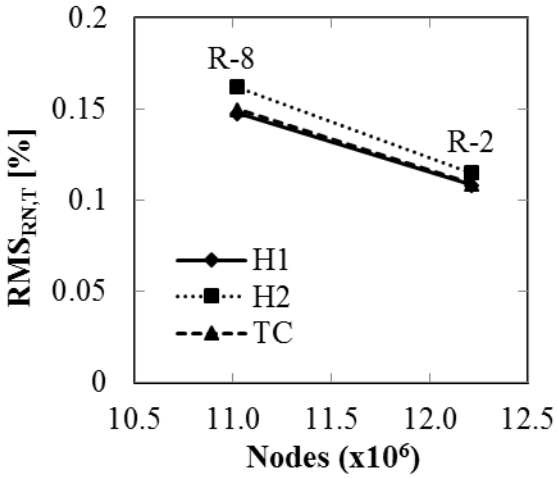

Figure 45: $RMS_{RN,T}$ vs. total nodes for meshes with different r cross section nodal spacing and identical z-θ cross section nodal spacing. Mesh R-7 is the reference mesh, and Line H1 is hidden underneath line TC.

Figure 45 shows that the $RMS_{RN,T}$ is only slightly dependent on the nodal spacing in the r-direction, since the maximum $RMS_{RN,T}$ is approximately 0.16 %, and drops to a minimum of approximately 0.11 %.

Mesh R-2 was again used to generate multiple new meshes, R-9 through R-13. These meshes had identical nodal spacing as mesh R-2 in the z and θ direction, but had different expansion ratios in the r-direction nearest to the wall in the fluid domain. Tables 35 to 38 provide mesh parameters of these six meshes that have identical z and θ cross section mesh parameters, and different r cross section parameters.

Table 35: Overall properties of meshes with different expansion ratios near the heated wall in the fluid domain in the r-direction and identical z-θ cross section nodal spacing, listed in descending order of total nodes.

Mesh ID	Total Nodes	Difference in Nodes Relative to Previous Mesh	Percentage Decrease in Nodes Relative to Previous Mesh
R-12	30,898,859	-	-
R-10	23,743,031	7,155,828	23.16
R-13	15,394,565	8,348,466	35.16
R-2	12,214,197	3,180,368	20.66
R-9	10,027,694	2,186,503	17.90
R-11	9,033,829	993,865	9.91

Table 36: Geometric parameters of meshes with different expansion ratios near the heated wall in the fluid domain in the r-direction and identical z-θ cross section nodal spacing.

Mesh ID	Max z-Spacing [mm]	Max θ-Spacing [mm]	Max r-Spacing, Fluid [mm]	Near Wall Grid Spacing [mm] / Expansion Ratio Next to H1 and H2	Near Wall Grid Spacing [mm] / Expansion Ratio Next to Shroud	Solid Domain Nodes in r-Direction: H1/H2
R-12	7.14286	0.022662	0.0975749	0.0008/1.07	0.0008/1.07	4/4
R-10	7.14286	0.022662	0.134311	0.0008/1.1	0.0008/1.1	4/4
R-13	7.14286	0.022662	0.140379	0.0008/1.2	0.0008/1.2	4/4
R-2	7.14286	0.022662	0.159105	0.0008/1.3	0.0008/1.3	4/4
R-9	7.14286	0.022662	0.153697	0.0008/1.5	0.0008/1.5	4/4
R-11	7.14286	0.022662	0.154065	0.0008/1.7	0.0008/1.7	4/4

Table 37: Maximum and minimum y^+ values of meshes with different expansion ratios near the heated wall in the fluid domain in the r-direction and identical z-θ cross section nodal spacing.

Mesh ID	y^+ Max	y^+ Min
R-12	0.836488	0.0554226
R-10	0.836267	0.0554313
R-13	0.836150	0.0555403
R-2	0.835873	0.0558415
R-9	0.830599	0.0565209
R-11	0.827896	0.0566784

Table 38: Mesh quality parameters in the fluid domain of meshes with different expansion ratios near the heated wall in the fluid domain in the r-direction and identical z-θ cross section nodal spacing.

Mesh ID	Min Angle [degree]	Max Expansion Factor	Max Aspect Ratio
R-12	42.9	1	33384
R-10	42.9	1	33384
R-13	42.9	2	33384
R-2	42.9	2	33384
R-9	42.9	2	33384
R-11	42.9	2	33384

The mesh with the greatest number of nodes and, thus, had the lowest expansion ratio in the r-direction, was the R-12 mesh with 30,898,859 nodes. The mesh with the least number of nodes was the R-11 mesh with 9,033,829 nodes. The $RMS_{RN,T}$ is plotted in Figure 46 for the results of these meshes using mesh R-12 as the reference mesh.

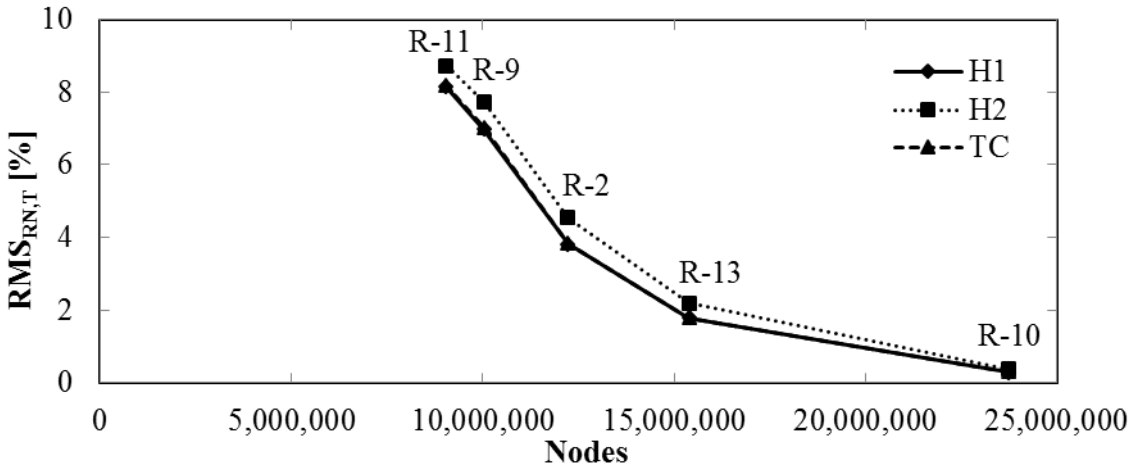

Figure 46: $RMS_{RN,T}$ vs. total nodes for meshes with different expansion ratios near the heated wall in the fluid domain in the r-direction and identical z-θ cross section nodal spacing. Mesh R-12 is the reference mesh, and Line H1 is hidden underneath line TC.

Figure 46 shows that the heated wall temperature is highly dependent on the expansion ratio in the r-direction closest to the wall. As the expansion ratio decreases, and in turn the number of nodes increases, the $RMS_{RN,T}$ converges towards zero. The mesh with 15,394,565 nodes, mesh R-13, had a maximum $RMS_{RN,T}$ of 2.2 %, which is reasonably low compared to the other meshes. The mesh with the next lowest $RMS_{RN,T}$ of 0.4 %, had 23,743,031 nodes, which is a substantial increase in nodes for a reduction in $RMS_{RN,T}$.

Mesh R-2 was once again used to generate multiple new meshes, R-14 through R-16. These meshes had identical nodal spacing as mesh R-2 in the z and r direction, but had different θ-direction spacing. Tables 39 to 42 provide mesh parameters of these four meshes that have identical z and r cross section mesh parameters, and different θ cross section parameters.

Table 39: Overall properties of meshes with different θ cross section nodal spacing and identical r-z cross section nodal spacing, listed in descending order of total nodes.

Mesh ID	Total Nodes	Difference in Nodes Relative to Previous Mesh	Percentage Decrease in Nodes Relative to Previous Mesh
R-16	27,523,658	-	-
R-15	18,374,190	9,149,468	33.24
R-2	12,214,197	6,159,993	33.53
R-14	9,224,722	2,989,475	24.48

Table 40: Geometric parameters of meshes with different θ cross section nodal spacing and identical r-z cross section nodal spacing.

Mesh ID	Max z-Spacing [mm]	Max θ-Spacing [mm]	Max r-Spacing, Fluid [mm]	Near Wall Grid Spacing [mm] / Expansion Ratio Next to H1 and H2	Near Wall Grid Spacing [mm] / Expansion Ratio Next to Shroud	Solid Domain Nodes in r-Direction: H1/H2
R-16	7.14286	0.0100075	0.159105	0.0008/1.3	0.0008/1.3	4/4
R-15	7.14286	0.0150071	0.159105	0.0008/1.3	0.0008/1.3	4/4
R-2	7.14286	0.0226620	0.159105	0.0008/1.3	0.0008/1.3	4/4
R-14	7.14286	0.0300761	0.159105	0.0008/1.3	0.0008/1.3	4/4

Table 41: Maximum and minimum y^+ values of meshes with different θ cross section nodal spacing and identical r-z cross section nodal spacing.

Mesh ID	y^+ Max	y^+ Min
R-16	0.839345	0.0454864
R-15	0.837809	0.0500213
R-2	0.835873	0.0558415
R-14	0.834166	0.0606075

Table 42: Mesh quality parameters in the fluid domain of meshes with different θ cross section nodal spacing and identical r-z cross section nodal spacing.

Mesh ID	Min Angle [degree]	Max Expansion Factor	Max Aspect Ratio
R-16	42.9	2	33385
R-15	42.9	2	33384
R-2	42.9	2	33384
R-14	42.9	2	33384

The mesh with the greatest number of nodes and, thus, had the smallest spacing in the θ-direction, was the R-16 mesh with 27,523,658 nodes. The mesh with the least number of nodes was the R-14 mesh with 9,224,722 nodes. The $RMS_{RN,T}$ is plotted in Figure 47 for the results of these meshes using mesh R-16 as the reference mesh.

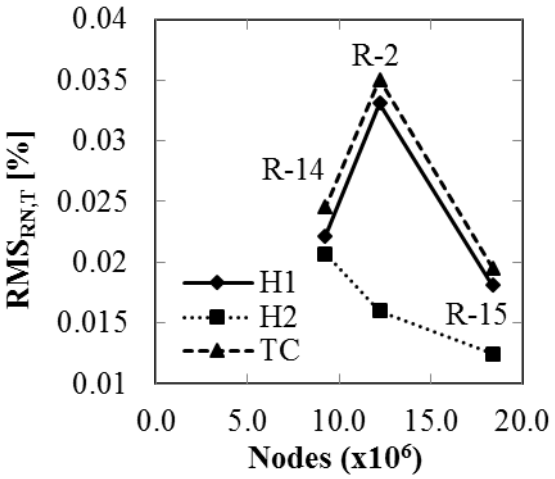

Figure 47: $RMS_{RN,T}$ vs. total nodes for meshes with different θ cross section nodal spacing and identical r-z cross section nodal spacing. Mesh R-16 is the reference mesh.

From the above plot it is clear that the θ spacing has little effect on $RMS_{RN,T}$ and, thus, little effect on the heated wall surface temperatures. This is evident by the maximum $RMS_{RN,T}$ of 0.04 %. Almost all the meshes generated up to now had the same refined θ spacing and expansion

ratio in the θ-direction in the top corner of the mesh. For the next mesh, R-17, the θ spacing will be uniform with no refinement in the top corner of the mesh. This mesh will be created from mesh R-13, which was shown to have a maximum $RMS_{RN,T}$ of 2.2 % when comparing meshes with different expansion ratios in the r-direction of the fluid domain. This $RMS_{RN,T}$ is reasonably low compared to the other meshes in the comparison.

Tables 43 to 46 provide mesh parameters of the two meshes that have identical z and r cross section mesh parameters, and different θ cross section parameters.

Table 43: Overall properties of meshes with different θ cross section nodal spacing and identical r-z cross section nodal spacing, listed in descending order of total nodes.

Mesh ID	Total Nodes	Difference in Nodes Relative to Previous Mesh	Percentage Decrease in Nodes Relative to Previous Mesh
R-13	15,394,565	-	-
R-17	15,362,651	31,914	0.21

Table 44: Geometric parameters of meshes with different θ cross section nodal spacing and identical r-z cross section nodal spacing.

Mesh ID	Max z-Spacing [mm]	Max θ-Spacing [mm]	Max r-Spacing, Fluid [mm]	Near Wall Grid Spacing [mm] / Expansion Ratio Next to H1 and H2	Near Wall Grid Spacing [mm] / Expansion Ratio Next to Shroud	Solid Domain Nodes in r-Direction: H1/H2
R-13	7.14286	0.0226620	0.140379	0.0008/1.2	0.0008/1.2	4/4
R-17	7.14286	0.0226052	0.140379	0.0008/1.2	0.0008/1.2	4/4

Table 45: Maximum and minimum y^+ values of meshes with different θ cross section nodal spacing and identical r-z cross section nodal spacing.

Mesh ID	y^+ Max	y^+ Min
R-13	0.836150	0.0555403
R-17	0.835805	0.0555312

Table 46: Mesh quality parameters in the fluid domain of meshes with different θ cross section nodal spacing and identical r-z cross section nodal spacing.

Mesh ID	Min Angle [degree]	Max Expansion Factor	Max Aspect Ratio
R-13	42.9	2	33384
R-17	42.9	1	33385

The $RMS_{RN,T}$ for mesh R-17 using mesh R-13 as the reference mesh is 0.07 %, 0.01 %, and 0.07 % for lines H1, H2, and TC, respectively. These are low $RMS_{RN,T}$ values, and so the conclusion can be drawn that mesh R-17 would give results that are very similar to mesh R-13 even though mesh R-17 has fewer nodes in the θ-direction.

As a final check, mesh R-17 was used to generate five other meshes, mesh R-18 through R-22. Only the z-direction spacing was modified between these meshes. Tables 47 to 50 provide mesh parameters of these six meshes that have identical r and θ cross section mesh parameters, and different z cross section parameters.

Table 47: Overall properties of meshes with different z cross section nodal spacing and identical r-θ cross section nodal spacing, listed in descending order of total nodes.

Mesh ID	Total Nodes	Difference in Nodes Relative to Previous Mesh	Percentage Decrease in Nodes Relative to Previous Mesh
R-22	43,748,463	-	-
R-21	36,184,112	7,564,351	17.29
R-20	21,913,223	14,270,889	39.44
R-17	15,362,651	6,550,572	29.89
R-18	12,087,365	3,275,286	21.32
R-19	9,903,841	2,183,524	18.06

Table 48: Geometric parameters of meshes with different z cross section nodal spacing and identical r-θ cross section nodal spacing.

Mesh ID	Max z-Spacing [mm]	Max θ-Spacing [mm]	Max r-Spacing, Fluid [mm]	Near Wall Grid Spacing [mm] / Expansion Ratio Next to H1 and H2	Near Wall Grid Spacing [mm] / Expansion Ratio Next to Shroud	Solid Domain Nodes in r-Direction: H1/H2
R-22	2.50000	0.0226052	0.140379	0.0008/1.2	0.0008/1.2	4/4
R-21	3.03030	0.0226052	0.140379	0.0008/1.2	0.0008/1.2	4/4
R-20	5.00000	0.0226052	0.140379	0.0008/1.2	0.0008/1.2	4/4
R-17	7.14286	0.0226052	0.140379	0.0008/1.2	0.0008/1.2	4/4
R-18	9.09091	0.0226052	0.140379	0.0008/1.2	0.0008/1.2	4/4
R-19	11.1111	0.0226052	0.140379	0.0008/1.2	0.0008/1.2	4/4

Table 49: Maximum and minimum y^+ values of meshes with different z cross section nodal spacing and identical r-θ cross section nodal spacing.

Mesh ID	y^+ Max	y^+ Min
R-22	0.835810	0.0553017
R-21	0.835372	0.0553275
R-20	0.836480	0.0554388
R-17	0.835805	0.0555312
R-18	0.834307	0.0556373
R-19	0.832493	0.0557059

Table 50: Mesh quality parameters in the fluid domain of meshes with different z cross section nodal spacing and identical r-θ cross section nodal spacing.

Mesh ID	Min Angle [degree]	Max Expansion Factor	Max Aspect Ratio
R-22	42.9	1	11685
R-21	42.9	1	14153
R-20	42.9	1	23369
R-17	42.9	1	33385
R-18	42.9	1	42489
R-19	42.9	1	51931

The mesh with the greatest number of nodes and, thus, had the smallest spacing in the z-direction, was the R-22 mesh with 43,748,463 nodes. The mesh with the least number of nodes was the R-19 mesh with 9,903,841 nodes. The $RMS_{RN,T}$ is plotted in Figure 48 for the results of these meshes using the mesh with the greatest number of nodes, mesh R-22, as the reference mesh.

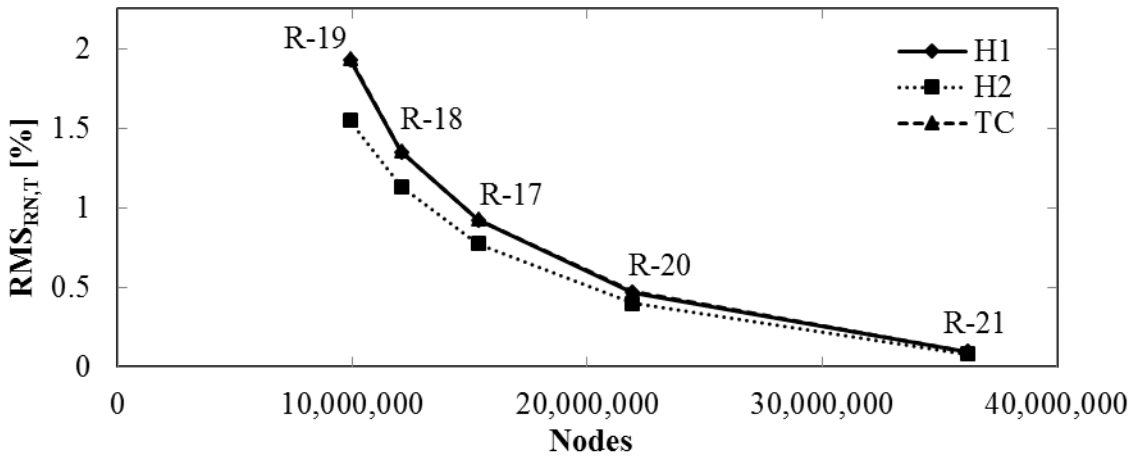

Figure 48: $RMS_{RN,T}$ vs. total nodes for meshes with different z cross section nodal spacing and identical r-θ cross section nodal spacing. Mesh R-22 is the reference mesh, and Line H1 is hidden underneath line TC.

Figure 48 shows once again that the heated wall surface temperature is dependent on the number of nodes in the z-direction. As the number of nodes in the z-direction increases, the $RMS_{RN,T}$ converges towards zero. The mesh with 15,362,651 nodes, mesh R-17, had a maximum $RMS_{RN,T}$ of 0.93 %, which is reasonably low compared to the other meshes. The mesh with the next lowest $RMS_{RN,T}$ of 0.47 %, had 21,913,223 nodes, which is a substantial increase in nodes for a minimal reduction in $RMS_{RN,T}$.

From these mesh comparisons, the mesh that provides a solution that is relatively independent of the mesh, while using a minimum number of nodes, is mesh R-17. This mesh was used to generate final results of cases 2 and 3 of the Richards experiments.

5.4 Results and Discussion

The numerical results of case 2 and 3 of the Richards experimental data are presented here. Case 2 was selected mainly because a large spike in heater rod surface temperature was present, which was evidence that HTD was present in this case. Case 3 was selected because it appeared to show normal heat transfer, as there was no a spikes in heater rod surface temperature, and the temperatures never reaches the pseudocritical temperature. Additionally, both Zhang et al. [72] and Huang et al. [71] performed numerical simulations of case 2 and 3, which are compared with the numerical results presented here.

Zhang et al. used CFX v11.0 and the SST, RNG k-ε, SSG Reynolds Stress, and the ω-RSM turbulence models to numerically simulate case 2 and 3 of the Richards experiments. Scalable wall functions were used with the RNG k-ε and SSG Reynolds Stress turbulence models, and automatic wall treatment was used with the SST and ω-RSM turbulence models. These authors

modelled 1/12th of the bundle cross section, and included a 0.4 [m] unheated inlet section, but no unheated outlet section.

Huang et al. used FLUENT v6.3.26 and the SST, k-ε, Reynolds Stress model (RSM), and the ω-RSM turbulence models to numerically simulate case 2 of the Richards experiments. These authors also used FLUENT and the RSM turbulence model to numerically simulate case 3 of the Richards experimental data. Both wall functions and EWT near wall treatments were used with the SST, k-ε, and Reynolds Stress model (RSM), while only EWT was used with the ω-RSM turbulence model.

Huang et al. modelled the entire bundle, not just a portion of the cross section, and included the inlet and outlet chambers and the associated inlet and outlet pipes that ran horizontally. The original experiments had a horizontal inlet pipe, 0.2 [m] in diameter that fed into an unheated inlet chamber that was 0.4 [m] in diameter. There was also an unheated outlet chamber, 0.4 [m] in diameter that was attached to a 0.2 [m] diameter outlet pipe that ran horizontally. The height of the inlet and outlet chambers was not stated in either the Richards 2012 Experiments or the Huang et al. study.

Huang et al. modelled the entire rod bundle, and not just a 1/12th section. Therefore, heater rod surface temperature data were given for all three thermocouple locations for any given x-y cross section. For this study, heater rod surface temperature data was collected from only one of the thermocouple locations from the Huang et al. study. This was the “TC1” thermocouple location given in the study. The remaining two thermocouple locations, “TC2” and “TC3”, gave heater rod surface temperatures that were similar to the “TC1” thermocouple location.

For the present study, the maximum residuals and domain imbalances were monitored during the following runs, and a solution was considered to be converged when these variables reached values given in Section 3.5.1 and Section 3.5.2 for CFX and FLUENT, respectively. Exceptions to this were case 2 using the SST turbulence model and FLUENT, case 3 using the RNG k-ε turbulence model with FLUENT, and case 3 using the SST turbulence model with FLUENT. The continuity residuals for these three cases were 2.62×10^{-3}, 7.72×10^{-3}, and 7.50×10^{-3}, respectively. The FLUENT Solver Modelling Guide recommends the residuals be less than 1×10^{-3} except for the energy residual which should be less than 1×10^{-5}. These three cases with the higher than desired continuity residuals were still considered converged because the solution variables at the monitor points did not change significantly over a large number of iterations, and all other imbalances and residuals were well below the desired values. Typically, the maximum change in temperature or pressure at a monitor location was less than 0.1 % over at least approximately 400 iterations, and the vast majority of monitor locations had much less than a 0.1 % change in temperature or pressure over the same number of iterations. It was also not possible to reduce the residual by changing under-relaxation factors or the pseudo time step, which are the only methods that can be used to affect convergence during FLUENT runs. The mesh could have been altered to possibly reduce the residuals, but a grid independence study would need to be performed on that mesh and all other cases would have to be performed again with the new mesh. For these reasons, the slightly larger continuity residual for the three cases were considered acceptable.

All CFX and FLUENT runs were performed on local servers at the University of Manitoba, which use the Linux operating system. The total wall clock time for case 3 CFX simulations was between 45 and 199 hours using between 4 and 40 cores in parallel computing. For case 3

FLUENT simulations, the total wall clock time was between 130 and 488 hours using between 4 and 40 cores in parallel. The total wall clock time for case 2 CFX simulations was between 60 and 478 hours using between 4 and 30 cores in parallel computing. For case 2 FLUENT simulations, the total wall clock time was between 263 and 527 hours using between 4 and 30 cores in parallel.

For a given z coordinate there exists temperature data from three thermocouples. The three locations on the x-y plane of these thermocouples are located at the same point when the entire domain is modelled as a $1/12^{th}$ section through the use of symmetry planes. The experimental data from the thermocouples at each of the z locations is therefore averaged in order to compare with numerical results. This averaged experimental data is given as "Experiment" in the plots of heater rod surface temperature.

5.4.1. Case 3

The numerical results of case 3 of the Richards experiments will be presented here, followed by a comparison with the other numerical results from Zhang et al. and Huang et al.

Figure 49 gives the heater rod surface temperatures of case 3 using CFX and the SST and k-ε turbulence models, FLUENT and the SST turbulence model, and the experimental temperatures along line TC.

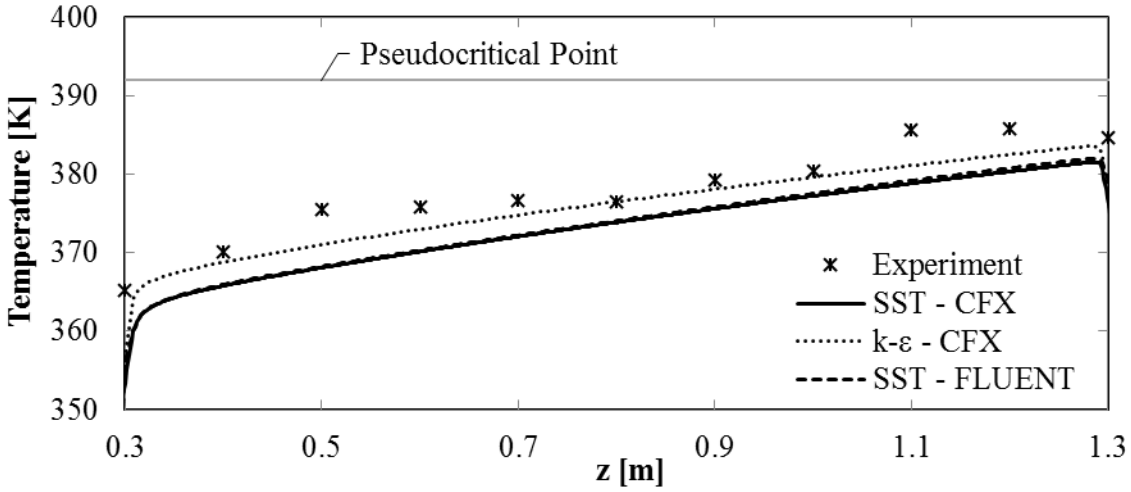

Figure 49: Heater rod surface temperatures along line TC for case 3 using CFX with the SST and k-ε turbulence model, and FLUENT with the SST turbulence model.

The k-ε turbulence model, implemented using CFX, slightly under-predicts the heater rod surface temperatures, although the results are relatively close to the experimental data compared to the results of the SST turbulence model using CFX and FLUENT. The SST turbulence model, implemented using CFX and FLUENT, under-predicts the heater rod surface temperatures over the entire heated section. The results of FLUENT and CFX, when using the SST turbulence model are very similar.

Figure 50 gives the heater rod surface temperatures of case 3 using FLUENT and the SST, RNG k-ε, Lam-Bremhorst Low-Re k-ε, and Yang-Shih Low-Re k-ε turbulence models, along with the experimental temperatures along line TC.

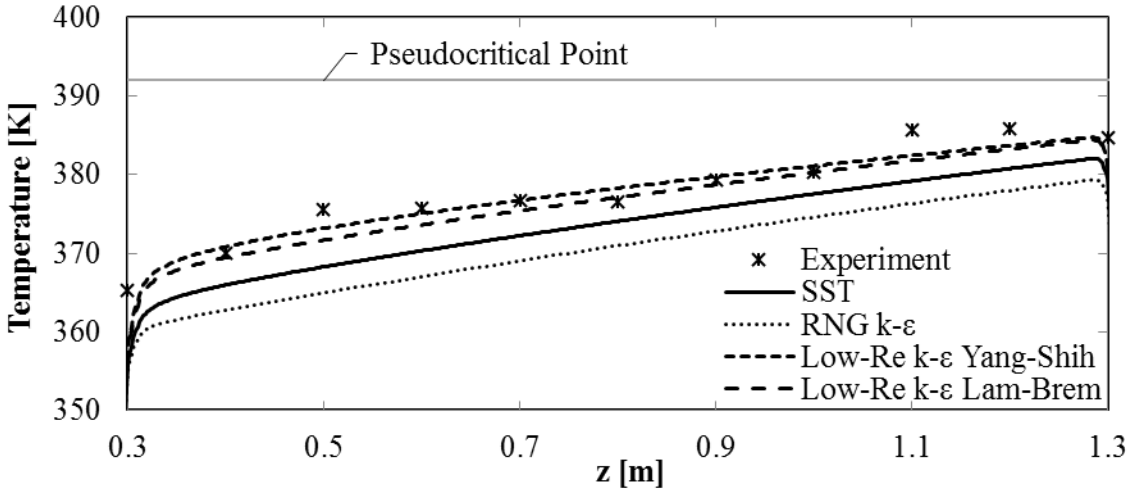

Figure 50: Heater rod surface temperatures line TC for case 3 using FLUENT

The heater rod surface temperatures of both the Lam-Bremhorst and Yang-Shih Low-Re k-ε turbulence model using FLUENT are relatively close to the experimental data, while those of the RNG k-ε turbulence model using FLUENT are all significantly lower than the experimental data. The SST turbulence model using FLUENT under-predicts the heater rod surface temperatures, although the results are not as bad as the RNG k-ε turbulence model.

To quantify the differences between the numerical predictions and experimental results of heater rod surface temperatures for case 3, the $RMS_{RN,T}$ is calculated and presented in Table 51. Equation (113) in Section 4.3 is used to calculate the $RMS_{RN,T}$, where the reference temperatures come from the experimental data.

Table 51: $RMS_{RN,T}$ between numerical results and experimental results for case 3.

Case	$RMS_{RN,T}$ [%]
3 SST CFX	30.48
3 k-ε CFX	20.91
3 SST FLUENT	26.42
3 RNG k-ε FLUENT	39.11
3 Low-Re k-ε Lam-Bremhorst FLUENT	15.80
3 Low-Re k-ε Yang-Shih FLUENT	13.79

The Yang-Shih Low-Re k-ε turbulence model using FLUENT gave the result that was in the best agreement with the experimental data. The Lam-Bremhorst Low-Re k-ε turbulence model using FLUENT gave the result that was next closest in terms of agreement with the experimental data. The RNG k-ε turbulence model using FLUENT and the SST turbulence model using CFX gave poorer results with regards to agreement between numerical and experimental data. When using the SST turbulence model, FLUENT yields results that are in slightly better agreement with experimental data compared to CFX.

Various plots from case 3 using CFX and the SST turbulence model are given to illustrate the trends in the flow when there is no HTD. A y^+ value of zero corresponds to the location of line H1 in the following plots.

Figure 51 shows the near wall fluid temperature profiles at various z locations of case 3 using CFX and the SST turbulence model.

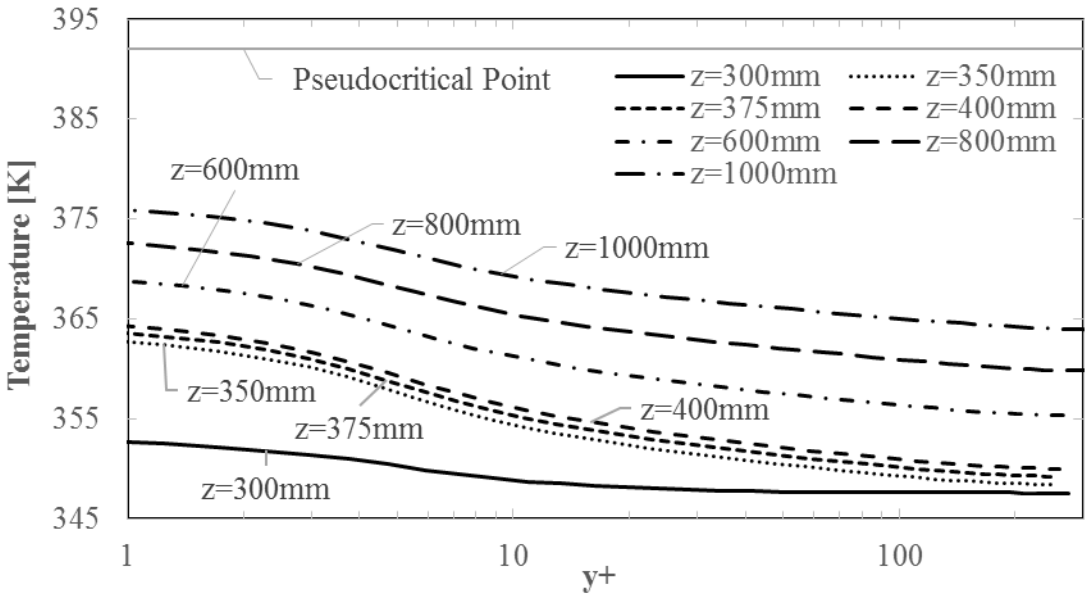

Figure 51: Fluid temperature vs. y+ at various z locations of case 3 using CFX and SST turbulence model. A y+ value of zero corresponds to the location of line H1.

The fluid closest to the heater rod surface gradually increase in temperature as the fluid progresses along z, but the temperature never reaches the pseudocritical temperature. The thermophysical properties of the fluid, therefore, do not change significantly at any location.

Figure 52 shows the near wall fluid density profiles at various z locations of case 3 using CFX and the SST turbulence model.

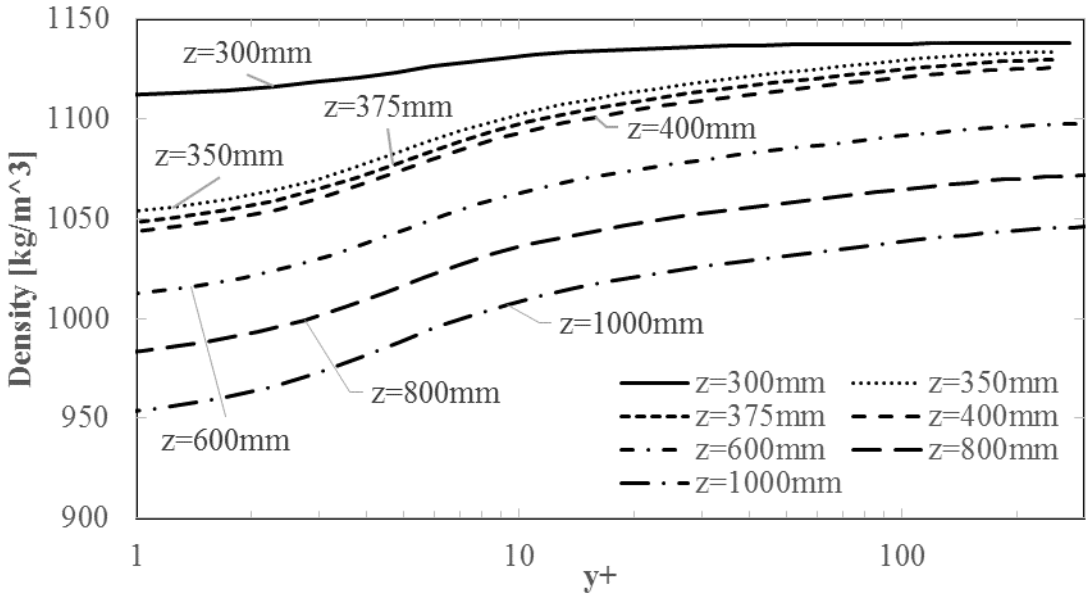

Figure 52: Density vs. y+ at various z locations of case 3 using CFX and SST turbulence model. A y+ value of zero corresponds to the location of line H1.

The density of the fluid decreases as it is heated by the heater rod, but the gradients are not relatively large compared to other cases in the present study that use supercritical fluids.

Figure 53 shows the near wall velocity *w* profiles at various z locations of case 3 using CFX and the SST turbulence model.

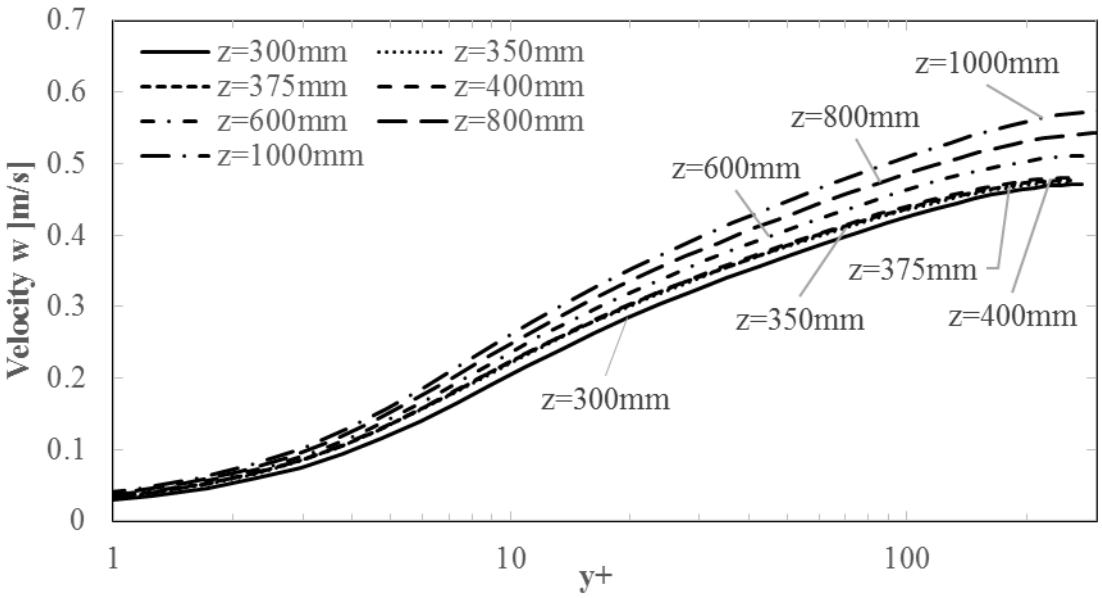

Figure 53: Velocity w vs. y+ at various z locations of case 3 using CFX and SST turbulence model. A y+ value of zero corresponds to the location of line H1.

The velocity *w* profiles at all z locations shown in Figure 53 follow similar trends, and no spikes in velocity *w* in the near wall region occur in this result, or any other case 3 result.

Figure 54 shows the μ_t/μ ratio profiles at various z locations of case 3 using CFX and the SST turbulence model.

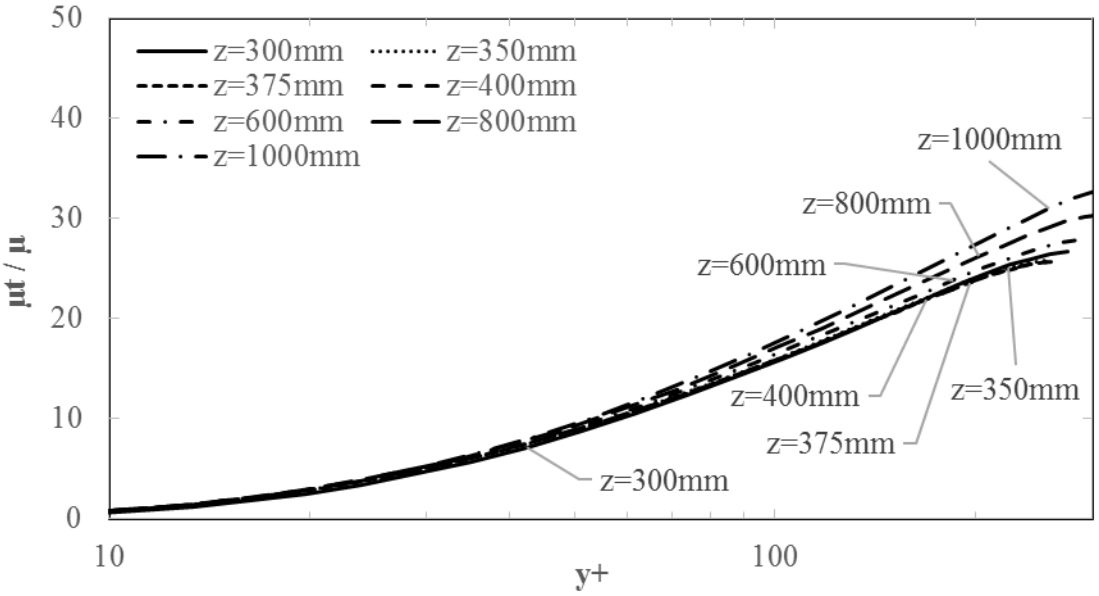

Figure 54: Ratio between eddy viscosity and dynamic viscosity vs. y+ at various z locations of case 3 using CFX and SST turbulence model. A y+ value of zero corresponds to the location of line H1.

The μ_t/μ ratio profiles at all z locations follow a similar trend, and there are no regions where the μ_t/μ ratio suddenly drops to values close to one for y^+ greater than 10.

Figure 55 shows the λ_t/λ ratio profiles at various z locations of case 3 using CFX and the SST turbulence model.

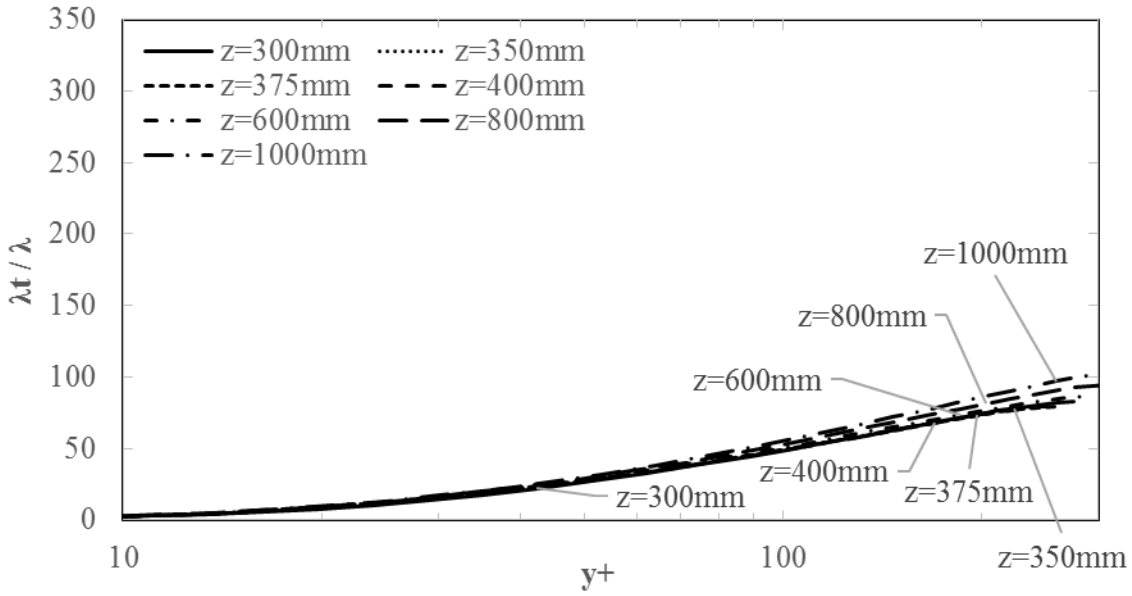

Figure 55: Ratio between turbulent thermal conductivity and thermal conductivity vs. y+ at various z locations of case 3 using CFX and SST turbulence model. A y+ value of zero corresponds to the location of line H1.

The λ_t/λ ratio profiles at all z locations follow a similar trend, and there are no regions where the λ_t/λ ratio suddenly drops to values close to one for y^+ greater than 10.

The trends found in Figures 51 to 55 for the various properties and variables can be found in all case 3 results. There are no large gradients or spikes in solution variables in any of the plots because the fluid does not reach the pseudocritical point.

The numerical data of Zhang et al. and Huang et al. for case 3 of the Richards 2012 Experiments will be compared to the numerical predictions from the present study. The heater rod surface temperatures of Zhang et al. for case 3 are given in Figure 56.

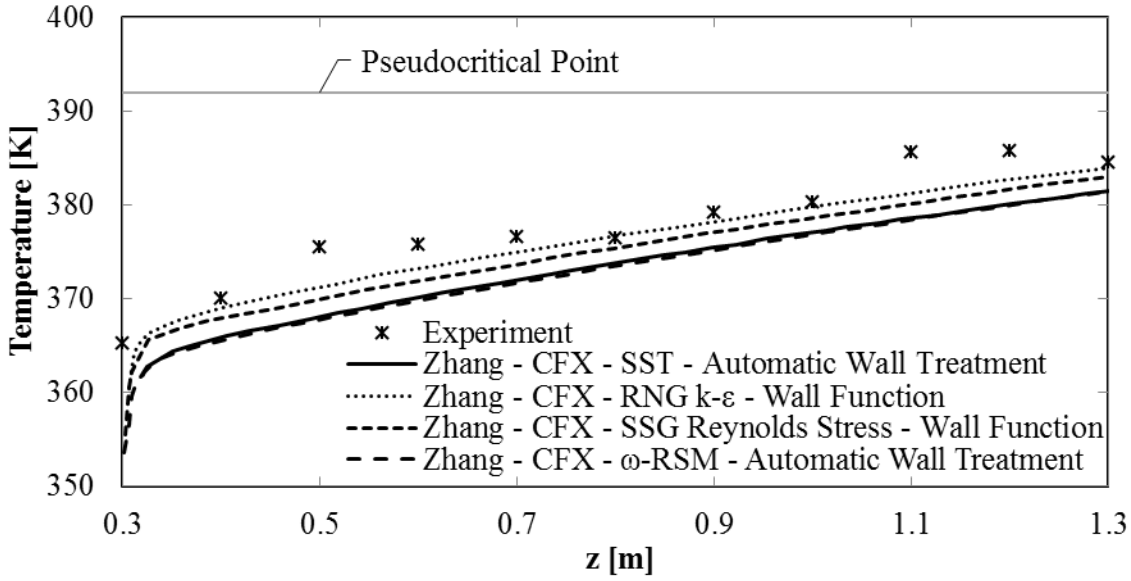

Figure 56: Heater rod surface temperatures from Zhang et al. 2014 for case 3 using CFX various turbulence models.

All heater rod surface temperature profiles from Zhang et al. are relatively similar, with the SST and ω-RSM both under-predicting temperatures. Both the SST and ω-RSM heater rod surface temperature profiles are also very similar.

The heater rod surface temperatures of Huang et al. for case 3 are given in Figure 57. The only turbulence model used by the authors for case 3 was the RSM turbulence model with EWT. They chose this turbulence model for case 3 because they argued that it can account for anisotropic stresses, leading to better prediction of secondary flows in rod bundles.

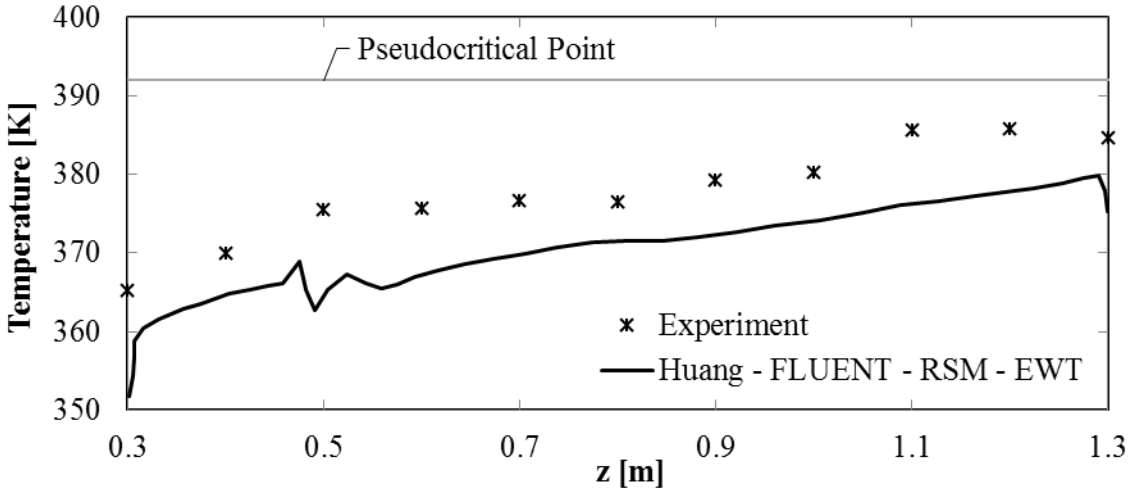

Figure 57: Heater rod surface temperatures from Huang et al. 2014 for case 3 using FLUENT RSM turbulence model.

The small oscillation in heater rod surface temperature that occurs around z = 500 [mm] appears to be purely numerical, is not a result of a phenomena present in the experiment. The fluid at this z location is not close enough to the pseudocritical temperature for there to be any sudden change in fluid properties.

Table 52 gives the $RMS_{RN,T}$ of all the case 3 results from Zhang et al. and Huang et al., in order to show how well each result agrees with the experimental data.

Table 52: $RMS_{RN,T}$ between numerical results of both Zhang et al. 2014 and Huang et al. 2014 and experimental results for case 3.

Case	$RMS_{RN,T}$ [%]
3 Zhang - CFX - SST - Automatic Wall Treatment	25.16
3 Zhang - CFX - RNG k-ε - Wall Function	17.03
3 Zhang - CFX - SSG Reynolds Stress - Wall Function	26.93
3 Zhang - CFX - ω-RSM - Automatic Wall Treatment	30.78
3 Huang - FLUENT - RSM - EWT	42.06

The RNG k-ε turbulence model, used by Zhang et al., gave results that were in better agreement with the case 3 experimental data than the other turbulence models. The RSM turbulence model with EWT gave the largest deviation from the experiments.

Table 53 gives the total pressure drop from the numerical predictions of the present study. The total pressure drop for the experiment was calculated using the difference between the measured outlet and inlet absolute pressures, 4.649 [MPa] and 4.645 [MPa], respectively [71].

Table 53: Total pressure drop from each result for case 3 of the Richards experiments, including the experimental measured value and percentage difference from experiment.

Case	Total Pressure Drop [Pa]	Percentage Difference From Experiment [%]
3 Experiment	4000	-
3 SST CFX	976	75.6
3 k-ε CFX	854	78.6
3 SST FLUENT	976	75.6
3 RNG k-ε FLUENT	1038	74.0
3 Low-Re k-ε Lam-Bremhorst FLUENT	875	78.1
3 Low-Re k-ε Yang-Shih FLUENT	774	80.7

None of the turbulence models predicted the experimental pressure drop very closely. The mesh that was used in the present study did not include spacers, and so if spacers were included, then the pressure drop should increase in value due to the increased frictional forces. This would bring the pressure drop of the numerical cases closer to the experimental value.

5.4.2. Case 2

The numerical results of case 2 of the Richards experiments will be presented here, followed by a comparison with the other numerical results from Zhang et al. and Huang et al.

Figure 58 gives the heater rod surface temperatures of case 2 using CFX and the SST and k-ε turbulence models, FLUENT and the SST turbulence model, and the experimental temperatures along line TC.

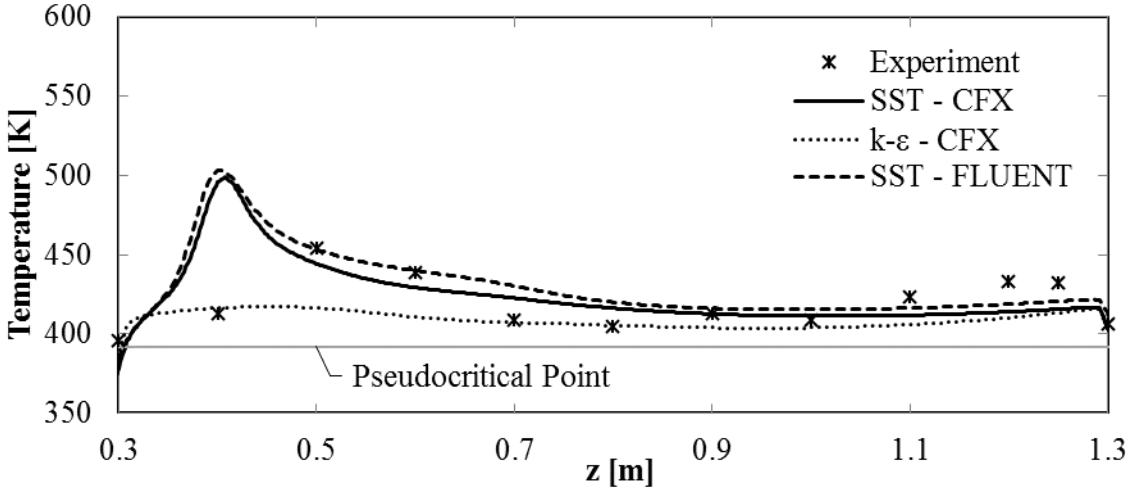

Figure 58: Heater rod surface temperatures along line TC for case 2 using CFX with the SST and k-ε turbulence model, and FLUENT with the SST turbulence model.

A prominent spike in heater rod surface temperature can be seen at z = 400 [mm] in the SST results, but not in the k-ε result. The spike in heater rod surface temperature does appear in the experimental data, although the magnitude of the spike is less than in the SST results and the maximum value of the spike in the experimental data occurs further downstream than in the SST results. The spike in heater rod surface temperature is evidence of HTD. Although the same SST turbulence model is used in both CFX and FLUENT, the FLUENT result tends to slightly over-predict the heater rod surface temperature over the entire length of the heated section.

Figure 59 gives the heater rod surface temperatures of case 2 using FLUENT and the RNG k-ε, Lam-Bremhorst Low-Re k-ε, and Yang-Shih Low-Re k-ε turbulence models, along with the experimental temperatures along line TC.

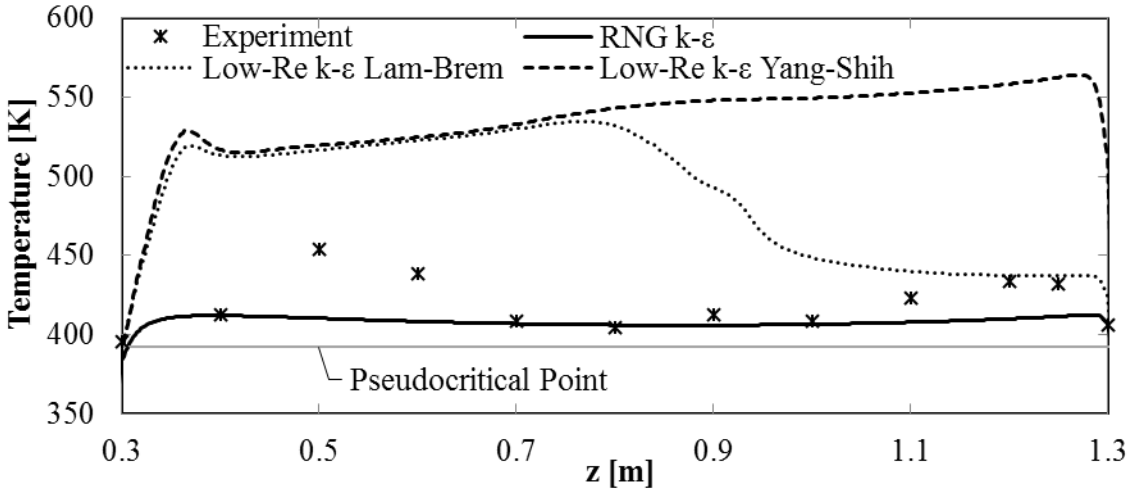

Figure 59: Heater rod surface temperatures line TC for case 2 using FLUENT

A prominent spike and plateau in heater rod surface temperature can be seen at z = 350 [mm] in both the Lam-Bremhorst and Yang-Shih Low-Re k-ε results, but not in the RNG k-ε result. The heater rod surface temperatures of the Lam-Bremhorst Low-Re k-ε result eventually drop back down around z = 800 [mm], while the temperatures of the Yang-Shih Low-Re k-ε result continue to increase until just before the end of the heated section at z = 1300 [mm]. The spike in heater rod surface temperature does appear in the experimental data, although the magnitude of the spike is less than that of the Lam-Bremhorst and Yang-Shih Low-Re k-ε results and the maximum value of the spike in the experimental data occurs further downstream than that of these numerical results.

To quantify the differences between the numerical predictions and experimental results of heater rod surface temperatures for case 2, the $RMS_{RN,T}$ is calculated and presented in Table 54. Equation (113) in Section 4.3 is used to calculate the $RMS_{RN,T}$, where the reference temperatures come from the experimental data.

Table 54: $RMS_{RN,T}$ between numerical results and experimental results for case 2.

Case	$RMS_{RN,T}$ [%]
2 SST CFX	46.28
2 k-ε CFX	30.03
2 SST FLUENT	48.81
2 RNG k-ε FLUENT	32.45
2 Low-Re k-ε Lam-Bremhorst FLUENT	122.87
2 Low-Re k-ε Yang-Shih FLUENT	196.49

The k-ε turbulence model using CFX gave the result that was in the best agreement with the experimental data. The RNG k-ε turbulence model using FLUENT provided the result that was a close second in terms of agreement with the experimental data. The results using the SST turbulence model and CFX and FLUENT gave similar results in terms of their agreement with the experimental data. Both the Low-Re k-ε turbulence models using FLUENT gave results that did very poorly in terms of agreement with the experimental data.

Case 2 using CFX and the SST turbulence model will be used to explain what causes the HTD, seen in Figure 58. Various solution variables and derived quantities are plotted with respect to y^+ in the following figures at different z locations. The y^+ values for the plots were calculated using Equation (34) in Section 3.1.2.1, where Δn is replaced with the wall distance. A y^+ value of zero corresponds to the location of line H1, shown in Figure 42 in Section 5.2, and y^+ increases in value in the negative y direction, normal to the Heater 1 surface. The heater rod surface temperatures along line H1 are nearly identical to those along line TC, which is where the thermocouples are located in the Richards 2012 Experiments. Figure 60 shows the heater rod surface temperatures along lines TC, H1, H2, H3, and H4 for this case. The location of these lines on the x-y plane can be seen in Figure 42 in Section 5.2.

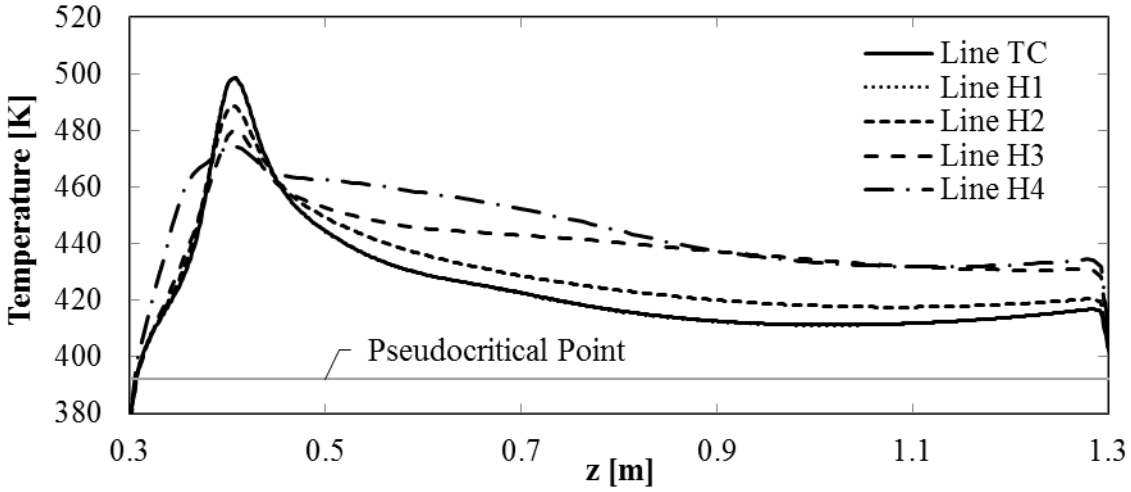

Figure 60: Heater rod surface temperatures along lines TC, H1, H2, H3, and H4 for case 2 using CFX with the SST turbulence model.

As can be seen in the plot, the heater rod surface temperatures along line H1 are identical to line TC. The largest spike in surface temperature also occur along lines H1 and TC, and line H4 experiences the smallest spike in heater rod surface temperature. These spikes in temperature occur at approximately z 400 [mm] for all lines.

Unless otherwise stated, a y^+ value of zero corresponds to the location of line H1 in the following plots. Figure 61 shows the near wall fluid temperature profiles at various z locations of case 2 using CFX and the SST turbulence model.

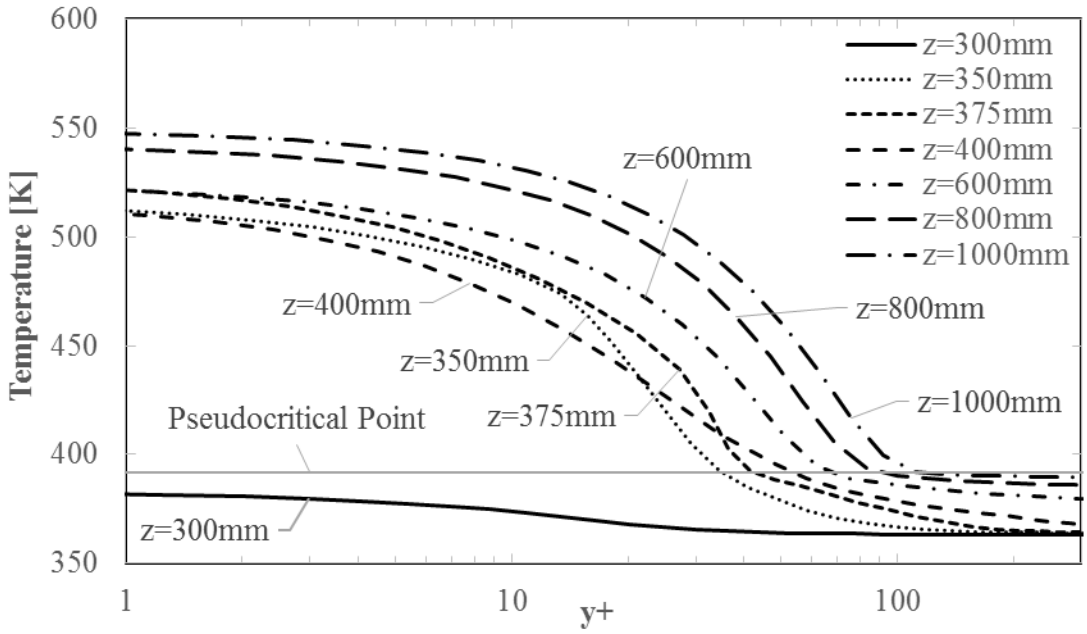

Figure 61: Fluid temperature vs. y+ at various z locations of case 2 using CFX and SST turbulence model. A y+ value of zero corresponds to the location of line H1.

The fluid reaches the start of the heated section at z = 300 [mm] and the fluid closest to the heater rod surface is already at a temperature close to the pseudocritical temperature. This is a result of axial heat conduction into the unheated portions of the heater rods, causing the ends of the unheated sections in contact with the heated sections of the heater rods to increase in temperature. The fluid passing these sections in turn becomes heated before the fluid even reaches the start of the heated sections of the heater rod.

Just after the fluid near the wall begins to be heated by the heater rod surface at z = 350 [mm], the fluid closest to the heater rod surface increases beyond the pseudocritical temperature. As the fluid progresses down the heater rod, the bulk of the fluid progressively increases in temperature, since the y^+ location where the fluid reaches the pseudocritical temperature gradually increases from y^+ = 35 at z = 350 [mm] to y^+= 110 at z = 1000 [mm].

Figure 62 shows the near wall fluid density profiles at various z locations of case 2 using CFX and the SST turbulence model.

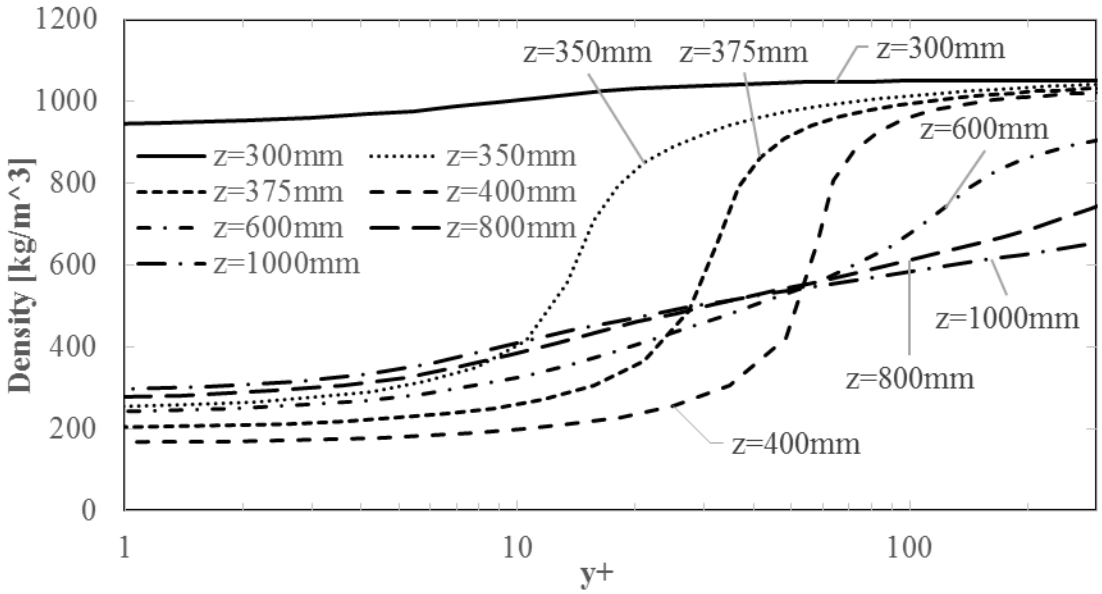

Figure 62: Density vs. y+ at various z locations of case 2 using CFX and SST turbulence model. A y+ value of zero corresponds to the location of line H1.

Looking at the density profile at z = 350 [mm], the density of the fluid closest to the heater rod surface decreases significantly in relation to the freestream density because the temperature of the fluid exceeds the pseudocritical temperature in the region closest to the heater rod surface at this z location. As was already seen in Figure 61, the temperature of the fluid away from the heater rod surface gradually increases past the pseudocritical temperature as the fluid progresses in the z direction and causes a region of very low density that increases in size in the y direction, away from the wall.

The large density gradients, seen at z = 350, 375, and 400 [mm], gradually reduce in magnitude as the fluid progresses along z, as the heat from the heater rod is transferred towards the freestream resulting in an increased temperature in this region, which in turn results in a decrease

in density. This decrease in density in the freestream, along with the resulting increase in density after the large spike in temperature after z = 400 [mm] combines to lessen the density gradients between the near wall region and the freestream.

Figure 63 shows the near wall velocity *w* profiles at various z locations of case 2 using CFX and the SST turbulence model.

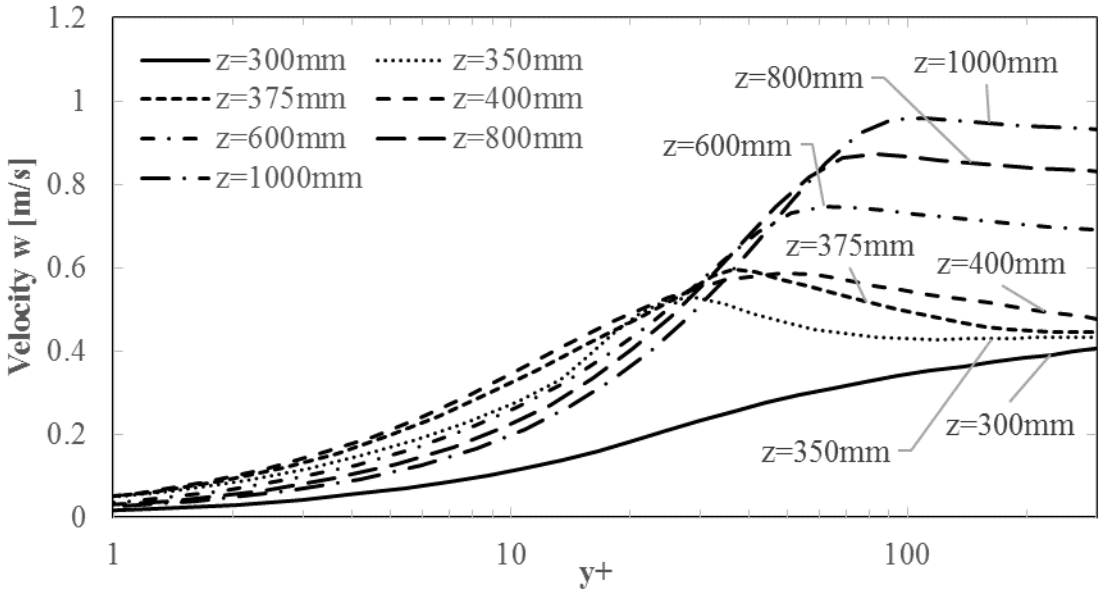

Figure 63: Velocity w vs. y+ at various z locations of case 2 using CFX and SST turbulence model. A y+ value of zero corresponds to the location of line H1.

The velocity profile of the fluid at the start of the heated section, at z = 300 [mm], appears to follow the log law of the wall. This is where there is a viscous sublayer adjacent to the wall, and a log law region away from the wall that is separated from the viscous sublayer by a buffer layer. The log law of the wall was derived assuming constant thermophysical properties, such as density, and therefore should not apply to cases with significant differences in thermophysical properties, such as the cases presented in the present study.

As the density of the fluid in the near wall region decreases, the effects of buoyancy become apparent: the low density fluid close to the wall at z = 350 [mm] accelerates upwards, as shown by the spike in velocity w at y^+ = 29. The high density fluid in the freestream maintains its velocity since the density in this region does not change significantly. As the temperature of the fluid further away from the wall increases as the fluid progresses in the z direction, the velocity of the fluid in the freestream increases, since the density decreases with these increasing temperatures.

Similar trends in the velocity w profiles can be found at other locations in the fluid domain. The velocity w profiles at z = 400 [mm] for locations H1, H2, H3, and H4 are plotted with respect to wall distance in Figure 64.

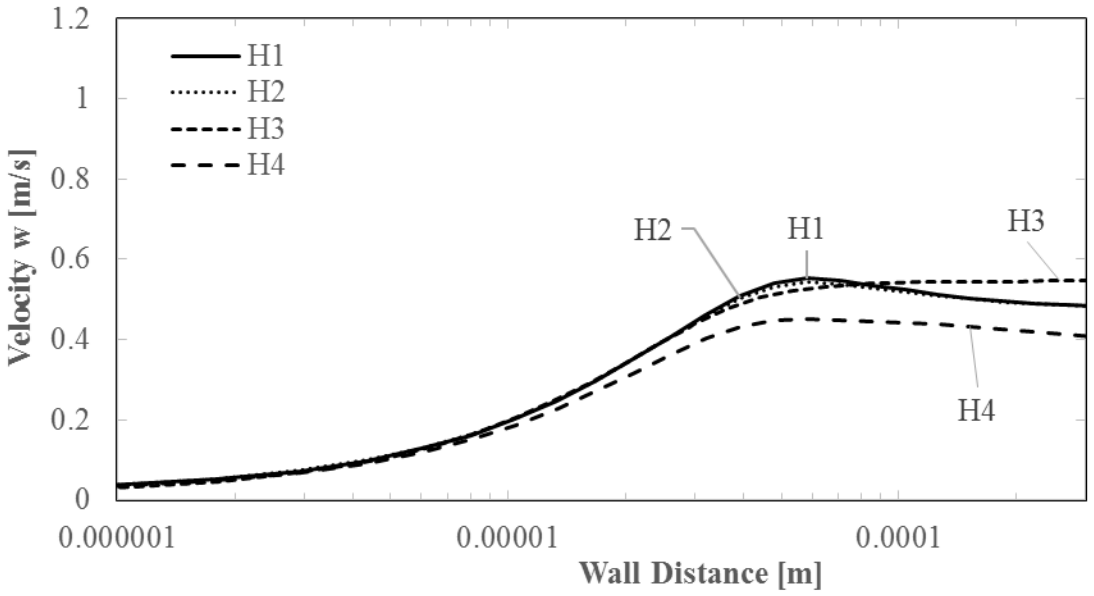

Figure 64: Velocity w profiles at z = 400 [mm] for case 2 using SST and CFX at locations H1, H2, H3, and H4.

The velocity profiles are nearly identical for H1 and H2, and the spike in velocity w at H3 is slightly less than the spike at H1 and H2. The smallest spike in velocity w occurs at H4. These

trends coincide with the heater rod surface temperature profiles along z, given in Figure 60, where the largest spike in heater rod surface temperature occur around z = 400 [mm] at H1, followed by H2, H3, and finally H4, in descending order.

Similar trends in the velocity *w* profile can be found in cases that have a spike in heater rod surface temperature, and are absent from cases without spikes in heater rod surface temperatures. The velocity *w* profiles at z = 400 [mm] for all case 2 results are given in Figure 65.

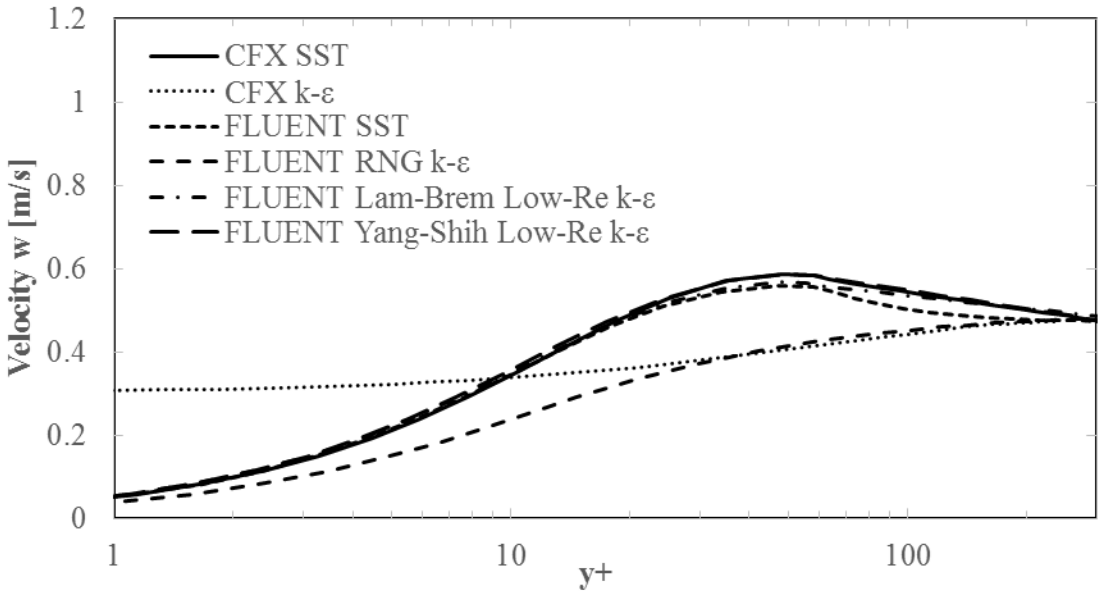

Figure 65: Velocity w vs. y+ at z = 400 [mm] for all case 2 results. A y+ value of zero corresponds to the location of line H1.

For cases with spikes in heater rod surface temperature, the velocity *w* profile just before or at the same z location as the temperature spike also shows a spike in velocity *w* in the near wall region. This occurs for the SST results using both CFX and FLUENT, as well as the Lam-Bremhorst and Yang-Shih Low-Re k-ε turbulence results using FLUENT. A spike in velocity *w* is not present in the near wall region for cases that do not have spikes in heater rod surface temperature. These are the k-ε results using CFX and the RNG k-ε result using FLUENT.

The velocity w of the k-ε case does not decrease in value close to the wall, such as for the other cases. The reason for this is that the k-ε turbulence model, when implemented with CFX, relies on scalable wall functions to determine the velocity in this near wall region. The turbulence model uses Equation (66) in Section 3.1.3.1 to determine the non-dimensional velocity in the near wall region as a function of the non-dimensional wall distance, y^*_{Scale}. However the value of the non-dimensional wall distance can never be less than 11.06 according to Equation (63) in Section 3.1.3.1. This means the velocity can never be less than the value of the velocity at y^*_{Scale} = 11.06. This non-dimensional wall distance, y^*_{Scale}, is closely related to non-dimensional wall distance used in the plots, y^+, since they are both functions of wall distance and fluid properties.

Similarly, the non-dimensional temperature in the near wall region is a function of the non-dimensional wall distance, as seen in Equation (66) in Section 3.1.3.1, and so the fluid temperature can never be less than the temperature at y^*_{Scale} = 11.06. The greatest fluid temperature gradients occur close to the wall, as can be seen in the plot of fluid temperature at various z locations using CFX and the SST turbulence model, Figure 61. Because scalable wall functions, used by the k-ε turbulence model, do not allow the fluid temperature to vary in this region close to the wall, the wall temperature cannot experience sudden increases in temperature that would be evident by large temperature gradients in the fluid in the region close to the wall.

He et al. [65] performed an in-depth numerical analysis on vertically oriented heated tubes with supercritical CO_2, and found that HTD, or spikes in surface temperature, were caused by flow laminarization. They used RANS turbulence models and compared their results with the DNS data of Bae et al. [64].

Buoyancy had the strong effect of producing high velocity gradients very close to the wall, which causes the velocity profile to flatten further away from the wall. The high velocity gradients were caused by a region of low density fluid very close to wall accelerating upwards faster than the higher density fluid in the region further away from the wall. The flattened velocity profile in the region away from the wall leads to a reduction in shear stress. Shear stress plays a dominant role in the Reynolds stresses, $\rho\overline{u_i u_j}$, and turbulence production, P_k, as can be seen in the equation for Reynolds stresses, Equation (3) in Section 3.1.1, and turbulence production due to viscous forces, Equation (26) in Section 3.1.2. Therefore, a reduction in shear stress leads to a reduction in turbulence. He et al. refers to this reduction in turbulence as flow laminarization.

Velocity w profiles from this study show large gradients very close to the wall, as evident by the initial spike in velocity, followed by a flattened velocity profile away from the wall. These trends match those described by He et al. The reduction in turbulence, caused by the reduced shear stress, can be seen by observing the eddy viscosity in the near wall region.

Profiles for the ratio between eddy viscosity and dynamic viscosity, μ_t/μ, at various z locations of case 2 using CFX and the SST turbulence model are shown in Figure 66.

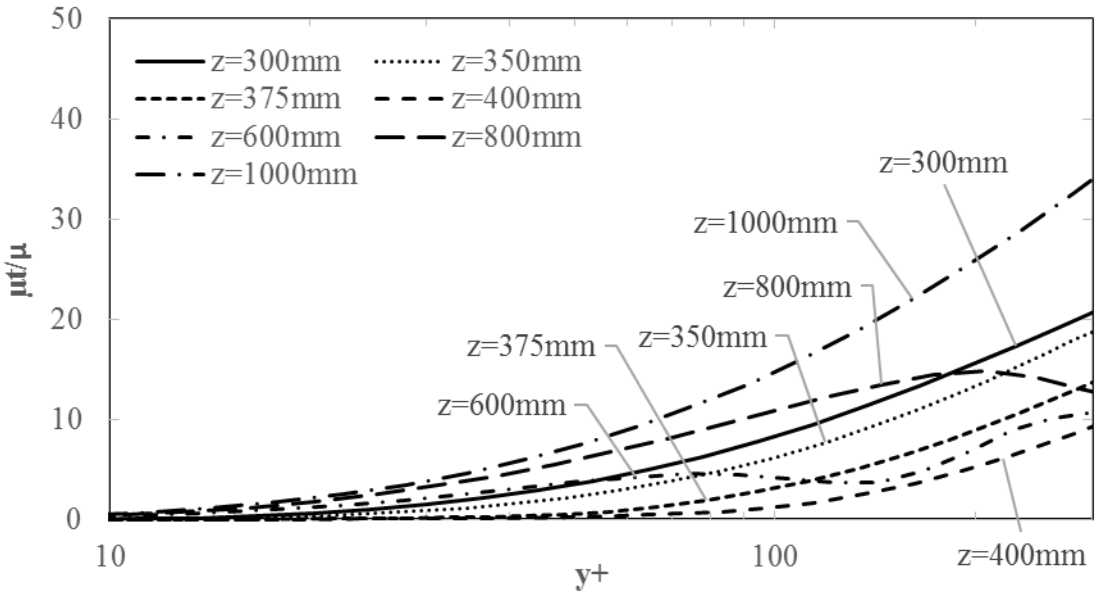

Figure 66: Eddy viscosity to dynamic viscosity ratio vs. y+ at various z locations of case 2 using CFX and SST turbulence model. A y+ value of zero corresponds to the location of line H1.

This ratio can be used to determine the strength of turbulence at any location. For a laminar flow, μ_t/μ should be less than one, and for flows with strong turbulence, μ_t/μ should be much greater than one. When the flow reaches the start of the heated section, the value of μ_t/μ is one at y^+ = 25. The values of μ_t/μ increase away from the wall and towards the freestream. One way to look at this is that the flow is close to laminar at y^+ = 25, and becomes more turbulent towards the freestream. The μ_t/μ values decrease in general as the flow progresses along z to the point where, at z = 400 [mm], the value of μ_t/μ is 1.1 at y^+ = 97. This means that a larger region of near-laminar flow is present at z = 400 [mm] than at any other z location. As can be seen in Figure 58, the spike in heater rod surface temperature for this case occurs around z = 400 [mm], which corresponds to the same z location as where the largest region of near-laminar flow occurs. As flow progresses past z = 400 [mm], the values of the μ_t/μ ratio increase, corresponding to the spike in heater rod surface temperature diminishing.

Further evidence that the μ_t/μ ratio and, more importantly the eddy viscosity, affects the heater rod surface temperature can be seen from Figure 67, which shows profiles of the turbulent thermal conductivity to thermal conductivity ratio, λ_t/λ, at various z locations of case 2 using CFX with the SST turbulence model.

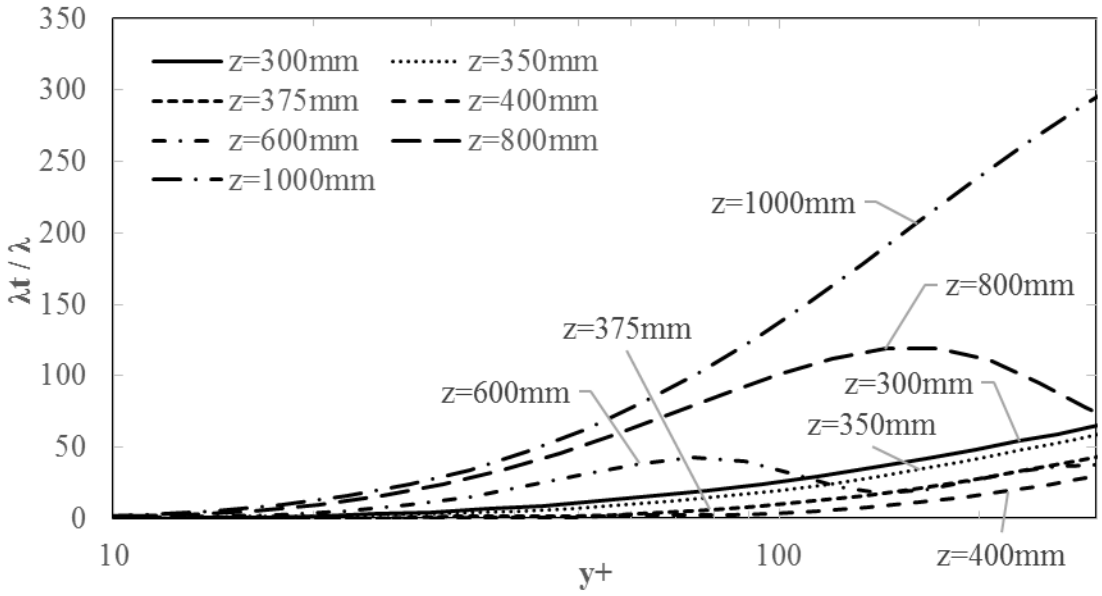

Figure 67: Turbulent thermal conductivity to thermal conductivity ratio vs. y+ at various z locations of case 2 using CFX and SST turbulence model. A y+ value of zero corresponds to the location of line H1.

The turbulent thermal conductivity, λ_t, is defined by Equation (14) in Section 3.1.1 and can be used as an indicator of the contribution to heat transfer by turbulence effects. The equation for λ_t includes the eddy viscosity, specific heat capacity at constant pressure, and the turbulent Prandtl number. The turbulent Prandtl number is a constant value, so only the eddy viscosity and specific heat capacity at constant pressure affect the value of the turbulent thermal conductivity. For a laminar flow, λ_t/λ should be less than approximately one, and for flows with strong turbulence, λ_t/λ should be much greater than one. Looking at the governing equations for energy used by CFX and FLUENT, Equation (10) and (11) in Section 3.1.1, respectively, it can be seen that a

fluid should conduct heat much better when the λ_t/λ ratio is much greater than one. This is because the turbulent thermal conductivity acts in the same way as the thermal conductivity in conducting heat. When the λ_t/λ ratio is less than approximately one, the flow is close to laminar and heat conduction through the fluid would be less than if the λ_t/λ ratio was greater.

The λ_t/λ profiles at the various z locations, as shown in Figure 67 follow the same trend as the μ_t/μ profiles at the same z locations, as shown in Figure 66. This trend indicates that the eddy viscosity has a direct effect on the turbulent thermal conductivity, and the ability of the fluid to conduct heat. The largest region of near-laminar fluid exists at z = 400 [mm] in the near wall region. The eddy viscosity in this region is very low, leading to a very low turbulent thermal conductivity, which reduces the ability of the fluid to conduct heat. This region of fluid with a low thermal conductivity effectively acts as an insulator, causing the adjacent heater rod surface temperature to spike in temperature, as the heat from the heater rod cannot be transferred to the fluid as easily as in other regions where the fluid does not have such large regions of near-laminar fluid.

The λ_t/λ profiles at z = 400 [mm] at locations H1, H2, H3, and H4 are plotted with respect to wall distance in Figure 68.

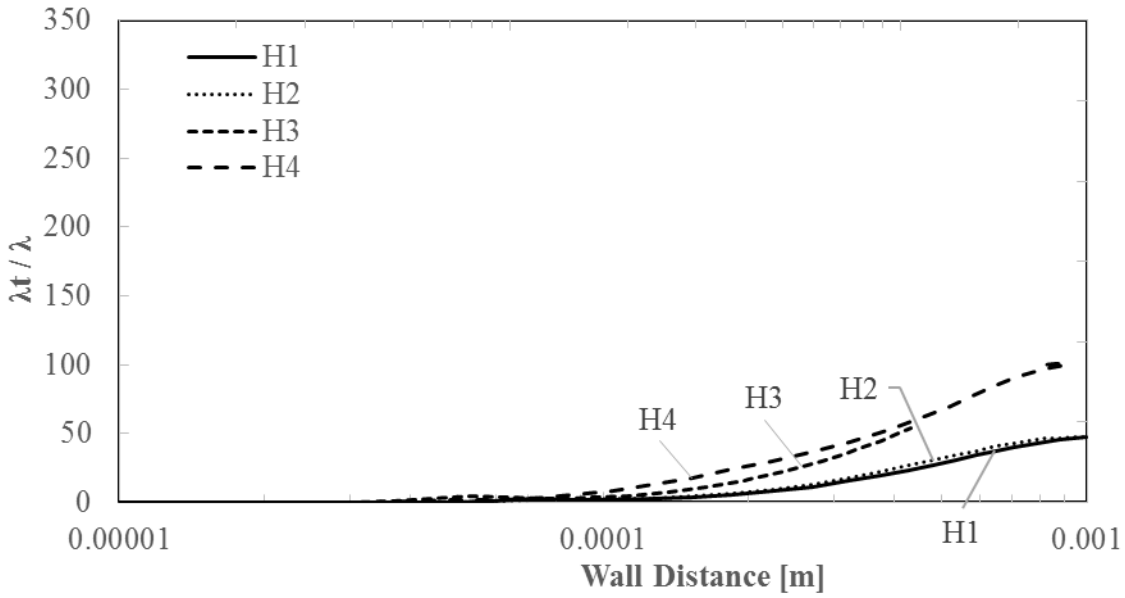

Figure 68: Turbulent thermal conductivity to thermal conductivity ratio profiles at z = 400 [mm] for case 2 using SST and CFX at locations H1, H2, H3, and H4.

As can be seen in the figure, the λ_t/λ values are small in the near wall region for all locations at z = 400 [mm]. These small values of λ_t/λ correspond to the z location where spikes in heater rod surface temperature occur, as can be seen in the heater rod surface temperature profiles along z, given in Figure 60. The largest spike in heater rod surface temperature occurs at line H1, followed by H2, H3, and finally H4, in descending order. Correspondingly, the λ_t/λ values are smallest for H1, followed by H2, H3, and finally H4, in ascending order.

and the spike in velocity w at H3 is slightly less than the spike at H1 and H2. The smallest spike in velocity w occurs at H4. These trends coincide with the heater rod surface temperature profiles along z, given in Figure 60, where the largest spike in heater rod surface temperature occur around z = 400 [mm] at H1, followed by H2, H3, and finally H4. The greater the spike in surface temperature, the greater the region of fluid with small λ_t/λ values.

The λ_t/λ profiles at various z locations of case 2 using FLUENT and both the Lam-Bremhorst and Yang-Shih Low-Re k-ε turbulence models are given by Figure 69 and Figure 70, respectively. The y^+ values corresponding to the midpoint of the flow channel of these cases at z = 300 [mm] is 256 and 244, respectively. The y^+ values at the midpoint further downstream are larger, and so it appears as though the profiles end prematurely z = 300 [mm].

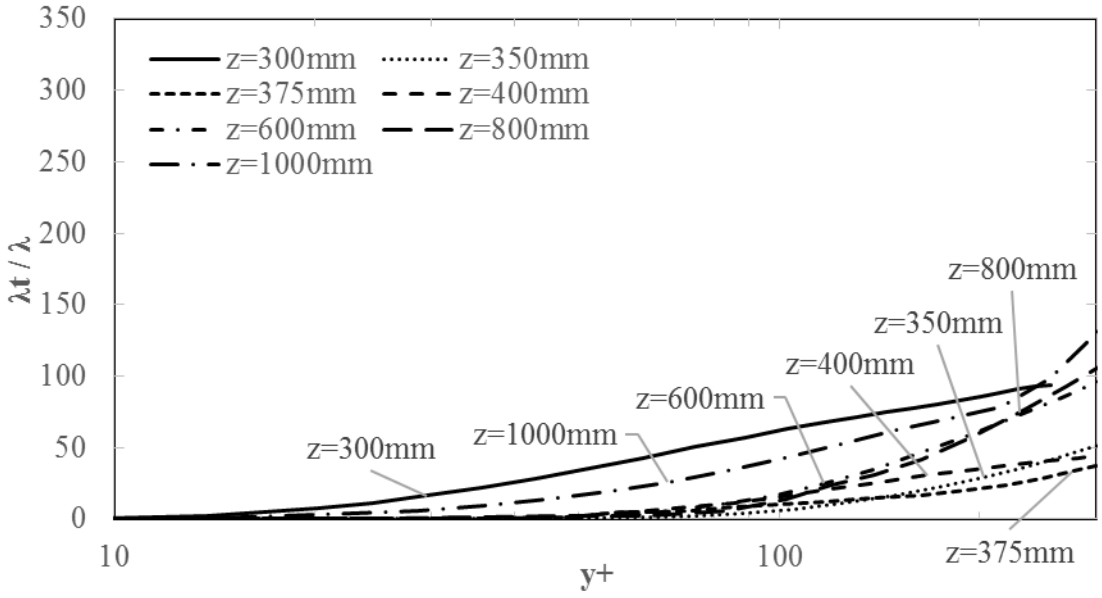

Figure 69: Turbulent thermal conductivity to thermal conductivity ratio vs. y+ at various z locations of case 2 using FLUENT and Lam-Bremhorst Low-Re k-ε turbulence model. A y+ value of zero corresponds to the location of line H1.

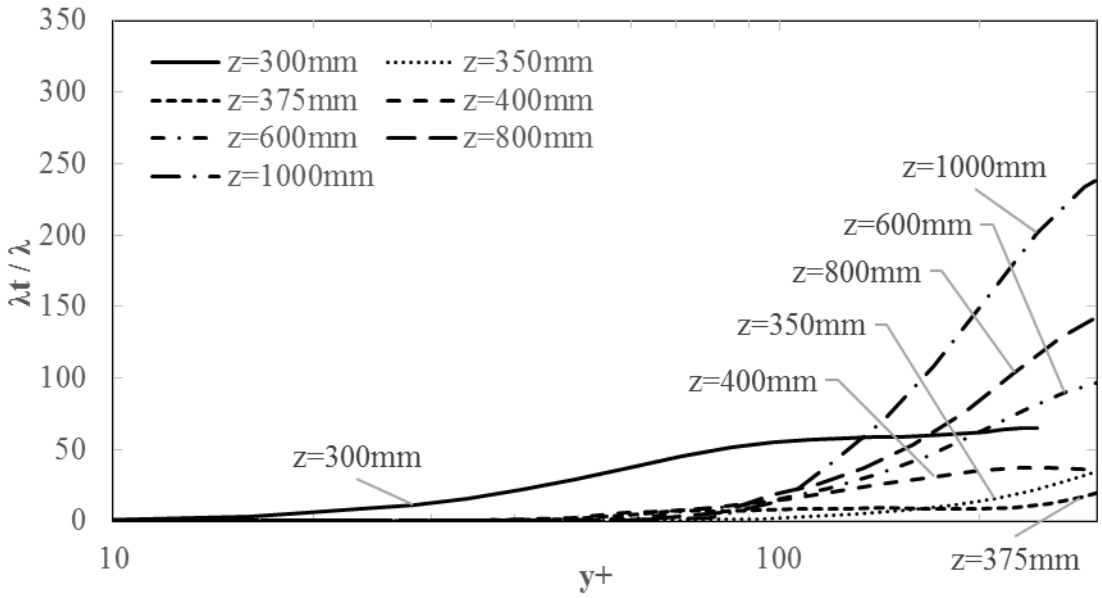

Figure 70: Turbulent thermal conductivity to thermal conductivity ratio vs. y+ at various z locations of case 2 using FLUENT and Yang-Shih Low-Re k-ε turbulence model. A y+ value of zero corresponds to the location of line H1.

For both the Lam-Bremhorst and Yang-Shih result, the heater rod surface temperature spikes around z = 350 [mm], as shown in Figure 59. This is the same z location where the largest region of fluid in which the λ_t/λ ratio is less than approximately one in the near wall region. The near-laminar region of the Lam-Bremhorst result in the near wall region shrinks at z = 1000 [mm], which corresponds to much lower heater rod surface temperatures. The heater rod surface temperatures of the Yang-Shih result do not drop until just before the end of the heated section, but there is no z location in Figure 70 that corresponds to this location.

Neither the k-ε result using CFX nor the RNG k-ε result using FLUENT show a large spike in heater rod surface temperature for case 2, as can be seen in Figure 58 and Figure 59, respectively. The profiles of the λ_t/λ ratio at various z locations for the k-ε result using CFX and the RNG k-ε result using FLUENT are given by Figure 71 and Figure 72, respectively.

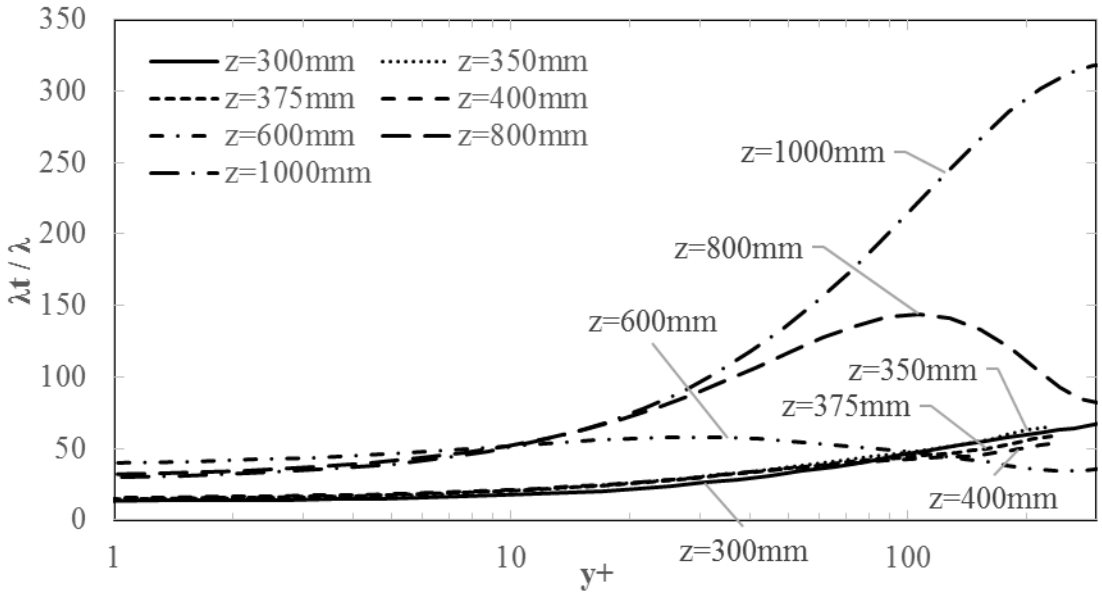

Figure 71: Turbulent thermal conductivity to thermal conductivity ratio vs. y+ at various z locations of case 2 using CFX and k-ε turbulence model. A y+ value of zero corresponds to the location of line H1.

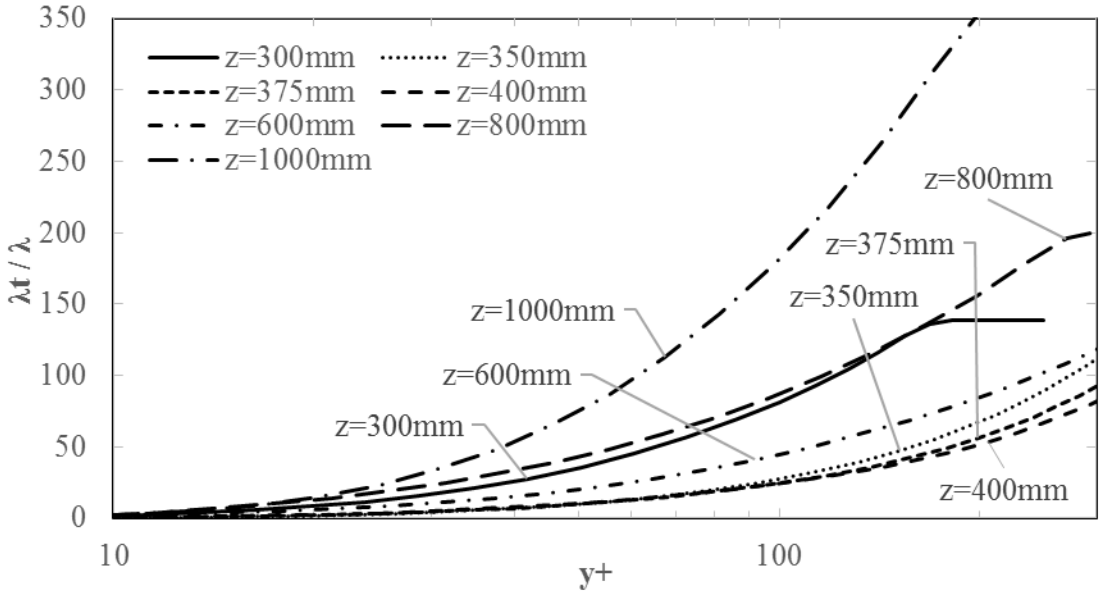

Figure 72: Turbulent thermal conductivity to thermal conductivity ratio vs. y+ at various z locations of case 2 using FLUENT and RNG k-ε turbulence model. A y+ value of zero corresponds to the location of line H1.

For the k-ε result using CFX, the λ_t/λ ratio never drops below 13. This means turbulence effects are always present in the heat transfer of this case. The lack of a spike in heater rod surface temperature is therefore expected, as there is no near-laminar region in the fluid that would act as an insulator.

For the RNG k-ε result using FLUENT, the λ_t/λ ratio has a value of 1.1 at y^+ = 16 at the z = 350 [mm] axial location. The near-laminar region at z = 350 [mm] is therefore confined to a much smaller region for this RNG k-ε result than for the results with spikes in heater rod surface temperature. The fluid therefore does not effectively act as an insulator due to this small region of near-laminar fluid.

The λ_t/λ ratio is directly related to the μ_t/μ ratio and more importantly the eddy viscosity. Each of the turbulence models used in the present study calculates the turbulence kinetic energy, k, and either the turbulence dissipation rate, ε, or the specific turbulence dissipation, ω, in order to calculate the eddy viscosity, μ_t. In the near wall region the various wall treatments: automatic wall treatment, scalable wall functions, and EWT, are the dominant factor that determine the profiles of the velocity, temperature, turbulence kinetic energy, and either the turbulence dissipation rate, or the specific turbulence dissipation. The governing equations of the turbulence quantities (k, ω, ε, and μ_t) and wall treatments differ between the various turbulence models, and the values of various coefficients of these equations may also differ. It is because of these differences in the way each turbulence model and the associated wall treatment calculate the eddy viscosity and solution variables in the near wall region that the λ_t/λ ratio differs between the results of each turbulence model, and the reason why certain turbulence models give spikes in heater rod surface temperature.

He et al. [65] compared numerical results obtained from RANS turbulence models with those obtained from DNS, and found that RANS turbulence models are not able to accurately model the turbulent heat flux, $\lambda_t \frac{\partial T}{\partial x_j}$. They attributed some of the inaccuracies of RANS turbulence models to using a constant turbulent Prandtl number for the turbulence thermal conductivity, λ_t.

The numerical data of Zhang et al. and Huang et al. for case 2 of the Richards 2012 Experiments will be compared to the numerical data from the present study. The heater rod surface temperatures of Zhang et al. for case 2 are given in Figure 73.

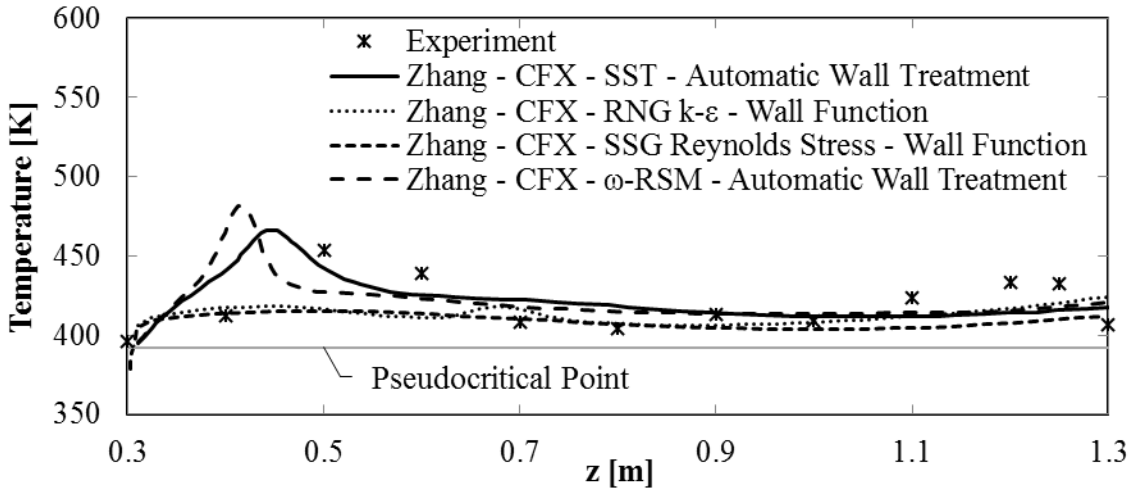

Figure 73: Heater rod surface temperatures from Zhang et al. 2014 for case 2 using CFX various turbulence models.

Both the SST and ω-RSM turbulence models gave spikes in heater rod surface temperatures, similar to the spikes found in the present study for the SST turbulence model. The temperature spike from the ω-RSM result is greater in magnitude and occurs over a shorter z range than the spike from the SST result. Both the RNG k-ε and the SSG Reynolds Stress turbulence models under-predicted the spike heater rod surface temperature found in the experimental data, similar to the k-ε and RNG k-ε turbulence model result from the present study.

The heater rod surface temperatures of Huang et al. for case 2 are given in Figure 74.

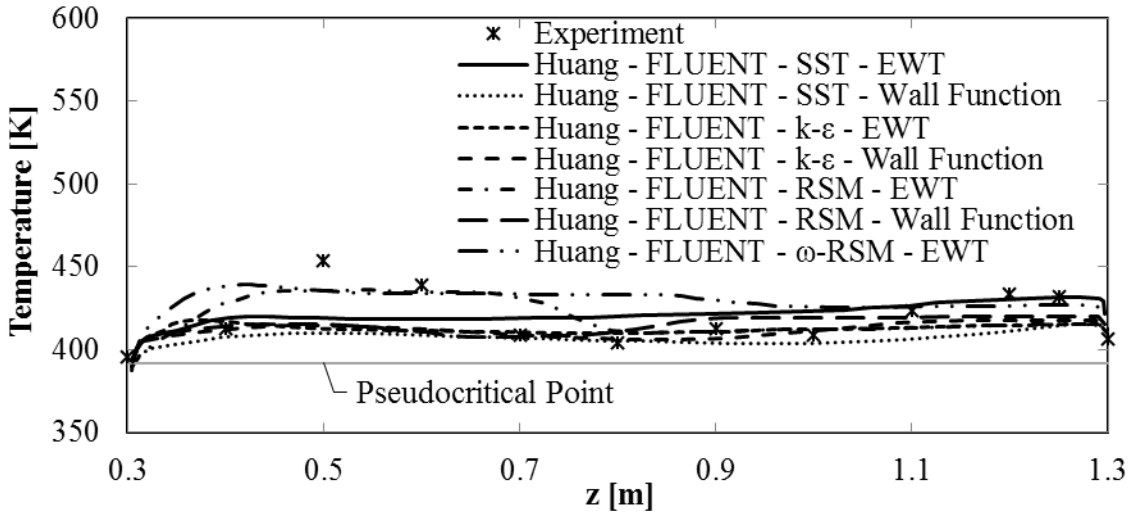

Figure 74: Heater rod surface temperatures from Huang et al. 2014 for case 2 using FLUENT and various turbulence models.

The ω-RSM and RSM, both using EWT, are the only turbulence models that produced a slight increase heater rod surface temperature near the inlet. The SST turbulence model, using both EWT and wall functions, did not produce a spike in heater rod surface temperature. This is surprising, given that the SST results of the present study and Zhang et al. all give a spike in heater rod surface temperature.

The RSM results of Huang et al. gave similar results as the SSG results of Zhang et al., where no spike in heater rod surface temperature was observed.

Table 55 gives the $RMS_{RN,T}$ of all the case 2 results from Zhang et al. and Huang et al., in order to show how well each result agrees with the experimental data.

Table 55: $RMS_{RN,T}$ between numerical results of both Zhang et al. 2014 and Huang et al. 2014 and experimental results for case 2.

Case	$RMS_{RN,T}$ [%]
2 Zhang - CFX - SST - Automatic Wall Treatment	24.81
2 Zhang - CFX - RNG k-ε - Wall Function	27.95
2 Zhang - CFX - SSG Reynolds Stress - Wall Function	33.49
2 Zhang - CFX - ω-RSM - Automatic Wall Treatment	34.52
2 Huang - FLUENT - SST - EWT	26.42
2 Huang - FLUENT - SST – Wall Function	31.80
2 Huang - FLUENT - k-ε - EWT	28.71
2 Huang - FLUENT - k-ε – Wall Function	26.77
2 Huang - FLUENT - RSM - EWT	22.30
2 Huang - FLUENT - RSM – Wall Function	27.44
2 Huang - FLUENT - ω-RSM - EWT	29.48

The results that gave the lowest $RMS_{RN,T}$ from Zhang et al. and Huang et al. used the SST turbulence model and automatic wall treatment, and the RSM turbulence model with EWT, respectively. The ω-RSM turbulence model with automatic wall treatment gave results that were in the worst agreement with experimental data.

Looking at the $RMS_{RN,T}$ results for Huang et al., the SST and RSM turbulence models with EWT gave better predictions of experimental data than when the turbulence models were used with wall functions. The opposite holds true for the k-ε turbulence model, where a better prediction of results was obtained when the turbulence model was used with wall functions than when it was used with EWT.

Figure 75 shows the numerical results of Zhang et al., Huang et al. and the present study for case 2 when using the SST turbulence model.

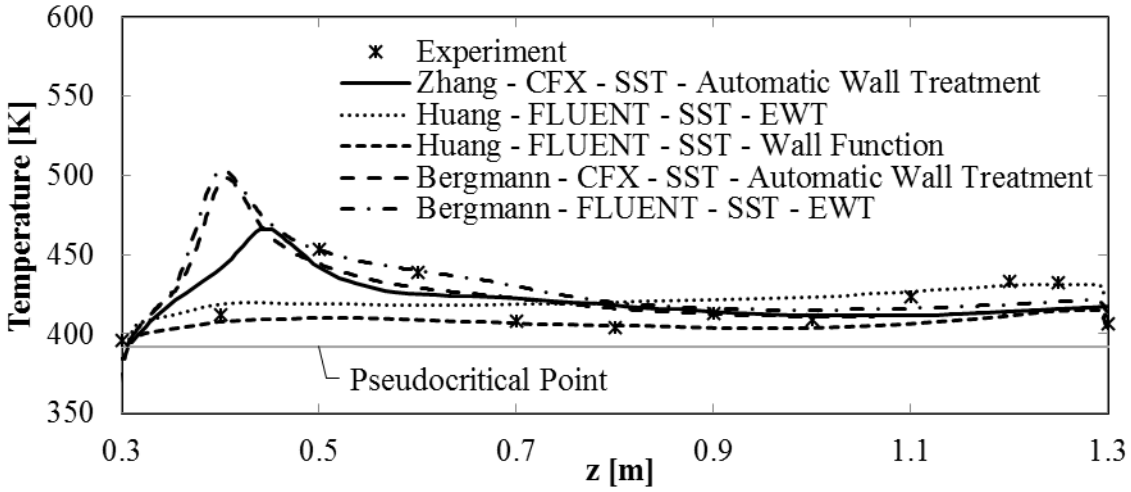

Figure 75: Heater rod surface temperatures from Zhang et al. 2014 and Huang et al. 2014 vs. results from the present study using SST, for case 2.

The largest spike in heater rod surface temperature was observed for both SST results from the present study. This spike occurred at a lower z location than both the Zhang et al. and the experimental result. A spike in surface temperature is not present in either of the Huang et al. SST results that used EWT and wall functions.

This present study found that using the SST turbulence model with both CFX and FLUENT gave similar heater rod surface temperature results, yet both Zhang et al. and Huang et al. gave heater rod surface temperature results that were very different. This is surprising, since Zhang et al. used CFX and Huang et al. used FLUENT, the same software used for this study.

One variable that could alter numerical predictions of heater rod surface temperatures is the turbulent Prandtl number, Pr_t, because of its presence in the equation of the turbulent thermal conductivity, λ_t (Equation (14) in Section 3.1.1), which has been shown to be related to the spikes in heater rod surface temperature. The value Pr_t was set at 0.85 for the Zhang et al. cases. Huang et al. set Pr_t to 0.85 in the freestream and either to 0.85 or 1.0 in the near wall region. The

value of Pr_t used in the present study was 0.9. When the value of Pr_t increases, λ_t should decrease, leading to greater values in heater rod surface temperature. Similarly, when the value of Pr_t decreases, λ_t should increase, leading to smaller values in heater rod surface temperature, which could explain the Zhang et al. result. To test this hypothesis, another CFX run was performed in which Pr_t was set to 0.85, the same value used by Zhang et al. The heater rod surface temperatures are plotted in Figure 76 for this case, the case using CFX and Pr_t set to 0.9, and the Zhang et al. case. Table 56 gives the $\mathrm{RMS}_{\mathrm{RN,T}}$ for these three cases.

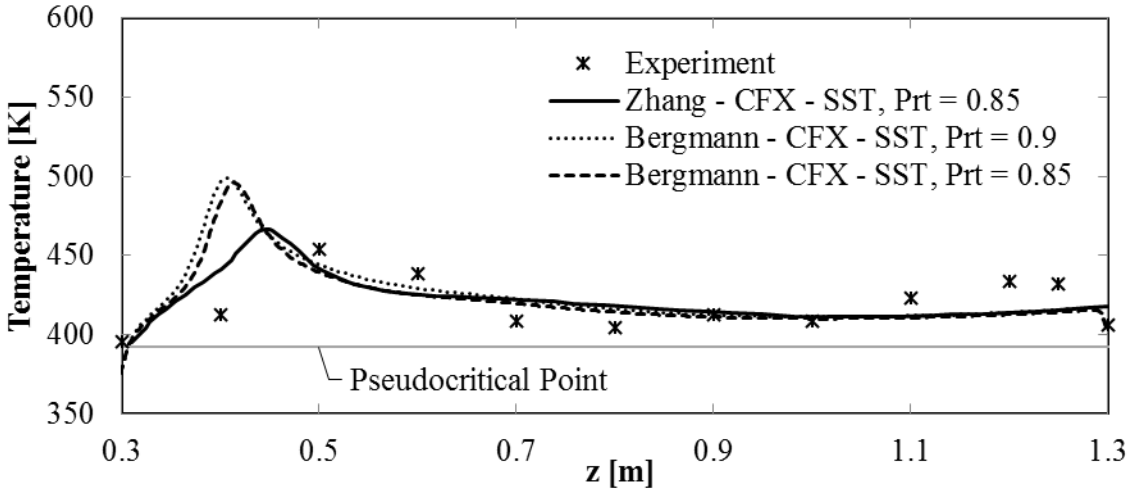

Figure 76: Heater rod surface temperatures of case 2 CFX runs using different turbulent Prandtl numbers.

Table 56: $\mathrm{RMS}_{\mathrm{RN,T}}$ between numerical results of Zhang et al. 2014 and the present study, and experimental results for case 2 using CFX and different turbulent Prandtl numbers.

Case	$\mathrm{RMS}_{\mathrm{RN,T}}$ [%]
2 Zhang - CFX - SST - Pr_t = 0.85	24.81
2 Bergmann – CFX – SST - Pr_t = 0.9	46.28
2 Bergmann – CFX – SST - Pr_t = 0.85	41.14

Comparing the two runs performed for this study that use different values of Pr_t, the case with the smaller Pr_t, 0.85, has a slightly lower maximum heater rod surface temperature, and either lower or nearly identical heater rod surface temperatures over most of the heated section. The case from the present study with the lower Pr_t more closely predicts the experimental heater rod surface temperatures, since the $\mathrm{RMS}_{\mathrm{RN,T}}$ drops from 46.3 % to 41.1 % when the Pr_t is reduced from 0.9 to 0.85. Changing the Pr_t to the same value used by Zhang et al. does not result in the same heater rod surface temperatures being predicted.

To test the hypothesis that smaller values of Pr_t lead to increasing values of λ_t and smaller values in heater rod surface temperature, the λ_t/λ ratio is plotted in Figure 77 at z = 350 and 400 [mm] for the two cases of this study that use different Pr_t.

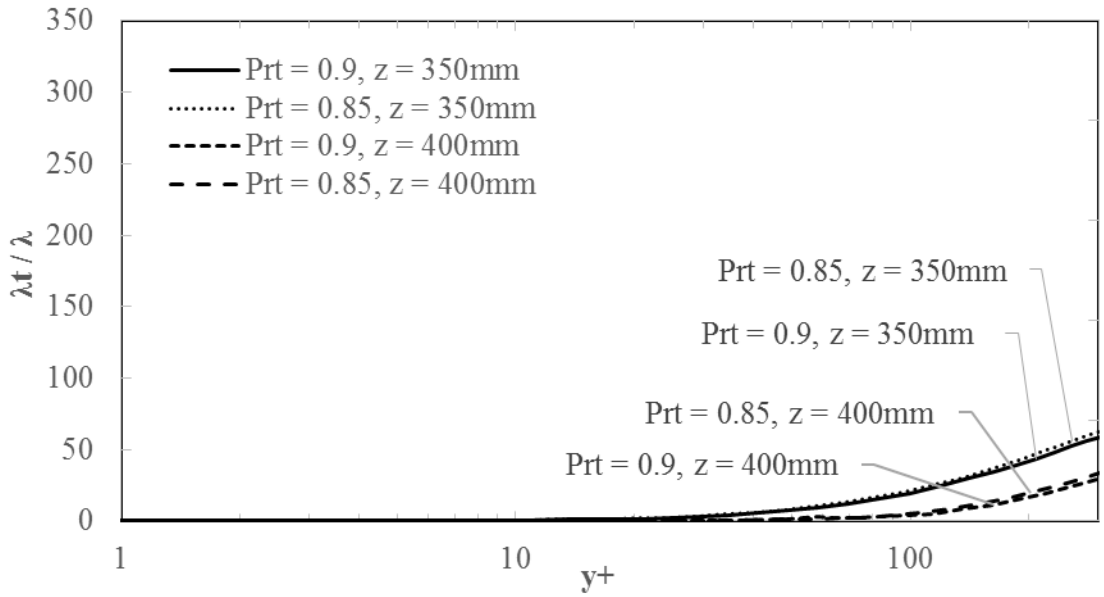

Figure 77: Turbulent thermal conductivity to thermal conductivity ratio of case 2 CFX runs using different turbulent Prandtl numbers. A y+ value of zero corresponds to the location of line H1.

The λ_t/λ ratio is slightly larger over all y^+ at both z = 350 and 400 [mm] for the case with the Pr_t set to 0.85 compared to the case with the Pr_t set to 0.9. This, combined with the result from

Figure 76 is evidence that supports the hypothesis that smaller values of Pr_t lead to increasing values of λ_t, therefore leading to smaller values in heater rod surface temperature.

It seems very unlikely that the lack of a spike in heater rod surface temperature in the Huang et al. cases are purely a result of using a different Pr_t, and instead could be attributed to a combination of factors that include mesh quality, difference in numerical domain, and possible incomplete convergence of numerical solutions. The maximum y^+ values of the Huang et al. cases is 1.25, which is greater than the maximum y^+ values used in the present study, 1.0. An x-y cross section of the mesh used by Huang et al. is given in their study, and it shows a very coarse mesh in the freestream region immediately adjacent to a fine mesh in the near wall region. This would cause high expansion ratios where the two regions meet, which are typically avoided when performing CFD analysis, and are advised against in the CFX Solver Modeling Guide. Huang et al. also modelled the inlet and outlet pipes and chambers, along with the entire bundle, not just a section of it, yet their meshes had 6.5M and 9M nodes for the runs that used wall functions and EWT, respectively. The mesh used for the present study that only modelled a $1/12^{\mathrm{th}}$ section of the entire domain had 15.4M nodes, meaning the Huang et al. meshes were much coarser than those used in the present study.

The differences in heater rod surface temperature between Zhang et al. and this study could be a result of Zhang et al. using a 0.4 [m] unheated inlet section, which is 0.1 [m] longer than the unheated inlet section used in the present study, 0.3 [m]. If the unheated inlet section is not long enough for the flow to become fully developed by the time the flow reaches the heated section, then increasing the length of this section to 0.4 [m] would alter the velocity profile of the flow. This difference in velocity profile could alter the temperature profile in the flow, causing the

difference in heater rod temperature profile that can be seen between the Zhang et al. results and those of the present study.

Neither Huang et al. nor Zhang et al. stated the boundary condition between the unheated inlet sections and the heated sections of the solid heater domains. For the present study, the boundary condition was defined such that heat flux was allowed to freely flow between these heated and unheated solid heater domains, previously stated in Table 26. This boundary condition led to a slight heating of the unheated inlet section, and caused the flow to increase in temperature in the near wall region before it even reached the heated section proper. If Huang et al. and Zhang et al. defined this boundary condition such that heat flux was prevented from flowing between these heated and unheated solid domains, than the flow would not increase in temperature in the near wall region before it reached the heated section. This could explain the spike in heater rod surface temperature of the Zhang et al. case appears further along z than the present study, since the flow would begin to increase in temperature at the start of the heated section, and not slightly before it, like in the present study.

Figure 78 shows the numerical results of Zhang et al. and the present study for case 2 when using the RNG k-ε turbulence model for case 2.

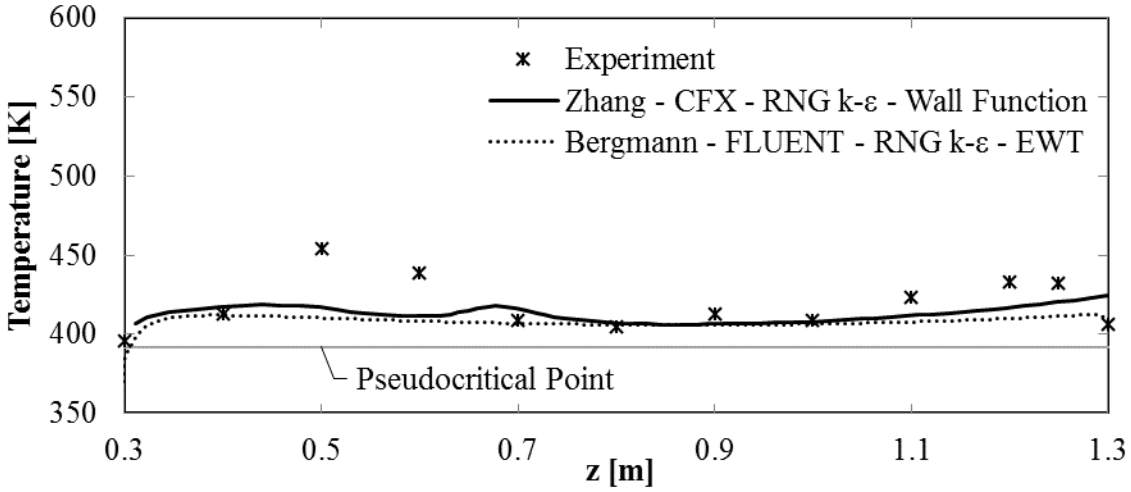

Figure 78: Heater rod surface temperatures from Zhang et al. 2014 vs. results from the present study using RNG k-ε, for case 2.

The result from Zhang et al. shows a slight bump in heater rod surface temperature near z = 700 [mm] and again near the outlet, otherwise both RNG k-ε results are similar.

Figure 79 shows the numerical results of Huang et al. and the present study for case 2 when using the k-ε turbulence model.

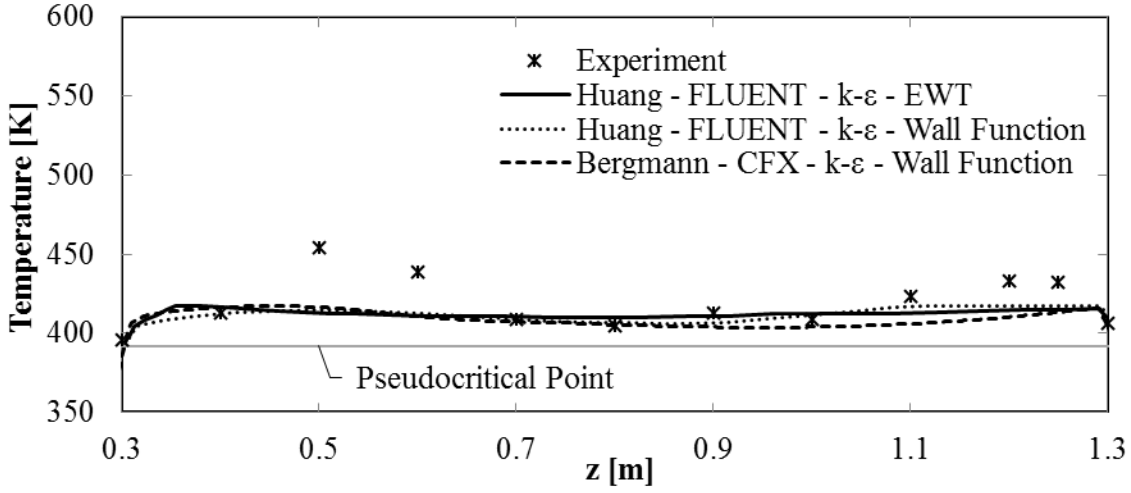

Figure 79: Heater rod surface temperatures from Huang et al. 2014 vs. results from the present study using k-ε, for case 2.

All three k-ε results from this figure are very similar, and predict the experimental heater rod surface temperatures reasonably well.

The heater rod surface temperature results of Zhang et al., Huang et al. and this study using the k-ε and RNG k-ε are similar for case 2. There are no large discrepancies between the numerical results, like those observed for the numerical results from using the SST turbulence model.

Table 57 gives the total pressure drop from the numerical predictions of the present study. The total pressure drop for the experiment was calculated using the difference between the measured outlet and inlet absolute pressures, 4.629 [MPa] and 4.628 [MPa], respectively [71].

Table 57: Total pressure drop from each result for case 2 of the Richards experiments, including the experimental measured value, and percentage difference from experiment.

Case	Total Pressure Drop [Pa]	Percentage Difference From Experiment [%]
2 Experiment	1000	-
2 SST CFX	935	6.5
2 k-ε CFX	942	5.8
2 SST FLUENT	749	25.1
2 RNG k-ε FLUENT	829	17.1
2 Low-Re k-ε Lam-Bremhorst FLUENT	542	45.8
2 Low-Re k-ε Yang-Shih FLUENT	468	53.2

The k-ε and SST turbulence models, implemented using CFX, more closely predicted the experimental pressure drop than the other turbulence models. The Low-Re k-ε turbulence models were the least close at predicting the experimental pressure drop. The mesh that was used in the present study did not include spacers, and so if spacers were included, then the pressure drop should increase in value due to the increased frictional forces. This would bring the pressure drop of the numerical cases closer to the experimental value.

CHAPTER 6: WANG ET AL. 2014 FOUR-ROD BUNDLE WITH WATER

6.1 Experimental Setup

Wang et al. obtained experimental data from the high temperature and high pressure steam-water test loop at Xi'an Jiaotong University. The experimental setup consists of four hollow AISI 304 stainless steel heater rods, orientated in a square arrangement, enclosed in a ceramic shroud to create a subchannel assembly with water flowing vertically upwards. The heater rods are 8 [mm] (0.314961 [in]) in diameter and have a thickness of 1.5 [mm] (0.0590551 [in]). The rods are spot-welded together at two locations along the length of the bundle to maintain a 1.44 [mm] (0.0566929 [in]) gap between the rods. A single pressure tap is located at the inlet of the bundle. 2 shows an x-y cross section of the Wang et al. experimental setup showing the hollow heater rods, water channel, shroud, and external housing. The symmetry planes that will be used to simplify the modelling of this rod bundle are also shown.

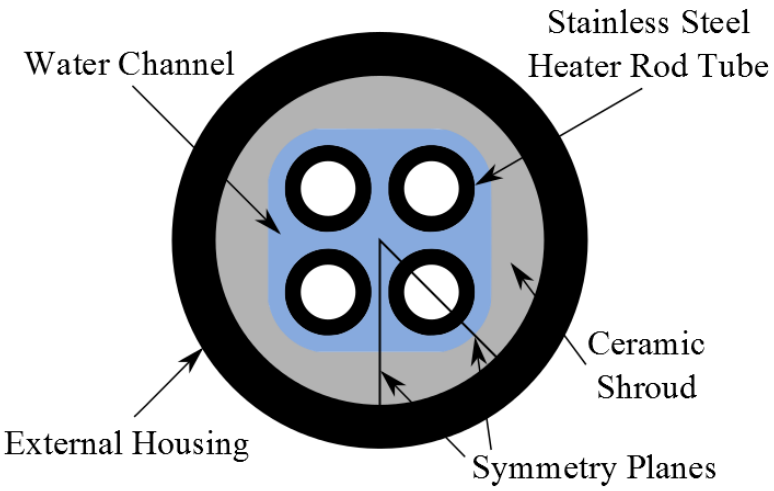

Figure 80: Cross section of Wang et al. 2014 four-rod bundle, showing heater rods, shroud, external housing, and planes of symmetry.

The bulk fluid temperature was measured at both the inlet and outlet. To measure the internal surface temperature of one of the heater rods, a movable probe with four thermocouples oriented 90º relative to one another, was positioned at five axial locations along the inside of the heater rod. The probe was rotated in increments of 22.5º at each of the five locations, so that an average temperature was obtained. This internal surface temperature was converted to an outer surface temperature using the one-dimensional heat conduction equation of Zhou [94]. The five axial locations are 100 [mm] (3.93700 [in]) apart from one another, with the first location at the beginning of the heated section. Four thermocouples, oriented 90º to one another, are fixed to the internal surface of the heater rod adjacent to the heater rod with the movable probe at the last of the five axial locations. The temperatures obtained from the movable probe and the fixed thermocouples were compared to ensure temperature readings were consistently reliable.

Figure 81 shows a y-z cross section of the Wang et al. experimental setup showing the unheated inlet and outlet sections, heated section, and the location of the five thermocouple measuring locations relative to the inlet.

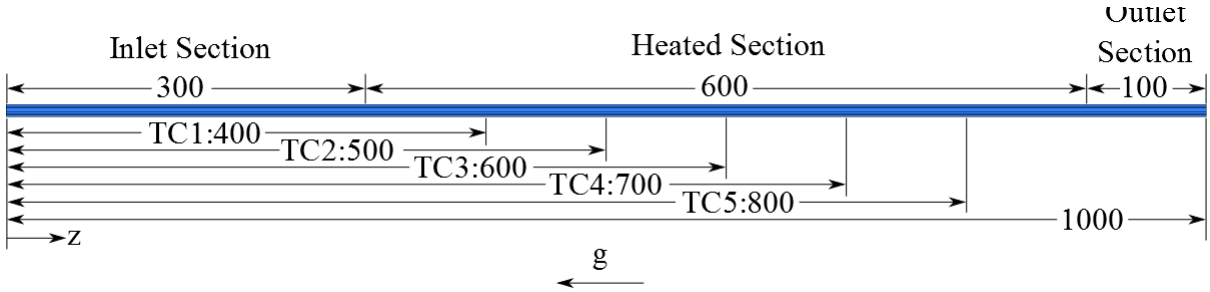

Figure 81: Schematic y-z cross section of the Wang et al. 2014 domain, showing the five wall temperature measurement locations (TC1 to TC5), inlet, heated section, and outlet relative to inlet. Dimensions are in [mm].

The inlet pressure, mass flux, and heat flux of the Wang et al. experiments are given in Table 58. For a given inlet pressure, mass flux, and heat flux, the inlet temperature was varied between 200

[ºC] (473.15 [K]) and 450 [ºC] (723.15 [K]) in steps, but the actual values of the inlet temperature for each case were not stated by the authors.

Table 58: Experimental conditions of Wang et al. 2014 experiments.

Inlet Pressure [MPa]	Mass Flux [kg/m^{2}s]	Heat Flux [kW/m^2]
23	350	200
23	700	200, 400
23	1000	200, 400, 600
25	350	200, 400
25	700	200, 400, 600
25	1000	200, 400, 600, 800, 1000
28	1000	400, 600

Cases that had an inlet pressure of 25 [MPa], mass flux of 350 [kg/m^{2}s], and a heat flux of 200 [kW/m^2] were selected for numerical simulation because they contained a case with the most pronounced peak in temperature. The inlet temperature was the only variable that changed for each of these cases in the present study; hence, the names of these cases refers to the inlet temperature as follows: case T47315 uses an inlet temperature of 473.15 [K], case T60072 uses an inlet temperature of 600.72 [K], and case T65000 uses an inlet temperature of 650.00 [K].

The pseudocritical temperature of water using the inlet pressures of cases T47315, T60072, and T65000 is 658.045 [K].

6.2 Numerical Domain Definition, Boundary Condition, and Mesh

A 1/8th section of the Wang et al. four-rod bundle was modelled, and symmetry was assumed on both section planes. The hydraulic diameter of the subchannel is 4.32611 [mm] (0.170319 [in]).

An x-y cross section of the bundle showing the section that has been modelled is given in Figure 80 in Section 6.1.

The total length of the domain is 1.0 [m] (3.28084 [ft]) in the z-direction, which includes a 0.3 [m] (0.984252 [ft]) inlet section, 0.6 [m] (1.96850 [ft]) heated section, and a 0.1 [m] (0.328084 [ft]) outlet section. The actual lengths of both the inlet and outlet sections were not given in the literature, so it was assumed that these lengths are similar to those of the Rohde et al. bundle. The outlet length was partially chosen so that the total length of the domain would be a 1.0 [m], a whole number. A y-z cross section, showing the five wall temperature measurement locations (labeled TC1 to TC5), the inlet, outlet, and heated section is given in Figure 81 in Section 6.1. The spot-welds securing the heater rods were not modelled in order to substantially reduce the total number of nodes. An x-y cross section of the $1/8^{th}$ section is shown in Figure 82, along with more details about the geometry of the computational domain. 0deg, 90deg, and 180deg are lines in the computational domain that run the entire z-axis length and are used to sample wall temperatures.

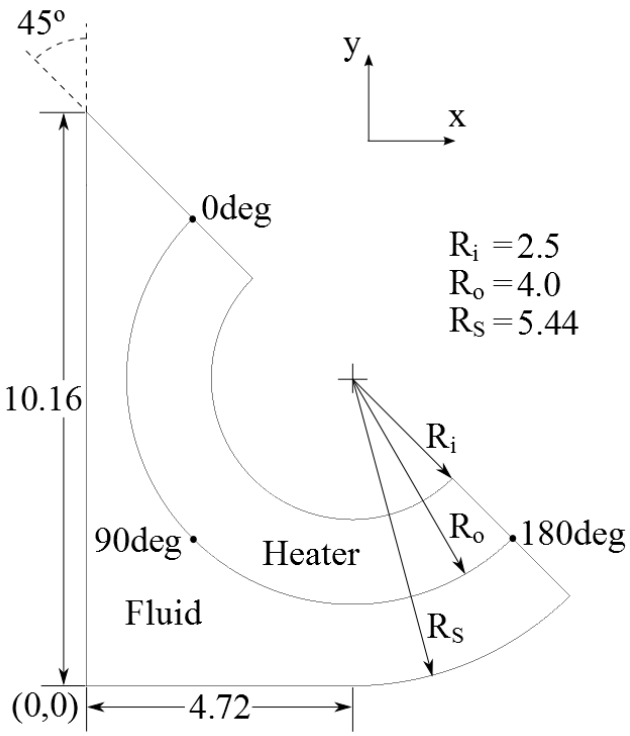

Figure 82: Typical x-y cross section of Wang et al. 2014 domain showing fluid domain, solid domain, and location of lines 0deg, 90deg, and 180deg. All dimensions in [mm].

Table 59 and Table 60 provide domain definitions and boundary conditions for each of the domains shown in Figure 82.

Table 59: Domain definition and boundary conditions of Wang et al. 2014 fluid domain.

Fluid	
Domain Properties	Material: Water Turbulence Model: SST, k-ε, RNG k-ε, Lam-Bremhorst Low-Re k-ε, Yang-Shih Low-Re k-ε Turbulent Prandtl Number (Pr_t): 0.9 Reference Pressure: 25 [MPa]
Material Properties	IAPWS-IF97 Database (CFX), NIST REFPROP v9.0 Database (FLUENT)
Inlet	Mass Flow Rate: 0.00816081 [kg/s] Temperature: 473.15 [K] (Case T47315), 600.72 [K] (Case T60072), 650.00 [K] (Case T65000) Turbulence: Low Intensity (I = 1 %), Low Eddy Viscosity Ratio (μ_t / μ = 1.0)[1] w = 0.391339 [m/s] (Case T47315), 0.503813 [m/s] (Case T60072), 0.708908 [m/s] (Case T65000) Re = 10659.3 (Case T47315), 18327.2 (Case T60072), 26568.1 (Case T65000)
Fluid Properties at Inlet, Case T47315	ρ = 881.348 [kg/m^3] μ = 1.39982x10^{-4} [Pa s] c_p = 4375.79 [J/kgK] λ = 0.683173 [W/mK]
Fluid Properties at Inlet, Case T60072	ρ = 686.524 [kg/m^3] μ = 8.16445x10^{-5} [Pa s] c_p = 5834.74 [J/kgK] λ = 0.529343 [W/mK]
Fluid Properties at Inlet, Case T65000	ρ = 488.911 [kg/m^3] μ = 5.64361x10^{-5} [Pa s] c_p = 15736.9 [J/kgK] λ = 0.404011 [W/mK]
Outlet	Reference Static Pressure: 0 [Pa]
Wall	Adiabatic no-slip at Shroud, coupled (FLUENT) or conservative interface heat flux (CFX) to Heater domain at R_o

[1]Same values as those used for the Rohde et al. cases, because they were found to provide more stable convergence than medium or high intensity inlet turbulence.

Table 60: Domain definition and boundary conditions of Wang et al. 2014 heater domains.

Heater	
Domain Properties	Material: AISI 304L Stainless Steel
Material Properties	ρ = 8030 [kg/m^3] c_p = 5.2 x10^{-5} [J/kgK^3] T^2 + 0.17 [J/kgK^2] T + 426.7 [J/kgK] λ: FORTRAN Subroutine (CFX), lookup table (FLUENT)
Wall	Adiabatic wall across *x*-*y* plane at *z* = 0.0 [m] and *z* = 1.0 [m], coupled (FLUENT) or conservative interface heat flux (CFX) across x-y plane at z = 0.3 [m] and z = 0.9 [m], coupled (FLUENT) or conservative interface heat flux (CFX) to Fluid domain at R_o Adiabatic wall at R_i
Heated Section Energy Source	Volumetric Heat Rate (from heat flux): 1.641026x10^8 [W/m^3]

Various solution variable monitor points are defined for CFX and FLUENT runs, to provide an additional means to check convergence of the runs. For FLUENT runs, these monitor points were placed at four axial locations along line 90deg to record temperature, additionally, the area averaged pressure at the inlet and outlet was monitored. For CFX runs, monitor points were placed at five axial locations along line 90deg to record temperature, and pressure was monitored at points that were in close proximity to the centroid of the inlet and outlet.

6.3 Grid Independence Study

A mesh of the 1/8th section of the four-rod bundle was generated using ICEM CFD. Figure 80 in Section 6.1 shows this 1/12th section defined by the symmetry planes in relation to the entire x-y cross section. CFX was used to numerically solve case T60072 using the SST turbulence model with automatic wall treatment. The SST turbulence model was chosen because, out of those turbulence models that were selected to provide final results, it was the only turbulence model that can be used in CFX that required a y^+ of less than one. The maximum residuals and domain

imbalances were monitored during the runs, and a solution was considered to be converged when these variables reached values given in Section 3.5.1.

A number of initial meshes were first generated for which solutions were obtained for case T60072 using CFX. Case T60072 was chosen because the fluid temperature at the inlet was close to the pseudocritical point, which would most likely cause great variation in the heat transfer phenomena near the wall.

A mesh with a large number of nodes was eventually created and a solution was obtained. This mesh is referred to here as the W-1 mesh and it had 6,143,320 nodes. Five other meshes were created by either increasing or decreasing the uniform z cross section grid spacing of this W-1 mesh. These meshes were given names that correspond to the order in which they were created, i.e. mesh W-1 was created first, and mesh W-6 was the sixth mesh to be created. The changes made to each mesh can be described using a cylindrical r-θ coordinate system. Figure 83 shows the equivalent r-θ coordinate system superimposed on an x-y cross section of the mesh that will eventually be selected as the mesh to be used for final results, mesh W-26. The z-axis has constant nodal spacing.

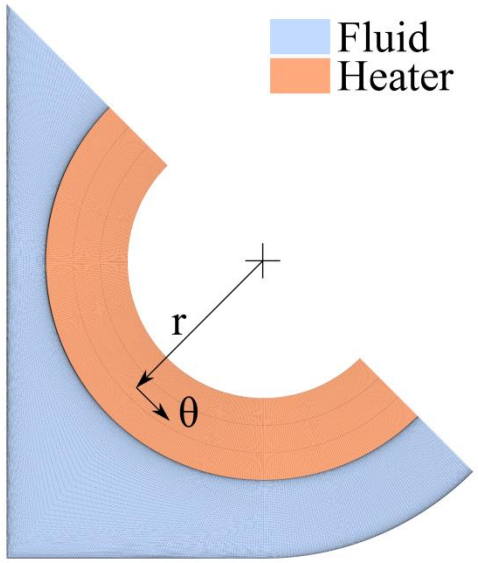

Figure 83: Equivalent r-θ coordinate system for describing mesh modification procedure shown on typical x-y cross section of Wang et al. W-26 mesh

Tables 61 to 64 provide mesh parameters of these six meshes that have identical r-θ cross section mesh parameters, and different z cross section parameters.

Table 61: Overall properties of meshes with different z cross section nodal spacing and identical r-θ cross section nodal spacing, listed in descending order of total nodes.

Mesh ID	Total Nodes	Difference in Nodes Relative to Previous Mesh	Percentage Decrease in Nodes Relative to Previous Mesh
W-4	18,405,448	-	-
W-6	12,283,576	6,121,872	33.26
W-1	6,143,320	6,140,256	49.99
W-2	3,698,248	2,445,072	39.80
W-3	2,650,360	1,047,888	28.33
W-5	2,080,456	569,904	21.50

Table 62: Geometric parameters of meshes with different z cross section nodal spacing and identical r-θ cross section nodal spacing.

Mesh ID	Max z-Spacing [mm]	Max θ-Spacing [mm]	Max r-Spacing, Fluid [mm]	Near Wall Grid Spacing [mm] / Expansion Ratio Next to Heater	Near Wall Grid Spacing [mm] / Expansion Ratio Next to Shroud	Solid Domain Nodes in r-Direction
W-4	1.00000	0.0502128	0.253514	0.002/1.3	0.002/1.3	4
W-6	1.50000	0.0502128	0.253514	0.002/1.3	0.002/1.3	4
W-1	3.03030	0.0502128	0.253514	0.002/1.3	0.002/1.3	4
W-2	5.06897	0.0502128	0.253514	0.002/1.3	0.002/1.3	4
W-3	7.14286	0.0502128	0.253514	0.002/1.3	0.002/1.3	4
W-5	9.09677	0.0502128	0.253514	0.002/1.3	0.002/1.3	4

Table 63: Maximum and minimum y^+ values of meshes with different z cross section nodal spacing and identical r-θ cross section nodal spacing.

Mesh ID	y^+ Max	y^+ Min
W-4	1.12781	0.0824092
W-6	1.02990	0.0825159
W-1	0.877596	0.0828585
W-2	0.875539	0.0835645
W-3	0.869552	0.0840567
W-5	0.869234	0.0845560

Table 64: Mesh quality parameters in the fluid domain of meshes with different z cross section nodal spacing and identical r-θ cross section nodal spacing.

Mesh ID	Min Angle [degree]	Max Expansion Factor	Max Aspect Ratio
W-4	41.0	2	2063
W-6	41.0	2	3094
W-1	41.0	2	6251
W-2	41.0	3	10456
W-3	41.0	4	14734
W-5	41.0	5	18764

The number of nodes in the r-direction in the solid domains will be kept at 4, as was used for and given in Table 28 in Section 5.3. This was done to reduce the number of different mesh combinations. The number 4 was chosen as this is one node more than the number of nodes in the r-direction of the solid domains selected for the final Rohde et al. mesh, BNSP-6. The mesh with the greatest number of nodes and, thus, had the finest z cross section spacing, was the W-4 mesh with 18,405,448 nodes. The mesh with the least number of nodes was the W-5 mesh with 2,080,456 nodes. The $RMS_{RN,T}$ parameter, defined by Equation (113) in Section 4.3, is used to quantify the heated wall surface temperature differences between the results of each of the meshes, where the sampled lines are lines 0deg, 90deg, and 180deg. The $RMS_{RN,T}$ was plotted in Figure 84 for the results of these meshes using mesh W-4 as the reference mesh.

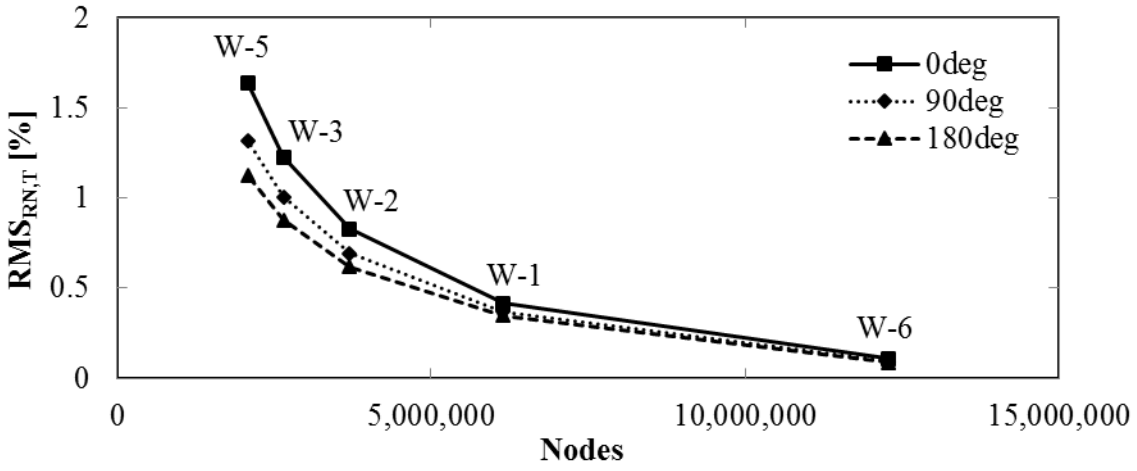

Figure 84: $RMS_{RN,T}$ vs. total nodes for meshes with different z cross section nodal spacing and identical r-θ cross section nodal spacing. Mesh W-4 is the reference mesh.

Figure 84 shows that the heated wall temperature is dependent on the number of z nodes, and that as the number of nodes in the z-direction increases, the $RMS_{RN,T}$ converges towards zero.

The mesh that had a maximum $RMS_{RN,T}$ slightly less than 1 %, mesh W-2, was then modified by either increasing or decreasing the number of nodes in the r-direction of the fluid domain while

maintaining the same expansion ratio close to the wall to create meshes W-7, W-8, and W-9. Tables 65 to 68 provide mesh parameters of these four meshes that have identical z and θ cross section mesh parameters, and different r cross section parameters.

Table 65: Overall properties of meshes with different r cross section nodal spacing and identical z-θ cross section nodal spacing, listed in descending order of total nodes.

Mesh ID	Total Nodes	Difference in Nodes Relative to Previous Mesh	Percentage Decrease in Nodes Relative to Previous Mesh
W-9	6,700,585	-	-
W-8	4,545,061	2,155,524	32.17
W-2	3,698,248	846,813	18.63
W-7	3,621,265	76,983	2.08

Table 66: Geometric parameters of meshes with different r cross section nodal spacing and identical z-θ cross section nodal spacing.

Mesh ID	Max z-Spacing [mm]	Max θ-Spacing [mm]	Max r-Spacing, Fluid [mm]	Near Wall Grid Spacing [mm] / Expansion Ratio Next to Heater	Near Wall Grid Spacing [mm] / Expansion Ratio Next to Shroud	Solid Domain Nodes in r-Direction
W-9	5.06897	0.0502128	0.0502315	0.002/1.3	0.002/1.3	4
W-8	5.06897	0.0502128	0.105890	0.002/1.3	0.002/1.3	4
W-2	5.06897	0.0502128	0.253514	0.002/1.3	0.002/1.3	4
W-7	5.06897	0.0502128	0.341401	0.002/1.3	0.002/1.3	4

Table 67: Maximum and minimum y^+ values of meshes with different r cross section nodal spacing and identical z-θ cross section nodal spacing.

Mesh ID	y^+ Max	y^+ Min
W-9	0.874243	0.0808881
W-8	0.875838	0.0833491
W-2	0.875539	0.0835645
W-7	0.875788	0.0835413

Table 68: Mesh quality parameters in the fluid domain of meshes with different r cross section nodal spacing and identical z-θ cross section nodal spacing.

Mesh ID	Min Angle [degree]	Max Expansion Factor	Max Aspect Ratio
W-9	41.0	3	10456
W-8	41.0	3	10456
W-2	41.0	3	10456
W-7	41.0	3	10456

The mesh with the greatest number of nodes and, thus, had the finest r cross section spacing, was the W-9 mesh with 6,700,585 nodes. The mesh with the least number of nodes was the W-7 mesh with 3,621,265 nodes. The $RMS_{RN,T}$ is plotted in Figure 85 for the results of these meshes using mesh W-9 as the reference mesh.

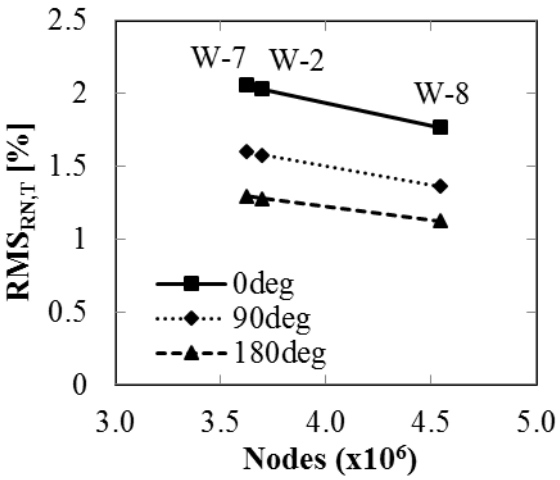

Figure 85: $RMS_{RN,T}$ vs. total nodes for meshes with different r cross section nodal spacing and identical z-θ cross section nodal spacing. Mesh W-9 is the reference mesh.

Figure 85 shows that the $RMS_{RN,T}$ is dependent on the nodal spacing in the r-direction, since the maximum $RMS_{RN,T}$ is approximately 2 %, for mesh W-7. The mesh with a minimum $RMS_{RN,T}$ of 1.8 % at 0deg, mesh W-8, had a maximum r-direction spacing of 0.10589 [mm] (0.00416810 [in]).

Mesh W-2 was again used to generate multiple new meshes: W-10 through W-14. These meshes had identical nodal spacing as mesh W-2 in the z and θ direction, but had different expansion ratios in the r-direction nearest to the wall in the fluid domain. Tables 69 to 72 provide mesh parameters of these six meshes that have identical z and θ cross section mesh parameters, and different r cross section parameters.

Table 69: Overall properties of meshes with different expansion ratios near the heated wall in the fluid domain in the r-direction and identical z-θ cross section nodal spacing, listed in descending order of total nodes.

Mesh ID	Total Nodes	Difference in Nodes Relative to Previous Mesh	Percentage Decrease in Nodes Relative to Previous Mesh
W-14	22,482,100	-	-
W-13	12,166,378	10,315,722	45.88
W-10	7,547,398	4,618,980	37.97
W-2	3,698,248	3,849,150	51.00
W-11	2,928,418	769,830	20.82
W-12	2,543,503	384,915	13.14

Table 70: Geometric parameters of meshes with different expansion ratios near the heated wall in the fluid domain in the r-direction and identical z-θ cross section nodal spacing.

Mesh ID	Max z-Spacing [mm]	Max θ-Spacing [mm]	Max r-Spacing, Fluid [mm]	Near Wall Grid Spacing [mm] / Expansion Ratio Next to Heater	Near Wall Grid Spacing [mm] / Expansion Ratio Next to Shroud	Solid Domain Nodes in r-Direction
W-14	5.06897	0.0502128	0.0301477	0.002/1.02	0.002/1.02	4
W-13	5.06897	0.0502128	0.0670903	0.002/1.05	0.002/1.05	4
W-10	5.06897	0.0502128	0.119123	0.002/1.1	0.002/1.1	4
W-2	5.06897	0.0502128	0.253514	0.002/1.3	0.002/1.3	4
W-11	5.06897	0.0502128	0.241499	0.002/1.5	0.002/1.5	4
W-12	5.06897	0.0502128	0.257148	0.002/1.7	0.002/1.7	4

Table 71: Maximum and minimum y^+ values of meshes with different expansion ratios near the heated wall in the fluid domain in the r-direction and identical z-θ cross section nodal spacing.

Mesh ID	y^+ Max	y^+ Min
W-14	0.874600	0.0770229
W-13	0.873409	0.0771720
W-10	0.872428	0.0775883
W-2	0.875539	0.0835645
W-11	0.887600	0.101262
W-12	0.889114	0.110884

Table 72: Mesh quality parameters in the fluid domain of meshes with different expansion ratios near the heated wall in the fluid domain in the r-direction and identical z-θ cross section nodal spacing.

Mesh ID	Min Angle [degree]	Max Expansion Factor	Max Aspect Ratio
W-14	41.0	2	10456
W-13	41.0	2	10456
W-10	41.0	2	10456
W-2	41.0	3	10456
W-11	41.0	3	10456
W-12	41.0	4	10456

The mesh with the greatest number of nodes and, thus, had the lowest expansion ratio in the r-direction, was the W-14 mesh with 22,482,100 nodes. The mesh with the least number of nodes was the W-12 mesh with 2,543,503 nodes. The $RMS_{RN,T}$ is plotted in Figure 86 for the results of these meshes using mesh W-14 as the reference mesh.

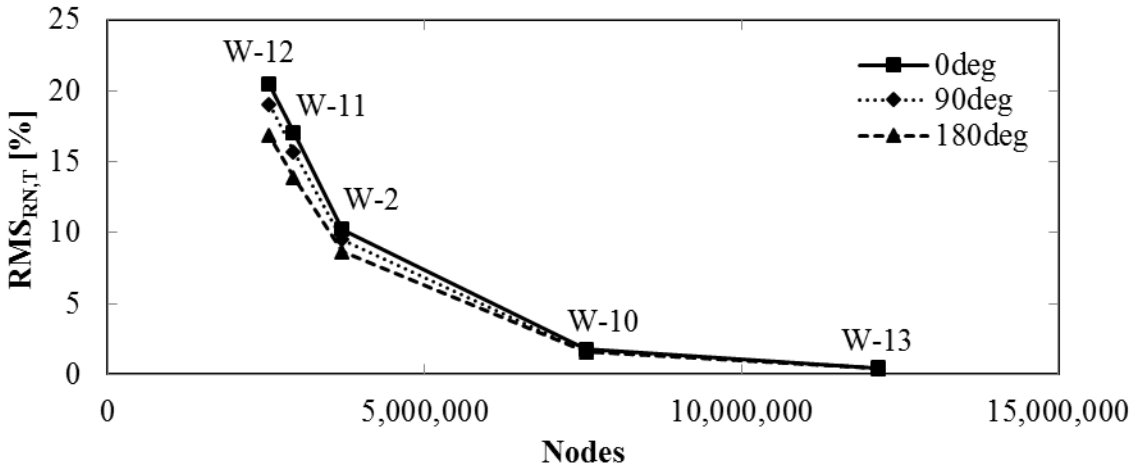

Figure 86: $RMS_{RN,T}$ vs. total nodes for meshes with different expansion ratios near the heated wall in the fluid domain in the r-direction and identical z-θ cross section nodal spacing. Mesh W-14 is the reference mesh.

Figure 86 shows that the heated wall temperature is highly dependent on the expansion ratio in the r-direction closest to the wall. As the expansion ratio decreases, and in turn the number of nodes increases, the $RMS_{RN,T}$ converges towards zero. The mesh with 7,547,398 nodes, mesh W-10, had a maximum $RMS_{RN,T}$ of 1.8 %, which is reasonably low compared to the other meshes. The maximum r-direction spacing of this mesh is 0.119123 [mm] (0.00468988 [in]), which is similar to the maximum r-direction spacing previously found to give a maximum $RMS_{RN,T}$ of 1.8 % when comparing meshes that only differ in their r-direction spacing. From Figure 86, the mesh with the next lowest $RMS_{RN,T}$ of 0.5 %, had 12,166,378 nodes, which is a substantial increase in nodes for a reduction in $RMS_{RN,T}$.

Mesh W-2 was once again used to generate multiple new meshes: W-15 through W-20. These meshes had identical nodal spacing as mesh W-2 in the z and r direction, but had different θ-direction spacing. Tables 73 to 76 provide mesh parameters of these seven meshes that have identical z and r cross section mesh parameters, and different θ cross section parameters.

Table 73: Overall properties of meshes with different θ cross section nodal spacing and identical r-z cross section nodal spacing, listed in descending order of total nodes.

Mesh ID	Total Nodes	Difference in Nodes Relative to Previous Mesh	Percentage Decrease in Nodes Relative to Previous Mesh
W-20	18,394,680	-	-
W-18	9,211,824	9,182,856	49.92
W-15	6,131,560	3,080,264	33.44
W-2	3,698,248	2,433,312	39.69
W-16	2,655,400	1,042,848	28.20
W-17	2,037,416	617,984	23.27
W-19	1,844,296	193,120	9.48

Table 74: Geometric parameters of meshes with different θ cross section nodal spacing and identical r-z cross section nodal spacing.

Mesh ID	Max z-Spacing [mm]	Max θ-Spacing [mm]	Max r-Spacing, Fluid [mm]	Near Wall Grid Spacing [mm] / Expansion Ratio Next to Heater	Near Wall Grid Spacing [mm] / Expansion Ratio Next to Shroud	Solid Domain Nodes in r-Direction
W-20	5.06897	0.0100000	0.253514	0.002/1.3	0.002/1.3	4
W-18	5.06897	0.0200000	0.253514	0.002/1.3	0.002/1.3	4
W-15	5.06897	0.0300637	0.253514	0.002/1.3	0.002/1.3	4
W-2	5.06897	0.0502128	0.253514	0.002/1.3	0.002/1.3	4
W-16	5.06897	0.0695890	0.253514	0.002/1.3	0.002/1.3	4
W-17	5.06897	0.0907692	0.253514	0.002/1.3	0.002/1.3	4
W-19	5.06897	0.100594	0.253514	0.002/1.3	0.002/1.3	4

Table 75: Maximum and minimum y^+ values of meshes with different θ cross section nodal spacing and identical r-z cross section nodal spacing.

Mesh ID	y^+ Max	y^+ Min
W-20	0.886277	0.0836560
W-18	0.882433	0.0836294
W-15	0.879541	0.0836241
W-2	0.875539	0.0835645
W-16	0.872663	0.0836665
W-17	0.871488	0.0837833
W-19	0.871552	0.0837458

Table 76: Mesh quality parameters in the fluid domain of meshes with different θ cross section nodal spacing and identical r-z cross section nodal spacing.

Mesh ID	Min Angle [degree]	Max Expansion Factor	Max Aspect Ratio
W-20	41.0	3	10464
W-18	41.0	3	10462
W-15	41.0	3	10450
W-2	41.0	3	10456
W-16	41.0	3	10448
W-17	41.0	3	10432
W-19	41.0	3	10435

The mesh with the greatest number of nodes and, thus, had the smallest spacing in the θ-direction, was the W-20 mesh with 18,394,680 nodes. The mesh with the least number of nodes was the W-19 mesh with 1,844,296 nodes. The $RMS_{RN,T}$ is plotted in Figure 87 for the results of these meshes using mesh W-20 as the reference mesh

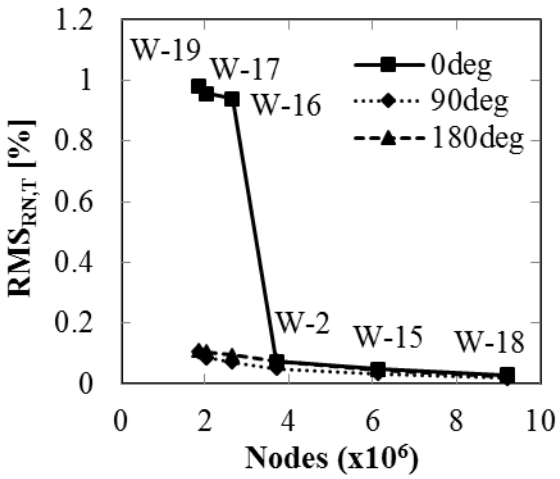

Figure 87: $RMS_{RN,T}$ vs. total nodes for meshes with different θ cross section nodal spacing and identical r-z cross section nodal spacing. Mesh W-20 is the reference mesh.

From the above plot it is clear that θ spacing has little effect on $RMS_{RN,T}$ and, thus, little effect on heated wall surface temperatures. This is evident by the maximum $RMS_{RN,T}$ of 1 %. There is a sudden drop in $RMS_{RN,T}$ as the mesh size increases from 2,655,400 nodes to 3,698,248 nodes, but only for temperatures sampled along line 0deg. The θ spacing for the 3,698,248 node mesh, mesh W-2, is identical to the θ spacing used in mesh W-10; this θ spacing will be used for the final mesh, as it had a low $RMS_{RN,T}$ and a low total number of nodes.

As a final check, mesh W-10 was used to generate five other meshes: W-21 through W-25. Only the z-direction spacing was modified between these meshes. Tables 77 to 80 provide mesh parameters of these six meshes that have identical r and θ cross section mesh parameters, and different z direction nodal counts.

Table 77: Overall properties of meshes with different z cross section nodal spacing and identical r-θ cross section nodal spacing, listed in descending order of total nodes.

Mesh ID	Total Nodes	Difference in Nodes Relative to Previous Mesh	Percentage Decrease in Nodes Relative to Previous Mesh
W-25	37,574,598	-	-
W-24	25,075,776	12,498,822	33.26
W-23	12,464,352	12,611,424	50.29
W-10	7,547,398	4,916,954	39.45
W-21	5,370,426	2,176,972	28.84
W-22	4,244,406	1,126,020	20.97

Table 78: Geometric parameters of meshes with different z cross section nodal spacing and identical r-θ cross section nodal spacing.

Mesh ID	Max z-Spacing [mm]	Max θ-Spacing [mm]	Max r-Spacing, Fluid [mm]	Near Wall Grid Spacing [mm] / Expansion Ratio Next to Heater	Near Wall Grid Spacing [mm] / Expansion Ratio Next to Shroud	Solid Domain Nodes in r-Direction
W-25	1.00000	0.0502128	0.119123	0.002/1.1	0.002/1.1	4
W-24	1.50000	0.0502128	0.119123	0.002/1.1	0.002/1.1	4
W-23	3.03030	0.0502128	0.119123	0.002/1.1	0.002/1.1	4
W-10	5.06897	0.0502128	0.119123	0.002/1.1	0.002/1.1	4
W-21	7.14286	0.0502128	0.119123	0.002/1.1	0.002/1.1	4
W-22	9.09677	0.0502128	0.119123	0.002/1.1	0.002/1.1	4

Table 79: Maximum and minimum y^+ values of meshes with different z cross section nodal spacing and identical r-θ cross section nodal spacing.

Mesh ID	y^+ Max	y^+ Min
W-25	1.13039	0.0773821
W-24	1.03172	0.0774093
W-23	0.878808	0.0774849
W-10	0.872428	0.0775883
W-21	0.870531	0.0776687
W-22	0.870510	0.0777729

Table 80: Mesh quality parameters in the fluid domain of meshes with different z cross section nodal spacing and identical r-θ cross section nodal spacing.

Mesh ID	Min Angle [degree]	Max Expansion Factor	Max Aspect Ratio
W-25	41.0	1	2063
W-24	41.0	1	3094
W-23	41.0	1	6251
W-10	41.0	2	10456
W-21	41.0	3	14734
W-22	41.0	4	18764

The mesh with the greatest number of nodes and, thus, had the smallest spacing in the z-direction, was the W-25 mesh with 37,574,598 nodes. The mesh with the least number of nodes was the W-22 mesh with 4,244,406 nodes. The $RMS_{RN,T}$ is plotted in Figure 88 for the results of these meshes using mesh W-25 as the reference mesh.

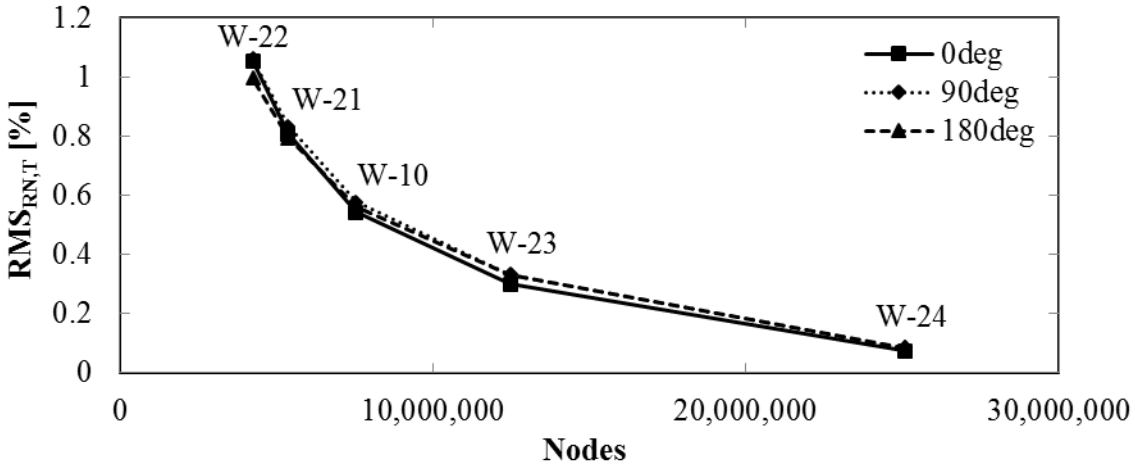

Figure 88: $RMS_{RN,T}$ vs. total nodes for meshes with different z cross section nodal spacing and identical r-θ cross section nodal spacing. Mesh W-25 is the reference mesh.

Figure 88 shows once again that the heated wall surface temperature is dependent on the number of nodes in the z-direction. As the number of nodes in the z-direction increases, the $RMS_{RN,T}$

converges towards zero. The mesh with 4,244,406 nodes, mesh W-30, had a maximum $RMS_{RN,T}$ of 1.1 %, which is reasonably low. For a modest increase in the total number of nodes, to 7,547,398 for mesh W-10, the maximum $RMS_{RN,T}$ is reduced to 0.6 %. This is a desirable mesh, as it provides a low $RMS_{RN,T}$ while having a minimum total number of nodes.

From these mesh comparisons, the mesh that should provide a solution that is relatively independent of the mesh, while using a minimum number of nodes, is mesh W-10.

For all the above mesh comparisons, the minimum z cross section had been set at 3 [mm] (0.118110 [in]) at z = 0 (the inlet). This was updated for mesh W-26, which is simply mesh W-10 with the minimum z cross section spacing eliminated. The total number of nodes are identical between these two meshes. Tables 81 to 84 provide mesh parameters of these two meshes that have identical r and θ cross section mesh parameters, and different z cross section parameters at the inlet near z = 0.

Table 81: Overall properties of meshes with different z cross section nodal spacing near the inlet at z = 0 and identical r-θ cross section nodal spacing, listed in descending order of total nodes.

Mesh ID	Total Nodes	Difference in Nodes Relative to Previous Mesh	Percentage Decrease in Nodes Relative to Previous Mesh
W-10	7,547,398	-	-
W-26	7,547,398	0	0.00

Table 82: Geometric parameters of meshes with different z cross section nodal spacing near the inlet at z = 0 and identical r-θ cross section nodal spacing.

Mesh ID	Max z-Spacing [mm]	Max θ-Spacing [mm]	Max r-Spacing, Fluid [mm]	Near Wall Grid Spacing [mm] / Expansion Ratio Next to Heater	Near Wall Grid Spacing [mm] / Expansion Ratio Next to Shroud	Solid Domain Nodes in r-Direction
W-10	5.06897	0.0502128	0.119123	0.002/1.1	0.002/1.1	4
W-26	5.00000	0.0502128	0.119123	0.002/1.1	0.002/1.1	4

Table 83: Maximum and minimum y^+ values of meshes with different z cross section nodal spacing near the inlet at z = 0 and identical r-θ cross section nodal spacing.

Mesh ID	y^+ Max	y^+ Min
W-10	0.872428	0.0775883
W-26	0.864469	0.0775863

Table 84: Mesh quality parameters in the fluid domain of meshes with different z cross section nodal spacing near the inlet at z = 0 and identical r-θ cross section nodal spacing.

Mesh ID	Min Angle [degree]	Max Expansion Factor	Max Aspect Ratio
W-10	41.0	2	10456
W-26	41.0	1	10314

The $RMS_{RN,T}$, using mesh W-10 as the reference mesh, are 0.06 %, 0.06 %, and 0.07 % for lines 0deg, 90deg, and 180deg, respectively. These are low $RMS_{RN,T}$ values, and so the conclusion can be drawn that meshes W-10 and W-26 would give very similar results, even though mesh W-10 has a smaller minimum spacing in the z-direction than mesh W-26.

From these mesh comparisons, the mesh that provides a solution that is relatively independent of the mesh, while using a minimum number of nodes, is mesh W-26. This mesh was used to generate final results of cases T47315, T60072, and T65000 of the Wang et al. experiments.

Regrettably, the heat rate used for all cases of this grid independence study was double what it should have been, and by the time this error was noticed all the runs were completed. To confirm the results of this grid independence study are still applicable when using the correct heat rate, four runs were re-performed with the correct heat rate. So long as the same trend was found between these runs and the runs with the doubled heat rate, then the grid independence study will still be applicable to the case with the correct heat rate. Runs using meshes W-10, W-21, W-22, and W-23 were re-performed using the correct heat rate. Only the z-direction spacing changes between these meshes. The $RMS_{RN,T}$ is plotted in Figure 89 using W-23 as the reference mesh.

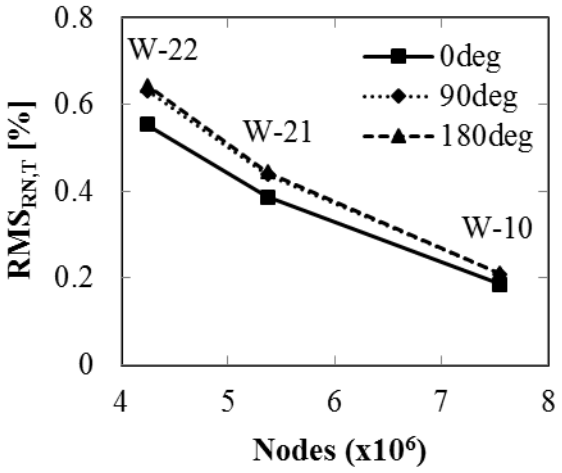

Figure 89: $RMS_{RN,T}$ vs. total nodes for meshes with different z cross section nodal spacing and corrected heat rate. Mesh W-23 is the reference mesh.

The trend in $RMS_{RN,T}$ between these runs and those that use the same meshes but a doubled heat rate, seen in Figure 88, is identical: as the number of nodes in the z-direction increases, the $RMS_{RN,T}$ converges towards zero. The actual values of $RMS_{RN,T}$ cannot be compared between

these runs and those seen in Figure 88 because they use a much finer reference mesh, W-25, that has 25,110,246 more nodes than the reference mesh used in Figure 89, mesh W-23.

From the results shown on Figure 89 it is clear that this grid independence study is still applicable to the case with the correct heat rate.

6.4 Results and Discussion

The results of case T47315 and T65000 are given here. Results for T60072 are given in Appendix A.5, since not all the turbulence models were used to generate those results and are considered to be a supplementary subset of results. Case T65000 was selected because the inlet temperature, 650 [K], was slightly below the pseudocritical temperature, 658.045 [K]. This was expected to lead to a scenario in which the fluid crosses the pseudocritical point soon after reaching the start of the heated section of the heater rod, causing significant changes in the thermophysical properties of the fluid. Case T47315 was selected because the inlet temperature, 473.15 [K], was far below the pseudocritical temperature; therefore sudden changes in thermophysical properties of the fluid were not expected to occur. Case T60072 was selected for the grid independence study, as the inlet temperature was close to, but still below the pseudocritical temperature. There do not exist any studies that compare numerical predictions with the experimental data of Wang et al.

For the present study, the maximum residuals and domain imbalances were monitored during the following runs, and a solution was considered to be converged when these variables reached values given in Section 3.5.1 and Section 3.5.2 for CFX and FLUENT, respectively. Additionally, the solution variables at various monitor points were checked to ensure the solution

was converged. These solution variables at the monitor points were not changing significantly over a large number of iterations, where the maximum change in temperature or pressure at a monitor location was less than 0.1 % over at least approximately 400 iterations, and the vast majority of monitor locations had much less than a 0.1 % change in temperature or pressure over the same number of iterations.

All CFX and FLUENT runs were performed on local servers at the University of Manitoba, which use the Linux operating system. The total wall clock time for case T47315 CFX simulations was between 41 and 61 hours using 4 cores in parallel computing. For case T47315 FLUENT simulations, the total wall clock time was between 274 and 417 hours using 4 cores in parallel. The total wall clock time for case T65000 CFX simulations using the k-ε turbulence model was 218 hours using 4 cores in parallel computing. For case T65000 FLUENT simulations using the Lam-Bremhorst Low-Re k-ε turbulence model, the total wall clock time was 392 hours using 4 cores in parallel.

Wang et al. provided plots of the average heater rod surface temperature versus bulk enthalpy at a single z location, TC5 as shown in Figure 81 in Section 6.1, for multiple cases where only the inlet temperature was changed. The pressure, heat flux, and mass flow rate were held constant for each of these cases.

7.4.1. Case T47315

The numerical results of case T47315 of the Wang et al. experiments will be presented here.

Figure 90 gives the average heater rod surface temperatures of case T47315 using CFX and the SST and k-ε turbulence models, FLUENT and the SST turbulence model, and the experimental temperatures.

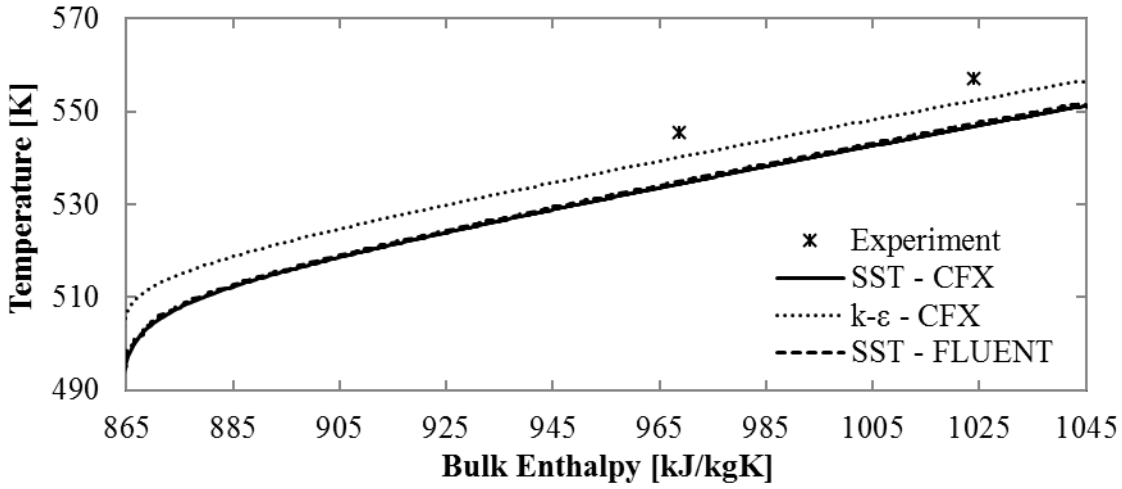

Figure 90: Average heater rod surface temperatures for case T47315 using CFX with the SST and k-ε turbulence model, and FLUENT with the SST turbulence model. The pseudocritical temperature is 658.045 [K].

The heater rod surface temperatures predicted by CFX and FLUENT using the SST turbulence model are nearly identical. Both the SST and k-ε turbulence models under-predict the heater rod surface temperatures, but the SST turbulence model under-predicts the surface temperatures to a greater degree than the k-ε turbulence model.

Figure 91 gives the average heater rod surface temperatures of case T47315 using the RNG k-ε, Lam-Bremhorst Low-Re k-ε, and Yang-Shih Low-Re k-ε turbulence models using FLUENT.

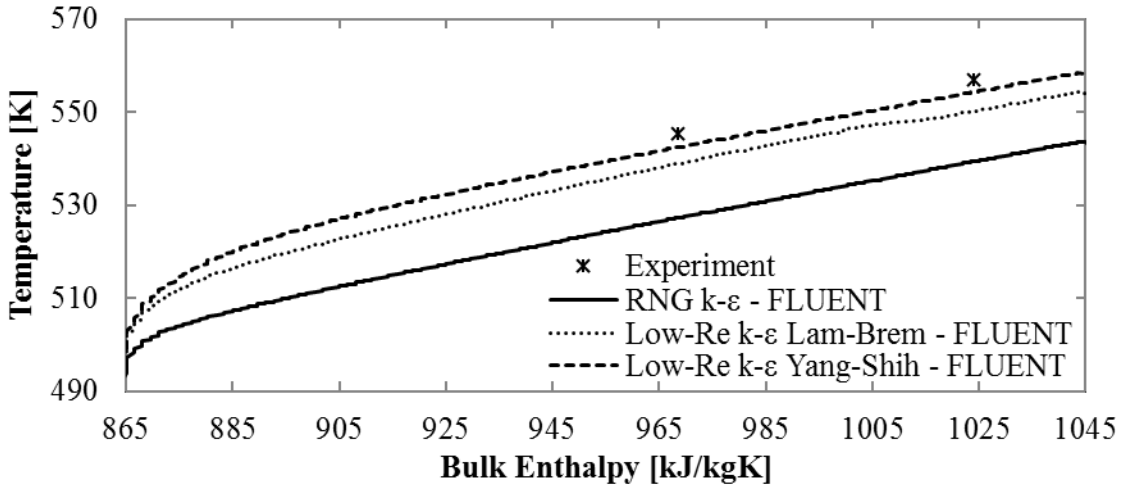

Figure 91: Average heater rod surface temperatures for case T47315 using FLUENT. The pseudocritical temperature is 658.045 [K].

The Yang-Shih Low-Re k-ε turbulence model predicts the heater rod surface temperatures closer than both the Lam-Bremhorst Low-Re k-ε and RNG k-ε turbulence models. All three turbulence models, however, under-predict the heater rod surface temperatures.

To quantify the differences between the numerical predictions and experimental results of heater rod surface temperatures for case T47315, the $RMS_{RN,T}$ is calculated and presented in Table 85. Equation (113) in Section 4.3 is used to calculate the $RMS_{RN,T}$, where the reference temperatures come from the experimental data and the maximum range in temperatures is calculated from the numerical result with the greatest range in surface temperatures. The maximum range is 85.29 [K], and comes from the numerical result using the Yang-Shih Low-Re k-ε turbulence model. This was done because for each case of Wang et al. there are two experimental data points with which to calculate the $RMS_{RN,T}$, and so the maximum range in surface temperatures in the experimental data is not representative of the actual experimental maximum range in surface temperatures.

Table 85: $RMS_{RN,T}$ between numerical results and experimental results for case T47315.

Case	$RMS_{RN,T}$ [%]
T47315 SST CFX	12.47
T47315 k-ε CFX	5.83
T47315 SST FLUENT	11.85
T47315 RNG k-ε FLUENT	20.99
T47315 Low-Re k-ε Lam-Bremhorst FLUENT	7.82
T47315 Low-Re k-ε Yang-Shih FLUENT	3.32

The Yang-Shih Low-Re k-ε turbulence model had the smallest overall deviation from the heater rod surface temperatures. The k-ε and Lam-Bremhorst Low-Re k-ε turbulence models gave the second and third closest prediction of the experimental data. The results of the SST turbulence model, when implemented with FLUENT and CFX gave the fourth and fifth closest prediction of experimental data, respectively. The RNG k-ε turbulence model, when implemented with FLUENT, gave the worst prediction of experimental heater rod surface temperatures.

Various plots from case T47315 using FLUENT and the Yang-Shih Low-Re k-ε turbulence model are given to illustrate trends in the flow when there is no HTD in either the experiment or numerical predictions. A y^+ value of zero corresponds to the location of line 180deg in the following plots.

Figure 92 shows the near wall fluid temperature profiles at various z locations of case T47315 using FLUENT and the Yang-Shih Low-Re k-ε turbulence model.

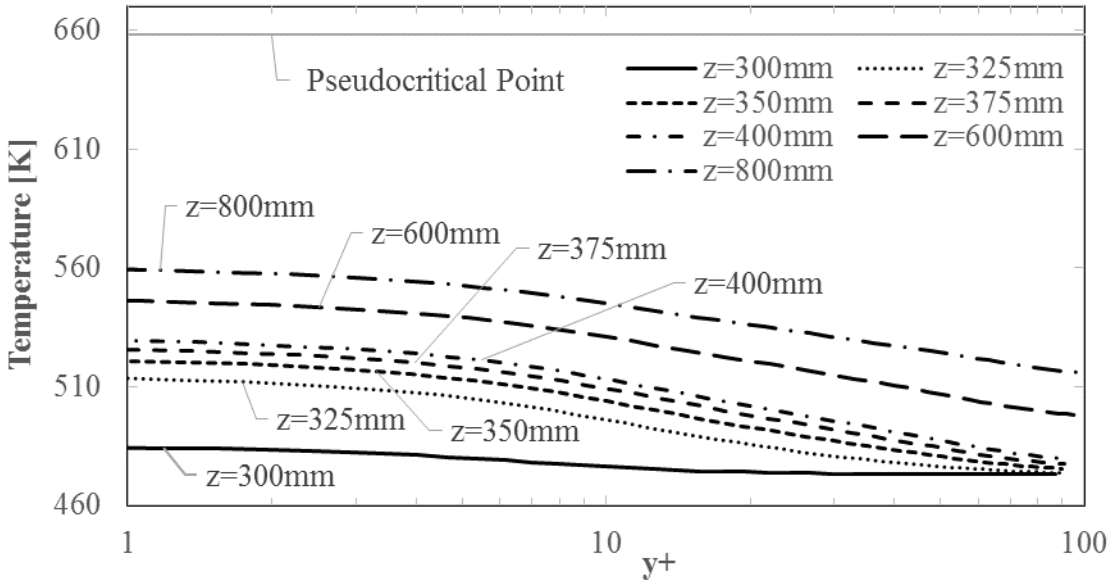

Figure 92: Fluid temperature vs. y+ at various z locations of case T47315 using FLUENT and Yang-Shih Low-Re k-ε turbulence model. A y+ value of zero corresponds to the location of line 180deg.

The fluid closest to the heater rod surface gradually increase in temperature as the fluid progresses along z, but the temperature never reaches the pseudocritical temperature. The thermophysical properties of the fluid therefore do not change significantly at any location.

Figure 93 shows the near wall fluid density profiles at various z locations of case T47315 using FLUENT and the Yang-Shih Low-Re k-ε turbulence model.

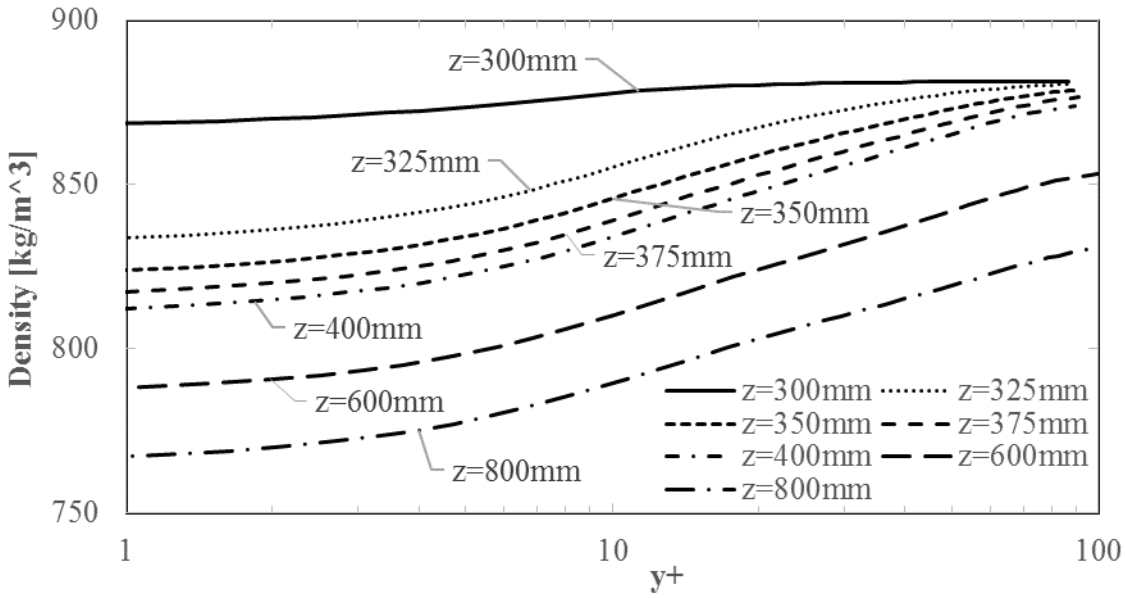

Figure 93: Density vs. y+ at various z locations of case T47315 using FLUENT and Yang-Shih Low-Re k-ε turbulence model. A y+ value of zero corresponds to the location of line 180deg.

The density of the fluid decreases as it is heated along z, but the gradients are not relatively large.

Figure 94 shows the near wall velocity *w* profiles at various z locations of case T47315 using FLUENT and the Yang-Shih Low-Re k-ε turbulence model.

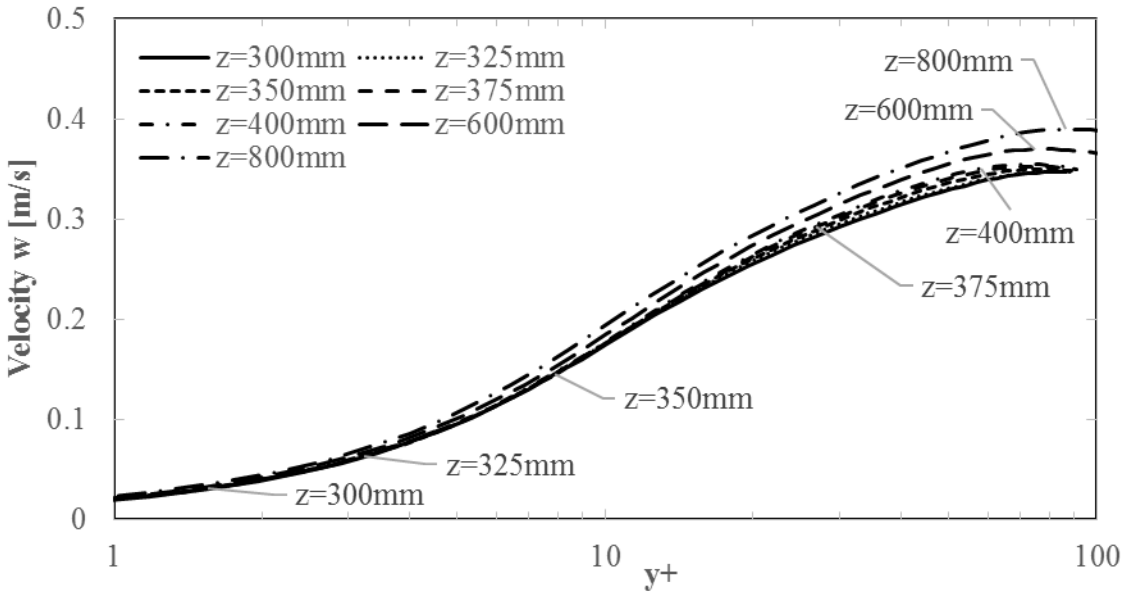

Figure 94: Velocity w vs. y+ at various z locations of case T47315 using FLUENT and Yang-Shih Low-Re k-ε turbulence model. A y+ value of zero corresponds to the location of line 180deg.

The velocity *w* profiles at all z locations follow similar trends, and no spikes in velocity *w* in the near wall region occur, nor does a flattening of the velocity profile occur.

Figure 95 shows the μ_t/μ ratio profiles at various z locations of case T47315 using FLUENT and the Yang-Shih Low-Re k-ε turbulence model.

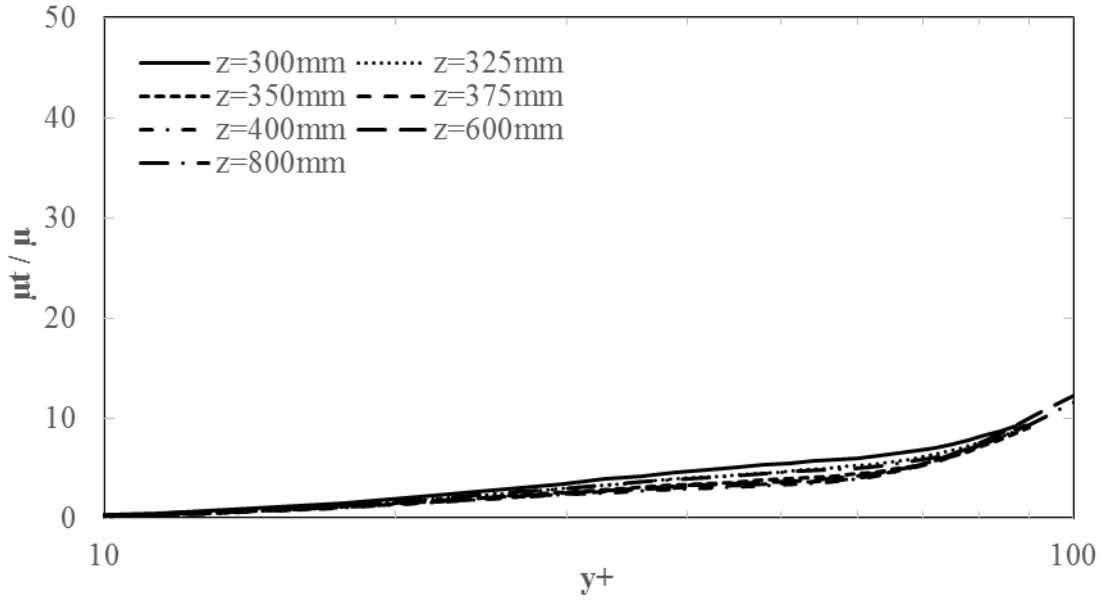

Figure 95: Ratio between eddy viscosity and dynamic viscosity vs. y+ at various z locations of case T47315 using FLUENT and Yang-Shih Low-Re k-ε turbulence model. A y+ value of zero corresponds to the location of line 180deg.

The μ_t/μ profiles at all z locations follow a similar trend, and are low in value over all y^+ values. This would suggest that the flow should be close to laminar in the near wall region, leading to HTD. This is not the case, since there are no spikes in heater rod surface temperature, as seen in Figure 91. A possible reason for these low μ_t/μ values could be that the Reynolds number at the inlet is 10,659, which is lower than the Reynolds for the T65000 case at the inlet, 26,568. It is also the lowest Reynolds number at the inlet for all cases in the present study (this includes the Richards 2012 Experiments and the Rohde et al. 2015 Experiments). The low Reynolds number is an indicator of low values of turbulence quantities; hence, the small eddy viscosity, μ_t, values.

Figure 96 shows the λ_t/λ ratio profiles at various z locations of case T47315 using FLUENT and the Yang-Shih Low-Re k-ε turbulence model.

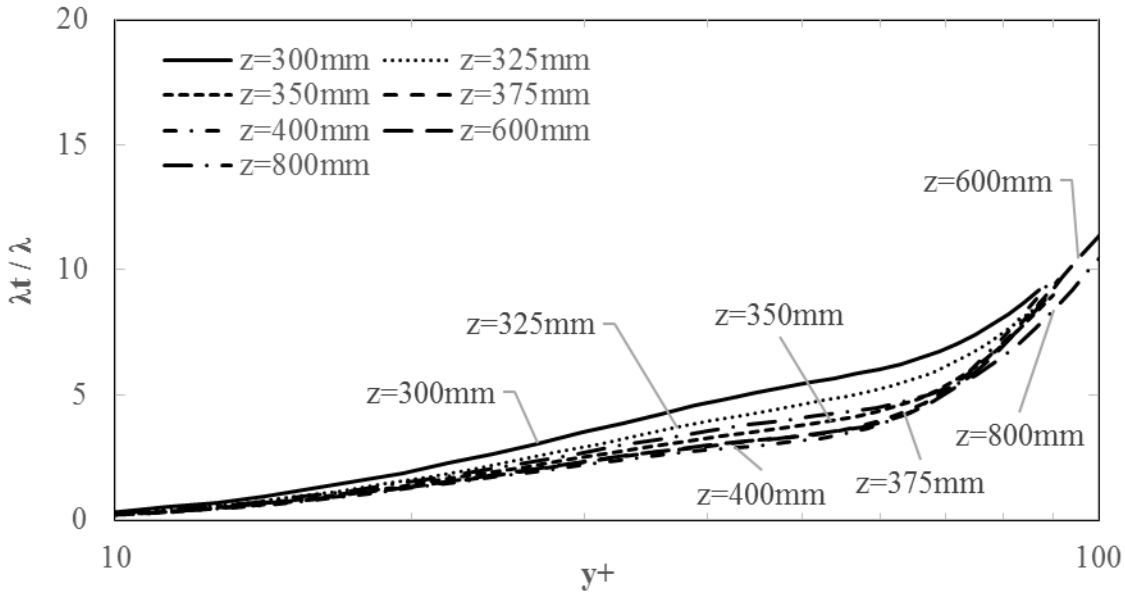

Figure 96: Ratio between turbulent thermal conductivity and thermal conductivity vs. y+ at various z locations of case T47315 using FLUENT and Yang-Shih Low-Re k-ε turbulence model. A y+ value of zero corresponds to the location of line 180deg.

Similar to the plot of μ_t/μ profiles of Figure 95 the λ_t/λ profiles at all z locations follow a similar trend, and are very low in value over all y^+ values. This suggests that the flow should be close to laminar in the near wall region, leading to HTD. This is not the case, since there are no spikes in heater rod surface temperature, as seen in Figure 91. Since λ_t/λ is closely related to μ_t/μ, the low turbulence conditions at the inlet, as evident by the low Reynolds number, is the cause of the very low λ_t/λ values. Similarly, low λ_t/λ values were found in case B1 of Rohde et al., as can be seen in Figure 21 in Section 4.4.1, even though HTD did not occur. The Reynolds number at the inlet for that case was 11,189, which is also close to laminar.

7.4.2. Case T65000

The numerical results of case T65000 of the Wang et al. experiments will be presented here.

Figure 97 gives the average heater rod surface temperatures of case T65000 using CFX and the SST and k-ε turbulence models, FLUENT and the SST turbulence model, as well as the experimental temperatures. The experimental data are for the heater rod surface temperatures for certain fluid bulk enthalpies. Additionally, Figure 98 gives the average heater rod surface temperatures plotted against z. There are no experimental data plotted in this figure because the z location is identical for all the experimental temperatures, only the bulk enthalpy is different due to the different inlet temperatures.

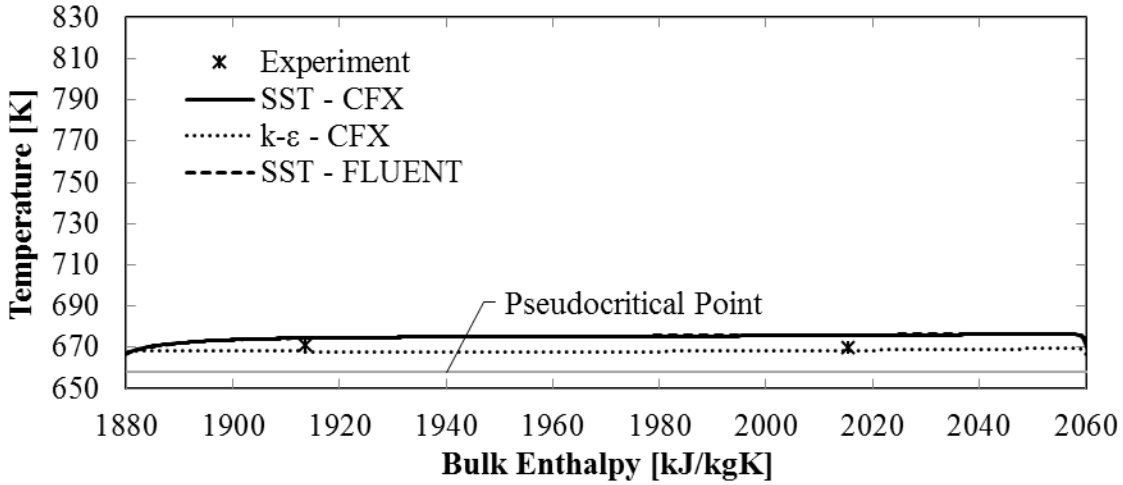

Figure 97: Average heater rod surface temperatures vs. bulk enthalpy for case T65000 using CFX with the SST and k-ε turbulence model, and FLUENT with the SST turbulence model.

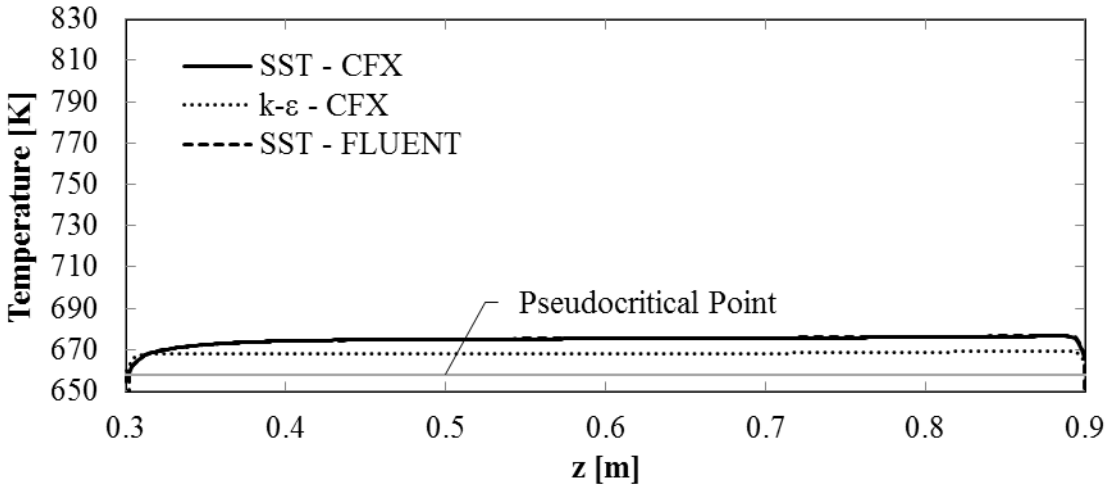

Figure 98: Average heater rod surface temperatures vs. z for case T65000 using CFX with the SST and k-ε turbulence model, and FLUENT with the SST turbulence model.

CFX and FLUENT give nearly identical results when the SST turbulence model is used; hence, it is difficult to distinguish between these two lines in Figure 97. The SST turbulence model slightly over-predicts the heater rod surface temperature, while the k-ε turbulence model slightly under-predicts heater rod surface temperatures.

Figure 99 gives the average heater rod surface temperatures of case T65000 using the RNG k-ε, Lam-Bremhorst Low-Re k-ε, and Yang-Shih Low-Re k-ε turbulence models using FLUENT. The experimental data are for the heater rod surface temperatures for certain fluid bulk enthalpies. Figure 100 gives the average heater rod surface temperatures plotted against z.

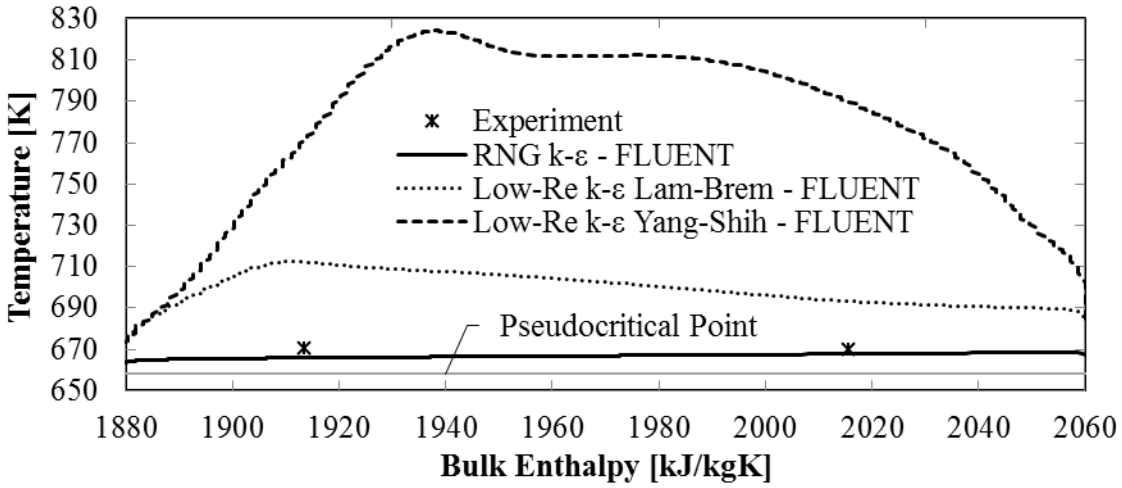

Figure 99: Average heater rod surface temperatures vs. bulk enthalpy for case T65000 using FLUENT.

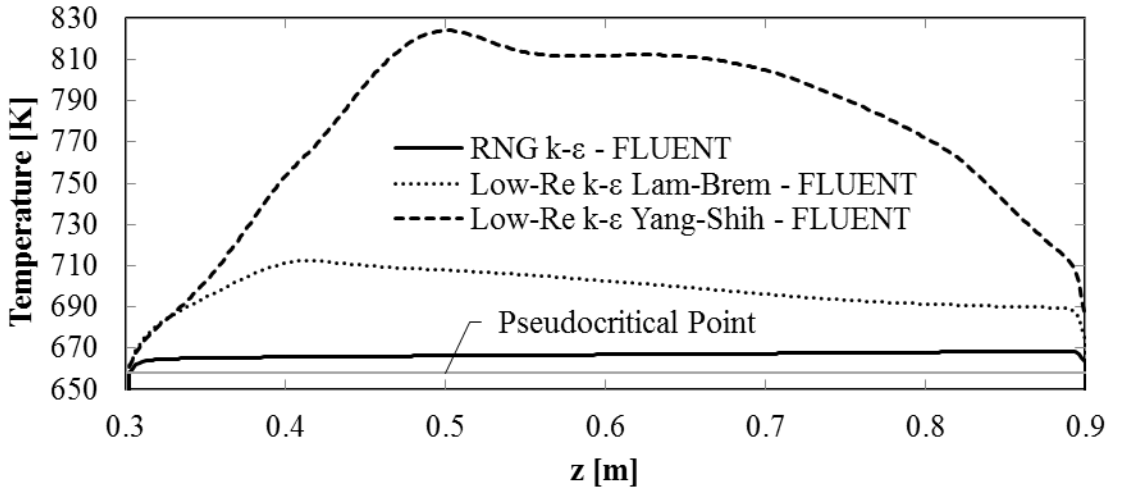

Figure 100: Average heater rod surface temperatures vs. z for case T65000 using FLUENT.

Both Low-Re k-ε turbulence models predict significant HTD, as evident by the over-prediction the heater rod surface temperatures, even though HTD does not occur in the experimental data. The Yang-Shih Low-Re k-ε turbulence model predicts a spike in heater rod surface temperature, a slight drop and plateau, followed by a gradual decline. The spike in the heater rod surface temperature of the Lam-Bremhorst case occurs earlier and with lower magnitude than the Yang-

Shih case, followed by a steady gradual decline. The RNG k-ε turbulence model slightly under-predicts heater rod surface temperatures.

To quantify the differences between the numerical predictions and experimental results of heater rod surface temperatures for case T65000, the $RMS_{RN,T}$ is calculated and presented in Table 86. Equation (113) in Section 4.3 is used to calculate the $RMS_{RN,T}$, where the reference temperatures come from the experimental data, and the maximum range in temperatures is calculated from the numerical result with the greatest range in surface temperatures. The maximum range is 174.13 [K], and comes from the numerical result using the Yang-Shih Low-Re k-ε turbulence model. This method for calculating $RMS_{RN,T}$ is slightly different than for the cases of Rohde et al. and Richards, and was done for reasons already given, in Section 7.4.1.

Table 86: $RMS_{RN,T}$ between numerical results and experimental results for case T65000.

Case	$RMS_{RN,T}$ [%]
T65000 SST CFX	2.80
T65000 k-ε CFX	1.27
T65000 SST FLUENT	2.85
T65000 RNG k-ε FLUENT	2.23
T65000 Low-Re k-ε Lam-Bremhorst FLUENT	19.30
T65000 Low-Re k-ε Yang-Shih FLUENT	63.49

The k-ε turbulence model, when implemented with CFX, had the smallest overall deviation from the experimental heater rod surface temperatures. The RNG k-ε turbulence model, when implemented with FLUENT; the SST turbulence model, when implemented with CFX; and the SST turbulence model, when implemented with FLUENT provide the second, third, and fourth closest results when compared with the experimental data, respectively. The Low-Re k-ε

turbulence models of Lam-Bremhorst and Yang-Shih do a very poor job of predicting the experimental data, with the Yang-Shih model giving the worst predictions.

The Yang-Shih Low-Re k-ε turbulence model shows the most severe HTD, therefore this case will be used to plot certain variables and derived quantities with respect to y^+ at different z locations to show the factors that cause HTD to be predicted. The y^+ values for the plots were calculated using Equation (34) in Section 3.1.2.1, where Δn is replaced with the wall distance. A y^+ value of zero corresponds to the location of line 180deg, shown in Figure 82 in Section 6.2, and y^+ increases in value normal to the heater surface. Figure 101 shows the heater rod surface temperatures along lines 0deg, 90deg, and 180deg for this case, plotted against z. The location of these lines on the x-y plane can be seen in Figure 82 in Section 6.2.

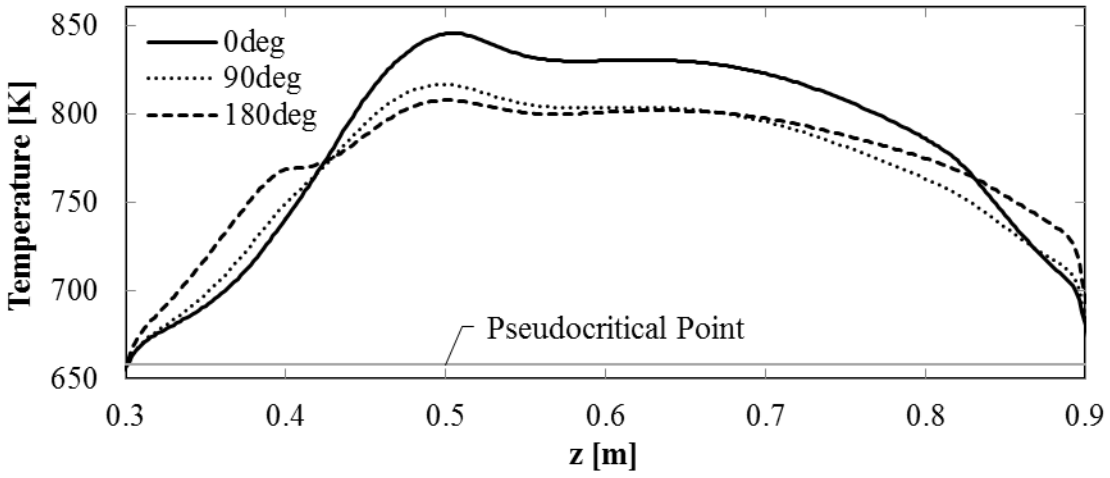

Figure 101: Heater rod surface temperatures along lines 0deg, 90deg, and 180deg for case T65000 using FLUENT and the Yang-Shih Low-Re k-ε turbulence model.

As can be seen in the plot, the heater rod surface temperatures quickly exceed the pseudocritical temperature when the flow reaches the start of the heated section, at z = 300 [mm]. There is a gradual rise in surface temperatures until a maximum is reached at approximately z = 500 [mm]

for all lines. The surface temperatures then drop slightly, plateau, and finally decrease in value towards the outlet.

For the following plots of solution variables and derived quantities, the y^+ value corresponding to the midpoint of the flow channel is different at each z location, and so it may appear as though the profiles end prematurely for certain z location profiles. Unless otherwise stated, a y^+ value of zero corresponds to the location of line 180deg in the following plots.

Figure 102 shows the near wall fluid temperature profiles at various z locations of case T65000 using FLUENT and the Yang-Shih Low-Re k-ε turbulence model.

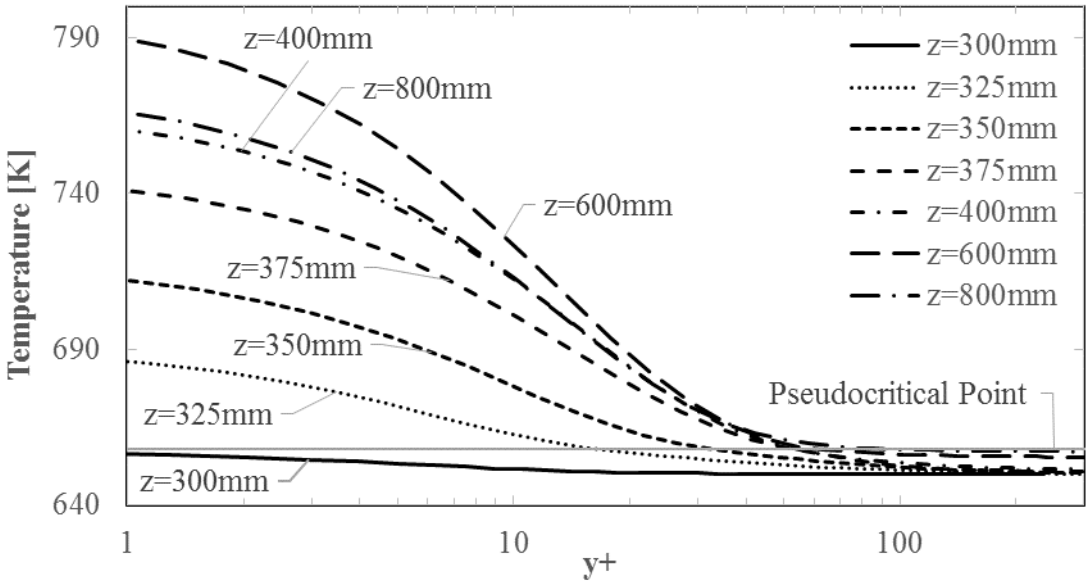

Figure 102: Fluid temperature vs. y+ at various z locations of case T65000 using FLUENT and the Yang-Shih Low-Re k-ε turbulence model. A y+ value of zero corresponds to the location of line 180deg.

The fluid reaches the start of the heated section at z = 300 [mm] and the fluid closest to the heater rod surface is already at a temperature close to the pseudocritical temperature. This is a result of axial heat conduction towards the unheated portions of the heater rods, causing the ends

of the unheated sections that are in contact with the heated sections of the heater rods to increase in temperature. This causes the fluid closest to the wall to increase in temperature before the start of the heated section.

The temperature of the fluid closest to the wall already exceeds the pseudocritical temperature before z = 325 [mm]. As the fluid progresses down the heater rod, the bulk of the fluid progressively increases in temperature, since the y^+ location where the fluid reaches the pseudocritical temperature gradually increases from y^+ = 18 at z = 325 [mm] to y^+= 86 at z = 800 [mm].

Figure 103 shows the near wall fluid density profiles at various z locations of case T65000 using FLUENT and the Yang-Shih Low-Re k-ε turbulence model.

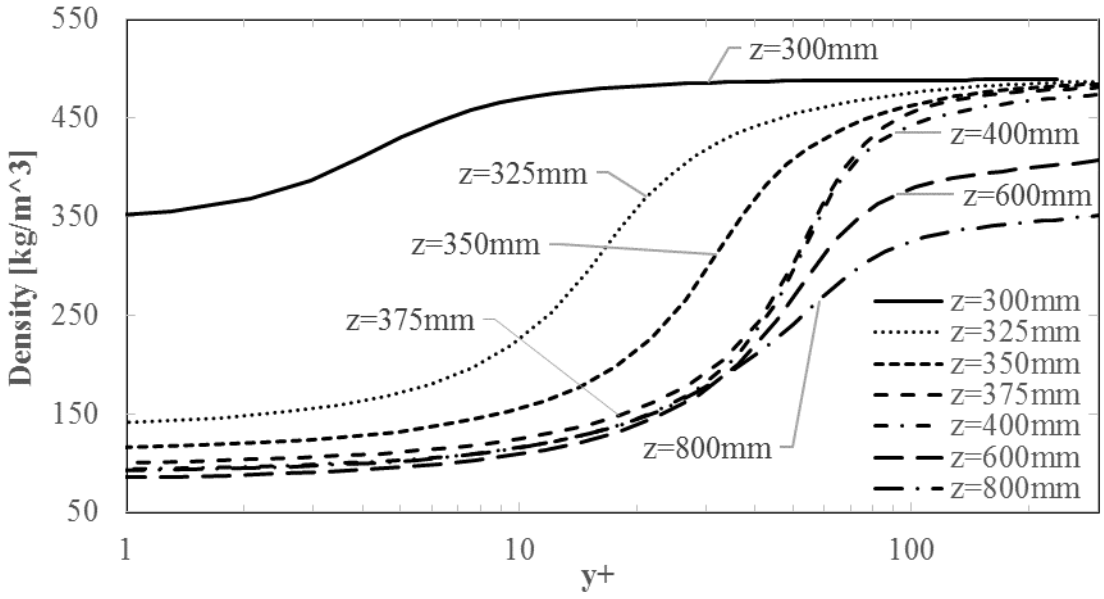

Figure 103: Density vs. y+ at various z locations of case T65000 using FLUENT and the Yang-Shih Low-Re k-ε turbulence model. A y+ value of zero corresponds to the location of line 180deg.

Looking at the density profile at z = 325 [mm], the density of the fluid closest to the heater rod surface is significantly less in relation to the freestream density because the temperature of the fluid exceeds the pseudocritical temperature in the region closest to the heater rod surface at this z location. This large density gradient gradually diminishes in size as the fluid in the freestream region increases in temperature.

Figure 104 shows the near wall velocity *w* profiles at various z locations of case T65000 using FLUENT and the Yang-Shih Low-Re k-ε turbulence model.

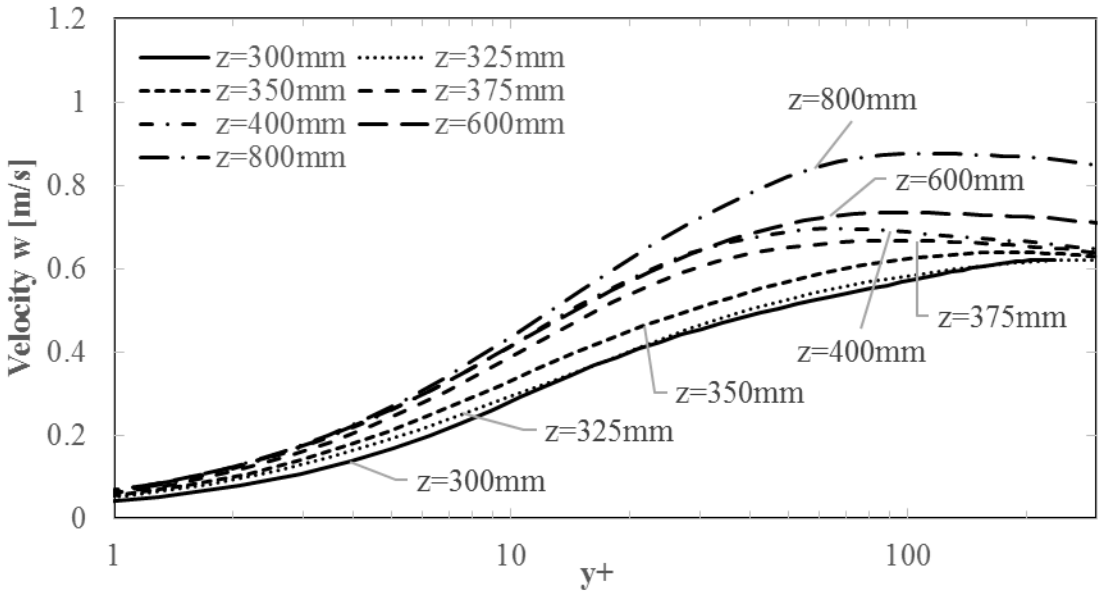

Figure 104: Velocity w vs. y+ at various z locations of case T65000 using FLUENT and the Yang-Shih Low-Re k-ε turbulence model. A y+ value of zero corresponds to the location of line 180deg.

The velocity profile of the fluid at the start of the heated section, at z = 300 [mm], appears to follow the log law of the wall, where there is a viscous sublayer adjacent to the wall, and a log law region away from the wall that is separated from the viscous sublayer by a buffer layer.

As the density of the fluid in the near wall region decreases, the effects of buoyancy become apparent: the low density fluid close to the wall at z = 375 [mm] accelerates upwards, as shown by the slight bump in velocity *w* around y^+ = 55. The high density fluid in the freestream maintains its velocity since the density in this region does not change as significantly as the fluid closest to the wall. A flattening of the velocity *w* profile is apparent at the z = 375, 400, 600, 800 [mm] locations, compared to the original velocity *w* profile at z = 300 [mm]. As the temperature of the fluid further away from the wall increases, the velocity of the fluid increases, since the density decreases.

Similar trends in the velocity *w* profiles can be found at other locations in the fluid domain. The velocity *w* profiles at z = 400 [mm] for locations 0deg, 90deg, and 180deg are plotted with respect to y^+ in Figure 105. The location of 0deg, 90deg, and 180deg on the x-y plane can be seen in Figure 82 in Section 6.2.

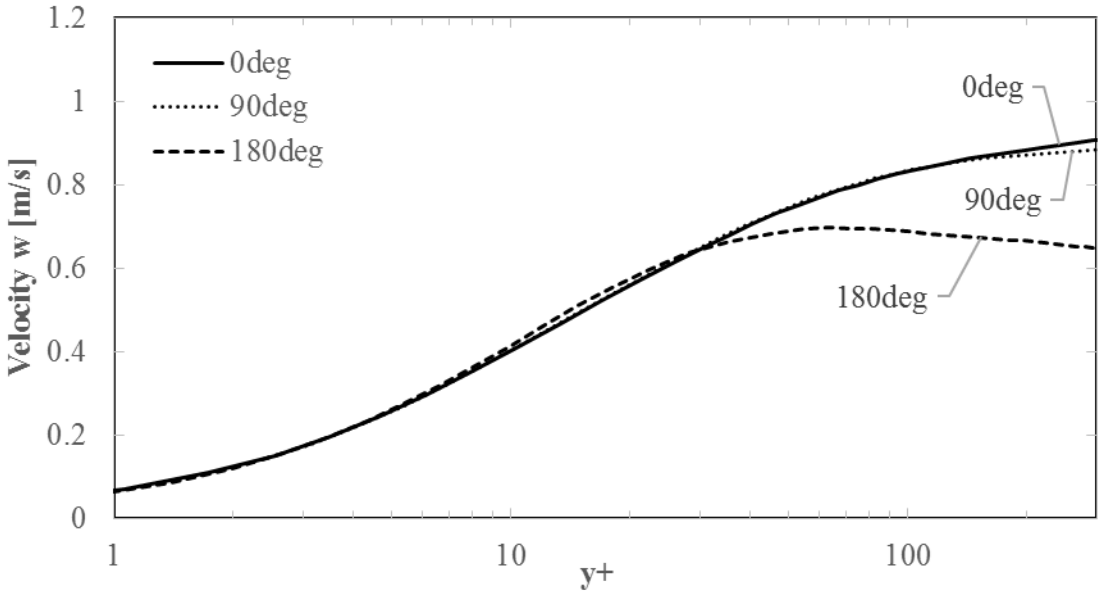

Figure 105: Velocity w profiles at z = 400 [mm] for case T65000 using FLUENT and the Yang-Shih Low-Re k-ε turbulence model at locations 0deg, 90deg, and 180deg.

The velocity profiles are nearly identical for 0deg and 90deg, and the maximum value of velocity *w* at 180deg is less than that at 0deg and 90deg. The largest spike in velocity *w* occurs at 0deg, followed closely by 90deg, then finally 180deg. These trends somewhat coincide with the heater rod surface temperature profiles along z, given in Figure 101, where the largest spike in heater rod surface temperature occur just after z = 400 [mm] at 0deg, followed by 90deg and 180deg, in descending order. All three locations feature a flattened velocity profile compared to the initial velocity profile at z = 300 [mm], as seen in Figure 104.

Similar trends in the velocity *w* profile can be found in the other case that has a spike in heater rod surface temperature, and are absent from cases without spikes in heater rod surface temperatures. The velocity *w* profiles at z = 400 [mm] for all case T65000 results are given in Figure 106.

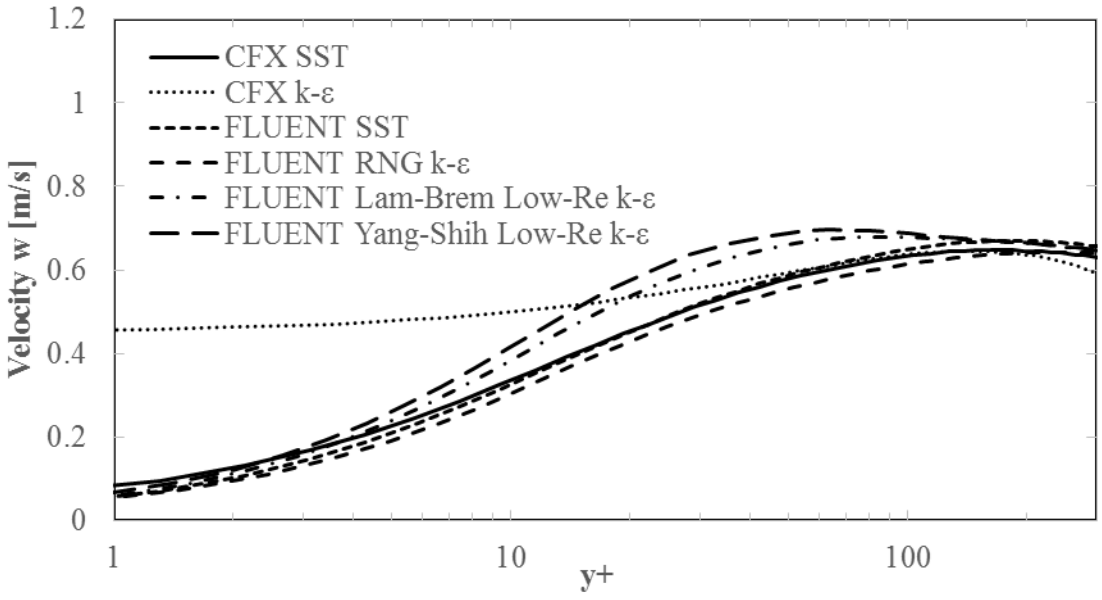

Figure 106: Velocity w vs. y+ at z = 400 [mm] for all case T65000 results. A y+ value of zero corresponds to the location of line 180deg.

For the two cases with spikes in heater rod surface temperature, Lam-Bremhorst and Yang-Shih Low-Re k-ε, the velocity w profile just before or at the same z location as the temperature spike also shows a spike in velocity w in the near wall region. A spike in velocity w is not present in the near wall region for cases that do not have spikes in heater rod surface temperature: k-ε, RNG k-ε, and both SST results.

The velocity w of the k-ε case does not decrease in value close to the wall, such as for the other cases. The reason for this is that the k-ε turbulence model, when implemented with CFX, relies on scalable wall functions to determine the velocity in this near wall region. The turbulence model uses Equation (66) in Section 3.1.3.1 to determine the non-dimensional velocity in the near wall region as a function of the non-dimensional wall distance, y^*_{Scale}. However the value of the non-dimensional wall distance can never be less than 11.06 according to Equation (63) in Section 3.1.3.1. This means the velocity can never be less than the value of the velocity at y^*_{Scale} = 11.06. This non-dimensional wall distance, y^*_{Scale}, is closely related to non-dimensional wall distance used in the plots, y^+, since they are both functions of wall distance and fluid properties.

Similarly, the non-dimensional temperature in the near wall region is a function of the non-dimensional wall distance, as seen in Equation (66) in Section 3.1.3.1, and so the fluid temperature can never be less than the temperature at y^*_{Scale} = 11.06. The greatest fluid temperature gradients occur close to the wall, as can be seen in the plot of fluid temperature at various z locations shows the near wall fluid temperature profiles at various z locations using the Yang-Shih Low-Re k-ε turbulence model, Figure 102. Because scalable wall functions, used by the k-ε turbulence model, do not allow the fluid temperature to vary in this region close to the

wall, the wall temperature cannot experience sudden increases in temperature that would be evident by large temperature gradients in the fluid in the region close to the wall.

The largest gradients in velocity w close to the wall occur for cases with spikes in heater rod surface temperature. These trends match those described by He et al. where a flattened velocity profile develops after the spike in velocity, leading to a reduction in shear stress. This reduction in shear stress leads to a reduction in turbulence, causing flow laminarization. The reduction in turbulence can be seen by observing the eddy viscosity in the near wall region.

Profiles for the ratio between eddy viscosity and dynamic viscosity, μ_t/μ, at various z locations of case T65000 using FLUENT and the Yang-Shih Low-Re k-ε turbulence model are shown in Figure 107.

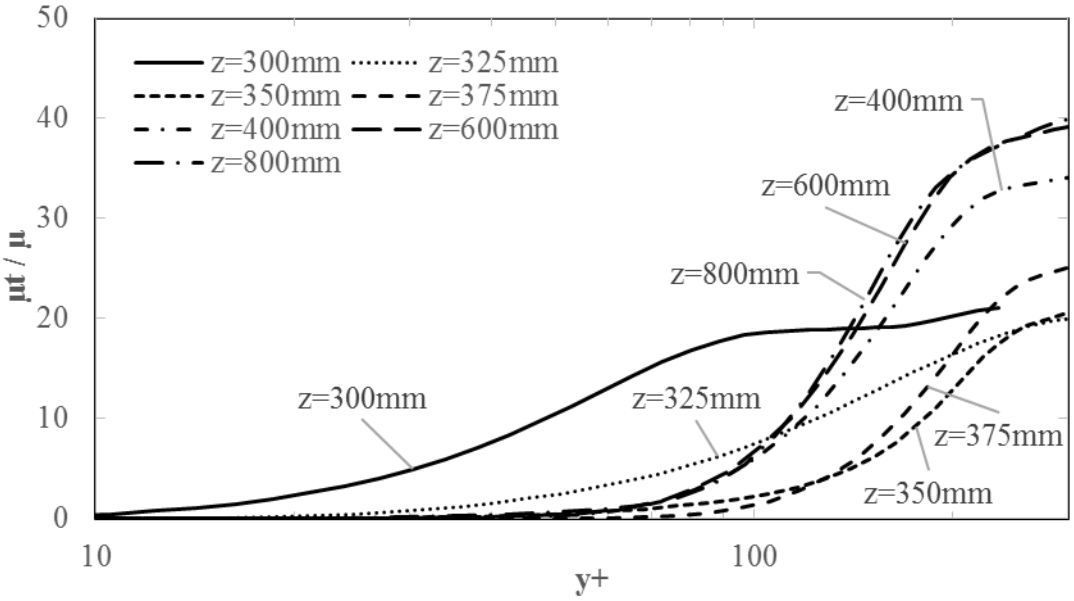

Figure 107: Eddy viscosity to dynamic viscosity ratio vs. y+ at various z locations of case T65000 using FLUENT and the Yang-Shih Low-Re k-ε turbulence model. A y+ value of zero corresponds to the location of line 180deg.

This ratio can be used as an indicator of the strength of turbulence at any location. For a laminar flow, μ_t/μ should be less than one, and for flows with strong turbulence, μ_t/μ should be much greater than one. When the flow reaches the start of the heated section, at z = 300 [mm], the value of μ_t/μ is approximately one at y^+ = 14. The values of μ_t/μ increase away from the wall towards the freestream. This may be viewed as follows: the flow is close to laminar at y^+ = 14, and becomes more turbulent towards the freestream. The μ_t/μ values decrease in general as the flow progresses along z, to the point where, at z = 375 [mm], the value of μ_t/μ is one at approximately y^+ = 95. This means that a larger region of near-laminar flow is present at z = 375 [mm] than at any other z location. As can be seen in Figure 101, the first spike in heater rod surface temperature along line 180deg occurs at z = 400 [mm], which is just after the location of the largest region of near-laminar fluid. Another spike in heater rod surface temperature occurs at z = 500 [mm]. As the fluid progresses past z = 375 [mm], the values of the μ_t/μ ratio increase away from the wall yet remain relatively low in the near wall region compared to the initial values at z = 300 [mm].

Figure 108 shows profiles of the turbulent thermal conductivity to thermal conductivity ratio, λ_t/λ, at various z locations of case T65000 using FLUENT and the Yang-Shih Low-Re k-ε turbulence model.

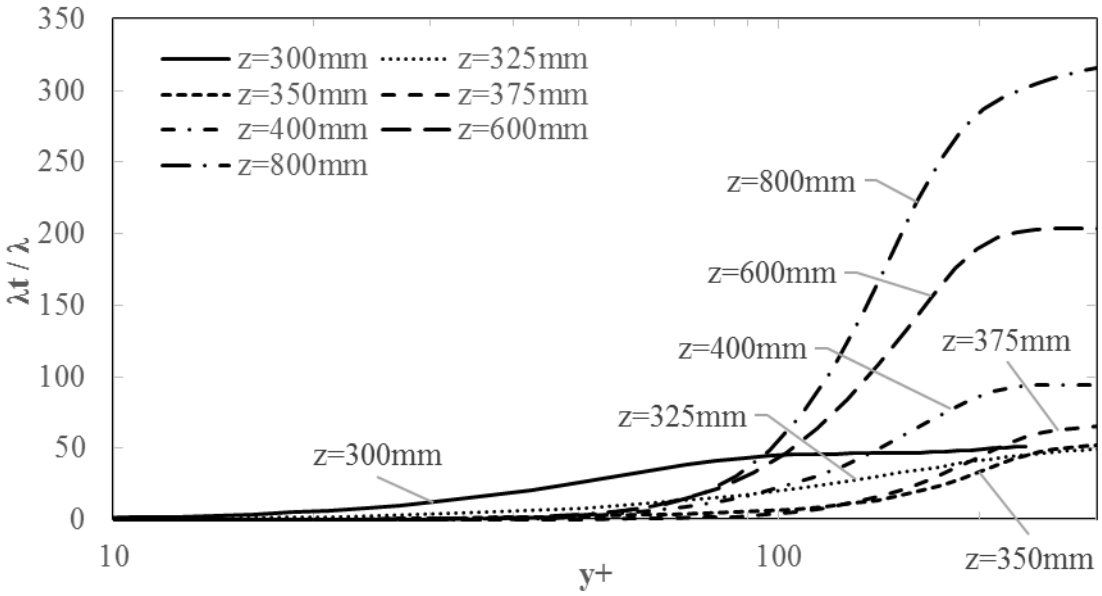

Figure 108: Turbulent thermal conductivity to thermal conductivity ratio vs. y+ at various z locations of case T65000 using FLUENT and the Yang-Shih Low-Re k-ε turbulence model. A y+ value of zero corresponds to the location of line 180deg.

The turbulent thermal conductivity, λ_t, is defined by Equation (14) in Section 3.1.1, and can be used as an indicator of the contribution to heat transfer by turbulence effects. For a laminar flow, λ_t/λ should be less than approximately one, and for flows with strong turbulence, λ_t/λ should be much greater than one. Looking at the governing equations for energy used by CFX and FLUENT, Equation (10) and (11) in Section 3.1.1, respectively, it can be seen that a fluid should conduct heat much better when the λ_t/λ ratio is much greater than one. This is because the turbulent thermal conductivity acts in the same way as the thermal conductivity in conducting heat. When the λ_t/λ ratio is less than approximately one, the flow is close to laminar and heat conduction through the fluid should be less than if the λ_t/λ ratio was greater.

The λ_t/λ profiles at the various z locations, as shown in Figure 108 follow the same trend as the μ_t/μ profiles at the same z locations, as shown in Figure 107. This trend indicates that the eddy viscosity has a direct effect on the turbulent thermal conductivity, and the ability of the fluid to

conduct heat. The largest region of near-laminar fluid exists at z = 375 [mm] in the near wall region. The eddy viscosity in this region is very low, leading to a very low turbulent thermal conductivity, which reduces the ability of the fluid to conduct heat. This region of fluid with a low thermal conductivity effectively acts as an insulator, causing the adjacent heater rod surface temperature to spike in temperature, as the heat from the heater rod cannot be transferred to the fluid as easily as in other regions where the fluid does not have such large regions of near-laminar fluid.

The λ_t/λ profiles at z = 400 [mm] at locations 0deg, 90deg, and 190deg are plotted with respect to y^+ in Figure 109.

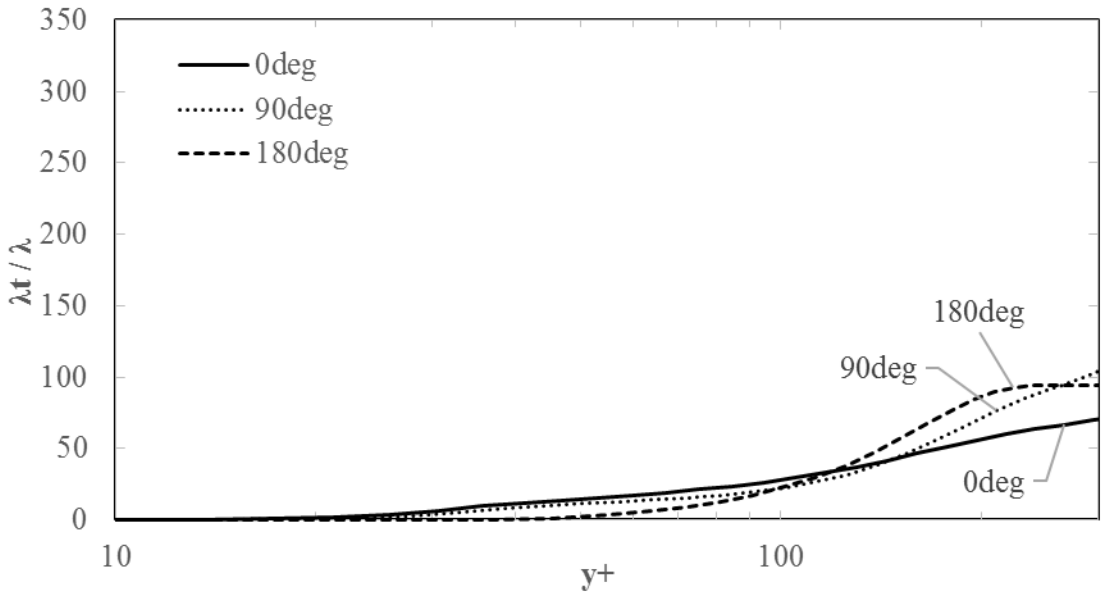

Figure 109: Turbulent thermal conductivity to thermal conductivity ratio profiles at z = 400 [mm] for case T65000 using FLUENT and the Yang-Shih Low-Re k-ε turbulence model at locations 0deg, 90deg, and 180deg.

As can be seen in the figure, the λ_t/λ values are small in the near wall region for all locations at z = 400 [mm]. The 180deg location experiences a local maximum in heater rod surface

temperature at z = 400 [mm], as can be seen in Figure 101, which corresponds to the large region where the λ_t/λ ratio is close to one. The 90deg and 0deg locations will experience a maximum surface temperature at z = 500 [mm], which explains why the λ_t/λ ratios are not as low as the 180deg location at z = 400 [mm] for y^+ values less than 100.

The λ_t/λ profiles at various z locations of case T65000 using FLUENT and the Lam-Bremhorst Low-Re k-ε turbulence model are given by Figure 110. This is the only other turbulence model that predicted HTD for the T65000 case.

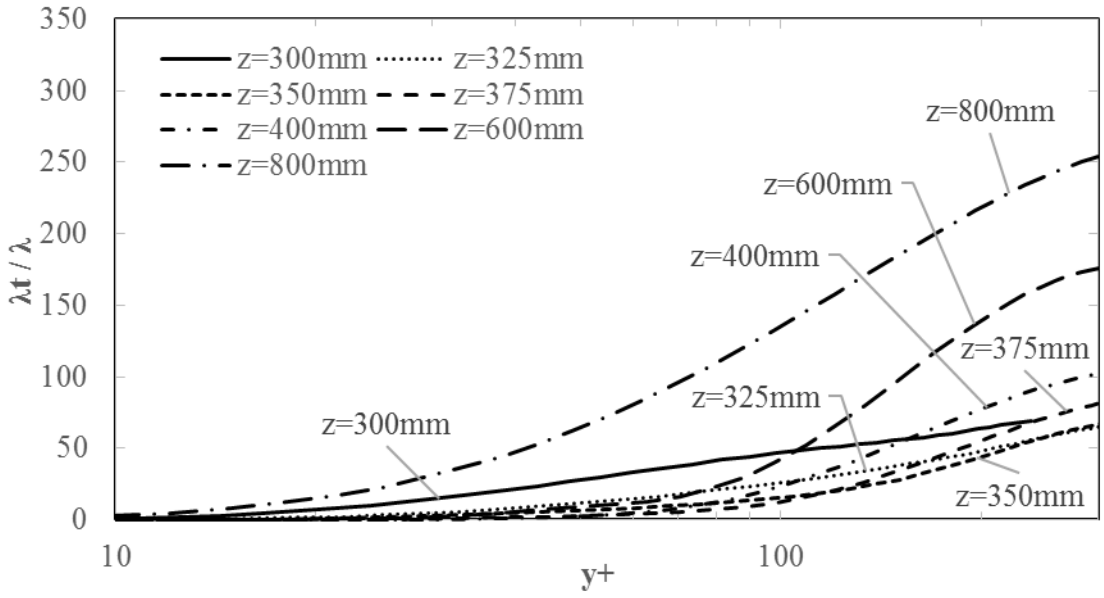

Figure 110: Turbulent thermal conductivity to thermal conductivity ratio vs. y+ at various z locations of case T65000 using FLUENT and the Lam-Bremhorst Low-Re k-ε turbulence model. A y+ value of zero corresponds to the location of line 180deg.

For the Lam-Bremhorst Low-Re k-ε result, the heater rod surface temperature spikes around z = 400 [mm], as seen in Figure 100. The λ_t/λ ratio is relatively small in the near wall region at this z location. This region where the λ_t/λ ratio is relatively small gradually decreases in size until z = 800 [mm], at which point the λ_t/λ ratio is greater over all y^+ values compared to the initial

λ_t/λ profile at z = 300 [mm]. These large λ_t/λ values at z = 800 [mm] explain why the heater rod surface temperatures are steadily decreasing in value at this z location.

The heater rod surface temperatures of the Yang-Shih result are not decreasing in value to the same degree as the Lam-Bremhorst result at z = 800 [mm], which explains why the λ_t/λ values are not as large in the near wall region at this location, as seen in Figure 108.

The k-ε, RNG k-ε, and both SST results do not show HTD for case T65000, as can be seen in Figure 97 and Figure 99. The profiles of the λ_t/λ ratio at various z locations for the SST result using FLUENT and the k-ε result using CFX are shown by Figure 111 and Figure 112, respectively. The trends in λ_t/λ found in the SST results using FLUENT are similar to those found in the SST results using CFX and the RNG k-ε result using FLUENT.

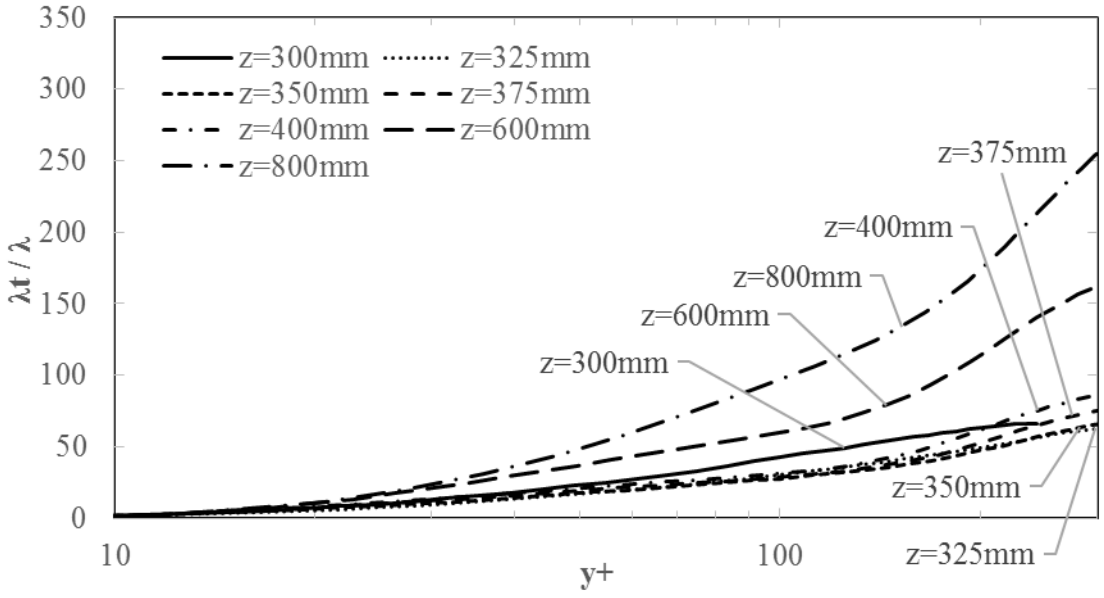

Figure 111: Turbulent thermal conductivity to thermal conductivity ratio vs. y+ at various z locations of case T65000 using FLUENT and the SST turbulence model. A y+ value of zero corresponds to the location of line 180deg.

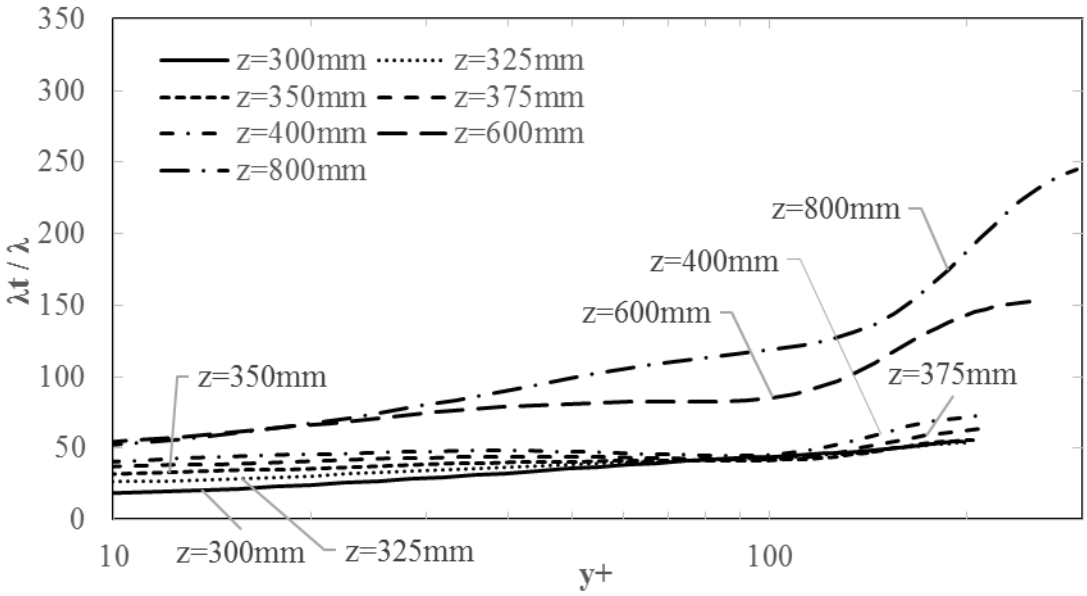

Figure 112: Turbulent thermal conductivity to thermal conductivity ratio vs. y+ at various z locations of case T65000 using CFX and the k-ε turbulence model. A y+ value of zero corresponds to the location of line 180deg.

For the SST result using FLUENT, the λ_t/λ ratio has a value of one at approximately y^+ = 9 at the z = 375 [mm] location. For the remaining z locations, the λ_t/λ ratio is relatively lower in value compared to the Low-Re k-ε results. The near-laminar regions at these z locations is therefore confined to a much smaller regions for this SST result than for the results with HTD. The fluid therefore does not effectively act as an insulator due to this smaller region of near-laminar fluid.

For the k-ε result using CFX, the λ_t/λ ratio never drops below 12. Effects of turbulence are therefore experienced by the fluid over the entire near wall region. The lack of a spike in heater rod surface temperature is therefore expected, as there is no near-laminar region in the fluid that would act as an insulator.

As was concluded in Section 5.4.2 for case 2 of the Richards Experiments, the λ_t/λ ratio is directly related to the μ_t/μ ratio and, more importantly, the eddy viscosity. Each of the turbulence models that are used in the present study calculates the turbulence kinetic energy, k, and either the turbulence dissipation rate, ε, or the specific turbulence dissipation, ω, in order to calculate the eddy viscosity, μ_t. In the near wall region the various wall treatments: automatic wall treatment, scalable wall functions, and EWT, are the dominant factor that determine the profiles of the velocity, temperature, turbulence kinetic energy, and either the turbulence dissipation rate, or the specific turbulence dissipation. The governing equations of the turbulence quantities (k, ω, ε, and μ_t) and wall treatments differ between the various turbulence models, and the values of various coefficients of these equations sometimes differ. It is because of these differences in the way each turbulence model, and the associated wall treatment, calculate the eddy viscosity and solution variables in the near wall region that the λ_t/λ ratio differs between the results of each turbulence model, and the reason why certain turbulence models give spikes in heater rod surface temperature.

The k-ε, RNG k-ε, and SST turbulence models all rely on various wall treatments that explicitly determine the near wall temperature using various equations: Equation (40) in Section 3.1.2.1 for automatic wall treatment, Equation (52) in Section 3.1.2.2 for EWT, and Equation (66) in Section 3.1.3.1 for scalable wall functions. However, Low-Re k-ε turbulence models do not use equations to explicitly determine the temperature in the near wall region. Instead, they rely solely on the governing equation of energy, Equation (11) in Section 3.1, to determine the temperature. A reason why both the Yang-Shih and Lam-Bremhorst Low-Re k-ε turbulence models predict HTD while the other turbulence models do not could be the Low-Re k-ε turbulence models do

not explicitly calculate the temperature in the near wall region, unlike the other turbulence models.

He et al. compared numerical results obtained from RANS turbulence models with those obtained from DNS, and found that RANS turbulence models are not able to accurately model the turbulent heat flux, $\lambda_t \frac{\partial T}{\partial x_j}$. They attributed some of the inaccuracies of RANS turbulence models to using a constant turbulent Prandtl number for the turbulence thermal conductivity, λ_t. The fact that RANS turbulence models cannot accurately model the turbulent thermal conductivity explains why some turbulence models, specifically the Yang-Shih and Lam-Bremhorst Low-Re k-ε turbulence models, predict HTD when it is not present in experimental data.

CHAPTER 7: SUMMARY AND CONCLUSIONS

The heated rod bundle experiments presented in Rohde et al. 2015, Richards 2012, and Wang et al. 2014 were numerically simulated in this study using the CFD codes ANSYS CFX and ANSYS FLUENT. Two cases from Rohde et al. and Richards, and three cases from Wang et al. were simulated. At least one case from each of the three experiments involved fluid that exceeded the pseudocritical temperature at some point along the length of the respective heated rod bundle. The two-equation RANS turbulence models that were used in this study, along with the wall treatment for each turbulence model, if applicable, are: SST with automatic wall treatment, SST with EWT, k-ε with scalable wall functions, RNG k-ε with EWT, Yang-Shih Low-Re k-ε, and Lam-Bremhorst Low-Re k-ε.

7.1 Turbulence Models and HTD

Evidence supporting the description of HTD given by He et al., presented in Section 4.4.2, 5.4.2, and 7.4.2, was found in the present study. For cases with HTD, the velocity w profile in the near wall region flattens to a greater degree than for cases without HTD. This flattening leads to a reduction in shear stress that causes a reduction in turbulence. This reduction in turbulence can be seen as a reduction in the eddy viscosity, or μ_t/μ ratio as is plotted in this study, in the near wall region. The turbulent thermal conductivity, which is directly related to the strength of the turbulence through the eddy viscosity (Equation (14) in Section 3.1.1), decreases in response to the decreased eddy viscosity. HTD becomes visible in the numerical results in the form of spikes in surface temperature. However, the magnitude and location along z where the spikes in surface

temperature occur are never predicted very accurately by the various turbulence models used in this study.

The k-ε and RNG k-ε turbulence models are never able to reproduce the spikes in surface temperature seen in the experimental data of the cases with HTD: Rohde et al. case B2, Richards case 2, and Wang et al. case T65000. A possible explanation for this is that both turbulence models are ε-based and use similar equations to determine the eddy viscosity, μ_t. The Low-Re k-ε turbulence models of Yang-Shih and Lam-Bremhorst are also ε-based, but their equation for eddy viscosity is different from that of the k-ε and RNG k-ε turbulence models, in that it also includes a damping function, f_μ. This damping function is sensitive to conditions very close to the wall, unlike the scalable wall functions used by the k-ε turbulence model. The damping functions approach zero as the distance to the wall approaches zero, thereby causing the eddy viscosity to approach zero in the viscous sublayer, a physically realistic phenomena. Scalable wall functions do not allow for the eddy viscosity to reach zero in the viscous sublayer, as can be seen in the plots of eddy viscosity ratio μ_t/μ for the various k-ε cases. The RNG k-ε turbulence model, implemented using FLUENT in this study, relies on EWT, which allows the eddy viscosity to approach zero in the region close to the wall, as can be seen in the plots of eddy viscosity ratio μ_t/μ for the various RNG k-ε cases. It would stand to reason that the RNG k-ε turbulence model, using EWT, should be able to predict HTD, just as the Low-Re k-ε turbulence models are able to predict HTD, because they use near wall treatment that allows for variables in the region close to the wall to take on values that are reserved for this region. However, this is not seen in any of the cases studied in this experiment. A possible reason for this is that the conditions of the experimental cases that were numerically simulated are not ideal for the RNG

k-ε turbulence model to predict HTD. To support this argument, the SST turbulence model, which predicted HTD for case 2 of the Richards experiments, did not predict the HTD that the Low-Re k-ε turbulence models predicted for case B2 of Rohde et al. experiments and case T65000 of Wang et al. experiments

The SST turbulence model, implemented using CFX and FLUENT, uses automatic wall treatment and EWT, respectively. The SST turbulence models predicted HTD in only one case, case 2 of the Richards Experimental data. The Low-Re k-ε turbulence models predicted HTD in three cases: case B2 of Rohde et al., case 2 of Richards, and case T65000 of Wang et al. Even if EWT is used with a turbulence model, HTD may still not be predicted when other wall treatments predict HTD: the Low-Re k-ε turbulence models with damping functions predicted HTD in case B2 of Rohde et al. and case T65000 of Wang et al., but the SST turbulence model with both automatic wall treatment and EWT did not predict HTD.

Low-Re k-ε turbulence models predicted HTD, even when none was present in the experimental data, such as case T65000 of Wang et al. The k-ε and RNG k-ε turbulence models, using scalable wall functions and EWT respectively, are not able to predict HTD in any of the experimental cases presented in this study. The SST turbulence model, using either automatic wall treatment or EWT, is able to predict HTD in one experimental case: case 2 of the Richards Experiment.

The use of a wall treatment that allow for the solution of variables in the viscous sublayer and buffer region: automatic wall treatment and EWT, do not guarantee that HTD will be predicted when it occurs in the experimental data. Wall treatment that does not allow for the solution of variables in the viscous sublayer and buffer region, scalable wall functions, are not be able to reproduce HTD, since they are not able to simulate the conditions necessary for HTD to occur.

7.2 CFX vs. FLUENT

A major drawback to using CFX with fluids other than water that do not have constant thermophysical properties, such as the R12 used for the Richards cases in this study, is that there are no built-in options to properly implement these fluids. Custom FORTRAN subroutines must be created by the user. FLUENT does not suffer from this drawback, since any one of a large number of real fluid models can be used by entering a few text commands in the command prompt.

As long as the working fluid is water, then setting up runs in CFX and FLUENT take similar amounts of time and require nearly identical information, in terms of boundary conditions, domain properties, initial conditions, etc. An exception to this is when using FLUENT with meshes that have many surfaces that must be defined as the same boundary condition, such as defining a symmetry boundary condition on many surfaces: each individual surface must be selected and defined as the desired boundary condition. In CFX, multiple surfaces can be selected at the same time, and a single boundary condition can be defined on those surfaces, saving time.

There are no major difference between extracting data from CFX and FLUENT results, only the names of some variables are different, and some variables exist in CFX but not in FLUENT and vice versa. For example, in CFX the variable, c_P, is named 'Specific Heat Capacity **at** Constant Pressure', while in FLUENT this variable is named 'Specific Heat Capacity **At** Constant Pressure'. Also, the variable 'Wall Distance' is available in CFX, which is the wall-normal distance, but is not available in FLUENT.

All things being equal, run times for CFX tend to be shorter than for FLUENT. This makes it especially time consuming to perform multiple runs with large meshes using FLUENT.

7.3 Conclusions

The k-ε turbulence model, implemented using CFX and scalable wall functions, provided numerical results that had the smallest overall deviation from experimental results for cases B1 of Rohde et al, case 2 of Richards, and case T65000 of Wang et al. Of the remaining cases, this turbulence model was the second best at predicting the experimental results of case T47315 of Wang et al., third best at predicting the experimental results of case 3 of Richards, but came in last place in terms of accuracy of predicting case B2 of Rohde et al.

The Yang-Shih Low-Re k-ε turbulence model, implemented using FLUENT, provided numerical results that had the smallest overall deviation from experimental results for case B2 of Rohde et al., case 3 of Richards, and case T47315 of Wang et al., but came in last place in terms of accuracy of predicting case 2 of Richards and case T65000 of Wang et al. For these two cases this turbulence model severely over-predicted the HTD of case 2 of Richards, and predicted severe HTD in the T65000 case of Wang et al., even though there was no HTD present in the experimental data of Wang et al.

Comparing results of the SST turbulence model implemented using different codes and slightly different wall treatment, CFX and FLUENT with automatic wall treatment and EWT respectively, one can see that FLUENT more closely predicts four of the cases presented in this study: case B2 and B1 of Rohde et al., case 3 of Richards, and case T47315 of Wang et al.

For cases with supercritical fluid, FLUENT, using the SST turbulence model, generally predicts greater heated surface temperatures compared to CFX when the SST turbulence model is used.

HTD, seen in up-flow experiments with supercritical fluids, is caused by the combined effects of buoyancy and large variation in thermophysical properties.

7.4 Recommendations

If one had to pick a single turbulence model to simulate the bundle experiments presented in this study, the k-ε turbulence model, implemented using CFX and scalable wall functions, would be the best option. This turbulence model provides numerical results that had the smallest overall deviation from experimental results for three of the six cases that were studied, and predicts the experimental data of the remaining three cases reasonably well, unlike other turbulence models that severely over-predict the experimental data, such as the Yang-Shih and Lam-Bremhorst Low-Re k-ε turbulence models.

To simulate the bundle experiments presented in this study that use water as the coolant, it is recommended that CFX should be chosen over FLUENT. This is due to the shorter run times of CFX and comparable accuracy in numerical solutions between the two codes. To simulate the bundle experiments presented in this study that use R12 as the coolant, FLUENT should be used. This is because thermophysical properties can be quickly defined in FLUENT for a number of fluids, unlike for CFX in which custom FORTRAN subroutines must be created by the user to define these properties for any fluid other than water.

Other turbulence models should be used to simulate the rod bundle experiments presented in the present study in order to gauge their effectiveness at predicting supercritical experiments, most

notably the v^2-f turbulence model, Reynolds stress turbulence models, and Large Eddy Simulation (LES). Ideally, Direct Numerical Simulation (DNS) could be used in order to obtain the most accurate numerical results, but the large amount of computational resources required makes this method impractical at present. Using other CFD codes, commercial or in-house, would allow for the use of other turbulence models which are not available in either CFX or FLUENT.

Additionally, modelling more than $1/12^{th}$ of the seven-rod experiments and more than $1/8^{th}$ of the four-rod experiment may provide different numerical results. Spacers also affect the numerical results. Therefore, it would be ideal to model the entire cross section of the rod bundle experiments and include the spacers, so that the effects of assuming symmetry and spacers can be better understood.

REFERENCES

[1] OECD Nuclear Energy Agency for the Generation IV International Forum, "Technology Roadmap Update For Generation IV Nuclear Energy Systems – January 2014," 2014.

[2] The National Institute of Standards and Technology (NIST), "Reference Fluid Thermodynamic and Transport Properties (REFPROP) v9.0," U.S. Secretary of Commerce on behalf of the United States of America, 2010.

[3] The National Institute of Standards and Technology (NIST), "NIST Chemistry WebBook," U.S. Secretary of Commerce on behalf of the United States of America, 2011. [Online]. Available: http://webbook.nist.gov. [Accessed 2014].

[4] ANSYS, Inc, "ANSYS Release 16.2," Pittsburgh, Pennsylvania, 2015.

[5] I. Pioro and R. Duffey, "Experimental heat transfer in supercritical water flowing inside channels (survey)," *Nuclear Engineering and Design*, vol. 235, pp. 2407-2430, 2005.

[6] D. Groeneveld, S. Tavoularis, P. Raogudla, S. Yang and L. Leung, "Analytical and experimental program of superlight heat transfer research at the Univeristy of Ottawa," *Nuclear Engineering and Technology, Special Issue on the 3rd International Symposium on SCWR*, vol. 40, no. 2, pp. 107-116, 2008.

[7] R. Duffey and I. Pioro, "Experimental heat transfer of supercritical carbon dioxide flowing inside channels (survey)," *Nuclear Engineering Design*, vol. 235, pp. 913-924, 2005.

[8] S. Yoshida and H. Mori, "Heat Transfer to Supercritical Pressures Fluids Flowing in Tubes," in *The 1st International Symposium on Supercritical Water-Cooled Reactor Design and Technology (SCR-2000)*, Tokyo, Japan, 2000.

[9] P. Jiang, Y. Xu, J. Lv, R. Shi, S. He and J. Jackson, "Experimental investigation of convection heat transfer of CO2 at super-critical pressures in vertical mini-tubes and in porous media," *Applied Thermal Engineering*, vol. 24, pp. 1255-1270, 2004.

[10] P. Kirillov, R. Pometko, A. Smirnov, V. Grabezhnai, I. Pioro, R. Duffey and H. Khartabil, "Experimental study on heat transfer to supercritical water flowing in 1- and 4-m-long vertical tubes," in *GLOBAL 2005 International Conference, Nuclear Energy Systems for Future Generation and Global Sustainability*, Tsukuba, Japan, 2005.

[11] S. He, P. Jiang, Y. Xu, R. Shi, W. Kim and J. Jackson, "A computational study of convection heat transfer to CO2 at supercritical pressures in a vertical mini tube," *International Journal of Thermal Sciences*, vol. 44, pp. 521-530, 2005.

[12] E. Pis'menny, V. Razumovskiy, E. Maevskiy, A. Koloskov and I. Pioro, "Heat transfer to supercritical water in gaseous state or affected by mixed convection in vertical tubes," in *Proceedings of the 14th International Conference on Nuclear Engineering*, Miami, Florida, USA, 2006.

[13] H. Kim, H. Kim, J. Song, B. Cho and Y. Bae, "Heat transfer test in a vertical tube using CO2 at supercritical pressures," *Journal of Nuclear Science and Technology,* vol. 44, no. 3, pp. 285-293, 2007.

[14] B. Cho, Y. Kim and Y. Bae, "Prediction of a heat transfer to CO2 flowing in an upward path at a supercritical pressure," *Nuclear Engineering and Technology,* vol. 41, no. 7, pp. 907-920, 2009.

[15] J. Song, H. Kim, H. Kim and Y. Bae, "Heat transfer characteristics of a supercritical fluid flow in a vertical pipe," *Journal of Supercritical Fluids,* vol. 44, pp. 164-171, 2008.

[16] Y. Bae and H. Kim, "Convective heat transfer to CO2 at a supercritical pressure flowing vertically upward in tubes and an annular channel," *Experimental Thermal and Fluid Sciences,* vol. 33, pp. 329-339, 2009.

[17] Y. Bae, H. Kim and D. Kang, "Forced and mixed convection heat transfer to supercritical CO2 vertically flowing in a uniformly-heated circular tube," *Experimental Thermal and Fluid Science,* vol. 34, pp. 1295-1308, 2010.

[18] D. E. Kim and M.-H. Kim, "Experimental investigation of heat transfer in vertical upward and downward supercritical CO2 flow in a circular tube," *International Journal of Heat and Fluid Flow,* vol. 32, pp. 176-191, 2011.

[19] J. Withag, J. Sallevelt, D. Brilman, E. Bramer and G. Brem, "Heat transfer characteristics of supercritical water in a tube: Application for 2D and an experimental validation," *Journal of*

Supercritical Fluids, vol. 70, pp. 156-170, 2012.

[20] G. Zhang, H. Zhang, H. Gu, Y. Yang and X. Cheng, "Experimental and numerical investigation of turbulent convective heat transfer deterioration of supercritical water in vertical tube," *Nuclear Engineering and Design*, vol. 248, pp. 226-237, 2012.

[21] S. Zhang, H. Gu, X. Cheng and Z. Xiong, "Experimental study on heat transfer of supercritical Freon flowing upward in a circular tube," *Nuclear Engineering and Design*, vol. 280, pp. 305-315, 2014.

[22] B. Dyadyakin and A. Popov, "Heat transfer and thermal resistance of tight seven-rod bundle, cooled with water flow at supercritical pressures," *Trans. VTI (In Russian)*, vol. 11, pp. 244-253, 1977.

[23] V. Silin, V. Voznesensky and A. Afrov, "The light water integral reactor with natural circulation of the coolant at supercritical pressure B-500 SKDI," *Nuclear Engineering Design*, vol. 144, pp. 327-336, 1993.

[24] V. G. Razumovskiy, E. N. Pis'mennyy, A. E. Koloskov and I. L. Pioro, "Heat transfer to supercritical water in vertical 7-rod bundle," in *Proceedings of the 16th International Conference on Nuclear Engineering*, Orlando, Florida, USA, 2008.

[25] V. G. Razumovskiy, E. N. Pis'mennyy, A. E. Koloskov and I. L. Pioro, "Heat transfer to supercritical water in vertical annular channel and 3-rod bundle," in *Proceedings of the 17th International Conference on Nuclear Engineering*, Brussels, Belgium, 2009.

[26] M. Mori, T. Kaida, M. Ohno, S. Yoshida and Y. Hamamoto, "Heat transfer to a supercritical pressure fluid flowing in sub-bundle channels," *Journal of Nuclear Science and Technology*, vol. 49, no. 4, p. 373–383, 2012.

[27] G. Richards, "Study of Heat Transfer in a 7-Element Bundle Cooled with the Upward Flow of Supercritical Freon-12," University of Ontario Institute of Technology, 2012.

[28] T. Yang, X. Liu and J. Yang, "Development and validation of a subchannel code applicable for SCWR," in *The 6th International Symposium on Supercritical Water-Cooled Reactors*, Shenzhen, Guangdong, China, 2013.

[29] M. Zhao, H. B. Li, J. Yang, H. Y. Gu and X. Cheng, "Experimental study on heat transfer to supercritical water flowing through circle tubes and 2 x 2 rod bundles.," in *The 6th International Symposium on Supercritical Water-Cooled Reactors (ISSCWR-6)*, Shenzhen, China, 2013.

[30] H. Wang, Q. Bi, L. Wang, H. Lv and L. Leung, "Experimental investigation of heat transfer from a 2 × 2 rod bundle to supercritical pressure water," *Nuclear Engineering and Design*, vol. 275, pp. 205-218, 2014.

[31] M. Rohde, J. W. R. Peeters, A. Pucciarelli, A. Kiss, Y. F. Rao, E. N. Onder, P. Mühlbauer, A. Batta, M. Hartig, V. Chatoorgoon, R. Thiele, D. Chang, S. Tavoularis, D. Novog, D. McClure, M. Gradecka and K. Takase, "A Blind, Numerical Benchmark Study on Supercritical Water Heat Transfer Experiments in a 7-Rod Bundle," in *The 7th International*

Symposium on Supercritical Water-Cooled Reactors, Helsinki, Finland, 2015.

[32] P. Kirillov, R. Pomet'ko, A. Smirnov and V. Grabezhnaia, "Experimental study of heat transfer on rod bundle at supercritical parameters of Freon-12," *Federal Agency for Atomic Energy State Scientific Center of RF-Institute for Physics and Power Engineering Named after A.I., Leypunsky, IPPE, Obninsk*, 2006.

[33] X. Liu, T. Yang and X. Cheng, "Development and assessment of a sub-channel code applicable for trans-critical transient of SCWR," *Nuclear Engineering and Design*, vol. 262, pp. 499-509, 2013.

[34] J. Xiong, X. Cheng and Y. Yang, "Numerical analysis on supercritical water heat transfer in a 2 x 2 rod bundle," *Annals of Nuclear Energy*, vol. 80, pp. 123-134, 2015.

[35] M. E. Shitsman, "Impairment of the heat transmission at supercritical pressures," *High Temperatures*, vol. 1, no. 2, pp. 237-244, 1963.

[36] W. K. Seo, M. H. Kim, M. H. Anderson and L. M. Corradini, "Heat transfer in a supercritical fluid: classification of heat transfer regimes," *Nuclear Technology*, vol. 154, pp. 335-349, 2006.

[37] Q. Wen and H. Gu, "Numerical simulation of heat transfer deterioration phenomenon in supercritical water through vertical tube," *Annals of Nuclear Energy*, vol. 37, pp. 1272-1280, 2010.

[38] H. S. Swenson, J. R. Carver and C. D. Kakarala, "Heat transfer to supercritical water in smooth-bore tubes," *Journal of Heat Transfer,* vol. 87, no. 4, pp. 477-483, 1965.

[39] A. Kiss and A. Aszodi, "Summary for three different validation cases of coolant flow in supercritical water test sections with the CFD code ANSYS CFX 11.0," *Nuclear Technology,* vol. 170, no. 1, pp. 40-53, 2010.

[40] H. Tanaka, N. Nishiwaki and M. Hirata, "Turbulent heat transfer in vertical tubes at supercritical pressures," in *JSME Semi-International Symposium*, Tokyo, Japan, 1967.

[41] C. Dang and E. Hihara, "In-tube cooling heat transfer of supercritical carbon dioxide. Part 2. Comparison of numerical calculation with different turbulence models," *International Journal of Refrigeration,* vol. 27, pp. 748-760, 2004.

[42] J. D. Jackson, The Supercritical Pressure Water Heat Transfer Study at Manchester with a Natural Circulation Test Facility, University of Manchester, UK, 2009.

[43] F. Zhou and D. Novog, "CFD Study of Convective Heat Transfer to Carbon Dioxide and Water at Supercritical Pressures in Vertical Circular Pipes," in *The 19th Pacific Basin Nuclear Conference*, Vancouver, British Columbia, Canada, 2014.

[44] A. Ornatskii, L. Glushchenko and S. Kalachev, "Heat transfer in rising and falling flows of water in tubes of small diameter at supercritical pressures," *Thermal Engineering,* vol. 18, no. 5, pp. 137-141, 1971.

[45] Q. L. Wen and H. Y. Gu, "Numerical investigation of acceleration effect on heat transfer deterioration phenomenon in supercritical water," *Progress in Nuclear Energy,* vol. 53, pp. 480-486, 2011.

[46] K. Yamagata, K. Nishikawa, S. Hasegawa, T. Fujii and S. Yoshida, "Forced convective heat transfer to supercritical water flowing in tubes," *International Journal of Heat and Mass Transfer,* vol. 15, no. 12, pp. 2575-2593, 1972.

[47] S. Kim, Y. Kim, Y. Bae and B. Cho, "Numerical Simulation of the Vertical Upward Flow of Water in a Heated Tube at Supercritical Pressure," in *Proceedings of ICAPP '04*, Pittsburgh, Pennsylvania, USA, 2004.

[48] X. Cheng, B. Kuang and Y. Yang, "Numerical analysis of heat transfer in supercritical water cooled flow channels," *Nuclear Engineering and Design 237 (2007),* vol. 237, no. 3, p. 240–252, 2007.

[49] J. Yang, Y. Oka, Y. Ishiwatari, J. Liu and J. Yoo, "Numerical investigation of heat transfer in upward flows of supercritical water in circular tubes and tight fuel rod bundles," *Nuclear Engineering and Design,* vol. 237, no. 4, p. 420–430, 2007.

[50] M. Sharabi and W. Ambrosini, "Discussion of heat transfer phenomena in fluids at supercritical pressure with the aid of CFD models," *Annals of Nuclear Energy,* vol. 36, pp. 60-71, 2009.

[51] J. Gou, Z. Shang, Y. Ishiwarari, Y. Oka, M. Yamakawa and S. Ikejiri, "CFD analysis of heat

transfer in subchannels of a super fast reactor," *Nuclear Engineering and Design,* vol. 240, no. 7, p. 1819–1829, 2010.

[52] Y. Zhang, C. Zhang and J. Jiang, "Numerical simulation of heat transfer of supercritical fluids in circular tubes using different turbulence models," *Journal of Nuclear Science and Technology*, vol. 48, no. 3, pp. 366-373, 2011.

[53] J. Li, J. Yu, G. Jiang and J. Yu, "Assessment of Performance of Turbulence Models of CFX in Predicting Supercritical Water Heat Transfer in a Vertical Tube," in *20th International Conference on Nuclear Engineering and the ASME 2012 Power Conference*, Anaheim, California, USA, 2012.

[54] H. Wang, Q. Bi, Z. Yang, W. Gang and R. Hu, "Experimental and numerical study on the enhanced effect of spiral spacer to heat transfer of supercritical pressure water in vertical annular channels," *Applied Thermal Engineering*, vol. 48, pp. 436-445, 2012.

[55] X. Y. Xu, M. Zeng, H. B. Zhu and Q. W. Wang, "Numerical simulation and comparison of turbulent heat transfer in supercritical and subcritical water," *Progress in Computational Fluid Dynamics,* vol. 13, no. 3/4, pp. 141-151, 2013.

[56] R. Weinberg, "Experimental and theoretical study of buoynacy effects in forced convection to supercritical pressure carbon dioxide," PhD thesis, University of Manchester, 1972.

[57] S. He, W. S. Kim, P. X. Jiang and J. D. Jackson, "Simulation of mixed convection heat transfer to carbon dioxide at supercritical pressure," *Proceedings of the Institution of*

Mechanical Engineers, Part C: Journal of Mechanical Engineering Science, vol. 218, no. 11, pp. 1281-1296, 2004.

[58] L. F. Glushchenko and O. F. Gandzyuk, "Temperature conditions at the wall of an annular channel with internal heating at supercritical pressures," *High Temp.*, p. 734–738, 1972.

[59] L. Liu, Z. Xiao, X. Yan, X. Zeng and Y. Huang, "Numerical simulation of heat transfer deterioration phenomenon to supercritical water in annular channel," *Annals of Nuclear Energy*, vol. 53, pp. 170-181, 2013.

[60] S. Mokry, "Development of a Heat-Transfer Correlation for Supercritical Water in Supercritical Water-cooled Reactor Applications," The Faculty of Energy Systems and Nuclear Science, University of Ontario Institute of Technology, 2009.

[61] A. Farah, "Assessment of FLUENT CFD Code as an Analysis Tool for SCW Applications," Master's Thesis, University of Ontario Institute of Technology, 2012.

[62] M. Sharabi, W. Ambrosini, S. He and J. D. Jackson, "Prediction of turbulent convective heat transfer to a fluid at supercritical pressure in square and triangular channels," *Annals of Nuclear Energy*, vol. 35, p. 993–1005, 2008.

[63] J. K. Kim, H. K. Jeon, J. Y. Yoo and J. S. Lee, "Experimental study on heat transfer characteristics of turbulent supercritical flow in vertical circular/non-circular tubes," in *NURETH-11*, Avignon, France, 2005.

[64] J. Bae, J. Yoo and H. Choi, "Direct numerical simulation of turbulent supercritical flows with heat transfer," *Physics of Fluids*, vol. 17, no. 105104, 2005.

[65] S. He, W. S. Kim and J. H. Bae, "Assessment of performance of turbulence models in predicting supercritical pressure heat transfer in a vertical tube," *International Journal of Heat and Mass Transfer*, vol. 51, pp. 4659-4675, 2008.

[66] Y. Zhang, "Convection Heat Transfer of CO2 at Supercritical Pressures in Mini/Micro Scale Tubes," M.Sc. Dissertation, Tsinghua University, 2006.

[67] M. Bazargan and M. Mohseni, "The significance of the buffer zone of boundary layer on convective heat transfer to a vertical turbulent flow of a supercritical fluid," *The Journal of Supercritical Fluids*, vol. 51, no. 2, p. 221–229, 2009.

[68] M. Mohseni and M. Bazargan, "The effect of the low Reynolds number k-e turbulence models on simulation of the enhanced and deteriorated convective heat transfer to the supercritical fluid flows," *Heat and Mass Transfer*, vol. 47, no. 5, pp. 609-619, 2011.

[69] H. Zahlan, S. Tavoularis, K. Jiang and D. Groeneveld, "Measurements of heat transfer coefficient, CHF and heat transfer deterioration in flows of CO2 at near-critical and supercritical pressures," in *ISSCWR6*, Shenzhen, China, 2006.

[70] H. Wang, Q. Bi, Z. Yang and L. Wang, "Experimental and numerical investigation of heat transfer from a narrow annulus to supercritical pressure water," *Annals of Nuclear Energy*, vol. 80, p. 416–428, 2015.

[71] X. Huang, K. Podila and Y. F. Rao, "CFD simulation of vertical seven-rod bundle cooled with supercritical Freon-12," *AECL Nuclear Review,* vol. 3, no. 1, pp. 17-28, 2014.

[72] S. Zhang, H. Gu, Z. Xiong and S. Gong, "Numerical investigation on heat transfer of supercritical fluid in a vertical 7-rod bundle," *The Journal of Supercritical Fluids,* vol. 92, pp. 8-15, 2014.

[73] D. Chang and S. Tavoularis, "Numerical Study of Supercritical Heat Transfer in a Seven-rod Bundle," in *The 7th International Symposium on Supercritical Water-Cooled Reactors (ISSCWR7)*, Helsinki, Finland, 2015.

[74] ANSYS Inc., "ANSYS 14.5 Help System," Canonsburg, PA, USA, 2012.

[75] C. Bergmann, "Grid Generation Tutorial Using ANSYS ICEM CFD: Wang et al. 2014 Four-Rod Bundle," University of Manitoba, Department of Mechanical Engineering, Winnipeg, Manitoba, Canada, 2015.

[76] F. R. Menter, "Two-equation eddy-viscosity turbulence models for engineering applications," *AIAA Journal*, vol. 32, no. 8, pp. 1598-1605, 1994.

[77] B. E. Launder and B. I. Sharma, "Application of the energy-dissipation model of turbulence to the calculation of flow near a spinning disc," *Letters in Heat and Mass Transfer,* vol. 1, pp. 131-138, 1974.

[78] D. C. Wilcox, "Reassessment of the scale-determining equation for advanced turbulence

models," *AIAA Journal,* vol. 26, no. 11, pp. 1299-1310, 1988.

[79] B. A. Kader, "Temperature and concetration profiles in fully turbulent boundary layers," *International Journal of Heat and Mass Transfer,* vol. 24, no. 9, pp. 1541-1544, 1981.

[80] F. White and G. Christoph, "A Simple New Analysis of Compressible Turbulent Skin Friction Under Arbitrary Conditions," Technical Report AFFDL-TR-70-133, February 1971.

[81] P. Huang, P. Bradshaw and T. Coakley, "Skin Friction and Velocity Profile Family for Compressible Turbulent Boundary Layers," *AIAA Journal,* vol. 31, no. 9, pp. 1600-1604, 1993.

[82] B. Launder and D. Spalding, "The numerical computation of turbulent flows," *Computer Methods in Applied Mechanics and Engineering,* vol. 3, pp. 269-289, 1974.

[83] V. Yakhot, S. A. Orszag, S. Thangam, T. B. Gatski and C. G. Speziale, "Development of turbulence models for shear flows by a double expansion technique," *Physics of Fluids A: Fluid Dynamics,* vol. 4, no. 7, pp. 1510-1520, 1992.

[84] Z. Yang and T. H. Shih, "New time scale based k-epsilon model for near-wall turbulence," *AIAA Journal,* vol. 31, no. 7, pp. 1191-1198, 1993.

[85] C. K. G. Lam and K. Bremhorst, "A modified form of the k-ε model for predicting wall turbulence," *Journal of Fluids Engineering,* vol. 103, no. 3, pp. 456-460, 1981.

[86] W. Wagner, J. R. Cooper, A. Dittmann, J. Kijima, H. J. Kretzschmar, A. Kruse, R. Mareš, K. Oguchi, H. Sato, I. Stöcker, O. Šifner, Y. Takaishi, I. Tanishita, J. Trübenbach and T. Willkommen, "The IAPWS industrial formulation 1997 for the thermodynamic properties of water and steam," *Journal of Engineering for Gas Turbines and Power,* vol. 122, no. 1, pp. 150-184, 2000.

[87] The National Institute of Standards and Technology (NIST), "Reference Fluid Thermodynamic and Transport Properties (REFPROP) Help Documentation," U.S. Secretary of Commerce on behalf of the United States of America, 2010.

[88] Y. S. Touloukian, Thermal Conductivity: Nonmetallic Solids, IFI/Plenum, 1970.

[89] R. S. Graves, T. G. Kollie, D. L. McElroy and K. E. Gilchrist, "The thermal conductivity of AISI 304L stainless steel," *International Journal of Thermophysics,* vol. 12, no. 2, pp. 409-415, 1991.

[90] C. Bergmann, S. J. Ormiston and V. Chatoorgoon, "Sensitivity Studies of Shear Stress Transport Turbulence Model Parameters on the Prediction of Seven-Rod Bundle Benchmark Experiments," *Journal of Nuclear Engineering and Radiation Sciences,* vol. 2, no. 1, 2016.

[91] C. M. Rhie and W. L. Chow, "A Numerical Study of the Turbulent Flow Past an Isolated Airfoil with Trailing Edge Separation," *AIAA Paper 82-0998*, 1982.

[92] T. J. Barth and D. C. Jesperson, "The Design and Application of Upwind Schemes on

Unstructured Meshes," *Technical Report AIAA-89-0366. AIAA 27th Aerospace Sciences Meeting, Reno, Nevada,* 1989.

[93] A. Shelegov, S. Leskin, I. Chusov and V. Slobodchuk, "Experimental investigation of heat transfer in the 7-rod bundle under supercritical parameters of Freon-12," IATE NRNI MEPhI, Obninsk, 2010.

[94] Q. T. Zhou, "Claculation of inner wall temperature for an electrically heated thick-walled tube," *Journal of Nanjing Institute of Technology,* vol. 4, pp. 38-43, 1985.

[95] W. P. Jones and B. E. Launder, "The prediction of laminarization with a two-equation model of turbulence," *International Journal of Heat and Mass Transfer,* vol. 15, pp. 301-314, 1972.

[96] A. A. Townsend, The Structure of Turbulent Shear Flow, 2nd ed., Cambridge: Cambridge University Press, 1976.

[97] B. Launder and N. Sandham, Closure Strategies for Turbulent and Transition Flows, Cambridge, UK: Cambridge University Press, 2002.

APPENDIX A: ADDITIONAL STUDIES

A.1 Description of SST Turbulence Model Parameters

The coefficients found in the transport equations of turbulence kinetic energy (k) and specific turbulence dissipation (ω) have values assigned to them based on simplifications to the equations and results of experimental data. The values of the coefficients can be different for various types of the same model. For example, the original k-ε model of Jones and Launder [95] uses slightly different values for $C_{\varepsilon 1}$ and $C_{\varepsilon 2}$ than the revised k-ε model of Launder and Sharma [77].

The Wilcox k-ω model [78] will be used to explain the origins of the coefficients of the SST model, since the governing equations were based on the k-ω model.

The non-steady turbulence kinetic energy and specific turbulence dissipation transport equations can be simplified for decaying homogeneous, isotropic turbulence as follows:

$$\frac{dk}{dt} = -\beta' \omega k \tag{115}$$

$$\frac{d\omega}{dt} = -\beta \omega^2 \tag{116}$$

The asymptotic solution for turbulence kinetic energy, given in [78] is:

$$k \sim t^{-\beta'/\beta} \tag{117}$$

Experiments of Townsend [96] give a value of 1.25±0.06 for the ratio β'/β. The Wilcox and SST models set the value of this ratio at 6/5 (1.2).

The governing equations of momentum, turbulence kinetic energy, and specific turbulence dissipation can be simplified for an incompressible constant pressure boundary layer in the near wall layer. In this near wall layer, the effects of dynamic viscosity are assumed negligible compared to the effects of eddy viscosity. The simplified equations are:

$$0 = \frac{\partial}{\partial y}\left(\nu_t \frac{\partial U}{\partial y}\right) \tag{118}$$

$$0 = \nu_t \left(\frac{\partial U}{\partial y}\right)^2 - \beta' \omega k + \sigma_k \frac{\partial}{\partial y}\left(\nu_t \frac{\partial k}{\partial y}\right) \tag{119}$$

$$0 = \alpha \left(\frac{\partial U}{\partial y}\right)^2 - \beta \omega^2 + \sigma_\omega \frac{\partial}{\partial y}\left(\nu_t \frac{\partial \omega}{\partial y}\right) \tag{120}$$

Note that the σ_k and σ_ω coefficients in the above simplifications are in the numerator, but in the governing equations section of this thesis the coefficients are in the denominator. This just results from the fact that Wilcox derived the k-ω model with these coefficients in the denominator. The solution to the above equations for the log-law region of the boundary layer is:

$$U = \frac{u_\tau}{\kappa} \ln\left(\frac{u_\tau y}{\nu}\right) \tag{121}$$

$$k = \frac{u_\tau^2}{\sqrt{\beta'}} \tag{122}$$

$$\omega = \frac{u_\tau}{\sqrt{\beta'}\kappa y} \tag{123}$$

where u_τ is the friction velocity. From the above solution and the governing equations, the following equation must hold, according to Wilcox:

$$\alpha = \frac{\beta}{\beta'} - \frac{\sigma_\omega \kappa^2}{\sqrt{\beta'}} \tag{124}$$

When σ_ω and σ_k are in the denominator of the transport equations of turbulence kinetic energy and specific turbulence dissipation (such as for the SST model), then Equation (124) becomes:

$$\alpha = \frac{\beta}{\beta'} - \frac{\kappa^2}{\sigma_\omega \sqrt{\beta'}} \tag{125}$$

Equation (125) will yield a value for the α coefficient when β, β' and σ_ω are assigned values.

The equation for β' can be derived from the solution for turbulence kinetic energy in the log-law region $\left(k = \mu_\tau^2/\sqrt{\beta'}\right)$, and the fact that the Reynolds shear stress (τ) is constant in the near wall region and is equal to u_τ^2:

$$\beta' = \left(\frac{\tau}{k}\right)^2 \tag{126}$$

Experiments described in [96] indicate that the ratio of Reynolds shear stress to turbulence kinetic energy (τ/k) is about 3/10 (0.3) in the near wall region. This gives a value of 0.09 for β'.

The values of σ_k and σ_ω come from a detailed analysis of the defect layer and sublayer. The variation of wake strength in the boundary layer to the dimensionless pressure gradient most closely matches experimental data when σ_k= σ_ω= 0.5 [78]. In CFX, these coefficients are actually 1/0.5 (2.0), since these two coefficients are in the denominator of the transport equations for turbulence kinetic energy and specific turbulence dissipation.

The constant a_1 appearing in the equation for eddy viscosity comes from the shear stress anisotropy:

$$a_1 = 2b_{12} \tag{127}$$

where the normalized Reynolds stress anisotropy is:

$$b_{ij} = \frac{\overline{u_i u_j}}{\overline{u_i u_i}} - \frac{\delta_{ij}}{3} = \frac{\tau_{ij}}{2k} - \frac{\delta_{ij}}{3} \tag{128}$$

In the constant shear stress log region, the ratio τ/k has been found to be 0.3, as previously stated for the constant β'. For the SST model this ratio is set to 0.31 [76]. This leads to the following equation for b_{12}:

$$b_{12} = \frac{\tau}{2k} \tag{129}$$

which leads to a value of 0.31 for a_1.

The SST model uses coefficients of the Wilcox k-ω model in the near wall region and the coefficients of the Launder and Sharma k-ε model away from the wall. The exception to this is the coefficient σ_{k1} of the SST model, as it has been recalibrated from Wilcox's σ_k so that the model properly predicts flat plate log-law behaviour near the wall [97].

The coefficients of the Launder and Sharma k-ε model have been converted in such a way that they can be used in the SST model as follows [97] (coefficients with a subscript of 2 refer to the SST model):

$$\sigma_{k2} = \sigma_k \tag{130}$$

$$\sigma_{\omega 2} = \sigma_\varepsilon \tag{131}$$

$$\beta_2 = C_\mu (C_{\varepsilon 2} - 1) \tag{132}$$

$$\alpha_2 = \frac{\beta_2}{C_\mu} - \frac{\kappa^2}{\sigma_{\omega 2}\sqrt{C_\mu}} = C_{\varepsilon 1} - 1 \tag{133}$$

where σ_ε is calculated using the following formula:

$$\sigma_\varepsilon = \frac{\kappa^2}{\sqrt{C_\mu}(C_{\varepsilon 2} - C_{\varepsilon 1})} \tag{134}$$

A.1.1 Turbulence Production and Dissipation Due to Buoyancy

The turbulence production due to buoyancy term has a single coefficient, a turbulent Schmidt number, σ_ρ. This value is the ratio between rates of turbulent transport of momentum and the turbulent transport of mass. The σ_ρ term has a value of 1.0.

The turbulence dissipation due to buoyancy has the dissipation coefficient C_3 which is equal to 1.0. This coefficient determines the ratio of turbulent production due to buoyancy to turbulence dissipation due to buoyancy.

A.1.2 Turbulent Heat Transfer

The only coefficient appearing in the thermal energy equation is the turbulent Prandtl number, Pr_t. This coefficient is the ratio of eddy viscosity to turbulent thermal diffusivity. Its default value in CFX is 0.9.

A.2 Sensitivity Studies of SST Turbulence Model Parameters for Case B2 of Rohde et al. 2015

Full details of these studies are given in [90].

A.3 Spacer vs. No Spacer for Rohde et al. 2015

Full details of these studies are given in [90].

A.4 Case A1 of Rohde et al. 2015

The SST turbulence model was used with automatic wall treatment and CFX to simulate case A1. This case was simulated in order to provide an overall pressure drop for the GIF SCWR 2013-2014 seven-rod subchannel benchmark exercise. Because case A1 of Rohde et al. was isothermal, temperature data was not produced from the numerical result. The mesh that was used included spacers, since they were found to cause an increase in pressure drop. Tables 87 to 89 give the domain definitions and boundary conditions of case A1.

Table 87: Domain definition and boundary conditions of Rohde et al. 2015 fluid domain, case A1 using CFX.

Fluid	
Domain Properties	Material: Water Turbulence Model: SST Reference Pressure: 24.9449 [MPa] Isothermal
Material Properties	IAPWS-IF97 Database
Inlet	Mass Flow Rate: 0.036569444 [kg/s] Temperature: 297.35 [K] Turbulence: Low Intensity (I = 1 %), Low Eddy Viscosity Ratio (μ_t / μ = 1.0) w = 2.21796 [m/s] Re = 7015.99
Fluid Properties at Inlet	ρ = 1008.2 [kg/m^3] μ = 9.05289x10^{-4} [Pa s] c_p = 4115.77 [J/kgK] λ = 0.61713 [W/mK]
Outlet	Static Pressure: 0 [Pa]
Wall	No-slip at all surfaces

Table 88: Domain definition and boundary conditions of Rohde et al. 2015 cladding 1 and 2 domains, case A1 using CFX.

Cladding 1 and 2	
Domain Properties	Material: Inconel 600
Material Properties	ρ = - 0.3922057147 [kg/m^{3}K] T + 8528.0312491363 [kg/m^3] c_p = 7.524x10^{-7} [J/kgK^4] T^3 - 0.0012939439 [J/kgK^3] T^2 + 0.9069264845 [J/kgK^2] T + 262.8297423839 [J/kg^{1}K^1] λ = 0.0160336023 [W/mK^2] T + 9.6331381197 [W/mK]
Wall	No boundary condition necessary, because of isothermal condition.

Table 89: Domain definition and boundary conditions of Rohde et al. 2015 insulator 1 and 2 domains, case A1 using CFX.

Insulator 1 and 2	
Domain Properties	Material: Boron Nitride
Material Properties	ρ = 2130 [kg/m^3] c_p = 1265.3 [J/kgK] λ = 1.792707x10^{-4} [W/mK^3] T^2 - 0.3714505815 [W/mK^2] T + 298.4687499009 [W/mK]
Wall	No boundary condition necessary, because of isothermal condition.

Table 90: Domain definition and boundary conditions of Rohde et al. 2015 heater 1 and 2 domains, case A1 using CFX.

Heater 1 and 2	
Domain Properties	Material: Nichrome
Material Properties	ρ = 8410 [kg/m^3] c_p = 420 [J/kgK] λ = 0.0179188239 [W/mK^2] T + 4.5115124321 [W/mK]
Wall	No boundary condition necessary, because of isothermal condition.

Table 91: Domain definition and boundary conditions of Rohde et al. 2015 spacer domains, case A1 using CFX.

Spacer	
Domain Properties	Material: AISI 316 Stainless Steel
Material Properties	ρ = 8238 [kg/m^3] c_p = 466.819 [J/kgK] λ = 13.4092 [W/mK]
Wall	No boundary condition necessary, because of isothermal condition.

The overall pressure drop for this case is 67.5 [kPa], and the actual pressure drop from the experiment is 58.1 [kPa]. The numerically determined pressure drop is 16.2 % different from the experiment.

A.5 Numerical Results for Case T60072 of Wang et al.

The numerical results of case T60072 of the Wang et al. experiments are presented here. The SST turbulence model, implemented using automatic wall treatment and EWT using the codes CFX and FLUENT, respectively, and the k-ε turbulence model, implement using scalable wall functions and CFX, were used to generate the results given in Figure 113.

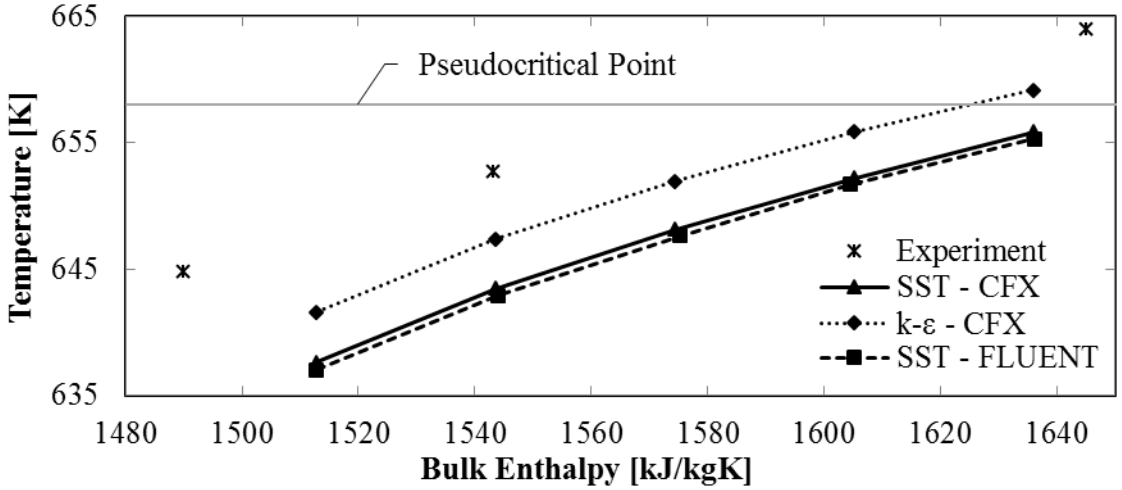

Figure 113: Average heater rod surface temperatures for case T60072 using CFX and FLUENT

The k-ε turbulence model best predicts the experimental heater rod surface temperatures. The results from using the SST turbulence model with both CFX and FLUENT are similar, however CFX closer predicts the experimental heater rod surface temperatures than FLUENT.

APPENDIX B: SPECIFIC DETAILS FOR RUNNING CFX AND FLUENT

B.1 Implementing R12 Properties Using FORTRAN Subroutines in CFX

The following instructions will explain how the thermophysical properties of R12 were enabled when defining a CFX run. Case 2 and the specific heat capacity at constant pressure will be used as the main example when necessary.

A Microsoft Excel workbook was created with six blank worksheets, using the following labels for these worksheets: P4.626_T350K, P4.646_T350K, R12cpCase2-data, R12rhoCase2-data, R12muCase2-data, and R12kCase2-data. The first two worksheets P4.626_T350K and P4.646_T350K contained all the thermophysical properties data of R12 at a pressure of 4.626 [MPa] and 4.646 [MPa], respectively. The thermophysical property data were directly copied from the NIST WebBook website [3] starting at a temperature of 350 [K], and incremental increasing to 525 [K], into the P4.626_T350K and P4.646_T350K worksheets. The temperature increment of 0.5 [K] was used whenever the rate of change in thermophysical property data was small, and 0.1 [K] is used whenever the rate of change in thermophysical property data was large, such as when the specific heat capacity increases then decreases sharply. The first few lines of the P4.626_T350K worksheet are given below as an example:

	A	B	C	D	E	F	G	H
1	T(K)	P(MPa)	**P(Pa)**	rho(kg/m3)	V(m3/kg)	i(kJ/kg)	h(kJ/kg)	E(J/g*K)
2	3.500E+02	4.626E+00	4.626E+06	1.125E+03	8.888E-04	2.741E+02	2.782E+02	1.240E+00
3	3.505E+02	4.626E+00	4.626E+06	1.123E+03	8.908E-04	2.746E+02	2.787E+02	1.242E+00
4	3.510E+02	4.626E+00	4.626E+06	1.120E+03	8.929E-04	2.752E+02	2.793E+02	1.244E+00
5	3.515E+02	4.626E+00	4.626E+06	1.117E+03	8.950E-04	2.757E+02	2.799E+02	1.245E+00
6	3.520E+02	4.626E+00	4.626E+06	1.115E+03	8.971E-04	2.763E+02	2.805E+02	1.247E+00
7	3.525E+02	4.626E+00	4.626E+06	1.112E+03	8.992E-04	2.769E+02	2.810E+02	1.249E+00
8	3.530E+02	4.626E+00	4.626E+06	1.109E+03	9.013E-04	2.774E+02	2.816E+02	1.250E+00
9	3.535E+02	4.626E+00	4.626E+06	1.107E+03	9.035E-04	2.780E+02	2.822E+02	1.252E+00
10	3.540E+02	4.626E+00	4.626E+06	1.104E+03	9.057E-04	2.786E+02	2.828E+02	1.253E+00
11	3.545E+02	4.626E+00	4.626E+06	1.101E+03	9.080E-04	2.791E+02	2.833E+02	1.255E+00
12	3.550E+02	4.626E+00	4.626E+06	1.099E+03	9.102E-04	2.797E+02	2.839E+02	1.257E+00
13	3.555E+02	4.626E+00	4.626E+06	1.096E+03	9.125E-04	2.803E+02	2.845E+02	1.258E+00
14	3.560E+02	4.626E+00	4.626E+06	1.093E+03	9.149E-04	2.809E+02	2.851E+02	1.260E+00
15	3.565E+02	4.626E+00	4.626E+06	1.090E+03	9.172E-04	2.814E+02	2.857E+02	1.262E+00
16	3.570E+02	4.626E+00	4.626E+06	1.087E+03	9.196E-04	2.820E+02	2.863E+02	1.263E+00
17	3.575E+02	4.626E+00	4.626E+06	1.085E+03	9.220E-04	2.826E+02	2.869E+02	1.265E+00
18	3.580E+02	4.626E+00	4.626E+06	1.082E+03	9.245E-04	2.832E+02	2.875E+02	1.267E+00

I	J	K	L	M	N	O
Cv(J/g*K)	Cp(J/g*K)	**Cp(J/kg*K)**	Sound Spd(m/s)	J-T(K/MPa)	mu(Pa*s)	k(W/m*K)
6.465E-01	1.134E+00	1.134E+03	3.442E+02	4.626E-01	1.165E-04	5.273E-02
6.470E-01	1.138E+00	1.138E+03	3.420E+02	4.757E-01	1.158E-04	5.256E-02
6.475E-01	1.141E+00	1.141E+03	3.399E+02	4.891E-01	1.151E-04	5.238E-02
6.480E-01	1.144E+00	1.144E+03	3.377E+02	5.028E-01	1.143E-04	5.221E-02
6.486E-01	1.147E+00	1.147E+03	3.355E+02	5.168E-01	1.136E-04	5.204E-02
6.491E-01	1.151E+00	1.151E+03	3.333E+02	5.311E-01	1.129E-04	5.186E-02
6.496E-01	1.154E+00	1.154E+03	3.311E+02	5.457E-01	1.122E-04	5.169E-02
6.502E-01	1.158E+00	1.158E+03	3.289E+02	5.606E-01	1.115E-04	5.151E-02
6.507E-01	1.161E+00	1.161E+03	3.267E+02	5.758E-01	1.108E-04	5.134E-02
6.512E-01	1.165E+00	1.165E+03	3.245E+02	5.914E-01	1.101E-04	5.116E-02
6.518E-01	1.169E+00	1.169E+03	3.223E+02	6.074E-01	1.093E-04	5.098E-02
6.524E-01	1.173E+00	1.173E+03	3.201E+02	6.237E-01	1.086E-04	5.081E-02
6.529E-01	1.177E+00	1.177E+03	3.178E+02	6.404E-01	1.079E-04	5.063E-02
6.535E-01	1.181E+00	1.181E+03	3.156E+02	6.575E-01	1.072E-04	5.045E-02
6.541E-01	1.185E+00	1.185E+03	3.133E+02	6.750E-01	1.065E-04	5.027E-02
6.547E-01	1.189E+00	1.189E+03	3.110E+02	6.929E-01	1.058E-04	5.009E-02
6.553E-01	1.193E+00	1.193E+03	3.087E+02	7.113E-01	1.051E-04	4.991E-02

Figure 114: First lines of the P4.626_T350K worksheet. Table has been split into top and bottom to fit on page.

The ‘P(Pa)’ and ‘Cp(J/kg*k)’ columns were manually added after all the thermophysical property data was added from the NIST WebBook website. The columns that contain the pertinent thermophysical data are the ‘rho(kg/m^3)’, ‘Cp(J/kg*k)’, ‘mu(Pa*s)’ and the ‘k(W/m*K)’ columns. These columns contain the density, specific heat capacity at constant pressure, dynamic viscosity, and thermal conductivity data, respectively.

A custom macro, written in the VBA programming language, converted tables of thermophysical property data into Microsoft Excel worksheets that contain the data in a lookup table format for later use in CFX as a FORTRAN subroutine. The following subroutine, when run in Microsoft Excel, will fill the ‘R12cpCase2-data’ worksheet with specific heat capacity at constant pressure data from both the ‘P4.626_T350K’ and ‘P4.646_T350K’ worksheets.

```
Sub R12_properties_fortran()

'!-->fortran sheet name
'FSheet = "R12rhoCase2-data"
'FSheet = "R12cpCase2-data"
'FSheet = "R12nuCase2-data"
FSheet = "R12kCase2-data"

'!-->NIST data sheet name, High pressure
NISTHPSheet = "P4.646_T350K"

'!-->NIST data sheet name, Low pressure
NISTLPSheet = "P4.626_T350K"
'column corresponding to temperature in NIST table
TNIST = 1
'column corresponding to pressure
pNIST = 3
'columns corresponding to density, cp, viscosity, and thermal conductivity in NIST table
rhoNIST = 4
cpNIST = 11
nuNIST = 14
kNIST = 15
'starting column and row in fortran table
c = 1
```

```
r = 1
'starting row in NIST table
rNIST = 3

'!-->Select property to create table for
'NIST = rhoNIST
'NIST = cpNIST
'NIST = nuNIST
NIST = kNIST

'Loop until reached end of NIST table
While Sheets(NISTHPSheet).Cells(rNIST, TNIST) <> ""
   If r = 1 Then
      Sheets(FSheet).Cells(r, c) = "XX     IF (T(ILOC).LE."
   Else
      Sheets(FSheet).Cells(r, c) = "XX     ELSE IF (T(ILOC).LE."
   End If
   Sheets(FSheet).Cells(r, (c + 1)) = Sheets(NISTHPSheet).Cells(rNIST, TNIST)
   Sheets(FSheet).Cells(r, (c + 2)) = ") THEN"

   '<property>1 low pressure
   r = r + 1
   If NIST = rhoNIST Then
      Sheets(FSheet).Cells(r, c) = "XX      RHO1="
   ElseIf NIST = cpNIST Then
      Sheets(FSheet).Cells(r, c) = "XX      CP1="
   ElseIf NIST = nuNIST Then
      Sheets(FSheet).Cells(r, c) = "XX      NU1="
   ElseIf NIST = kNIST Then
      Sheets(FSheet).Cells(r, c) = "XX      K1="
   End If

   Sheets(FSheet).Cells(r, (c + 1)) = (Sheets(NISTLPSheet).Cells(rNIST, NIST) -
Sheets(NISTLPSheet).Cells((rNIST - 1), NIST)) / (Sheets(NISTLPSheet).Cells(rNIST, TNIST) -
Sheets(NISTLPSheet).Cells((rNIST - 1), TNIST))
   Sheets(FSheet).Cells(r, (c + 1)).NumberFormat = "0.00000000000E+00"
   Sheets(FSheet).Cells(r, (c + 2)) = "*(T(ILOC)-"
   Sheets(FSheet).Cells(r, (c + 3)) = Sheets(NISTLPSheet).Cells((rNIST - 1), TNIST)
   Sheets(FSheet).Cells(r, (c + 4)) = ")+("
   Sheets(FSheet).Cells(r, (c + 5)) = Sheets(NISTLPSheet).Cells((rNIST - 1), NIST)
   Sheets(FSheet).Cells(r, (c + 5)).NumberFormat = "0.00000000000E+00"
   Sheets(FSheet).Cells(r, (c + 6)) = ")"

   '<property>2 high pressure
   r = r + 1
```

```
   If NIST = rhoNIST Then
      Sheets(FSheet).Cells(r, c) = "XX      RHO2="
   ElseIf NIST = cpNIST Then
      Sheets(FSheet).Cells(r, c) = "XX      CP2="
   ElseIf NIST = nuNIST Then
      Sheets(FSheet).Cells(r, c) = "XX      NU2="
   ElseIf NIST = kNIST Then
      Sheets(FSheet).Cells(r, c) = "XX      K2="
   End If
   Sheets(FSheet).Cells(r, (c + 1)) = (Sheets(NISTHPSheet).Cells(rNIST, NIST) -
Sheets(NISTHPSheet).Cells((rNIST - 1), NIST)) / (Sheets(NISTHPSheet).Cells(rNIST, TNIST)
- Sheets(NISTHPSheet).Cells((rNIST - 1), TNIST))
   Sheets(FSheet).Cells(r, (c + 1)).NumberFormat = "0.00000000000E+00"
   Sheets(FSheet).Cells(r, (c + 2)) = "*(T(ILOC)-"
   Sheets(FSheet).Cells(r, (c + 3)) = Sheets(NISTHPSheet).Cells((rNIST - 1), TNIST)
   Sheets(FSheet).Cells(r, (c + 4)) = ")+("
   Sheets(FSheet).Cells(r, (c + 5)) = Sheets(NISTHPSheet).Cells((rNIST - 1), NIST)
   Sheets(FSheet).Cells(r, (c + 5)).NumberFormat = "0.00000000000E+00"
   Sheets(FSheet).Cells(r, (c + 6)) = ")"

   '<property>(ILOC) at T(ILOC)
   r = r + 1
   If NIST = rhoNIST Then
      Sheets(FSheet).Cells(r, c) = "XX      RHO(ILOC)=((RHO2-RHO1)/("
   ElseIf NIST = cpNIST Then
      Sheets(FSheet).Cells(r, c) = "XX      CP(ILOC)=((CP2-CP1)/("
   ElseIf NIST = nuNIST Then
      Sheets(FSheet).Cells(r, c) = "XX      NU(ILOC)=((NU2-NU1)/("
   ElseIf NIST = kNIST Then
      Sheets(FSheet).Cells(r, c) = "XX      K(ILOC)=((K2-K1)/("
   End If
   Sheets(FSheet).Cells(r, (c + 1)) = (Sheets(NISTHPSheet).Cells(rNIST, pNIST) -
Sheets(NISTLPSheet).Cells(rNIST, pNIST))
   Sheets(FSheet).Cells(r, (c + 2)) = "))*(P(ILOC)-"
   Sheets(FSheet).Cells(r, (c + 3)) = Sheets(NISTLPSheet).Cells(rNIST, pNIST)
   Sheets(FSheet).Cells(r, (c + 4)) = ")+CP1"
   If NIST = rhoNIST Then
      Sheets(FSheet).Cells(r, (c + 4)) = ")+RHO1"
   ElseIf NIST = cpNIST Then
      Sheets(FSheet).Cells(r, (c + 4)) = ")+CP1"
   ElseIf NIST = nuNIST Then
      Sheets(FSheet).Cells(r, (c + 4)) = ")+NU1"
   ElseIf NIST = kNIST Then
      Sheets(FSheet).Cells(r, (c + 4)) = ")+K1"
   End If
```

```
   rNIST = rNIST + 1
   r = r + 1
Wend

'modify last "else if" statement
r = r - 4
Sheets(FSheet).Cells(r, c) = "XX     ELSE"
Sheets(FSheet).Cells(r, (c + 1)) = ""
Sheets(FSheet).Cells(r, (c + 2)) = ""
r = r + 4
Sheets(FSheet).Cells(r, c) = "XX     END IF"

End Sub
```

This subroutine is also used to fill the ‘R12rhoCase2-data’, ‘R12muCase2-data’, and ‘R12kCase2-data’ worksheets by removing and adding comments where necessary at the beginning of the subroutine.

After the ‘R12cpCase2-data’, ‘R12rhoCase2-data’, ‘R12muCase2-data’, and ‘R12kCase2-data’ worksheets were populated with their respective thermophysical property data, each of the worksheets was saved separately as a .F file, with the ‘–data’ tag removed from each of the filenames. These new files, ‘R12cpCase2.F’, ‘R12rhoCase2.F’, ‘R12muCase2.F’, and ‘R12kCase2.F’ were moved onto a Linux server where the CFX runs were to be performed. These files were then modified slightly as follows, to insure the files conform to the FORTRAN language format. The following text is entered in a terminal. (% is not entered, it symbolizes the start of the command line):

```
% sed –i ‘s/XX/  /g;s/E+/D+/g;s/E-/D-/g’ R12cpCase2.F
```

The above command is repeated for the remaining ‘R12rhoCase2.F’, ‘R12muCase2.F’, and ‘R12kCase2.F’ files.

The .F files created so far still needed to be placed in a template .F file that contains the necessary lines that enable the file to be used as a subroutine in CFX. Below is an example of the FORTRAN subroutine, ‘R12cpCase2.F’, with the lines at the beginning and end added to enable its use in CFX as a subroutine.

```
#include "cfx5ext.h"
dllexport(cp_case2)
      SUBROUTINE CP_CASE2 (
     & NLOC,NRET,NARG,RET,ARGS,CRESLT,CZ,DZ,IZ,LZ,RZ)
C .....
C
C ------------------------------
C        Argument list
C ------------------------------
C
      INTEGER NLOC, NRET, NARG
      CHARACTER CRESLT*(*)
      DOUBLE PRECISION RET(1:NLOC,1:NRET), ARGS(1:NLOC,1:NARG)
C
      INTEGER IZ(*)
      CHARACTER CZ(*)*(1)
      DOUBLE PRECISION DZ(*)
      LOGICAL LZ(*)
      REAL RZ(*)
C
C .....
C
C ------------------------------
C    Executable statements
C ------------------------------
C
C-------------------------------------------------------------
C     RHO, CP, NU, K = RET(1:NLOC,1)
C     T = ARGS(1:NLOC,1)
C     P = ARGS(1:NLOC,2)
C-------------------------------------------------------------
C
C---- Low level user routine
      CALL CP_CASE2_SUB (NLOC,RET(1,1),ARGS(1,1),ARGS(1,2))
C
```

```
      CRESLT = 'GOOD'
      END

      SUBROUTINE CP_CASE2_SUB (NLOC,CP,T,P)
C
C .....
C
C ------------------------------
C        Local Variables
C ------------------------------
      INTEGER NLOC, ILOC
      DOUBLE PRECISION CP(NLOC), T(NLOC), P(NLOC), CP1, CP2
C-------------------------------------------------------
CCC
C-------------------------------------------------------
C --------------------------
C    Executable Statements
C --------------------------
      DO ILOC=1,NLOC
       CP(ILOC) = 0.0
       CP1 = 0.0
       CP2 = 0.0
       IF (T(ILOC).LE.350.5) THEN
        CP1=6.25316778000E+00*(T(ILOC)-350)+(1.13445364575E+03)
        CP2=6.22000760000E+00*(T(ILOC)-350)+(1.13380832518E+03)
        CP(ILOC)=((CP2-CP1)/(20000))*(P(ILOC)-4626000)+CP1
       ELSE IF (T(ILOC).LE.351) THEN
        CP1=6.37543896000E+00*(T(ILOC)-350.5)+(1.13758022964E+03)
        CP2=6.34102592000E+00*(T(ILOC)-350.5)+(1.13691832898E+03)
        CP(ILOC)=((CP2-CP1)/(20000))*(P(ILOC)-4626000)+CP1
       ELSE IF (T(ILOC).LE.351.5) THEN
        CP1=6.50193358000E+00*(T(ILOC)-351)+(1.14076794912E+03)
        CP2=6.46620442000E+00*(T(ILOC)-351)+(1.14008884194E+03)
        CP(ILOC)=((CP2-CP1)/(20000))*(P(ILOC)-4626000)+CP1
```

(Multiple rows of similar code have been omitted)

```
       ELSE IF (T(ILOC).LE.524.5) THEN
        CP1=-3.56766808000E-01*(T(ILOC)-524 )+(8.45312999041E+02)
        CP2=-3.62714288000E-01*(T(ILOC)-524 )+(8.45841875845E+02)
        CP(ILOC)=((CP2-CP1)/(20000))*(P(ILOC)-4626000)+CP1
       ELSE
        CP1=-3.51946428000E-01*(T(ILOC)-524.5)+(8.45134615637E+02)
        CP2=-3.57838400000E-01*(T(ILOC)-524.5)+(8.45660518701E+02)
        CP(ILOC)=((CP2-CP1)/(20000))*(P(ILOC)-4626000)+CP1
       END IF
      END DO
C
      END
```

Various lines must be modified and labels must be changed so that the ‘R12rhoCase2.F’, ‘R12muCase2.F’, and ‘R12kCase2.F’ files can be used with the same template given above.

In order for CFX to use a FORTRAN subroutine as a shared library, the “cfx5mkext” command must be used. An example of using this command is given below, where the text is entered in a terminal on the local system which will also be used to run CFX:

% cfx5mkext –name R12cpCase2 –dest . –double R12cpCase2.F

The FORTRAN subroutine, “R12cpCase2.F”, must be placed in the same location as the desired shared library, and the above command line is executed in this same location. The shared library “R12cpCase2.so” will be created in the present directory.

In CFX-Pre, a User Routine was created with the name, ‘CpRoutine’. The details of this User Routine are as follows:

- Option = User CEL Function
- Calling Name = cp_case2
- Library Name = R12cpCase2
- Library Path = <path to the shared library folder that contains the ‘R12cpCase2.so’ shared library>

A Function was then created with the name, ‘cp’. The details of this Function are as follows:

- Option = User Function

- User Routine Name = CpRoutine
- Argument Units = [K],[Pa]
- Result Units = [J kg^-1 K^-1]

The above procedure, starting with generating a FORTRAN subroutine, must be repeated for the density, thermal conductivity, and dynamic viscosity.

A new material, named R12, was then be created in the Materials tab. In the ‘Specific Heat Capacity’ section of the ‘Material Properties’ tab, the following is entered:

- Option = Value
- Specific Heat Capacity = cp(Temperature, Absolute Pressure)
- Specific Heat Type = Constant Pressure

The density, thermal conductivity, and dynamic viscosity were also given in the ‘Material Properties’ tab in order to fully define R12, or any fluid for that matter. Additionally, the ‘Min. Temperature’ is 350 [K], the ‘Max. Temperature’ is 525 [K], and the ‘Min. Absolute Pres.’ and the ‘Max. Absolute Pres.’ were set to values that are the minimum and maximum expected absolute pressures in the R12 domain, which are 4.626 [MPa] and 4.646 [MPa] for case 2, respectively.

Under the R12 Domain tab, in the ‘Fluid 1’ options, R12 was selected as the ‘Material’.

By performing the above steps, it was possible to perform numerical analysis using supercritical R12 in CFX.

B.2 Implementing Supercritical Fluid Properties in FLUENT

In FLUENT, the National Institute of Standards and Technology (NIST) real gas model is used to calculate the physical properties of water and R12 whenever needed by the solver. This model uses the NIST Thermodynamic and Transport Properties of Refrigerants and Refrigerant Mixtures Database Version 9.0 (REFPROP v9.0. To enable this model, the following text was entered into the FLUENT console prompt (% is not entered, it symbolizes the start of the console prompt):

% define/user-defined/real-gas/nist-real-gas-model

The following question appears in the console prompt, and was answered as follows:

% use real gas? [no] yes

The list of available fluids that can be selected was then be displayed. To select either water or R12, “water.fld” or “R12.fld” was entered, respectively, making sure to include the double brackets as shown below.

% select real-gas data file [""] "water.fld"

The NIST real gas model was then enabled for water, and any information appearing in the materials panel for the fluid is ignored.

APPENDIX C: SUPPLEMENTARY MATERIAL

C.1 AISI 304L Stainless Steel Specific Heat Capacity

Table 92 gives values of thermal conductivity at various temperatures for AISI 304L stainless steel. These data were used to define the thermal conductivity of AISI 304L stainless steel in both CFX and FLUENT.

Table 92: Thermal conductivity of AISI 304L stainless steel at various temperatures. Data from Graves et al. [89].

T [K]	λ [W/mK]
333.7	14.92
354.9	15.27
380.1	15.62
380.3	15.77
402.4	16.16
423.1	16.63
450.4	17.04
450.5	17.06
474.8	17.42
476.1	17.58
573.1	18.99
673.2	20.46
975.3	24.33

C.2 Scalable Wall Functions - FLUENT

Scalable wall functions can be used in FLUENT for the k-ε turbulence models and are based on those of Launder and Spalding [82]. These wall functions only use equations that are specific to the log layer. The non-dimensional distance from the wall for this wall treatment is

$$y^*_{FLUENT} = \frac{\rho C_\mu^{1/4} k^{1/2} \Delta n}{\mu} \tag{135}$$

where Δn is the wall-normal distance between the first and second mesh points away the wall. When the value of y^*_{FLUENT} is less than 11.225, then the minimum value of y^*_{FLUENT} that is used in the equations for the wall treatment is 11.225. The variable $\tilde{y}^*_{FLUENT}$ is used in place of y^*_{FLUENT} in the boundary layer equations for this reason:

$$\tilde{y}^*_{FLUENT} = Max(y^*_{FLUENT}, 11.225) \tag{136}$$

This ensures the log layer equations are never used in a region of the boundary layer that they were not intended for. The lower value of y^* (y^*_{FLUENT}) used in FLUENT, 11.225, is very close to the minimum value of y^* (y^*_{Scale}) used in CFX, 11.06. These values represent the approximate location in the boundary layer below which the log layer equations cease to be valid.

The law-of-the-wall for the non-dimensional velocity is:

$$u^+ = \frac{1}{\kappa} \ln(9.793\ \tilde{y}^*_{FLUENT}) \tag{137}$$

The velocity can then be calculated using the following equation

$$U = \frac{u^+ (u_\tau)^2}{C_\mu^{1/4} k^{1/2} \Delta n} \tag{138}$$